CERN-THESIS-2010-269

Exclusive $\omega\pi^0$ production with muons at COMPASS

Massimo Maria BETTINELLI

München, 2010

Exclusive $\omega\pi^0$ production with muons at COMPASS

Dissertation
an der Fakultät für Physik
der Ludwig–Maximilians–Universität
München

vorgelegt von
Massimo Maria BETTINELLI
aus
Gallarate (Italien)

München, den 2. Februar 2010

Erstgutachter: Prof. Dr. Wolfgang Dünnweber
Zweitgutachter: Prof. Dr. Otmar Biebel
Tag der mündlichen Prüfung: 25. März 2010

Contents

List of Figures

List of Tables

Zusammenfassung

In der vorliegenden Arbeit wird die exklusive Reaktion $\mu+N \to \mu'+\omega\pi^0+N$ aus Kollisionen eines polarisierten Myon Strahls (160 GeV/c Impuls) gegen ein polarisiertes ^{6}LiD Target untersucht. Das Ziel ist die quantitative Bestimmung des Spin-Parität (J^P) 1^--Anteils im $\omega\pi^0$ Signal, das in theoretischen Modellen mit der ersten radialer Anregung des $\rho(770)$ Meson mit Masse $\sim$ 1250 MeV/c^2 identifiziert wird. Der konkurrierende 1^+-Zustand in diesem Massenbereich ist das bekannte $b_1(1235)$, mit dominantem $\omega\pi^0$-Zerfall.

Die Leistungsfähigkeit des elektromagnetischen Kalorimeters ECAL2 wurde mittels exklusiver ω-Produktion untersucht und das Vorhandensein schlechter Kristalle nachgewiesen. Es stellte sich heraus, dass der Beitrag der Energieeichung eines einzigen Kristalls zu der beobachteten π^0-peak Breite klein ist.

Die $\omega\pi^0$-Selektion für das $\omega\pi^0$ ergibt den kinematischen Bereich der Reaktion: quadrierte Masse des virtuellen Photons (γ^*): $\langle Q^2\rangle \sim 10^{-1}$ (GeV/c^2)^2; Bjorken Variable: $\langle x_B\rangle \sim 10^{-3}$; Energie in dem Photon-Nukleon-Schwerpunkt Ruhesystem: $\langle W\rangle \sim$ 13.5 GeV; Steigung der exponentiellen t-Verteilung: $b = 5.27 \pm 0.29$ GeV^{-2}. Der Untergrund aus falsch identifizierten ω in dem exklusiven $(\pi^+\pi^-\pi^0)\pi^0$ Quartett wurde dank eines Fits der assozierten λ-Verteilung in Höhe von $19 \pm 4\%$ ($< 11\%$ im $\omega\pi^0$-Peak für inkoherente Streuung) festgestellt.

Die Spin-Parität im Signal wurde durch die Betrachtung zahlreicher Winkelverteilungen für die relativen Orientierungen von Myon Streu-, $\omega\pi^0$-Produktions- und Zerfallsebenen untersucht. Akzeptanzkorrekturen wurden mit Hilfe eines selbstentwickelten Monte Carlo Generators berechnet.

Wir beobachten einen $42.1 \pm 29.2\%$ starken $J^P = 1^-$-Anteil im $\omega\pi^0$-Peak ($77.2^{22.8}_{-35.2}\%$ für inkoherente Streuung), kompatibel mit theoretischen Vorhersagen. Für diesen Anteil gilt die Erhaltung der Helizität für $\gamma^* \to \omega\pi^0$ (SCHC). Der ungefähr gleich starke b_1-Anteil stammt aus non-SCHC Prozessen. Die obere Grenze für SCHC b_1-Produktion beträgt 4.2%. Die zwei Spin-Parität Systeme zeigen keine Interferenz miteinander.

Unsere Ergebnisse sind mit einer ρ'-Produktion via SCHC Pomeron- und b_1-Produktion via spin-flip, non-SCHC Reggeon Austausch kompatibel.

Chapter 1

Introduction

The exclusive photoproduction of an $\omega\pi^0$ mesonic system has been investigated with much interest since a long time, aiming at the identification of a low-mass radial excitation of the ρ meson.

An early LBL-SLAC hydrogen bubble chamber experiment [B$^+$74] studied the photoproduction reaction

$$\gamma p \to \pi^+\pi^- p + \text{neutral(s)} \tag{1.1}$$

by means of polarized photon beams of three different energies below 10 GeV, and observed an enhancement at 1240 MeV/c^2 for the mesonic system recoiling against the proton; they were able to show that $\omega(\pi^+\pi^-\pi^0)\pi^0$ was the major decay mode, compatible with a $J^P = 1^+$ b_1 meson, a 1^- unestablished meson or background from Deck effect through diffractive production. The angular correlations were found compatible with s-channel helicity conservation (SCHC) in the production mechanism.

Improvement came from a subsequent experiment [A$^+$80], where the neutrals could be fully reconstructed. Using a photon beam in the energy range 20–70 GeV, an exclusive $\omega\pi^0$ enhancement with mass $\sim$ 1250 MeV/c^2 and width $\sim$ 300 MeV/c^2 was observed to be diffractively produced. Assuming the validity of SCHC and inspecting angular correlations in the decay process, a mixed spin-parity with a dominant 1^- contribution was reported. However, without the SCHC hypothesis, other solutions could not be excluded.

A further investigation at CERN [A$^+$84] by the Omega Photon Collaboration, using polarized photons in the same energy range as in [A$^+$80], came to opposite conclusions, finding the data consistent with a non-SCHC production mechanism of the (1^+) $b_1(1235)$ meson with a small s-wave background of the same spin-parity, as might be expected from a Deck effect mechanism. Only about 20% could be ascribed to 1^-. This contribution was interpreted as $\omega\pi^0$ decay in the tail of the $\rho(770)$. If 0^- was allowed in their fit, a solution with about an equal amount of 1^- and 1^+ could not be excluded. In addition, the diffractive production mechanism was confirmed.

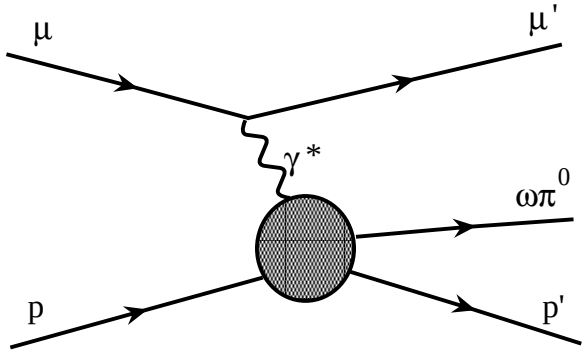

Figure 1.1: *Exclusive $\omega\pi^0$ leptoproduction with muons at the COMPASS experiment.*

The previous interpretation was confirmed by an experiment at SLAC [B$^+$88], whose data "*marginally*" (in their words) favoured a b_1 interpretation and were inconsistent with s-channel helicity conservation.

The controversial experimental situation has been reviewed by Donnachie and Kalashnikova [DK02], including results from e^+e^- annihilation and τ decay. In their interpretation, two 1^- states with mixed configurations are present between the ground state $\rho(770)$ and the only other established recurrance $\rho'(1700)$. The latter fits well in the constituent quark model as the first orbital excitation 1^3D_1. The two additional states are the one at 1250 MeV/c^2, with dominant $q\bar{q}$ configuration 2^3S_1, being the first radial excitation and decaying preferably via $\omega\pi$, and the heavier one at about 1450 MeV/c^2 with dominant hybrid or quartet configuration, preferring alternative decay channels like, e.g., $a_1\pi$.

A subsequent experimental study of the annihilation reaction $\bar{p}n \rightarrow \omega\pi^-\pi^0$, performed by the Crystal Barrel Collaboration [A$^+$04], supports such scheme, suggesting three ρ excitations at 1200, 1400 and 1700 MeV/c^2. The lowest-lying state stands out by dominant $\omega\pi^0$ decay, in contrast to other 4π decays not related to the ω. The 1^- candidate at 1200-1250 MeV/c^2 is not recognized as a resonance by the Particle Data Group [A$^+$08b], whereas the $\rho(1450)$ is an established resonance.

Concerning b_1 and ρ' competition in photoproduction, Donnachie [Don05] has suggested that helicity-flip reggeon exchange, resulting in b_1, should prevail at the mean energies of refs. [A$^+$84, B$^+$88], while helicity-conserving pomeron exchange, resulting in ρ', should dominate at higher energy.

In the following, we report on $\omega\pi^0$ leptoproduction via quasi-real photons in inelastic muon scattering (Figure 1.1). Following [Don05], at the available γ^*p center of mass energy of about 13 GeV, b_1 and ρ' production should be of comparable size.

1.1 Kinematic of exclusive meson leptoproduction

Exclusive meson leptoproduction

$$l + N \rightarrow l' + v + N \tag{1.2}$$

is generally described in the context of the so called *one photon exchange* approximation, where the scattered lepton interacts with the target nucleon via the exchange of a single virtual photon (Figure 1.1). Such approximation has been tested in the past in various experiments, and was found not to be in contrast with the data.

If $k = (k^0, \vec{k})$ and $k' = (k'^0, \vec{k'})$ are the 4-momenta of the incoming and scattered lepton l and l', p and p' the corresponding 4-momenta for the nucleon target before and after the collision, and v the 4-momentum of the exclusively produced vector meson, the following quantities completely characterize the reaction:

- The 4-momentum of the exchanged virtual photon is $q = k - k'$ and the opposite of its square

  $$Q^2 = -q^2 = -(k - k')^2 \tag{1.3}$$

  characterizes the scale which can be investigated by the photon itself: Q^2 can be interpreted as the "mass" of the virtual photon, and is sometimes called the *virtuality* of the reaction. The time-component of q in the laboratory system is the energy transfer from the lepton to the hadronic system and it is defined by

  $$\nu = E - E', \tag{1.4}$$

  where E and E' are the energies of the beam and scattered lepton, respectively.

- The mass squared of the resulting hadronic system is given by

  $$W^2 = (q + p)^2 = (v + p')^2. \tag{1.5}$$

  The first equality is general, whereas the second one is valid for the present case of exclusive meson production. From the previous equation we see that

  $$W^2 = q^2 + p^2 + 2q \cdot p = \tag{1.6}$$
  $$= -Q^2 + M_p^2 + 2q \cdot p = \tag{1.7}$$
  $$= M_p^2 - Q^2 + 2M_p\nu, \tag{1.8}$$

  where $p^2 = M_p^2$ is the proton (nucleon) mass squared and the last line is obtained evaluating the scalar product $q \cdot p$ in the laboratory frame

(scalar products of two 4-vectors are Lorentz invariant quantities). In the laboratory system we have in fact $p = (M_p, \vec{0})$ and $q = (\nu, \vec{k} - \vec{k'})$. Note that the previous equation, taking into accout the Bjorken scale variable

$$x_B = \frac{Q^2}{2M_p\nu}, \tag{1.9}$$

can be rewritten as

$$\begin{aligned} W^2 &= M_p^2 - Q^2 + \frac{Q^2}{x_B} = \\ &= M_p^2 - \left(1 - \frac{1}{x_B}\right)Q^2. \end{aligned} \tag{1.10}$$

For elastic scattering ($x_B = 1$) we find that the hadronic system invariant mass W coincides with the nucleon mass M_p, as it must be, whereas in the inelastic range we have $0 < x_B < 1$. In general we have thus $W > M_p$, and many hadronic states can be produced once the relative threshold is reached with the appropriate Q^2 and x_B values.

- One can consider leptoproduction, in analogy to *real* photoproduction, as a 2-body scattering process of the form

$$\gamma^* + N \rightarrow v + N' \tag{1.11}$$

and then apply the formalism of Mandelstam, introducing the four variables s, t and u, defined in our case as:

$$s = (q + p)^2, \tag{1.12}$$

$$t = (q - v)^2, \tag{1.13}$$

$$u = (q - p')^2, \tag{1.14}$$

together with the equivalent ones derived from the previous applying 4-momentum conservation $q+p = v+p'$. In particular we have $W = \sqrt{s}$. Of great interest is the variable t, the *4-momentum transfer squared*. The behaviour of the differential cross section of *diffractive* scattering in hadronic and photon-induced reactions follows the law

$$\frac{d\sigma}{dt} \propto e^{-b|t|} \tag{1.15}$$

1.2 Vector meson decay angular distributions

A theoretical description of vector meson electroproduction was given by Schilling and Wolf [SW73] for the case of the (at that time already) well known ρ, $\omega(782)$ and $\phi(1020)$. The exclusive leptoproduction process can

be subdivided in three major steps: 1) the scattering of the lepton with the emission of a virtual photon γ^*, 2) the interaction with the target nucleon (or nucleus) and 3) the decay of the produced vector meson. Schilling and Wolf considered the decay into two or three (for the ω) pseudoscalar mesons (pions and kaons):

$$1^- \rightarrow 0^- + 0^-(+0^-). \tag{1.16}$$

For the $\omega\pi^0$, the possible existence of a vector meson states leads to the consideration of the decay

$$1^- \rightarrow 1^- + 0^-. \tag{1.17}$$

In Ref. [SW73] the interaction of unpolarized and polarized leptons with unpolarized target nucleons was also examined. In the present case, the longitudinal polarization of the COMPASS target is not taken into account, and the contributions of two opposite polarizations in the target cells are averaged.

In addition to the variables involving energies and momenta of particles as defined in the previous section, some other purely geometrical quantities, specifically angles, are needed to fully describe the vector meson leptoproduction and subsequent decay (see Figure 5.3):

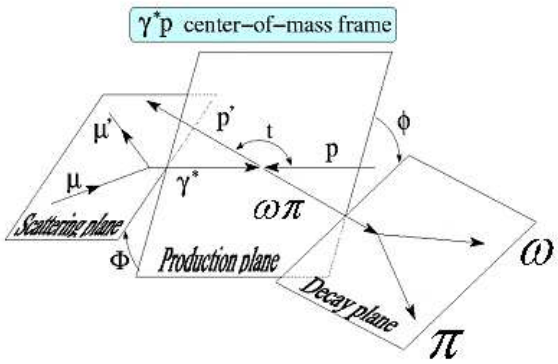

Figure 1.2: *The exclusive $\omega\pi^0$ leptoproduction and subsequent decays.*

- The azimuthal angle Φ between the *lepton scattering plane*, formed by the momenta $\vec{k}$ and $\vec{k'}$ of the incoming and scattered lepton, and the *production plane*, which contains the momenta of the virtual photon $\vec{q}$ and of the produced vector meson $\vec{v}$. A boost along $\vec{q} = \vec{k} - \vec{k'}$ into the hadronic ($\gamma^* N$) center-of-mass frame (or from this, back to the laboratory frame) leaves Φ unchanged.

- The azimuthal angle ϕ between the production plane and the *decay plane*. For two-body decays in two pseudoscalars (like the case of

$\rho \to \pi^+\pi^-$ and $\phi \to K\bar{K}$) this plane contains the direction of motion of the vector meson and of one of the decay products. In case of the three-body decay like $\omega \to \pi^+\pi^-\pi^0$, where the three pions lie in the same plane in the ω rest frame, ϕ is the azimuthal orientation fixed by the unit vector

$$\boldsymbol{n} = \frac{\boldsymbol{p}_1 \times \boldsymbol{p}_2}{|\boldsymbol{p}_1 \times \boldsymbol{p}_2|}, \tag{1.18}$$

perpendicular to the decay plane itself, where $\boldsymbol{p}_1$ and $\boldsymbol{p}_2$ are the momenta of any two out of the three pions. For the present case $\omega\pi^0 \to \omega + \pi^0$, the decay plane contains the direction of motion of the $\omega\pi^0$ (or, better, the opposite of the scattered nucleon direction) and of the ω in the $\omega\pi^0$ rest frame. Also ϕ remains unchanged after a boost from the overall $\gamma^* N$ rest frame to the (vector) meson rest frame.

- The polar angle θ: for a two-body decay, this angle is formed by the direction of motion of one of the daughter particles in the parent rest frame, respect to the parent particle momentum direction; in case of a three-body decay, it represents the polar orientation of the previously defined vector $\boldsymbol{n}$.

1.2.1 The photon spin density matrix

The differential cross section for scattering of the lepton l against the nucleon N and exclusive production of a vector meson is

$$\frac{d\sigma(lN \to l'Nv)}{dE'd\Omega d\Phi dt} = \frac{1}{16(2\pi)^5}\frac{E'}{E}\frac{m^2}{Q^4\sqrt{v^2+Q^2}}\sum_{spin}|M|^2, \tag{1.19}$$

where, apart from the already defined quantities E, E' and Q^2, we have the vector meson 4-momentum v and the matrix element of the scattering process M, which takes the form

$$|M|^2 = \frac{e^4}{m^2}L_{\mu\nu}T^{\mu\nu} \tag{1.20}$$

with $L_{\mu\nu}$ and $T_{\mu\nu}$ being the lepton and hadron tensors [SW73]. The first one can be calculated exactly from pure QED, and in the hadron c.m. helicity frame takes the form of the photon spin density matrix:

$$L_{\lambda\lambda'} = \frac{Q^2}{2(1-\epsilon)}\cdot \\ \cdot \begin{pmatrix} 1 & e^{-i\Phi}\sqrt{\epsilon(1+\epsilon+2\delta)} & -\epsilon e^{-2i\Phi} \\ e^{i\Phi}\sqrt{\epsilon(1+\epsilon+2\delta)} & 2(\epsilon+\delta) & -e^{-i\Phi}\sqrt{\epsilon(1+\epsilon+2\delta)} \\ -\epsilon e^{-2i\Phi} & -e^{i\Phi}\sqrt{\epsilon(1+\epsilon+2\delta)} & 1 \end{pmatrix}; \tag{1.21}$$

the indexes λ and λ' refer to the helicity states of the photon, Φ is the azimuthal orientation of the scattering plane relative to the production plane, ϵ is the *polarization parameter*, defined by

$$\epsilon^{-1} = 1 + 2\frac{Q^2+\nu^2}{Q^2(1-\frac{Q^2_{min}}{Q^2})}\tan^2\frac{\Theta}{2}, \tag{1.22}$$

where Θ is the lepton scattering angle in the laboratory frame, and

$$Q^2_{min} = Q^2 - 2|\vec{k}||\vec{k'}|\sin\Theta\tan\frac{\Theta}{2}. \tag{1.23}$$

The quantity

$$\delta = \frac{2m^2}{Q^2}(1-\epsilon) \tag{1.24}$$

is a factor introduced to take into account the finite lepton mass m, which is usually omitted in case of electroproduction due to the small value of the electron mass.

The previous form of the photon spin density matrix refers to the scattering of unpolarized leptons. If we take into account the polarization

$$P_\mu = P(\cos\alpha_1\sin\alpha_2, \sin\alpha_1\sin\alpha_2, \cos\alpha_2, 0), \tag{1.25}$$

where the two angles α_1 and α_2 (in polar coordinates) give the orientation of the polarization vector $\vec{P} = (P_1, P_2, P_3)$ in the lepton rest frame, we obtain, always in the helicity basis:

$$M_{\lambda\lambda'} = mQ\begin{pmatrix} P_0 & \frac{1}{\sqrt{2}}(P_1+iP_2)e^{-i\Phi} & 0 \\ \frac{1}{\sqrt{2}}(P_1-iP_2)e^{i\Phi} & 0 & \frac{1}{\sqrt{2}}(P_1+iP_2)e^{-i\Phi} \\ 0 & \frac{1}{\sqrt{2}}(P_1-iP_2)e^{i\Phi} & -P_0 \end{pmatrix}. \tag{1.26}$$

The final form of the photon spin density matrix, normalized to the unit flux of transverse photons, is then

$$\rho(\gamma)_{\lambda\lambda'} = \frac{1-\epsilon}{Q^2}(L_{\lambda\lambda'} + M_{\lambda\lambda'}). \tag{1.27}$$

The virtuality of the exchanged photon implies the presence of a longitudinal component (helicity state with $\lambda = 0$) in addition to the usual transverse polarization characteristic of real photons. The ratio of longitudinal to transverse photon flux is $\Gamma_L/\Gamma_T = \epsilon + \delta$.

The photon spin density matrix can be decomposed into an orthogonal set of nine independent hermitian matrices Σ^α, $\alpha = 0, 1, \ldots, 8$, with contributions from transverse photons ($\alpha = 0, \ldots, 3$, equivalent to the two-dimensional Pauli matrices for real photoproduction), longitudinal photons

($\alpha = 4$), and longitudinal-transverse interference terms ($\alpha = 5, \ldots, 8$). This characteristic can be put in evidence from the explicit form:

$$\Sigma^0 = \begin{pmatrix} 1 & 0 & 0 \\ 0 & 0 & 0 \\ 0 & 0 & 1 \end{pmatrix}, \quad \Sigma^1 = \begin{pmatrix} 0 & 0 & 1 \\ 0 & 0 & 0 \\ 1 & 0 & 0 \end{pmatrix}, \quad \Sigma^2 = \begin{pmatrix} 0 & 0 & -i \\ 0 & 0 & 0 \\ i & 0 & 0 \end{pmatrix},$$

$$\Sigma^3 = \begin{pmatrix} 1 & 0 & 0 \\ 0 & 0 & 0 \\ 0 & 0 & -1 \end{pmatrix}, \quad \Sigma^4 = 2 \begin{pmatrix} 0 & 0 & 0 \\ 0 & 1 & 0 \\ 0 & 0 & 0 \end{pmatrix}, \quad \Sigma^5 = \frac{1}{\sqrt{2}} \begin{pmatrix} 0 & 1 & 0 \\ 1 & 0 & -1 \\ 0 & -1 & 0 \end{pmatrix},$$

$$\Sigma^6 = \frac{1}{\sqrt{2}} \begin{pmatrix} 0 & -i & 0 \\ i & 0 & i \\ 0 & -i & 0 \end{pmatrix}, \quad \Sigma^7 = \frac{1}{\sqrt{2}} \begin{pmatrix} 0 & 1 & 0 \\ 1 & 0 & 1 \\ 0 & 1 & 0 \end{pmatrix}, \quad \Sigma^8 = \frac{1}{\sqrt{2}} \begin{pmatrix} 0 & -i & 0 \\ i & 0 & -i \\ 0 & i & 0 \end{pmatrix}. \tag{1.28}$$

1.2.2 The vector meson density matrix

So far, we have dealt with the lepton-photon vertex only. In the present picture, the virtual photon interacts with the target nucleon producing a vector meson whose properties are best described within the spin density formalism. It is customary to describe the reaction $\gamma N \to vN'$ by means of the helicity amplitudes of Jacob and Wick [JW59]

$$T_{\lambda_v \lambda_{N'} \lambda_\gamma \lambda_N} \tag{1.29}$$

where the four subscripts denote the helicities of the four particles involved in the reaction. It describes the transition from a photon state with helicity λ_γ to a vector meson state with helicity λ_v (and corresponding states for the target nucleon).

The fundamental relation between the photon and the vector meson spin density matrix is the von Neumann formula

$$\rho(V) = \frac{1}{2} T \rho(\gamma) T^+ \tag{1.30}$$

The vector meson spin density matrix is decomposed in the same way as the photon density matrix, which yields a set of nine matrices $\rho^\alpha_{\lambda\lambda'}(V)$.

The decay angular distribution for vector mesons can be written in terms of the Wigner D-function $D^j_{mm'}(\theta, \phi)$ resulting, for decay to *pseudoscalars*, in

$$W(\cos\theta, \phi) = \frac{3}{4\pi} \sum_{\lambda,\lambda'} D^1_{\lambda' 0}(\theta, \phi) \rho(V)_{\lambda\lambda'} D^1_{\lambda 0}(\theta, \phi) \tag{1.31}$$

1.2.3 Vector meson angular distribution and SCHC

Taking into account the results of the last two subsections, we obtain, for the case of exclusive vector meson leptoproduction, the following angular distributions:

$$W(\cos\theta) = \frac{3}{4}[(1 - r^{04}_{00}) + (3r^{04}_{00})\cos^2\theta], \tag{1.32}$$

$$W(\phi) = \frac{1}{2\pi}[1 - 2r^{04}_{1-1}\cos 2\phi + P_\mu\sqrt{1-\epsilon^2}\Im m(r^3_{1-1})\sin 2\phi], \tag{1.33}$$

$$W(\Phi) = \frac{1}{2\pi}[1 - (2r^1_{11} + r^1_{00})\epsilon\cos 2\Phi + \tag{1.34}$$

$$+ (2r^5_{11} + r^5_{00})\sqrt{2\epsilon(1+\epsilon)}\cos\Phi + \tag{1.35}$$

$$+ (2r^8_{11} + r^8_{00})P_\mu\sqrt{2\epsilon(1-\epsilon)}\sin\Phi], \tag{1.36}$$

$$W(\psi) = \frac{1}{2\pi}[1 + 2\epsilon r^1_{1-1}\cos 2\psi], \tag{1.37}$$

where $\psi = \phi - \Phi$ and the quantities $r^{04}_{\lambda\lambda'}$ and $r^{\alpha}_{\lambda\lambda'}$ are linear combinations of the spin-density matrix elements $\rho^{\alpha}_{\lambda\lambda'}$:

$$r^{04}_{\lambda\lambda'} = \frac{\rho^0_{\lambda\lambda'} + (\epsilon+\delta)R\rho^4_{\lambda\lambda'}}{1 + (\epsilon+\delta)R}, \tag{1.38}$$

$$r^{\alpha}_{\lambda\lambda'} = \begin{cases} \frac{\rho^{\alpha}_{\lambda\lambda'}}{1+(\epsilon+\delta)R}, & \alpha = 1,2,3; \\ \frac{\sqrt{R}\rho^{\alpha}_{\lambda\lambda'}}{1+(\epsilon+\delta)R}, & \alpha = 5,6,7,8; \end{cases}$$

$R = \sigma_L/\sigma_T$ being the ratio of longitudinal and transversal γ^*N cross sections.

Equation (1.37) is valid only if 1) the leptoproduction proceeds via SCHC, which formally reads

$$T_{\lambda_V\lambda_N\lambda_\gamma\lambda_{N'}} = T_{\lambda_V\lambda_N\lambda_\gamma\lambda_{N'}}\delta_{\lambda_V\lambda_\gamma}\delta_{\lambda_N\lambda_{N'}}, \tag{1.39}$$

and means that photon γ^* and vector meson V have the same helicity (the same is valid for the target nucleon), and 2), in the t-channel picture, *natural parity exchange* is valid, which implies the relation

$$P = (-1)^J \tag{1.40}$$

between the parity P of the exchanged particle and its spin J [SW73][1].

In addition, the validity of SCHC alone implies constant distributions for the angles Φ and ϕ ($W(\Phi) = W(\phi) = 1/2\pi$), whereas the quantity r^{04}_{00} which appears in the formula for $\cos\theta$ is directly related to R, permitting the determination of the relative contribution of longitudinal versus transverse vector meson production.

[1] *unnatural* parity exchange is defined by the similar relation $P = -(-1)^J$

Chapter 2

The COMPASS experiment

The *COmmon Muon Proton Apparatus for Structure and Spectroscopy* (COMPASS) (Figure 2.1) is a fixed target two stage magnetic spectrometer installed at the end of the M2 extraction line of the SPS[1] machine at CERN.

After the commissioning phase, which took place until 2001, data for physics analysis with a polarized 160 GeV/c μ^+ beam were taken during the years 2002-2007, with a break in 2005 due to commissioning work at the PS[2] and SPS machines in view of the LHC[3] start-up.

At the end of the 2004 data taking, a 190 GeV/c hadron beam, consisting mainly of π^- ($\sim$97%) and K^- ($\sim$3%) with a tiny contamination of antiprotons ($\bar{p}$), was used to test the spectrometer response in view of the planned hadron program.

The two stages of the spectrometer, the upstream *Large Angle Spectrometer* (LAS) and *Small Angle Spectrometer* (SAS), were developed to detect reaction products in different kinematical ranges. The LAS, covering a larger angular acceptance, detects low momentum charged particles, which are strongly bent in the magnet field of the first magnet SM1 positioned immediately after the target region, whereas the SAS detects higher momentum charged particles which are mainly influenced by the magnetic fields of the second magnet (SM2) positioned far downstream.

A Cherenkov detector based on a ring imaging technique gives informations about the particle nature in the momentum range $5 < p < 50$ GeV/c.

The electromagnetic and hadronic calorimetry complete the information about the produced particles.

Muons are selected with the help of two Muon Walls (MW1 and 2), which are iron (for MW1) and concrete (for MW2) walls sandwiched between scintillation hodoscopes. Since hadrons are mostly absorbed in the walls,

[1] Super Proton Synchrotron
[2] Proton Synchrotron
[3] The Large Hadron Collider

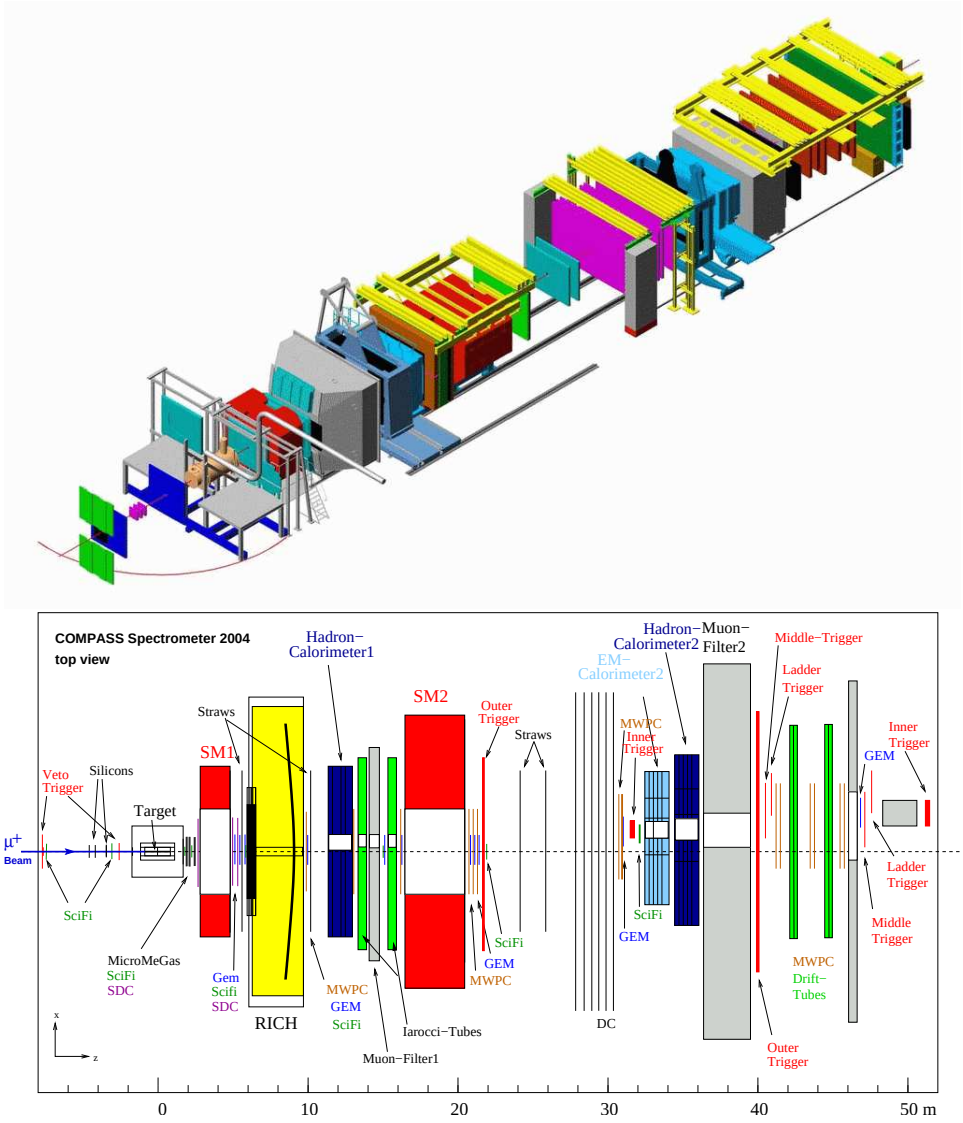

Figure 2.1: *The COMPASS experiment: a pictorial (top) and detailed top view (bottom) of the 2004 setup, showing the disposition of the various spectrometer components along the beam axis z.*

tracks reconstructed after the muon walls have a very low probability to be hadrons, and are thus tagged as muons.

A general description of the apparatus and a detailed discussion of each of its hardware components (polarized target, tracking system, particle identification by means of Cherenkov detectors and energy measurment with hadron- and electromagnetic calorimeters) can be found in ref. [A$^+$07a], together with a description of the Detector Control System (DCS) and of the Data Aquisition System (DAQ).

In the following sections, we briefly outline the main characteristics and purpose of each spectrometer subsystem. For more precise and complete informations about the physics program of COMPASS, the reader is referred to references [BKT96] and [A$^+$07a].

Published results can be found in references [A$^+$05a, A$^+$05c, A$^+$05b, A$^+$06, A$^+$07c, A$^+$07b, A$^+$07d, CA$^+$, A$^+$08a, A$^+$09a, A$^+$09b].

2.1 The polarized muon beam

For the muon program, positively charged muons were obtained from the decay of π^+, which are in turn produced from the interaction of protons coming from the SPS with target. More precisely, with a duty cycle of ∼4 s within a period of ∼16 s, protons are extracted from the SPS and directed against a beryllium target: the produced hadrons, mainly pions and kaons, are momentum selected by means of bending magnets and directed against an hadron absorber, located about 600 m downstream. Along this path, the decays

$$\pi^+ \to \mu^+ + \nu_\mu$$
$$K^+ \to \mu^+ + \nu_\mu$$

take place. The produced muons can propagate through the absorber and become available for physics in the spectrometer, whereas hadrons are fully absorbed.

The polarization of the beam is a direct consequence of the maximal parity violation in π and K leptonic decay. The muon polarization P_μ is

$$P_\mu = -\frac{\cos^2\frac{\theta}{2} - r\sin^2\frac{\theta}{2}}{\cos^2\frac{\theta}{2} + r\sin^2\frac{\theta}{2}}$$

where θ is the angle between the μ^+ and $\pi^+(K^+)$ directions in the rest frame of the decaying meson, and the constant r is the ratio squared

$$r = \left(\frac{m_\mu}{m_{\pi,K}}\right)^2$$

between the muon mass m_μ and the decaying meson mass $m_\pi(m_K)$. Figure 2.2 shows the dependance of the muon polarization on the decay angle θ,

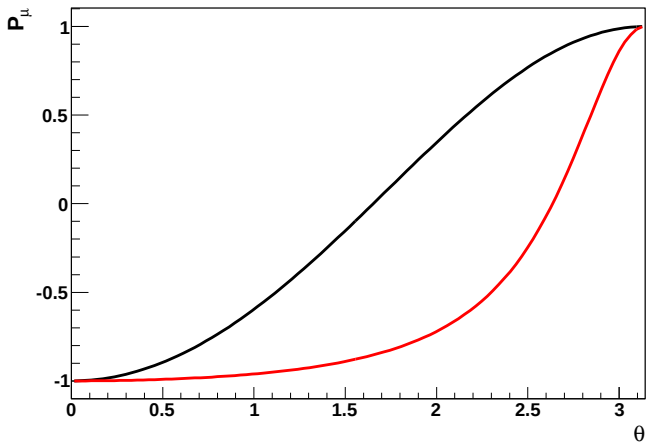

Figure 2.2: *Muon polarization P_μ as a function of the decay angle θ between the μ and decaying meson in its rest frame: π (black line) and K (red line).*

calculated from the previous formulae. The polarization has a minimum (maximum) for $\theta = 0(\pi)$, and decreases with increasing angle. If one selects muons with a high longitudinal momentum in the laboratory system, corresponding small values for θ can be obtained, once the boost to the $\pi(K)$ rest frame is taken into account, and a high grade of polarization in the beam can be achieved. The primary pion beam is not strictly monoenergetic, and the same holds for the muon beam. Due to the fact that COMPASS takes advantage of the same muon beam as the SMC experiment, no direct polarization measurement was made. The polarization calculation, performed with the aid of a Monte Carlo simulation, gives, for a 160 GeV/c muon beam, an average polarization

$$P_\mu = -0.75 \pm 0.04,$$

in good agreement with the SMC measurement.

Beam momenta are measured in the *Beam Momentum Station* (BMS), which is schematically shown in Figure 2.3.

2.2 The polarized target

COMPASS has so far taken advantage of different targets, depending on the nature of the physical goals.

For the muon program, the use of a new polarized target and new superconducting magnet with a high acceptance (±180 mrad) was originally planned, but due to serious problem during its development, the old SMC target (Figure 2.4) was employed during the years 2002-2004. It consisted

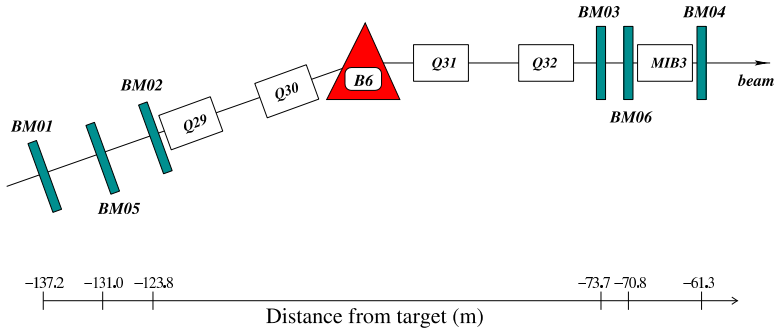

Figure 2.3: *Layout of the COMPASS BMS for muon beam.*

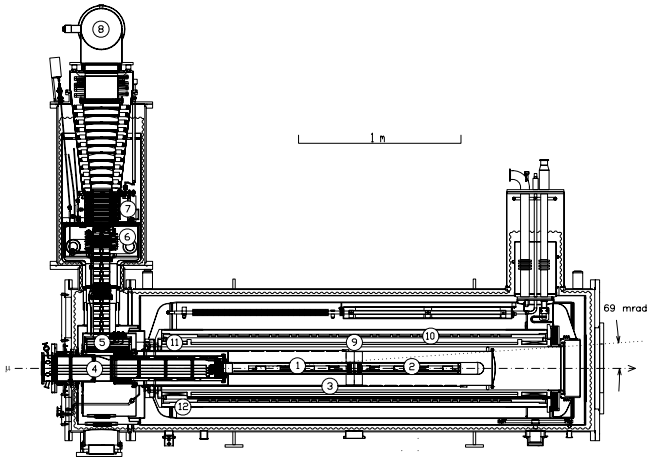

Figure 2.4: *The SMC two-cells polarized target used at COMPASS in 2004.*

of a solid ^{6}LiD two cell apparatus maintained at a temperature below 1 K by means of ^{3}He-^{4}He dilution. The two cylindrical cells were each 60 cm long with 3 cm diameter, and were separated by a 10 cm wide gap. The cells had opposite polarization, which could be periodically rotated in both at the same time. Two main configurations were adopted: longitudinal and transversal polarization. This could be obtained by means of a strong magnetic field (2.5 T) with a high homogeneity along the cells ($\Delta B/B \approx 10^{-5}$). Low temperatures are needed to avoid relaxation phenomena and maintain the polarization constant over the long period.

In the year 2006 the foreseen magnet and target were delivered to the Collaboration, and a further modification was made: the two cells were replaced by a three cell module, maintaining the previous material: The upstream and downstream cells were shortened to 30 cm length, whereas the central cell remained 60 cm long. The polarization configuration could be chosen to be $(+,-,+)$ or $(-,+,-)$.

During year 2007, the target material was substituted by polarized am-

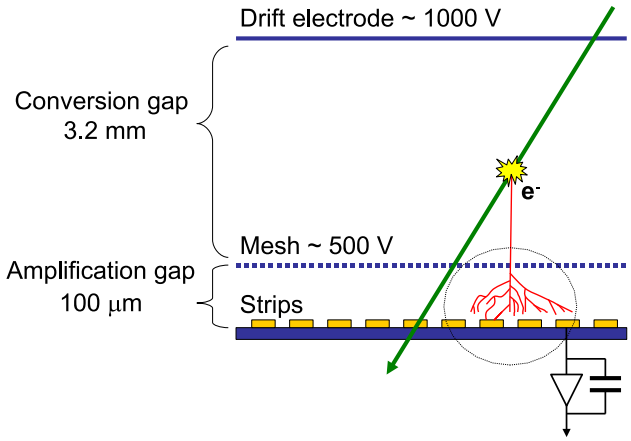

Figure 2.5: *Principle of a Micromega detector.*

monia (NH_3).

2.3 Tracking detectors

At COMPASS, track reconstruction is achieved using a rather complicated set of different detectors, which covers different kinematical regions of the particles to be detected. In principle, the track detectors can be divided in three groups:

- the *Very Small Area Tracker* (VSAT), placed in the immediate vicinity of the beam region, are exposed to a high flux of particles and are characterised by a good spatial and time resolution. We can distinguish two different types of *Scintillating Fiber Station* (the so called SCIFI-J and SCIFI-G), with time resolution of ≈400 ps, which are used to get the right timing in the event; the *Silicon Detectors* (SI), placed upstream the target in the muon program, which are involved in the beam reconstruction and momentum measurement.

- The *Small Area Trackers* (SAT), characterized by a larger active area, consist of Micromegas (*Micromesh Gaseous Structure*, Figure 2.5) and GEMs (Figure 2.6). They both operate by measuring the electron avalanche produced by ionising tracks in the gas which fills the detectors. Due to the high rates near the beam, the central region is deactivated to avoid unwanted discharges in the gas.

  i) COMPASS is the first high energy experiment using Micromegas. These detectors are based on a parallel plate electrode structure, with 1024 microstrips each for the readout, and a metallic micromesh which separates two regions between the plates: 1) a

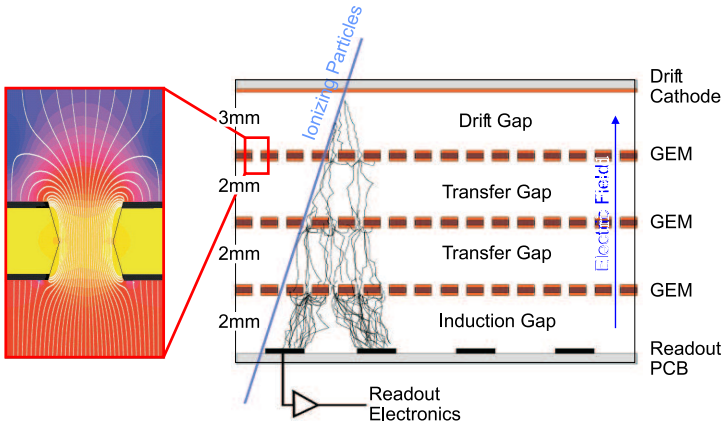

Figure 2.6: *Schematic cross section of a triple GEM detector, with the electric field lines in the micro-holes shown in the insert.*

conversion gap of about 3.2 mm width and 1 kV/cm electric field intensity, where ionisation takes place resulting in a primary electron drift, and 2) an amplification gap, only 100μm wide, with a corresponding higher electric field intensity (about 50 kV/cm), where the avalanche takes place and ions are captured by the mesh whereas electrons are captured by the readout strips. The gas mixture is $Ne/C_2H_6/CF_4$ (80/10/10), active area is 40 $\times$ 40 cm^2 with a central dead zone of 5 cm diameter. The readout strip pitch is 360 μm in the central part (512 strips) and 420 μm in the outer parts (2 $\times$ 256 strips). The average efficiency has been measured to be $\sim$97%. The twelve detector planes, which form three stations of four planes each, are located between the polarized target and the first magnet SM1.

ii) COMPASS is also the first high energy experiment to employ gaseous micropattern detectors with amplification in GEMs only. The GEM consist of a 50 μm thin Polyimide foil with Cu cladding on both sides, into which a large number of micro-holes (about $10^4/cm^2$) have been chemically etched by means of photolithographic techniques. Applying a potential difference of several 100 V across the foil, primary electrons drift into the holes when GEMs are placed in a parallel plate electrode detector filled with gas. The chosen mixture is Ar/CO_2 (70/30). Suitable electric fields extract the electron from the holes on the other side and guide them to the next stage of GEMs. After repeating the procedure with more GEMs mounted parallel to each other and separated by a thin spacer of 2 mm height, the produced electron cloud induces a fast signal in the readout anode, segmented into two sets of 768 strips with a pitch of 400 μm each, perpedicular to

each other and separated by a thin insulating layer, thus gaining space informations about the track in both the x and y directions, perpendicular to the beam axis z. The active area of a GEM is 31×31 cm^2, with a deactivated central region of 5 cm diameter (it can be activated at low beam intensity for alignment of the detectors). Eleven stations are installed along the spectrometer.

- The *Large Area Trackers* (LAT) cover the region far from beam, where the particle flux is lower and a very high resolution is not required. To this group belong conventional *Drift Chambers* (DC and W45), *MultiWire Proportional Chambers* (MWPC) and *Straw Chambers*.

2.4 Particle identification with the RICH

For every detected charged track, hadron identification is performed with the aid of a *Ring Imaging CHerenkov* (RICH-1) detector (Figure 2.7).

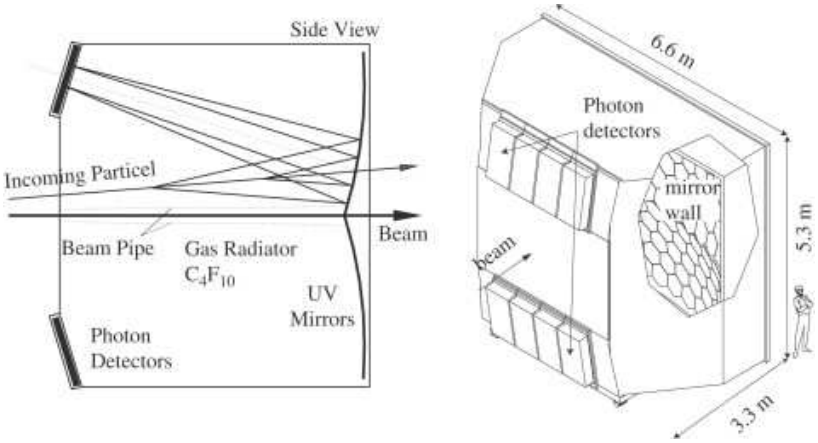

Figure 2.7: *COMPASS RICH-1: principle and artistic view.*

The RICH performs hadron identification in the momentum range 5-43 GeV/c (extended to 50 GeV/c after the upgrade of year 2006). It has a large size to cover the full LAS acceptance of $\pm$180 mrad in the vertical and $\pm$250 mrad in the horizontal plane. The radiator gas consists of high purity C_4F_{10} with low contamination of water vapour (1 ppm) and oxygen (3 ppm) to obtain a high level of light transmission through the 3 m long vessel, at the downstream end of which, a system of two spherical mirrors (formed by 116 hexagonal and pentagonal reflecting units, of a total area larger than 21 m^2), reflects the Cherenkov photons produced by the propagation of the charged track in the radiator to the *photon detectors* (PD), which are positioned outside the LAS acceptance region, in order to avoid damage and high level of background during signal extraction.

The PDs surface amounts to 5.6 m^2 and is covered by eight multiwire proportional chambers (MWPCs), filled with methane, each one divided in two submodules. MWPCs are equipped with CsI electron converters. The radiator gas and the PD are separated by a quartz window, which imposes a lower limit to the detectable wavelength at ≈ 165 nm.

The radiator gas is contained in a vessel of about 80 m^3 and temperature and pressure are continuosly monitored and kept in predefined operational ranges on the long time period of data taking. The refractive index n and the low chromaticity dn/dE_γ make it adequate for hadron identification in the particle momentum range above 5 GeV/c.

The eight PDs are subdivided in 82944 pad channels in total. This fine subsdivision permits the reconstruction of rings produced by a single particle along its path through the vessel. For the reconstructed RICH event, the mean number of detected photons, the Cherenkov angle

$$\cos\theta = \frac{1}{n\beta} \tag{2.1}$$

and its resolution can be determined (β is the velocity of the charged particle moving in the radiator gas in $c = 1$ units). The measured values are $\sim$ 14 reconstructed photons at the maximum angle θ =55 mrad with a corresponding resolution of $\sim$ 1.2 mrad

Starting from year 2006, the central part of the RICH was upgraded with the installation of a new PD system based on *Multi-Anode Photo-Multiplier Tubes* (MAPMTs) coupled to optical lenses to improve photon detection performance. About 60 photons per ring have been measured, and the obtained angular resolution is about 0.45 mrad (expected resolution: 0.3 mrad).

In addition, new hardware for high rate signal extraction was installed on the readout system side, both in the central area, to adapt to the new PDs, as in the outer regions. Lower dead time values have been reached in order to face with the high trigger rates characteristic of the experiment ($\sim$ 50 kHz).

2.5 Calorimetry

The energy of particles is measured at COMPASS by hadronic and electromagnetic calorimeters. The two stages of the spectrometer have their own calorimeter station, with the electromagnetc calorimeters (ECAL1 and 2) placed in front of the respective hadronic calorimeter counterparts (HCAL1 and 2). This configuration has been reached for the first time in 2006; starting from 2002, when only hadronic calorimeters were operative, ECAL2 was partially instrumented and began to take data in 2003; it was subsequently enlarged and completed between 2004 and 2006. ECAL1 has been taking data for physics analysis since 2006.

The HCALs are made of cells of a sandwiched activator-scintillator-plates type. The activator material is iron. The light signal from the scintillator part is extracted by wave-length-shift fibres. The measured resolutions are

$$\frac{\sigma(E)}{E} = \frac{59.4\%}{\sqrt{E}} \oplus 7.6\% \quad \text{for } \pi \tag{2.2}$$

$$\frac{\sigma(E)}{E} = \frac{24.3\%}{\sqrt{E}} \oplus 0.6\% \quad \text{for } e^- \tag{2.3}$$

for HCAL1, and

$$\frac{\sigma(E)}{E} = \frac{65\%}{\sqrt{E}} \oplus 4\% \quad \text{for } \pi \tag{2.4}$$

for HCAL2. The HCAL output is used not only for energy measurement, but also for trigger purposes.

The two ECALs have a different structure.

ECAL1 has an overall dimension of 4.00 $\times$ 2.91 m^2 to cover the angular acceptance $\pm$180 mrad of the new COMPASS polarized target. It is made up of crystals of three different types and dimensions: (i) the central part is equipped by 576 blocks of 38.2 $\times$ 38.2 mm^2 from the GAMS calorimeter (hence the name GAMS for these crystals), whereas in the intermediate region 580 blocks of 75 $\times$ 75 mm^2 from the calorimeter of the WA89 experiment at CERN have been employed (they are reffered to as the Mainz crystals). Finally, the outer part is filled with 320 blocks from the OLGA calorimeter, the dimension of each block being 143 $\times$ 143 mm^2. The resolution for this last type is known to be

$$\frac{\sigma(E)}{E} = \frac{5.8\%}{\sqrt{E}} \oplus 2.3\%. \tag{2.5}$$

The central region of ECAL1 is empty, the hole leaving the high momentum particles to freely pass through and be detected in the second stage of the spectrometer. The corresponding acceptance region is covered by the calorimetry in the SAS.

ECAL2 [A$^+$07a] is made of 2972 lead glass crystals from the GAMS-4000 experiment (Figure 2.8 for a view of one of such modules). The crystals are disposed in a matrix of 64 $\times$ 48 raws$\times$columns and each module has a dimension of 38 $\times$ 38 $\times$ 450 mm^3, corresponding to about 16 radiation lenghts. The central part can be (un)mounted to adapt to the needs of the different physics programs. During the measurements with polarized muons, a central hole of 10 $\times$ 10 modules was obtained, slightly shifted toward the positive x direction to leave place for the deflected beam to pass through and avoid damage of ECAL2 because of the high radiation exposure.

Concerning detection mechanism and performance, a high energy gamma ray (or an electron) produces a shower in the interaction with the active part of the calorimeter and the emitted Cherenkov light is collected by a

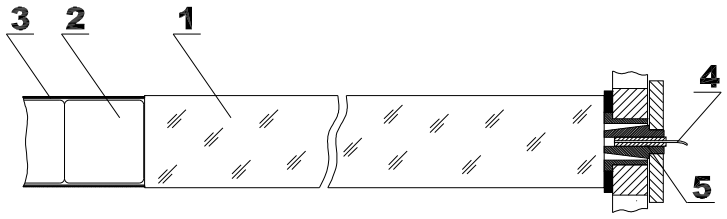

Figure 2.8: *A counter of ECAL2 calorimeter: (1) TF1-000 lead glass radiator, (2) FEU-84-3 PMT, (3) permalloy magnetic screen, (4) quartz fibre to distribute the light pulse of the monitoring system, (5) light guide connector.*

photomultiplier after propagation through the active glass. Two different types of lead glass are used in ECAL2: in fact, in the central region, a radiation hardened type obtained by adding a small quantity of cerium was employed, to cope with the higher radiation dose. For the same reason, starting from year 2007, the central region was furnished by new, radiation-hard Shashlik-type cells.

A system of LEDs is used for monitoring purposes; the calibration has been performed using a 40 GeV electron beam and was repeated during each period[4] of data taking. To this purpose, the whole calorimeter can be moved to test each crystal and only few thousend events for each module are required.

The measured values for the energy and space resolution are:

$$\frac{\sigma(E)}{E} = \frac{5.5\%}{\sqrt{E}} \oplus 1.5\%, \tag{2.6}$$

$$\sigma(x) = \frac{6\,\mathrm{mm}}{\sqrt{E}} \oplus 0.5\,\mathrm{mm}, \tag{2.7}$$

with the energy E in GeV.

2.6 The Data Acquisition System

The *Data AcQuisition* (DAQ) system is schematically shown in Figure 2.9. It was designed to cope with the high flux rate of 2×10^8 μ^+/spill, for a typical event size of 35 kB and a trigger rate of $\sim$10 kHz for the muon beam and a designed 50-100 kHz for the hadron beam. The 250,000 detector channels and the 580 TB data recorded per year, heavily conditioned the design.

The data from detectors are digitalized directly at the frontend by custom-designed ADCs (*Analog-to-Digital Converters*) and TDCs (*Time-to-Digital*

[4]COMPASS data are subdivided in *periods*, which corresponds to time intervals during data taking characterised by a stability in the spectrometer performance and/or setup.

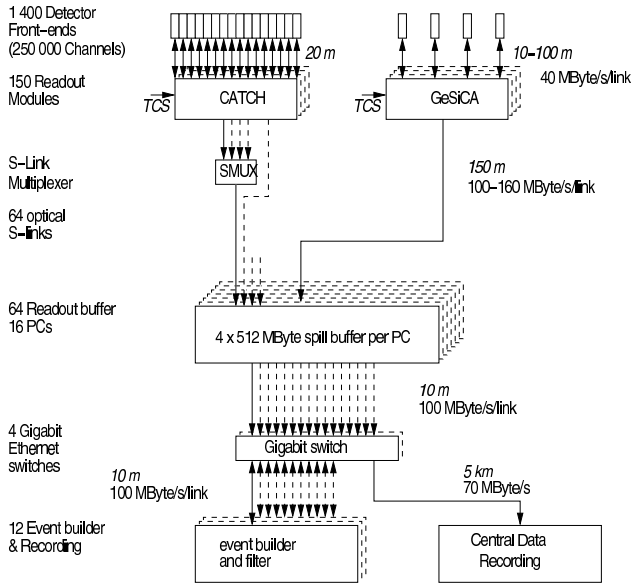

Figure 2.9: *General architecture of the DAQ system. Digitised data from the detector front ends are combined on the readout modules named CATCH and GeSiCA close to the detectors. The storage of the data during the spill and the event building is performed locally. The data are recorded at the CERN computer centre.*

Converters). This is achieved employing different types of chips coupled to the different detectors.

After this stage, the read out from the various channels grouped together is sent to CATCH (*COMPASS Accumulate, Transfer and Control Hardware*) and GeSiCA (*GEM and Silicon Control and Acquisition*) modules, where the information is formatted. These two readout components receive in addition the timing signal from the TCS (*Trigger Control System*) for synchronisation with signal digitising and event identification.

Data are subsequently directed via optical S-links to *ReadOut Buffers* (ROBs), which store the information gained during the spill. For each single event, different parts of the information generally reside at first on different ROBs. To complete the event reconstruction, all these informations must be put together, and this is achieved reading the data out of the ROBs and sending them to the *EVent Builders* (EVBs) through a Gigabit Ethernet switch. The event bulding is performed on high performance PCs, and takes place during the in- and off-spill time.

After this task is completed for all the events of a single run, which consisted until 2004 of about 100 spills grouped together, the data are sent back to the switch, which now redirects them to the *Central Data Recording* (CDR), where they are stored for a limited amount of time on hard disks

of the *COMPASS Computing Facility* (CCF), until they are finally copied on tape on the *CERN Advanced STORage* (CASTOR) system. This data sample constitutes the so called *raw data*.

2.7 The event reconstruction with CORAL

The starting point of every physics analysis is the collection of events obtained from measurement.

The various signals from the channels of a particular set of detector must be used to reconstruct the event, i.e. to determine the topology of the event, the number of tracks, their momenta, the type of particle associated to each tracks etc.

This is a rather complicated task, that begins with the raw data stored on tape at CASTOR. The mean event size at this stage is about 40 kB, and the information in the raw data are basically the readout of every single channel from every detector.

The event reconstruction is performed by the *COmpass Reconstruction and AnaLysis* (CORAL) program in four subsequent steps:

Decoding: Information about the hits in the detectors, which is stored in raw data in a particular format, are associated with the help of mapping files to the particular physical detector in which a hit was found. The spatial positions of the hits are thus obtained.

Clusterization: If a particle has interacted with a detector producing a hit in a particular channel, it is probable that other hits are found in neighbour channels. The clusterization process finds and clusters these hits together and calculates the position where the interaction took place, weighing the coordinates of all hits concerned with their relative signal amplitude.

Tracking: This is a rather complex procedure, aiming to find a particle track starting from the reconstructed clusters. For this purpose, five different regions are defined along the spectrometer where the effect of magnetic bending and multiple scattering in the detectors' material is considered to be negligible. As a consequence, charged particles are expected to propagate following a straight path. The five zones are found (i) upstream the target, (ii) between target and the first magnet SM1, (iii) between SM1 and SM2, (iv) between SM2 and the second muon-wall MW2 and, finally, (v) downstream MW2.

In a first step, the tracking algorithm checks all cluster pair combinations and associates straight segments to them. The width of the path from detector to detector depends on the space resolution of the

detector itself. If other hits lie on the segment's path, they are associated to the segment. At the end, the best segment is selected by the highest number of hits and, if more than one segment shares this property, by the lowest χ^2-value from the fitting procedure.

The *bridging* follows, i.e. a procedure to associate different segments in different zones to form a unique continuous track. This task implies a precise knowledge of the values of the magnetic fields in SM1 and SM2. If more than one candidate are present after bridging, the value of a *Quality Function* (QF), based on χ^2-estimation, selects the best candidate.

As a last step, applying the *Kalman filter* algorithm and starting from the most upstream part of the track, the track parameters (the x and y position at given z, the two slopes dx/dz and dy/dz and the inverse momentum $1/p$) and the associated error matrix are calculated and their values updated recursively moving downstream along the various hits in the track.

The identification of the scattered muon(s) then follows: an identified scattered muon is a positive charged tracks whose trajectory is compatible with the hodoscope hits as given in a trigger matrix. In addition, the track must cross the entrance and the exit of the polarized target at a distance from the beam axis smaller than 5 cm.

The momenta of low energy particles emitted at large angles and not going through the SM1 aperture are calculated from their trajectory in the fringe field of the magnet, although with lower precision.

Vertexing: The tracks are now extrapolated in the target region, and vertex position and parameter (like the χ^2 of the fit which gives the vertex position) are calculated by means of geometrical cut, e.g. inspecting the distance of closest approach. Applying the Kalman filter algorithm, the vertex is located and the new information gained is used to update also the track parameters.

In addition, also so called V^0-vertices, i.e. vertices with only two outgoing and no incoming tracks, are reconstructed. This is particularly important, in view of the identification of neutral kaons and $\Lambda^0 \to p\pi^-$ decays (and charged conjugate).

At this point, cluster reconstruction in the calorimeters and a particular reconstruction algorithm for the RICH complete the information about the event.

For its particular importance in the context of the present analysis, we spend few more words on cluster recontruction in the calorimeters (the procedure is common to hadron and electromagnetic calorimeters).

The starting point is the identification of a local maximum in the energy deposition by setting a threshold value for the energy in a single cell: energy and position of the cell corresponding to this local maximum are taken as initial parameters in the shower reconstruction. The energy of the whole shower is estimated by inspecting neighbouring crystals: for low energies a 3×3 cells matrix is used, at higher energies a 5×5 cells matrix. Two local maxima can be located at nearby cells, and at this stage the two showers are not separated.

Once the expected amount of energy from the shower in each cell has been estimated, a fitting procedure is applied for a precise determination of the value of 1) energy and 2) position of the shower:

1. the energy is calculated summing the cell energies for each cell in the shower and correcting for energy leaks and shower overlaps;

2. the shower position is determined by the so called *inverse cumulative shower profile function* (for details, see [Led95]): the theoretical two-dimensional shower surface is projected to two planes perpendicular to the calorimeter surface, one horizontally and the other vertically oriented. Analytic functions with parameters optimised to hadronic and electromagnetic showers are used to fit the shower profile, and the position of the shower axis which gives the best fit to the energy distribution in the cells for the identified shower determines the x and y coordinates of the shower.

At the end of the reconstruction procedure, the data are written in so called *Data Summary Tape* (DST) files. These data are the most complete source of information for the event, but they contain much more information (like digits and hits position) than generally needed for physical analysis. To facilitate it, smaller files, so called *miniDST* (mDST) files, are produced on a run-by-run basis (if the number of events per run is too high and the mDSTs consequently too big, data are split in many smaller mDSTs), and these constitute the data sample commonly used in analysis. A mDST contains mainly two kind of information: a description of the spectrometer setup at the time the run was taken, and a very complete description of the event concerning vertices, tracks, type of the involved particles, calorimeter cluster number and energies, etc.

2.8 The analysis framework

Data which satisfy standard quality criteria are used in the analysis and inspected using the *PHysics Analysis Software Tools*[5] (PHAST) program.

[5] http://ges.home.cern.ch/ges/phast/index.html

This a software package based on ROOT libraries and written in C++, which provides the user with a set of functions to sequentially inspect the events in a sample of mDSTs, filter those ones which satisfy selection criteria established by the user writing her/his own C++ code, and create, if wished, a new, smaller mDST (often called informally microDST, μDST) which contains only the filtered events. This is a very useful characteristic of the program, which eases and speeds up the analysis procedure. As will be seen, the repeated creation of μDSTs has been frequently used in the present work. MiniDST files are written in `.root` format.

ROOT[6] is a physics analysis framework developed at CERN. It enables the storage of data as ntuples and so called *trees*, which are the extension of ntuples in the object-oriented paradigma of modern programming languages like C++, and permitting the storage of *objects* and not only of simple numerical values as is the case of ntuples. Further, it provides tools for data 1-, 2- and 3D-histogramming, fitting of data points with default or user defined functions, storage of pictures into many different formats for publishing purposes and much more.

ROOT has its own C++ interpreter, called CINT, which can handle almost all features of the C and C++ languages. This feature enables the user to write scripts to perform systematic analysis of trees and ntuples; for quick development and inspection of temporary results, a graphical user interface (GUI) is also available.

[6] http://root.cern.ch/drupal/

Chapter 3

ECAL2 performance in exclusive ω production

The performance of ECAL2 has been studied using exclusive ω production

$$\mu + N \rightarrow \mu' + \omega + N \tag{3.1}$$

followed by the decay $\omega \rightarrow \pi^+\pi^-\pi^0$, which, with a branching ratio of 89.7 ± 0.7 % [A$^+$08b], is the main decay channel of the ω.

The analyzed data correspond to the longitudinal target polarisation and were taken during year 2004.

3.1 Event selection

The events were selected by the following requirements:

- The best primary vertex (b.p.v.) is reconstructed, and 3 and only 3 outgoing charged tracks. In COMPASS, a reconstructed vertex is called *primary* if the incoming track belongs to the reconstructed beam muon; in one event, there may often be more than one primary vertex, the best one is determined by the following criteria:
  - the vertex with the highest number of tracks leaving the vertex is chosen as best primary vertex;
  - if more than one primary vertex satisfy the previous criterium, the χ^2-value obtained by the vertex reconstruction with CORAL is considered: the lowest χ^2 selects the b.p.v.

  One of the outgoing tracks must be an identified muon (the scattered muon μ'), the other two must correspond to oppositely charged particles, taken to be pions (pion mass hypothesis). No particle identification using RICH information was required.

- At least two separate ECAL2 clusters must be present in the event. To correspond to photons, no reconstructed charged tracks must be associated to the clusters (they are hence called *neutral* clusters). No other cut has been applied (e.g. a cut on the cluster energy).

- To identify the π^0, the two-photon invariant mass

$$m(\gamma\gamma) = \sqrt{2E_1E_2(1-\cos\theta)} \tag{3.2}$$

was calculated for each pair of neutral clusters in the event, and the cut 120 MeV/c^2 $< m(\gamma\gamma) <$ 150 MeV/c^2 was applied. In the previous equation, E_1 and E_2 are the measured energies of the two photons, to be identified with the measured cluster energies, and the angle θ is the $\pi^0 \to \gamma\gamma$ decay opening angle as seen in the laboratory frame. The trajectories of the two photons are assumed to originate in the b.p.v. To further improve the signal-to-background (S/B) ratio in the $\gamma\gamma$-mass spectrum, a cut on this last variable was chosen:

$$\theta < 0.025 \text{ rad.} \tag{3.3}$$

This requirement, corresponding to a lowest energy threshold $E_{\pi^0} \sim 11$ GeV for the π^0 in the laboratory system, is of a rather empirical nature, and it is based on the observation that S/B dramatically improves when the cut is applied.

- To select the exclusive sample, the missing energy in the reaction was calculated. This quantity is defined as

$$E_{miss} = \frac{M_X^2 - M_p^2}{2M_p} \tag{3.4}$$

where $M_X^2 = (p+q-v)^2$ is the missing mass squared of the hadronic system recoiling with respect to the ω, and M_p is the proton (nucleon) mass. Exclusivity requires that the target nucleon remains intact during reaction, and this corresponds to the condition $M_X = M_p$ or, equivalently, $E_{miss} = 0$. Due to the finite resolution of the apparatus, the exclusive sample was selected within the interval -5 GeV $< E_{miss} <$ 5 GeV.

- Finally, the ω-candidate was selected imposing the constraint 750 MeV/c^2 $< m(\pi^+\pi^-\pi^0) <$ 830 MeV/c^2 to the 3π-invariant-mass.

Figure 3.1 shows the exclusive $\pi^+\pi^-\pi^0$ invariant mass spectrum with all the previous selection cuts applied, with the exception of the one on the 3π-mass itself. It refers to a subsample of the whole data available (period W37); the dominant structures seen are the two peaks corresponding to exclusive ω and $\phi(1020) \to \pi^+\pi^-\pi^0$ production. For the ω, a simple gaussian fit gives for mass and width: $m_\omega = 787 \pm 22$ MeV/c^2.

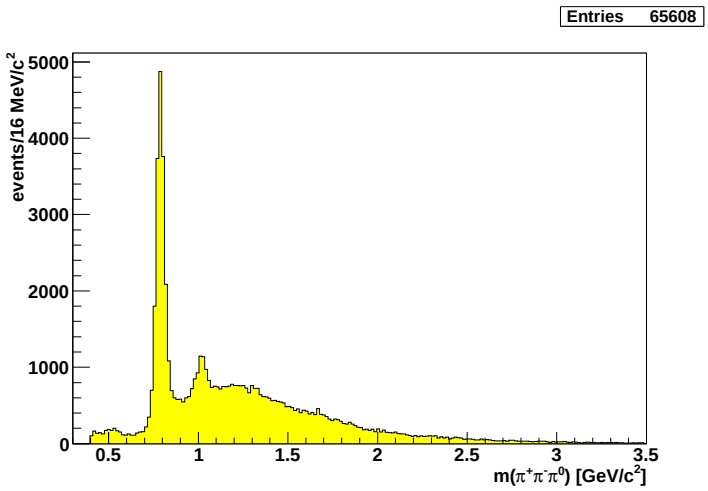

Figure 3.1: *($\pi^+\pi^-\pi^0$)-invariant mass, period W37. All selection cuts applied, except for the mass itself. Clearly visible the two peaks corresponding to the* $\omega(782)$ *and* $\phi(1020)$.

3.2 ECAL2 performance

Having a pure sample of ω's gives us the possibility to study the performance of ECAL2 in 2004 using the π^0 from the decay. In particular, the period dependence have been studied by inspecting the same set of quantities in each period.

Figures 3.2 and 3.3 show the $\pi^+\pi^-\pi^0$ invariant mass, the missing energy distribution, the 2γ invariant mass and the cluster center distribution (in the xy-plane, transversal to the beam axis z) at the calorimeter surface for two different periods (W37 and W26 respectively), which represent the typical behaviour of ECAL2 in 2004. To obtain the plots shown, all the previously listed cuts have been applied, except the one corresponding to the represented variable.

In 2004, some periods were characterized by good performance, permitting the identification of the most important physics signals, and a sample of "bad" periods, typically concentrated in the first part of the data taking, in which the signal extraction can be said to be "problematic".

In good periods (like W37), the ω and ϕ peaks are clearly seen, and the same holds for the exclusive peak centered at $E_{miss} \approx 0$ GeV; also the π^0 signal (in the plot, the π^0 peak was fitted with a gaussian superimposed to an exponential for the background) can be easily seen, characterized by the parameters $m(\pi^0) = 134.4 \pm 8.3$ MeV/c^2. The cluster center distribution in the xy-plane at the ECAL2 surface shows how most $\gamma\gamma$ pairs (2 entries/event in the plots) are found near the geometrical center of ECAL2. This is good news: as a matter of fact, the outer parts of ECAL2, expecially in the

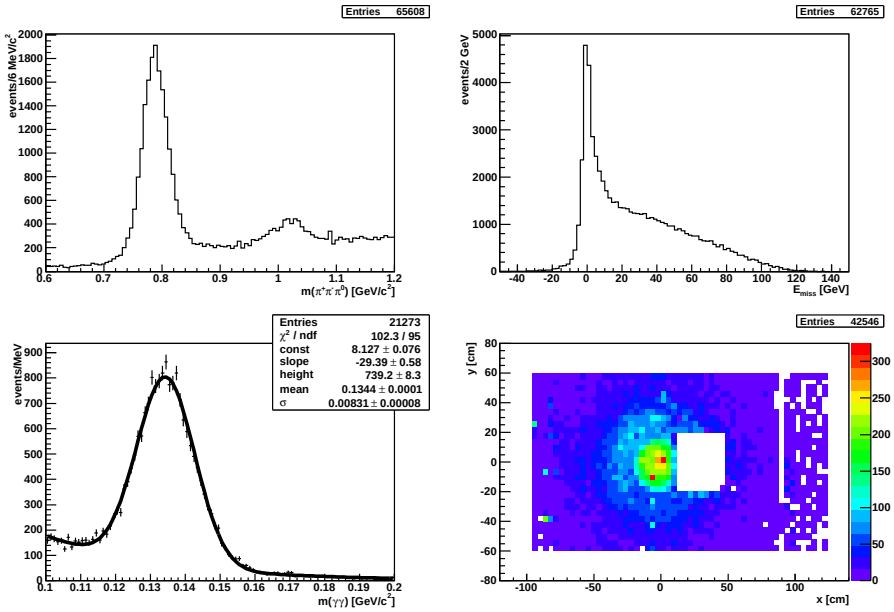

Figure 3.2: *$(\pi^+\pi^-\pi^0)$-invariant mass, missing energy, reconstructed π^0 signal and cluster center distribution (four entries/event) for a period with good ECAL2 performance (period W37).*

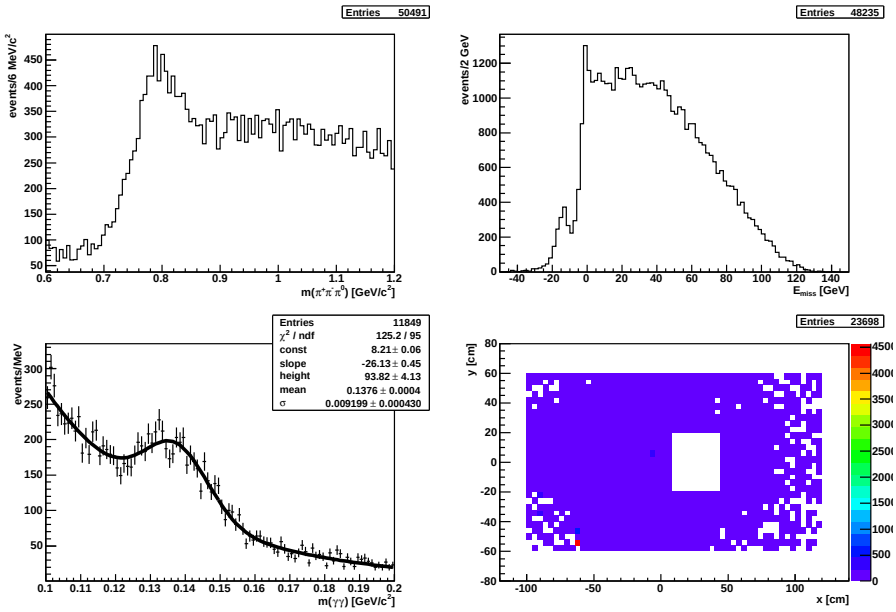

Figure 3.3: *3π invariant mass, missing energy, π^0 signal and cluster center distribution (four entries/event) for a period with bad ECAL2 performance (period W26).*

Period	$M \pm \Gamma$ (MeV/c^2)	S/B
W22	-	-
W23	141.5 ± 15.5	2.12
W26	137.6 ± 9.2	1.57
W27	133.3 ± 7.9	1.43
W28	136.2 ± 8.8	4.75
W29	135.7 ± 8.9	5.47
W30	134.7 ± 8.9	5.00
W31	134.2 ± 8.7	5.34
W32	134.0 ± 8.9	5.57
W37	134.4 ± 8.3	8.20
W38	137.9 ± 8.3	8.78
W39	139.1 ± 8.1	6.31
W40	138.2 ± 8.3	8.42

Table 3.1: *Period dependence of π^0 mass and width and signal-to-background ratio in π^0-peak.*

positive x direction (e.g., $x > 90$ cm, where one recognizes the presence of dead cells or even columns of cells), do not strongly affect the π^0 signal.

For bad periods, the quality of the data is much worse: a much smaller ω peak stands above a huge background, the ϕ peak is hardly to be seen, the missing energy shows a weak indication of an exclusive peak, which is plagued by dominant noise background; something similar is valid in the case of the π^0 signal. The usual fit (exponential + gaussian, this time applied to period W26 data) gives: $m(\pi^0) = 137.6 \pm 9.2$ MeV/c^2. We thus conclude that bad calorimeter performance affects mostly the S/B ratio rather than the value of the mass and width of the reconstructed π^0 peak.

To summarize the situation for ECAL2 in 2004:

- the first few periods (W22-23-26-27), are characterized by a bad performance, which leads to a poor determination of the π^0 peak and, consequently, of the exclusive ω-sample;

- starting from period W28, ECAL2 performance improves and remains stable (periods W33 to W36, which correspond to transverse polarisation of the target, were not analysed); small fluctuations are still observed on a period-by-period basis.

Table 3.1 shows the period dependence of the π^0 mass, width and S/B in the π^0-peak mass window. Evident is ECAL2 bad performance until period W27 (for period W22, no π^0-peak is visible in the data), and the two major improvements in S/B obtained starting from periods W28 and W37, respectively.

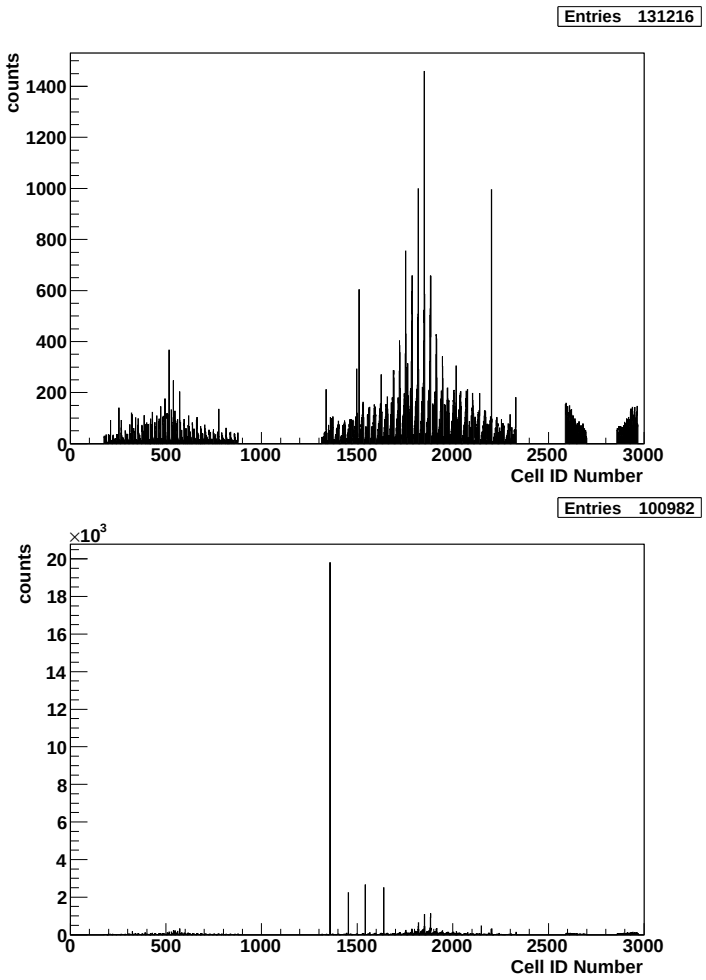

Figure 3.4: *Cluster cell occupancy for a typical good period (W37, top) and a typical bad period (W26, bottom).*

It is interesting to investigate the cause of the bad behaviour in the first part of data taking.

Let's consider a single cluster which satisfies the selection cut imposed in the analysis: it consists of a number of calorimeter crystals (cells) which are grouped together in the clusterization procedure during the event reconstruction. Every single cell has its own measured amount of deposited energy and in normal situation there is a cell with the highest energy of all: we will call this cell the *central cell*. For every identified π^0 (cluster pair) in the ω sample, a counter was inserted to determine how often a particular cell is the central cell of the respective cluster.

Figures 3.4 shows this *cell occupancy* distribution for a typical good and bad period (W37 and W26, respectively). For bad periods, few cells have

very high occupancy as compared with nearby cells. Due to the fact that, for these cells, the occupancy can be up to 100 times higher than normal neighbour cells, their contribution to combinatorics during cluster pairing becomes significant, resulting in a conspicuous amount of background under the π^0- and ω-peak. A possible cure would be the removal of such cells (after their identification) during the event selection procedure to compare the quality of the $\gamma\gamma$-spectra before and after the removal. This has been performed for each period for the case of exclusive ω production. On the contrary, in the present analysis of the $\omega\pi^0$ leptoproduction (see next Chapter), "bad" cells and runs were *not* excluded. It was checked *a posteriori* that the contribution to the exclusive $\omega\pi^0$ sample from these cells and corresponding runs with abnormal behaviour are negligible. This was found to be mostly due to the high selectivity of the cut on the mass of the $\omega(\pi^+\pi^-\pi^0)$-peak, which, with a measured width of ~ 22 MeV/c^2 [KKMN08], is a rather narrow resonance.

3.3 Contribution of calibration to the π^0 width

To study the effect on the width of π^0's peak from the calibration of the calorimeter, the spread of the contribution to the π^0 signal from a single cell was investigated. A simple method was applied (cf. [A$^+$92]): a matrix of 20×20 cells in the central region of the calorimeter was examined and for every cluster i with central cell in the matrix, the invariant mass $m_i = m(\gamma_i\gamma_j)$ for the cluster pair (i,j) was calculated, with fixed i but varying index j. For every such distribution m_i, the mean value of $m(\pi^0)$ was obtained after fitting the data with a gaussian for the signal and an exponential for background. For each one of the obtained 400 values m_i, the difference $m_i - m_{\pi^0}$ was plotted, to determine the spread of the m_i's around the "true" π^0 mass value m_{π^0}, as tabulated in the PDG [A$^+$08b]. The result is shown in Figure 3.5, and the spread is well fitted by a simple gaussian. Its width amounts to 2.5 MeV/c^2, well below the measured average width of the π^0 peak, which is of the order of 8 MeV/c^2 for 2004 data. This shows the stability and the independence on position of the calibration in the central part of ECAL2.

It is thus concluded that inaccuracies of the energy calibration of the calorimeter cells are not the primary source of the experimental π^0 width.

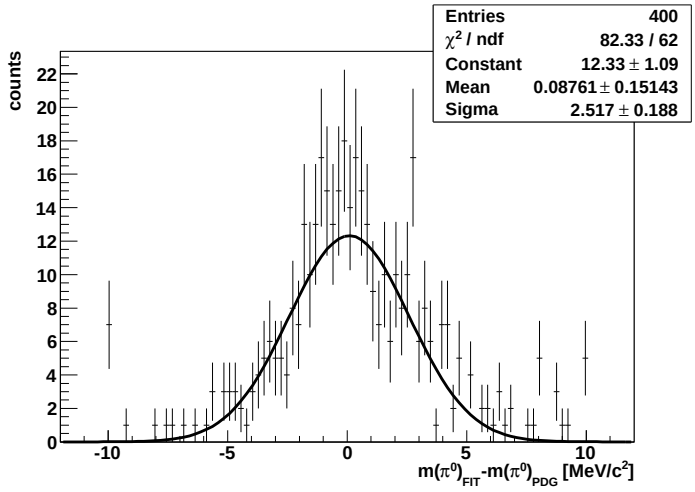

Figure 3.5: *Spread of the reconstructed π^0 mass relative to the PDG value.*

Chapter 4

Exclusive $\omega\pi^0$ leptoproduction with muons

The exclusive reaction

$$\mu + N \rightarrow \mu + \omega\pi^0 + N \tag{4.1}$$

followed by the decays $\omega \rightarrow \pi^+\pi^-\pi^0$ and $\pi^0 \rightarrow \gamma\gamma$ was investigated. The analysed data sample was recorded in 2003, 2004 and 2006. Table 4.1 lists the periods examined, which correspond to longitudinal polarization of the target only, and the number of mDST files processed.

4.1 Event selection

The event selection was subdivided in subsequent steps, each one using a particular PHAST routine, which analyzed the result of a previous selection. The selected event subsample was saved in a smaller mDST, to be inspected in the next step.

4.1.1 Event topology

To select exclusive $\omega\pi^0$ events, a first selection on the reaction topology was performed imposing the following conditions:

- a reconstructed best primary vertex (b.p.v.) with identified beam and scattered muons.
- three and only three reconstructed charged tracks leave the b.p.v.: they must correspond to the scattered muon and to the two oppositely charged tracks not identified as muons;
- no information from the RICH was used for particle identification. Particles other than beam and scattered muon were assumed to be charged pions (pion mass hypothesis);

Year	**Period**	**Number of mDSTs**
2003	P1A	203
	P1B	145
	P1C	163
	P1D	193
	P1E	292
	P1F	178
	P1I	303
	P1J	426
	Total	**1903**
2004	W22	529
	W23	338
	W26	325
	W27	188
	W28	263
	W29	218
	W30	278
	W31	249
	W32	439
	W37	398
	W38	492
	W39	276
	W40	207
	Total	**4200**
2006	W32	102
	W33	562
	W34	534
	W35	379
	W36	872
	W37	546
	W40	685
	W41	669
	W42	704
	W43	665
	W44	189
	W45	688
	W46	367
	Total	**6962**
2003+2004+2006	**Total**	**13065**

Table 4.1: *Data sample used in the present analysis.*

- *at least* four ECAL2 clusters not associated with any reconstructed charged track (neutral clusters) were found in the event. To reduce background, only clusters with energy above 1 GeV were considered for 2004 data, no such cut was applied for 2003 and 2006 data. In addition, no quality cuts concerning the reconstructed cluster, like the ratio E_{max}/E between the energy of the cell with the maximum deposited energy E_{max} (the "central" cell) and the energy E of the cluster itself, was applied. During 2006, ECAL1 was installed and taking data, but to preserve uniformity in the event selection procedure and ease comparison between different years, data from ECAL1 are ignored in this analysis.

The constraint on the number of ECAL2 neutral clusters could be made more restrictive, due to the fact that one needs only four clusters to search for the two π^0's in the reaction (4.1), but imposing this tight cut already at the beginning of the selection may lead to underestimate the number of reconstructed π^0's, and thus of $\omega\pi^0$ events in the final exclusive sample. The reason is the combinatorial background contribution which is not yet known at this point of the analysis.

Let us consider an event with, e.g., *five* neutral ECAL2 clusters, and assume that this event is a good one, i.e. out of the five clusters we are able to reconstruct two distinct π^0's (we assume that the fifth cluster is due to noise or other background). Had we at this point excluded the event from the further analysis, we would have lost one possible $\omega\pi^0$ event. The problem is of course also present for events with *more* than five clusters.

The events selected so far were saved in new μDSTs (one for each analysed run) to be used for further selection.

4.1.2 Event with at least two π^0's

Neutral pions were identified looking for all cluster pairs and imposing the cut 120 MeV/c^2 $< m(\gamma\gamma) <$ 150 MeV/c^2 on the 2-photon invariant mass

$$m(\gamma\gamma) = \sqrt{2E_1E_2(1-\cos\theta)}, \tag{4.2}$$

where E_1 and E_2 are the energies of the two photons, identified with the energy of the clusters, and θ is the angle between the photon directions as measured in the lab system. It is assumed that the π^0 decay position coincides with the b.p.v., each of the two photons propagating toward the corresponding cluster center position.

To inspect all possible pairs may become an heavy task. Figure 4.1 (left) shows, for events satisfying the preselection criteria for event topology, the number of ECAL2 neutral clusters per event. As can be seen, one faces a high cluster multiplicity in the events. Given N clusters per event, the

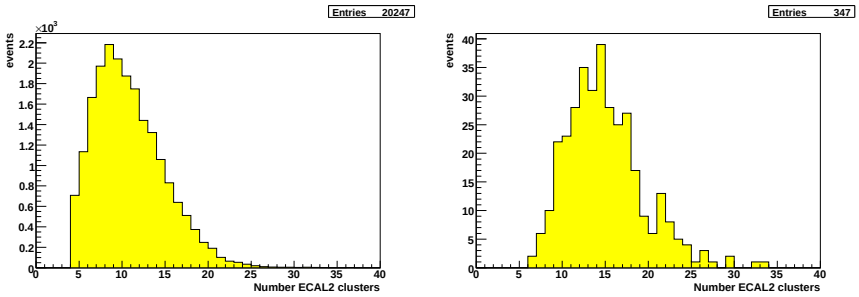

Figure 4.1: *Number of ECAL2 neutral clusters per event (after selection on event topology) in a typical run (left), and same distribution for events with a least 2 reconstructed π^0 (2006 data).*

number of possible cluster pairs is

$$\binom{N}{2} = \frac{N(N-1)}{2}$$

To search for two different π^0 we must repeat the procedure for the remaining $N-2$ clusters, which gives $\binom{N-2}{2} = \frac{(N-2)(N-3)}{2}$ possibilities. Thus the final number of possible π^0 candidates before mass selection is

$$\frac{1}{2}\binom{N}{2}\binom{N-2}{2} = \frac{N(N-1)(N-2)(N-3)}{8} \tag{4.3}$$

which grows with N like $\sim N^4$. The factor $1/2$ in equation (4.3) is needed to avoid double counts of the same pair of pions after exchange of the respective clusters. This procedure can be a very time consuming task: for the mean number of cluster $N = 9$, one has to check 378 possible π^0 pairs per event, and then find the good one imposing the cut on the 2-photon invariant mass for each cluster pair.

Figure 4.2 shows, for a typical run, the number of reconstructed π^0 (left). Most of the events have no or just one π^0 reconstructed: only in $\sim 2\%$ of the events *at least* two π^0 can be fully reconstructed (right). Figure 4.3 shows for these events the 2-photon invariant mass spectrum, when both clusters have energy $E > 2$ GeV. Here and in the following, π^0 *identification always implies this cut on cluster energy* (the energy value 2 GeV has been chosen in order to reduce the large background due to clusters with a lower energy). Without the cut no π^0 peak can be distinguished.

The new, smaller, μDST written so far contains events of the previous sample, i.e. events with *at least* two π^0.

An important aspect must be kept in mind at this point of the selection: a π^0 candidate is individuated by a cut on the $\gamma\gamma$ invariant mass. Each pair of photons, i.e. each pair of neutral cluster with energy $E > 2$ GeV, corresponds to a pair of cluster indexes (i_1, i_2). Let us suppose that pairs

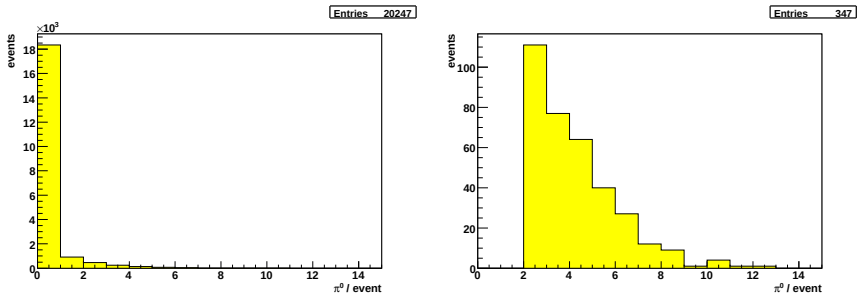

Figure 4.2: *Number of reconstructed π^0 per event in a typical run (left), and same distribution for events with a least 2 reconstructed π^0 (2006 data). A cut on cluster energy ($E > 2$ GeV) has been applied.*

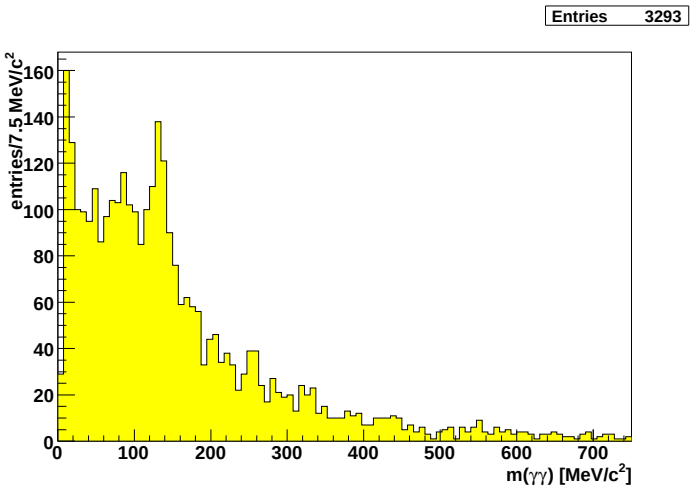

Figure 4.3: *The 2-photon invariant mass for events with at least four reconstructed neutral clusters. The spectrum shows results from a typical run from 2006 data.*

$(1,2)$ and $(1,3)$ correspond to invariant masses in the allowed region for π^0 selection: it is clear that we face an ambiguity, only one pair can correspond to a real π^0 (if any). In a first step of the selection, this fact was not taken into account, with the aim to gain informations about the quality of the $\pi^+\pi^-\pi^0$ mass spectrum and relative background contribution.

Nevertheless, a counter has been introduced to determine in the same event sample the number of π^0 pairs, with indexes (i_1, i_2) for the first pion, and (i_3, i_4) for the second, where all the four indexes are different from each other. The aim was to select all the possible configuration of the type:

$$\mu + N \rightarrow \mu' + \pi^+\pi^-\pi^0\pi^0 + X, \tag{4.4}$$

where X indicates the unobserved hadron recoil system (equal to N for exclusive events). The problem to face here is the possibility to have more than one single pair of π^0's. We can face, e.g., the following situations:

i) the cluster pairs are $(1,2)$ and $(3,4)$: this event is a good candidate for reaction (4.4).

ii) $(1,2)$ and $(1,3)$: this event has two π^0-candidates, but only one of them (if any) can be a real π^0, because the two candidates have now a cluster in common and *accidentally* both have a 2-photon invariant mass in the correct mass-window. The event must then be rejected, as will be done in a subsequent step.

iii) $(1,2)$-$(3,4)$ and $(1,2)$-$(5,6)$ are good candidates: in this case we can speak of an event with three different reconstructed π^0's and two possible π^0-pairs. This is ambiguous, but it was not rejected: each of the two possibility could in fact form a good ω-candidate in a subsequent step of the event selection. For the case of two different good ω candidates, the rejection takes indeed place at a later point during analysis.

iv) The contribution due to the combinatorial background of the $\pi^+\pi^-\pi^0$ and $\pi^+\pi^-\pi^0\pi^0$ spectra (for the exclusive and non-exclusive sample as well) comes from the case in which, e.g., the pairs $(1,2)$-$(3,4)$ and $(1,3)$-$(2,4)$ are both valid π^0 pairs. This events were not rejected, a decision thus taken in the subsequent steps of the analysis.

Point iv) illustrates the general problem of combinatoric, which become more and more important the higher the number of π^0-candidates that can be found in the event.

4.1.3 The ω and $\omega\pi^0$ selection

Out of these new μDST, the invariant mass of each $\pi^+\pi^-\pi^0$ triplet (e.g., from period W43 in year 2006) is shown in Figure 4.4. Clearly visible is the

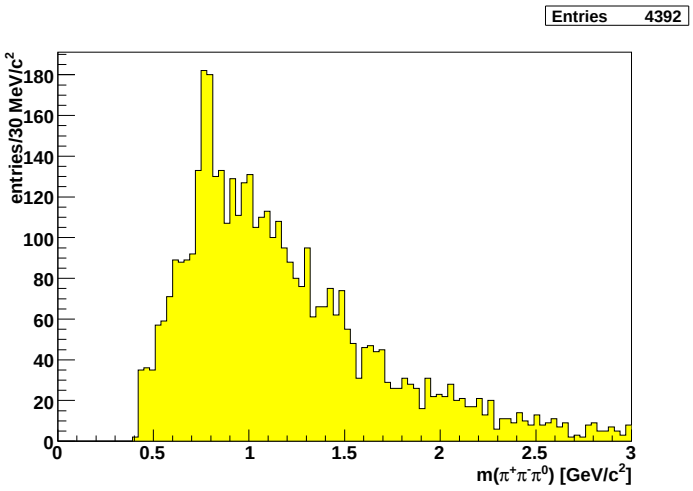

Figure 4.4: *Invariant mass spectrum for identified $\pi^+\pi^-\pi^0$ triplet. Due to selection, there can be more than one entry per event. The ω-peak at $\sim$ 782 MeV/c^2 can be seen over a large combinatorial background.*

ω peak at a mass of $\sim$ 782 MeV/c^2, outstanding over a large combinatorial background. From the event sample selected so far, consisting of events with at least 2 neutral pions, a new subsample was created with the following cuts:

- The selection of the ω was performed imposing the condition 750 MeV/c^2 $< m(\pi^+\pi^-\pi^0) <$ 810 MeV/c^2. The number of different $\pi^+\pi^-\pi^0$ triplets in this mass range is shown in Figure 4.5 (left): only a tiny fraction of the events has *at least* one ω-candidate (there are events in which the cut on the 3π mass gives up to five possibilities, to select an ω from the data). From the knowledge gained during the study of ECAL2 performance by means of exclusive ω production, *bad*

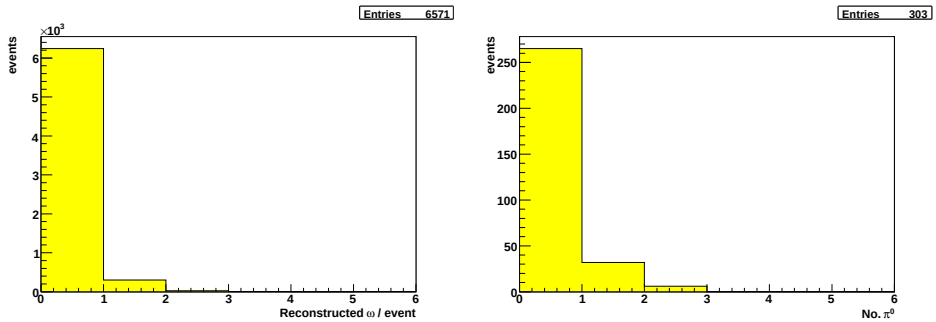

Figure 4.5: *Number of ω candidates per event (left) and, for event with one and only one ω, number of reconstructed additional π^0 (period 06W42). Only the sample with one single π^0 was chosen for the further analysis.*

periods of year 2004 were excluded from analysis; these are periods W22-23-26-27-28.

- In view of the spin-parity study for the final $\omega\pi^0$ system, we need to avoid such uncertainties in the ω identification. We then searched for events with a uniquely identified ω. Events with no or more than one candidate were rejected. The amount of events with *more* than one candidate relative to the sample with *at least* one candidate is found to be about 7-8 %, small fluctuations are period-dependent.

- In the same Figure 4.5 (right), the number of reconstructed π^0 other than the one used for ω identification is shown. The histogram refers to events with *one and only one* ω.

Few words of comment are useful about this last figure: having a sample with at least two π^0 per event, one of them forming with the charged pions a 3π system with invariant mass in the right mass range for an ω, one would expect to have always *at least* one other π^0. Figure 4.5 (right) shows clearly that this is not the case in the majority of combinations. The reason is simple and can be reconduced to what explained about the difference between the requirement to have at least two possible π^0 and the requirment to have at least *one pion pair*. In the π^0-selection so far we have selected events of the first type. The sample with no second pion, which amounts to about the 87% of the events with one single identified ω, corresponds to those events where the pion candidate which survives the mass cut has at least one of its two clusters in common with those used to reconstruct the π^0 associated to the ω-candidate. This is indeed to be expected, due to the high level of background under the π^0 peak visible in Figure 4.3.

A new subsample was thus selected requiring not only one single ω-candidate in the event, but *one and only one* further π^0, whose cluster indexes are distinct from those of the π^0 of the identified ω.

In addition, the number of ECAL2 cluster in the event was inspected, and events with only four ECAL2 neutral cluster with energy $E > 2$ GeV were selected: this corresponds to the 45% of the so far selected $\omega\pi^0$'s. The purpose here has been to obtain the cleanest $\omega\pi^0$ sample from which to select the exclusive sample.

We point out that, at this point of the analysis, we deal with an event sample corresponding to the reaction

$$\mu + N \rightarrow \mu' + \omega\pi^0 + X, \tag{4.5}$$

where X indicates the unobserved system recoiling opposite the $\omega\pi^0$ and which in general differs from the target nucleon N. The case $X = N$ corresponds to exclusive production, discussed in the next section.

4.1.4 Exclusive $\omega\pi^0$ sample

Within the sample of uniquely reconstructed $\omega\pi^0$ events, the distribution of the missing energy was examined. This quantity is defined as

$$E_{miss} = \frac{M_X^2 - M_p^2}{2M_p} \tag{4.6}$$

where M_X^2 is the missing mass of the undetected (hadronic) system recoiling opposite to the $\omega\pi^0$ (in the $\gamma^* p$ center of mass), and M_p is the proton mass.

Figure 4.6 shows the $\omega(\pi^+\pi^-\pi^0)\pi^0$ invariant mass vs. E_{miss} (left), and a projection on the E_{miss} axis, where a peak at $E_{miss} \sim 0$ can be clearly seen.

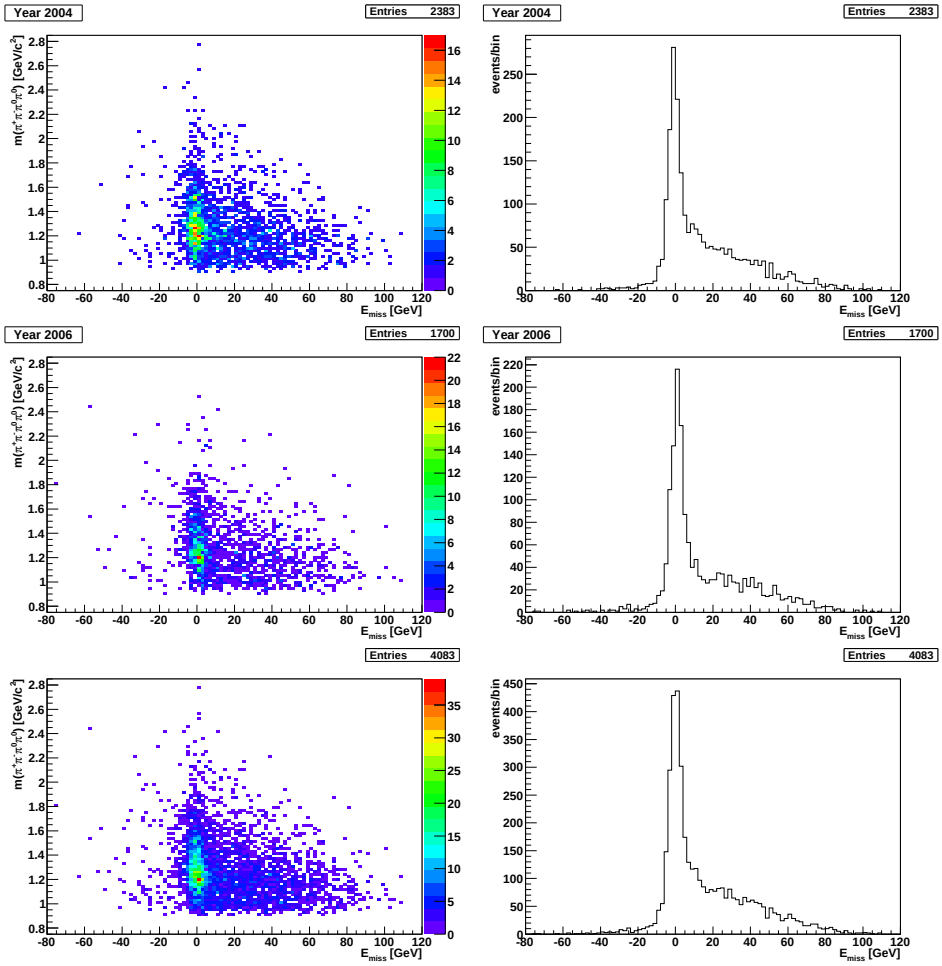

Figure 4.6: *$\omega\pi^0$ invariant mass vs. missing energy E_{miss} for events with a singly reconstructed $\omega\pi^0$ system: year 2004 (top), year 2006 (middle) and whole statistics (bottom).*

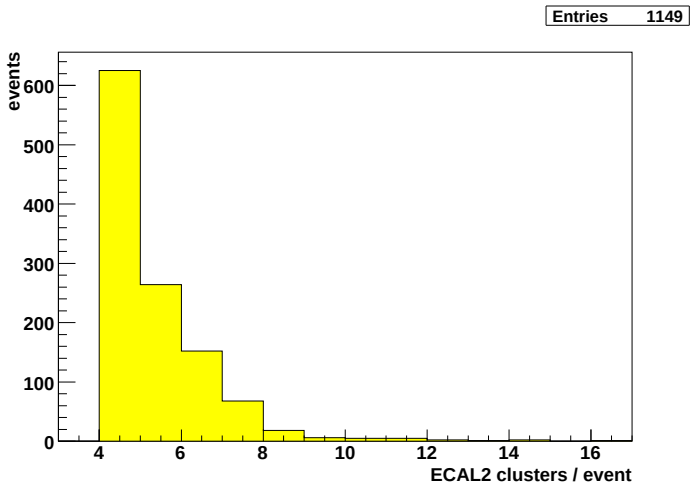

Figure 4.7: *Number of ECAL2 neutral clusters for exclusive $\omega\pi^0$ events with more than four neutral clusters.*

Exclusive events corresponding to this peak were selected imposing the cut -5 GeV/c^2 < E_{miss} < 5 GeV/c^2 for 2003 and 2006 data, and -6 GeV/c^2 < E_{miss} < 4 GeV/c^2 for 2004 data.

The previous plots refer to the event sample in which *four and only four* ECAL2 clusters are found in the event, as explained in the previous section. It is interesting to estimate the effect of the cut on ECAL2 clusters number. If we do not cut on this number, but directly select for exclusive events, we clearly obtain a larger exclusive $\omega\pi^0$ sample. This approach have also been tried: for year 2004 only, Figure 4.7 shows the number of neutral clusters for events with a unique exclusive $\omega\pi^0$ found: we see that proceeding this way, the 55% of events have four and only four ECAL2 neutral clusters.

4.1.5 Cut on the angle θ

As a last step to reduce the background under the exclusive peak, a cut on the angle θ between the two photon direction in the decay $\pi^0 \to \gamma\gamma$ was imposed for the two pions:

$$\theta_{1,2} < 0.025 \text{ rad.}$$

The motivation for this cut is the same as for the cut used for reconstruction of exclusive ω production (see previous Chapter). Taking into account the relation between the minimal opening angle θ and the energy in the laboratory system of the decaying π^0 [Moi03]

$$\theta_{\gamma\gamma} = 2\frac{m}{E_{\pi^0}}, \tag{4.7}$$

(m is the pion mass), this corresponds to an energy threshold $E_{\pi^0} \approx 11$ GeV. Low energy pions are thus excluded from analysis, due to the high background level present in this range.

4.1.6 Effect of the selection cuts on sample statistic

In the following we will study the exclusive event sample selected so far for years 2004 and 2006 *only*.

Table 4.2 lists the various selection cuts explained so far and the relative contribution (in %) of the selected sample after the corresponding cut is applied.

Selection cut	Fraction of events
COMPASS event sample	1
$\mu + N \to \mu' + N' + \pi^+ + \pi^- + (n \geq 4)\gamma$	$5.3 \cdot 10^{-2}$
at least 2 π^0 ($E_\gamma > 2$ GeV)	$1.0 \cdot 10^{-3}$
one and only one ω	$3.7 \cdot 10^{-5}$
one and only one $\omega\pi^0$	$4.1 \cdot 10^{-6}$
4 and only 4 ECAL2 clusters/event	$1.9 \cdot 10^{-6}$
Exclusive $\omega\pi^0$ events	$3.3 \cdot 10^{-7}$
$\theta_{1,2} < 0.025$ rad	$2.4 \cdot 10^{-7}$

Table 4.2: *Dependence of the number of events, normalized to unit, on the various selection cuts.*

The final statistics for every year is listed in the Table 4.3. The total

Year	Reconstructed $\omega\pi^0$
2003 ($E_\gamma > 2$ GeV)	348 (not used)
2004 ($E_\gamma > 2$ GeV)	929
2006 ($E_\gamma > 2$ GeV)	711
2004+2006	**1640**
2003+2004+2006	**1988**

Table 4.3: *Number of reconstructed exclusive $\omega\pi^0$ events.*

number of reconstructed exclusive $\omega\pi^0$ events amounts to 1988. If we consider only years 2004 and 2006, characterized, for neutral decay channels, by a better detector performance, the statistic reduces to 1640 counts.

The $\omega\pi^0$-mass for exclusive events is shown in Figure 4.8.

In Figure 4.9, for the 2004 data, the acceptance is also shown superimposed (red continuous line): it has been calculated from Monte Carlo simulation of detection and reconstruction efficiency (as discussed in the next chapter). We anticipate this result for logical consistency. A 30% acceptance variation from the peak region to 2 GeV/c^2 is observed .

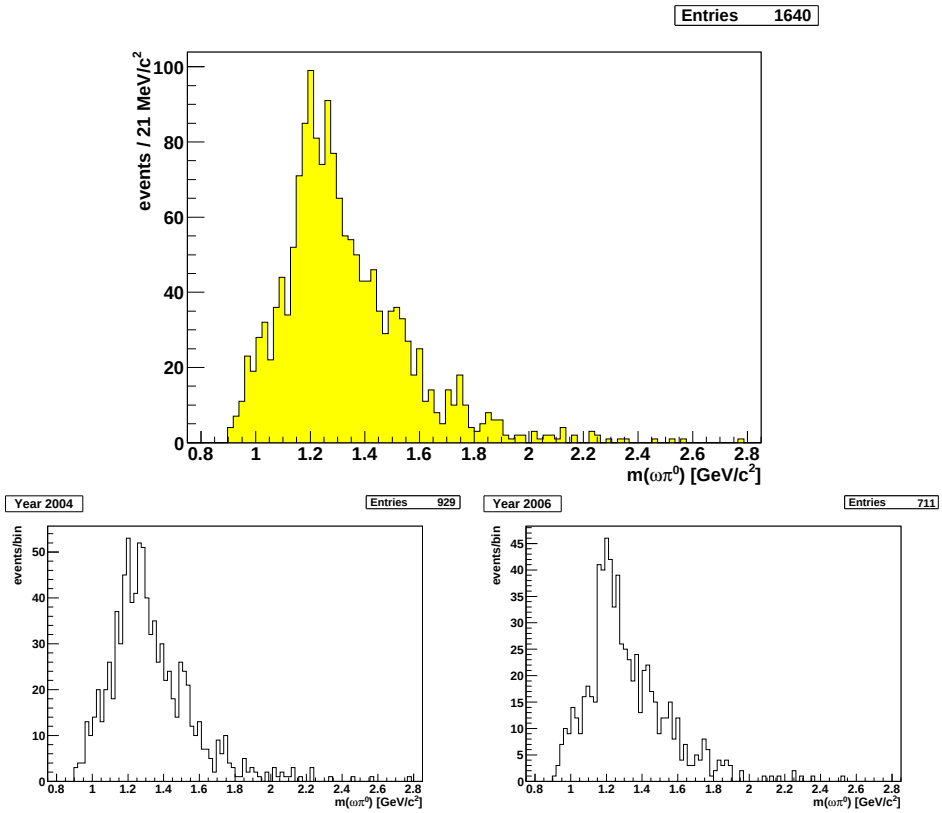

Figure 4.8: *Exclusive $\omega\pi^0$ invariant mass for both years (top) and, separately, for years 2004 (bottom-left) and 2006 (bottom-right).*

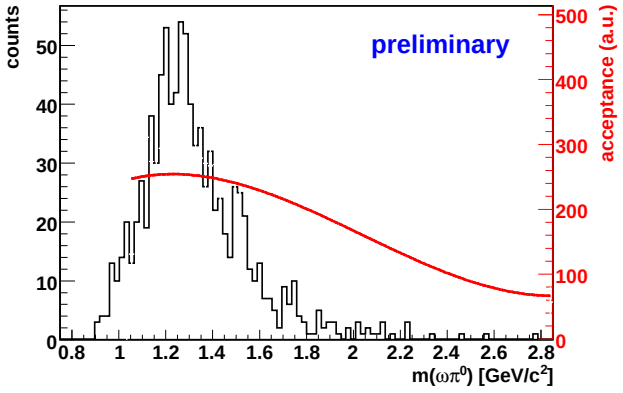

Figure 4.9: *Invariant mass spectrum for exclusive $\omega(\pi^+\pi^-\pi^0)\pi^0$ events (year 2004, not acceptance corrected), with the acceptance dependence (red line) on the $\omega\pi^0$ mass superimposed. From ref. [BD08].*

We thus confirm the presence of an enhancement at ∼1250 MeV/c^2, with a width of ∼300 MeV/c^2, broader than for correspondent results of previous photoproduction experiments.

4.1.7 Alternative selection procedures

An alternative selection is conceivable and has also been tried, even if only for a small subsample of the whole data: period W42, year 2006.

This second try runs parallel to our main selection until the event sample with *at least two* π^0*'s*. At this point, events has been further selected requiring *two and only two distinct* π^0*'s* found in the event, to univoquely have the signature

$$\mu + N \rightarrow \mu' + \pi^+\pi^-\pi^0\pi^0 + X. \tag{4.8}$$

As usual, X is the undetected hadronic system recoiling off the 4π system. This sample corresponds to about the 75% of the events with at least two π^0's. This cannot be evinced from Figure 4.2, due to the previously discussed ambiguities concerning cluster pairs.

If we further search events with *at least* an identified ω, the sample reduces to 15% of that of reaction (4.8).

Of these events, ∼17% have *more* than one ω-candidate. Thus events of the type

$$\mu + N \rightarrow \mu' + \omega(\pi^+\pi^-\pi^0)\pi^0 + X, \tag{4.9}$$

with *one and only one* identified ω, correspond to ∼13% of those in reaction (4.8). If we proceed further and select the exclusive sample, we obtain 105 counts, which is a ∼19% gain in statistics compared with what obtained in the same period in our analysis.

The observed increase is indeed expected, due to the better selection of events concerning π^0 pair identification. It is also most probable, that an even better selection of good events already at the ECAL2 cluster level, meaning better cluster/cell quality selection criteria, may help to further enhance the statistics. We reserve to do so in a future, better optimized analysis work.

4.2 Events within the target cells

In COMPASS, the right-handed coordinate system is defined to have the z-axis directed along the incoming beam direction, the y-axis oriented vertically upwards, and $x = y \times z$. Figure 4.10 shows the coordinate distributions for the reconstructed best primary vertices for the 2004 and 2006 $\omega\pi^0$ exclusive samples. As already explained, in 2006 the new three-cell target was employed for the first time, bringing an enhanced geometrical acceptance and increased number of reconstructed vertices per event. It can be seen

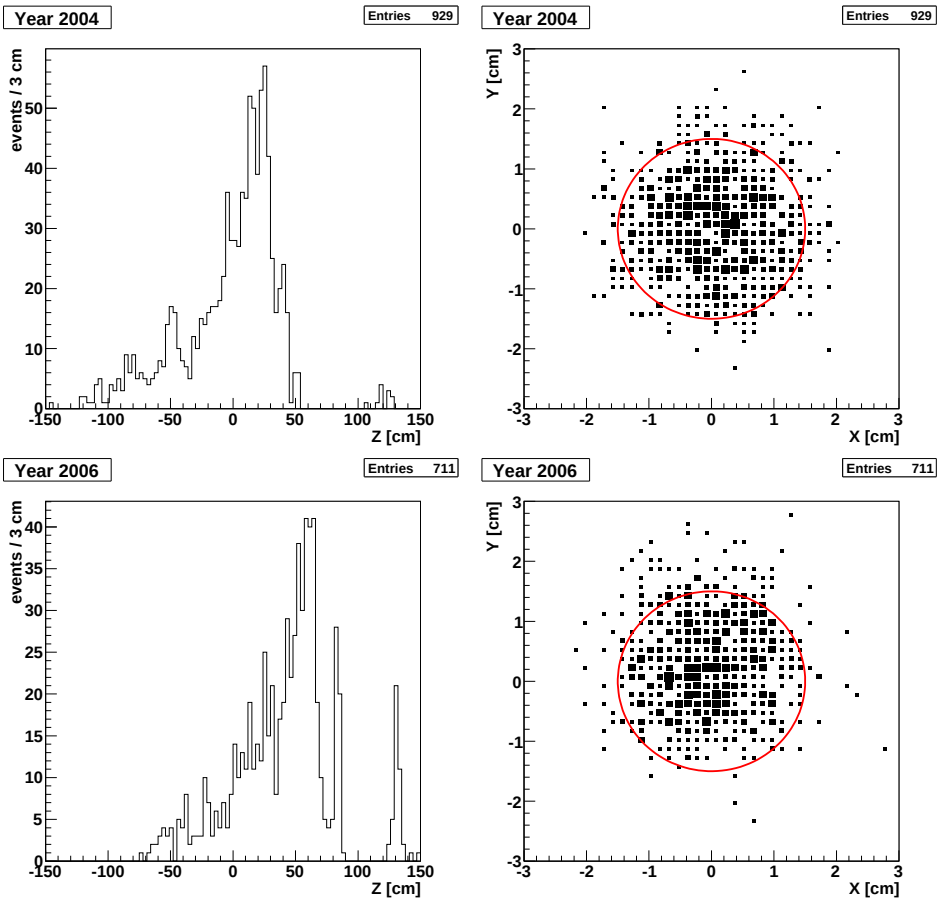

Figure 4.10: *Distribution of the b.p.v. along the beam direction z (left) and xy section (right) for 2004 (top) and 2006 (bottom) of exclusive $\omega\pi^0$ events.*

that for both targets the majority of reconstructed $\omega\pi^0$ events originates in the downstream cell. Unfortunately, for 2006 data a bigger amount of exclusive events is reconstructed outside the target cells, as compared with previous years.

As can be seen from Figure 4.10, some of the reconstructed exclusive $\omega\pi^0$ events are found to be produced outside the target cells. This is particularly evident for the year 2006 data: the three cell structure can be seen, together with a shift of the whole target cell position downstream along the z axis with respect to the position in year 2004. The presence of a comparatively much bigger sample of $\omega\pi^0$ events which are produced in the window layer of the target vessel or, expecially for 2006 data, in a tracking detector plane at $z \approx 120$ cm is clearly visible. In the same Figure, the primary vertex distribution in the xy-plane is shown, together with the nominal section of the target (the red circle). A small amount of events are found to be produced outside the

target cell. In addition, one sees that the vertex distribution is somewhat "tilted" towards opposite directions for the two years, finding more events in the lower (upper) part in 2004 (2006) data.

Nothing forbids the production of exclusive $\omega\pi^0$ from interaction of beam muons with nucleons and/or nuclei belonging to materials other than the target cells. On the other side, some kinematical distributions like, e.g., the transverse momentum squared p_t^2 of the $\omega\pi^0$ with respect to the virtual photon direction $\vec{q}$, may depend on the nature of the target. To avoid confusion and enhance coherence with other COMPASS analysises on meson production, we have used the standard geometrical cuts on vertex position applied by the COMPASS Collaboration: the geometrical limit along the z-axis are listed in Table 4.4, whereas for both the cut on the cell diameter

$$r_v = \sqrt{x_v^2 + y_v^2} < 1.4\,\mathrm{cm} \tag{4.10}$$

applies; x_v and y_v are the respective transversal coordinate of the reconstructed b.p.v.

Target cell [cm]	2004	2006
uspstream	$z \in [-100, -40]$	$z \in [-63, -33]$
central	-	$z \in [-28, 32]$
downstream	$z \in [-30, 30]$	$z \in [37, 67]$

Table 4.4: *Target cell geometrical dimensions along the z-axis.*

The b.p.v. selection has been performed with the aid of a routine already available within PHAST.

Small deviations from the nominal geometrical dimensions of target seen in the vertex distribution plots are explained with the (observed) incomplete filling of target cells with the solid target material (^{6}LiD), which does not form a unique sample, but an aggregate of small crystal grains, thus leaving some part of the cells empty.

The final statistic for events within the target cells is shown in Table 4.5. We see that requiring the b.p.v. to be in a target cell results in a statistic loss of 30.8% for year 2004, 35.5% for year 2006, and a total 32.8% loss for the sum of the two years.

In the following, if not explicitely different stated, we will refer to the

Year	**Reconstructed $\omega\pi^0$**
2004 ($E_\gamma > 2$ GeV)	643
2006 ($E_\gamma > 2$ GeV)	459
2004+2006	**1102**

Table 4.5: *Number of exclusive $\omega\pi^0$ events reconstructed within target cells.*

exclusive $\omega\pi^0$ sample with b.p.v. *within* a target cell as the *($\omega\pi^0$) final sample*.

Chapter 5

Results

Having illustrated, in the previous Chapter, the selection procedure for exclusive $\omega\pi^0$ events within a target cell, we now study the kinematical aspects of the reaction.

5.1 Kinematics of the exclusive $\omega\pi^0$ sample

Figure 5.1 shows the 4π invariant mass for the exclusive $\omega\pi^0$ sample.

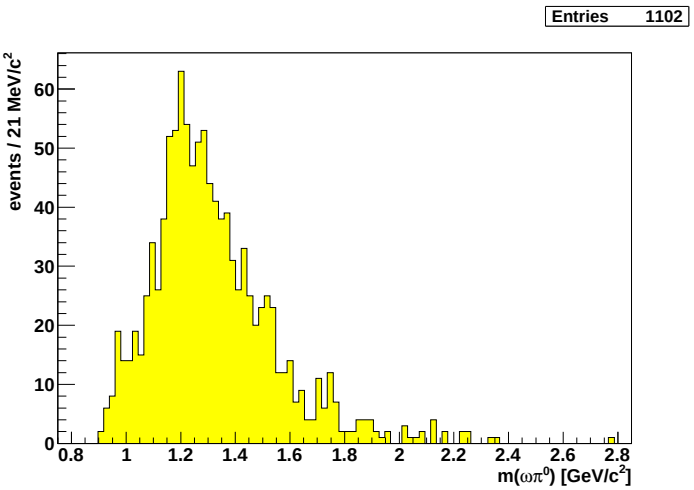

Figure 5.1: *Invariant mass spectrum for the exclusive* $\omega(\pi^+\pi^-\pi^0)\pi^0$ *final sample (not acceptance corrected). The nominal threshold for* $\omega\pi^0$ *is 0.92 GeV/*c^2.

Figures 5.2 to 5.7 show, for the final sample, some important kinematic distributions: the virtual photon mass squared Q^2, the Bjorken scale variable x_B, their correlation, the virtual photon energy ν, the polarization coefficient ϵ, the invariant mass squared of the hadronic system W, the momentum of

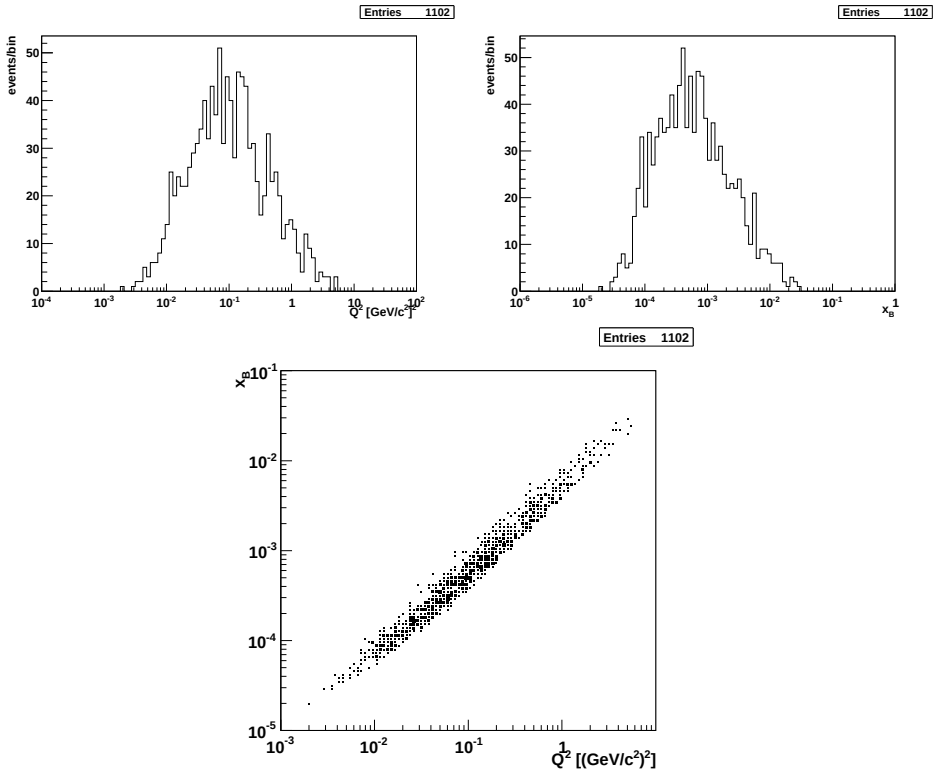

Figure 5.2: *Virtual photon mass squared Q^2 (top-left), Bjorken variable (top-right) and their correlation (bottom) for the final sample.*

the $\omega\pi^0$ in the laboratory frame and the exchanged 4-momentum squared t.

The t-distribution is compatible with a diffractive production of the $\omega\pi^0$ system, but due to experimental resolution, events at low t are poorly reconstructed, and a sample with non-physical values at $t > 0$ can be seen. In the literature (cf. [A$^+$84]) a value for the slope $b = 5.0 \pm 0.3$ GeV^{-2} is reported in the interval $[-1, 0]$ GeV^2 (units $c = 1$). If we fit the data with an exponential, we obtain

$$b = 5.27 \pm 0.29 \text{ GeV}^{-2}. \tag{5.1}$$

Although the two values are in agreement, our fit is not satisfactory: in fact, in our data sample two regions with different slopes in the t-distribution can be identified:

i) a low-t range, approximately -0.25 GeV^2 $< t <$ 0 GeV^2, characterized by a rapid exponential decrease $b = 6.88 \pm 0.57$ GeV^{-2};

ii) a high-t range, corresponding to -1 GeV^2 $< t <$ 0.25 GeV^2, where the

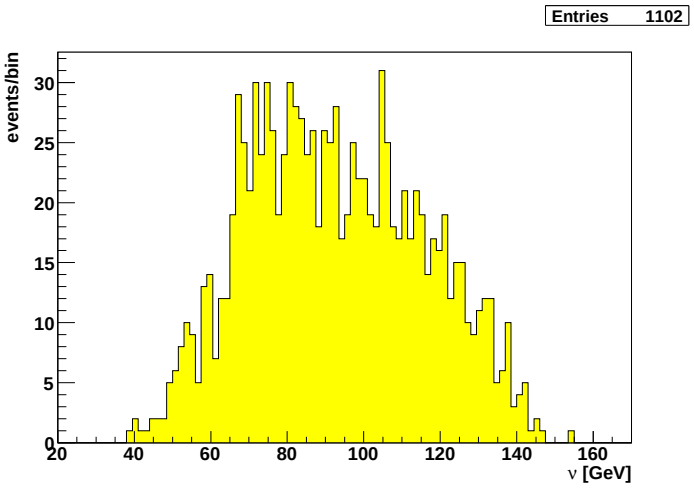

Figure 5.3: *Virtual photon energy distribution $\nu = E_\mu - E_{\mu'}$ in the laboratory system.*

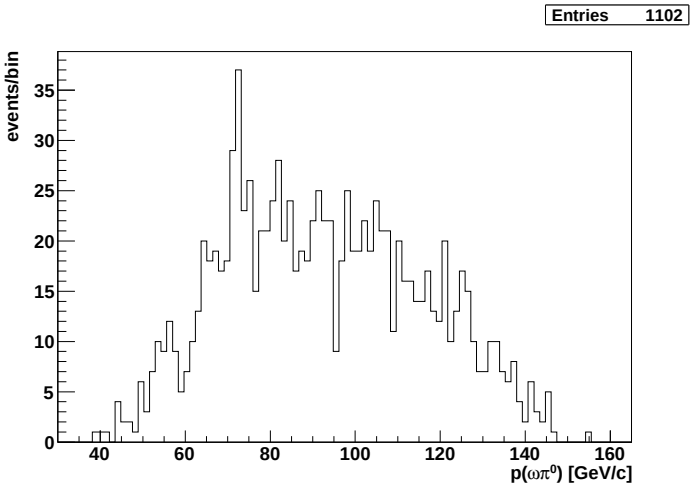

Figure 5.4: *$\omega\pi^0$-momentum distribution in the laboratory system.*

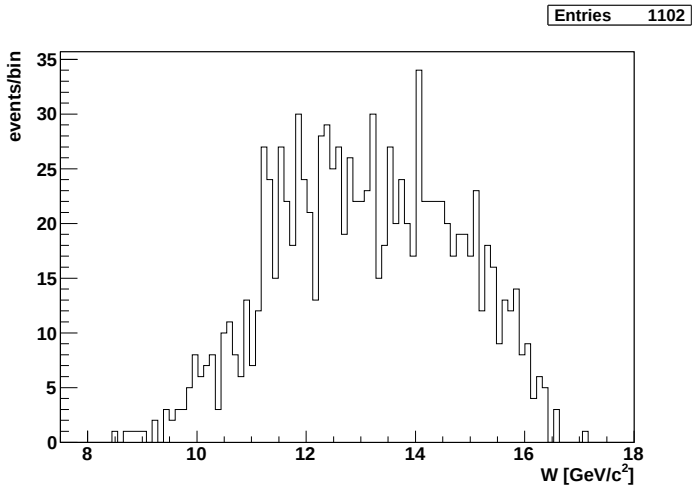

Figure 5.5: *Final sample $\gamma^* p$ center-of-mass energy W.*

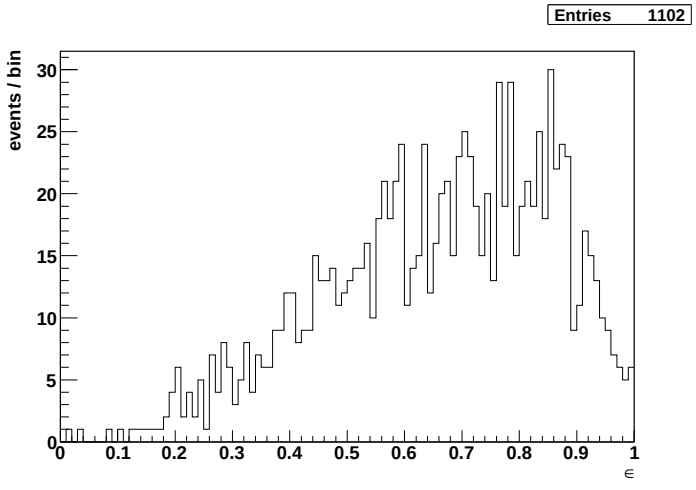

Figure 5.6: *Final sample ϵ-distribution (for a definition, see eq.* (1.22)*, pag. 7).*

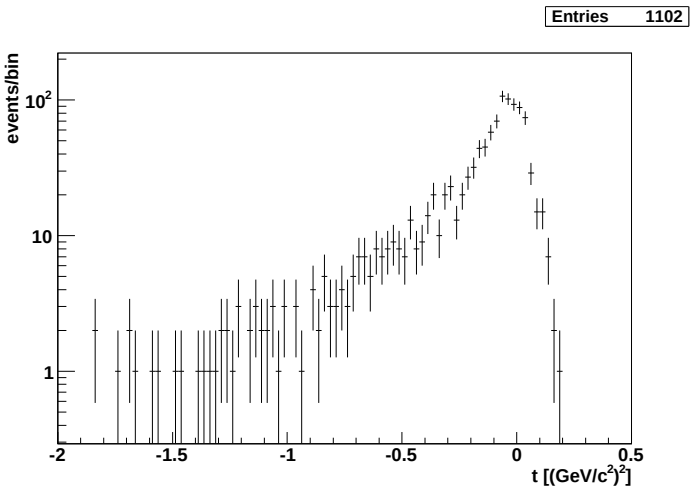

Figure 5.7: *t-distribution for the exclusive $\omega\pi^0$ final sample.*

exponential fit gives a much lower value for the slope $b = 3.07 \pm 0.36$ GeV^{-2}.

This behaviour can be understood, considering a related quantity, i.e. the transversal (relative to the virtual photon direction) momentum squared p_t^2 of the produced mesonic system [BdGS04]. Small value of t corresponds to small values of p_t^2 of the produced meson (and vice versa).

Figure 5.8 shows the p_t^2 distribution of the final sample for the whole statistics and, separately, for the years 2004 and 2006. In addition, p_t^2 is better reconstructed, and thus we can use this quantity instead of t.

With this in mind and to gain more physical insight, the dependence of the exclusivity of the reaction from p_t^2 has been inspected. This quantity is particularly important for the distinction of meson resonance production from a nucleus (we have in fact complex nuclei in the target material at COMPASS) as a whole entity (in which case one speaks of *coherent* scattering), or from a single nucleon considered as a quasi-free particle (*incoherent* scattering). The two production mechanisms are characterized by different values of p_t: in the low range coherent production dominates, whereas incoherent production gains importance with increasing p_t. On the other side, at very high p_t also non-exclusive events which contribute to background in the exclusivity peak reagion, can easily be produced in this p_t^2 range. Taking these considerations into account, the final sample missing energy in the three following p_t^2 ranges has been examined:

i) $p_t^2 < 0.15$ (GeV/c)^2;

ii) 0.15 (GeV/c)^2 $< p_t^2 < 0.5$ (GeV/c)^2;

iii) $p_t^2 > 0.5$ (GeV/c)^2;

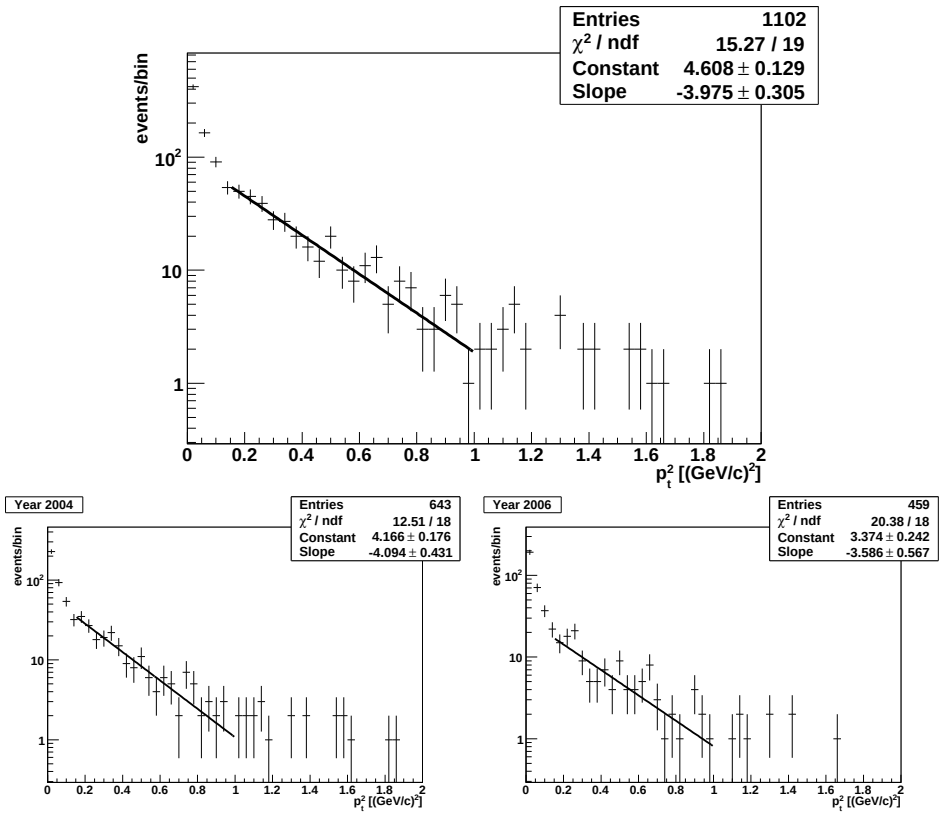

Figure 5.8: *p_t^2-distribution for the final sample (top) and for year 2004 (bottom-left) and 2006 (bottom-right).*

Figure 5.9 shows the corresponding results: the non-exclusive background contamination to the exclusive peak increases together with the p_t^2-values in the three distinct ranges.

5.2 Background

Two possible sources of background in the final sample have been examinated:

- Non-ω related background: this corresponds to exclusive production of an overall neutral four pion system from phase space and/or other possible combination of 2π and 3π subsystem. The quantitative estimation of such contribution can be evaluated by means of the so called λ-distribution, as explained in detail below.
- Nuclear/nucleon excitation: possible contaminations from processes like, e.g., $\gamma^* + p \rightarrow \omega + N^*$, where N^* is an excited state of the nucleon with decay $N^* \rightarrow N + \pi^0$.

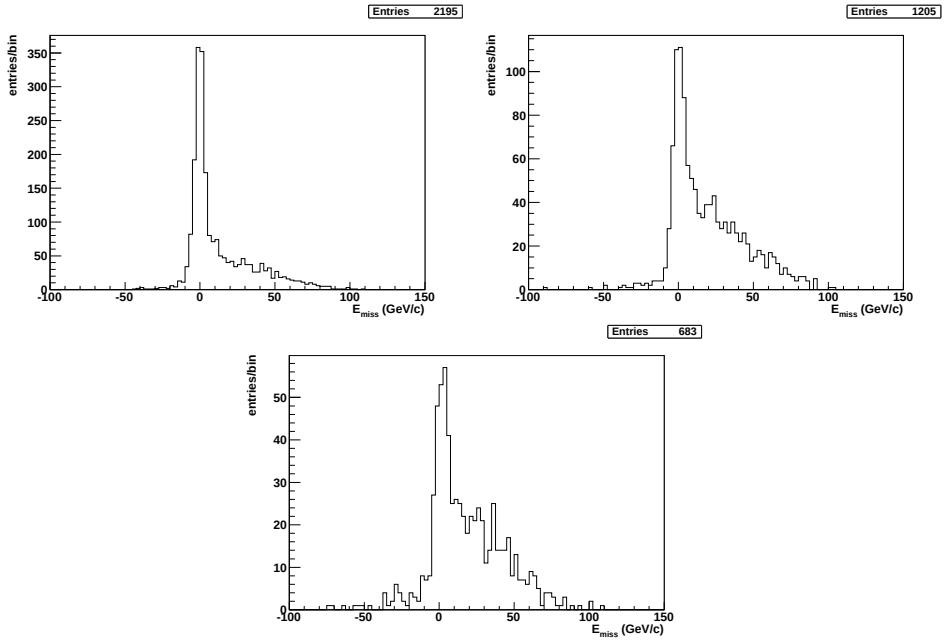

Figure 5.9: *Dependence of the intensity of the exclusive signal on* p_t^2. *Top-left:* $p_t^2 < 0.15$ *(GeV/c)*^{2}. *Top-right:* 0.15 *(GeV/c)*$^2 < p_t^2 < 0.5$ *(GeV/c)*^{2}. *Bottom:* $p_t^2 > 0.5$ *(GeV/c)*^{2}.

5.2.1 Non-ω-related events

An estimate of the non-ω related background can be achieved inspecting the distribution of the quantity λ, defined by the formula [A$^+$84]

$$\lambda = \frac{|\boldsymbol{p}_1 \times \boldsymbol{p}_2|^2}{|\boldsymbol{p}_1 \times \boldsymbol{p}_2|^2_{max}}, \tag{5.2}$$

where $\boldsymbol{p}_1$ and $\boldsymbol{p}_2$ are the momenta of any two out of the three pions from ω decay, their value taken in the ω rest frame. In this analysis, the momenta of the two charged pions were taken, because of the better precision achieved in the reconstruction of charged particle compared to neutral ones. The quantity at denominator in formula (5.2) can be calculated [A$^+$84]:

$$|\boldsymbol{p}_1 \times \boldsymbol{p}_2|^2_{max} = Q^2\left(\frac{Q^2}{108} + \frac{Qm_\pi}{9} + \frac{m_\pi^2}{3}\right).$$

Here m_π is the pion mass (the mass difference between charged and neutral pions were neglected) and $Q = m_\omega - 3m_\pi$ (not to be confused with the photon virtuality!) is equal to the sum of the kinetic energies of the three pions in the ω decay; m_ω is the ω mass (it is taken as a constant, thus neglecting the small effect introduced by the event-dependent experimental values spread around the ω-mass mean value).

From the previous formula, we see that λ is constrained to the interval $[0, 1]$. For a $J^P = 1^-$ resonance decaying to three pseudoscalar mesons (like the ω), [A$^+$84] predicts a linear increase, whereas non-resonant background is characterized by a flat distribution. The resulting distribution for the final sample is thus expected to be a linear increase superimposed to a constant basis.

Figure 5.10 shows the behaviour of λ for the $\omega\pi^0$ final sample. From the intercept of the linear fit at $\lambda = 0$ the background contribution can be estimated to be of the order of 13%, 16% and 23% for the years 2003 (not used in analysis and not shown in Figure 5.10), 2004 and 2006, respectively. As we consider mainly data from these last two years, a mean background contribution amounts to about 20%.

The precise value, calculated from the parameters and their errors, are listed in Table 5.1

Year	Non-ω background [%]
2004	14.8 ± 5.1
2006	25.4 ± 6.4
2004+2006	19.1 ± 4.4

Table 5.1: *Non-ω related background contribution to the exclusive $\omega\pi^0$ sample. B.p.v. in the target cells.*

That the λ distribution for background, on the contrary, is flat, is shown in Figure 5.11 (see ref. [BD08]). The value of λ calculated for events in the side bands 0.7 GeV/c^2 $< m(\pi^+\pi^-\pi^0) <$ 0.73 GeV/c^2 and 0.83 GeV/c^2 $< m(\pi^+\pi^-\pi^0) <$ 0.9 GeV/c^2 (in red) are superimposed to the corresponding distribution for the $\omega\pi^0$ final sample ($m(\pi^+\pi^-\pi^0)$ within the ω-peak). It is assumed that the background in the peak region behaves as the events in the two side bands.

Another possible background contribution is related to the production of ρ mesons: Figure 5.12 shows the invariant mass of the neutral (top) and charged (middle) dipion system for the events in the final sample. The $\pi^+\pi^-$ invariant mass lies outside the window characteristic of the broad ρ resonance, thus excluding ρ^0-production as a main contribution to background.

In addition, also the $\pi^0\pi^0$ invariant mass spectrum do not show any particular structure.

Regarding the $\pi^\pm\pi^0$ system, the particular form of the corresponding invariant mass spectrum requires some explanation. These distributions (in each of the two histograms we have *two* entries per event) characterize two subsamples: 1) the charged dipion system formed with the π^0 associated to the ω during selection (middle-left), and 2) the charged dipion system built with the other π^0 (middle-right). The latter is in general the most energetic

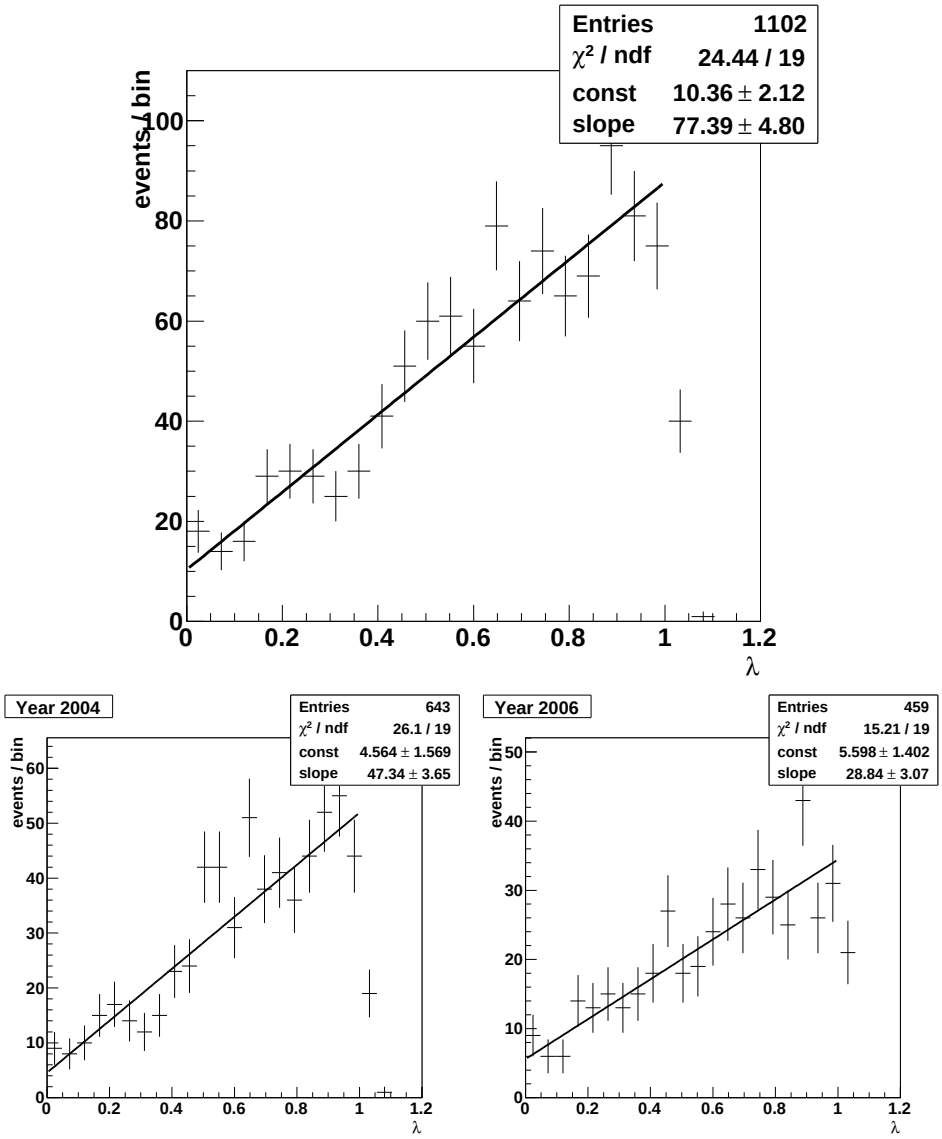

Figure 5.10: *Final sample λ-distribution: whole statistics (top) and, separately, for year 2004 (bottom-left) and 2006 (bottom-right). Data not corrected for acceptance.*

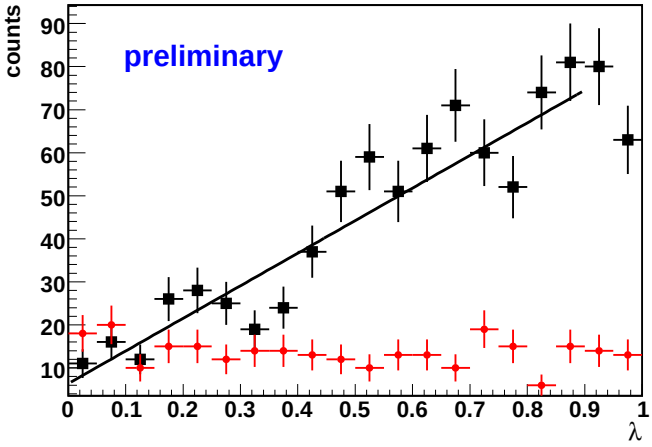

Figure 5.11: *λ distribution for exclusive* $(\pi^+\pi^-\pi^0)\pi^0$ *sample within the* ω*-peak (in black) and in side bands (in red). 2004 data.*

of the two, due to the kinematical cut for the ω selection, thus being the main contribution to the shoulder at mass $m(\pi^\pm\pi^0) > 650$ MeV/c^2. The fifth histogram (bottom) in Figure 5.12 is the sum of the previous two. Also for the charged dipion system, no particular structure related to the $\rho^\pm$ resonance can be seen, thus excluding a possible $\rho^+\rho^-$-contribution to the background.

We may thus conclude that no contribution to background from ρ-production is found in the data.

5.2.2 Target excitation

To examine this processes, the missing mass $M_{X\pi^0}$ of the produced hadron system, the identified ω excluded, was calculated for the data in the $\omega\pi^0$ exclusive final sample, from the relation

$$M^2_{X\pi^0} = (p + q - v_\omega)^2, \tag{5.3}$$

where v_ω stands for the 4-momentum of the ω. Equivalently, $M_{X\pi^0}$ is the invariant mass of the observed π^0 together with the unobserved recoiling target (the nucleon in ideal exclusive production).

Figure 5.13 shows the mass spectrum of the $X\pi^0$-system for the events in the final sample. No structure can be seen; the threshold value at ≈4 GeV/c^2, mainly due to acceptance, excludes the presence of a strong contamination of *low mass* nucleon excitations, like the N^*'s, in our data. These resonances are indeed a real problem in experiment at lower energy than that of COMPASS ($W \approx 13.5$ GeV). That the threshold at 4 GeV is due mainly to acceptance, can be understood if one consider the cut on the 2-photon

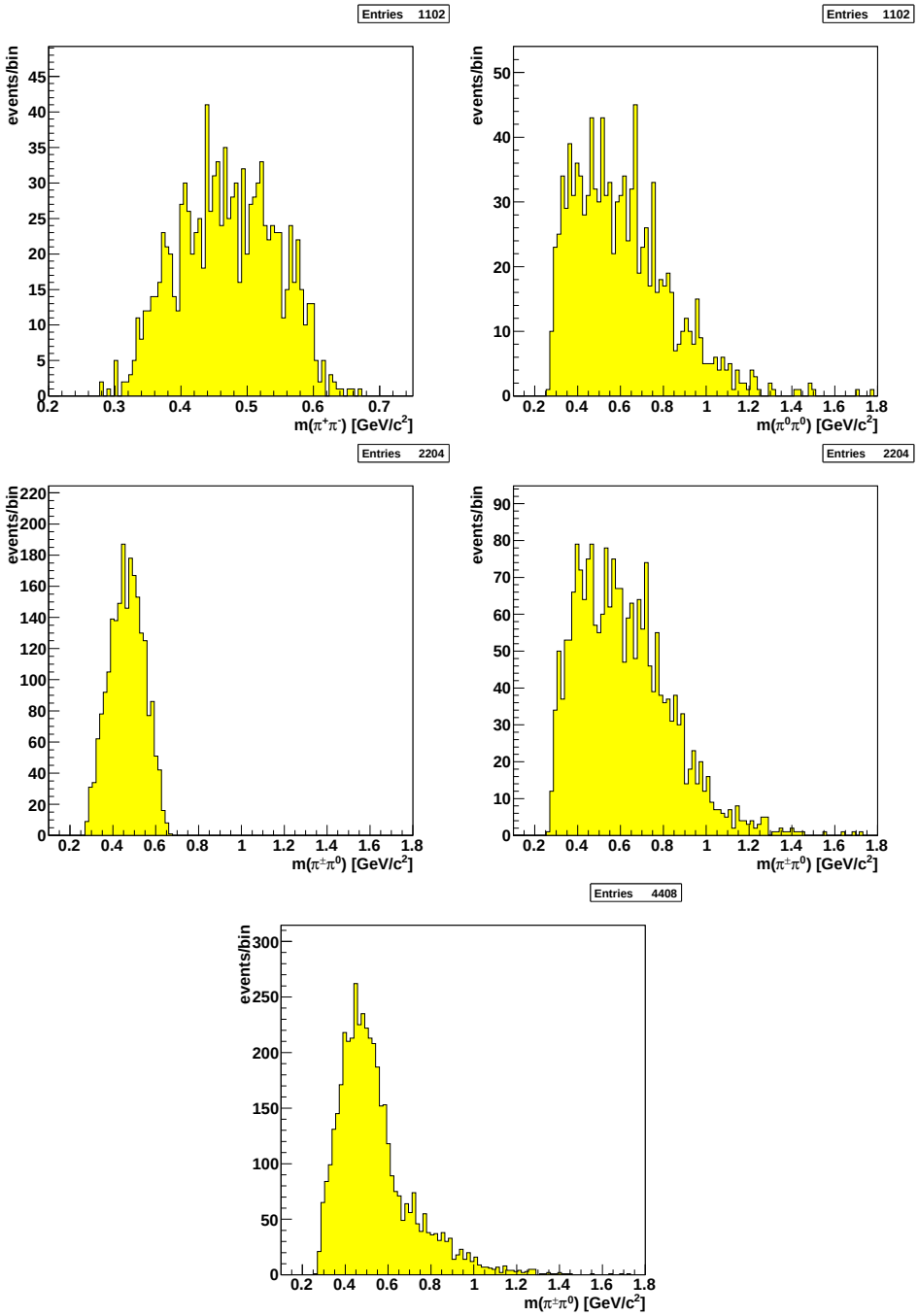

Figure 5.12: *Invariant mass of the neutral (top) and charged (middle) dipion system for the final sample. The last histogram (bottom) is the sum of the two contributions from the charged dipion system.*

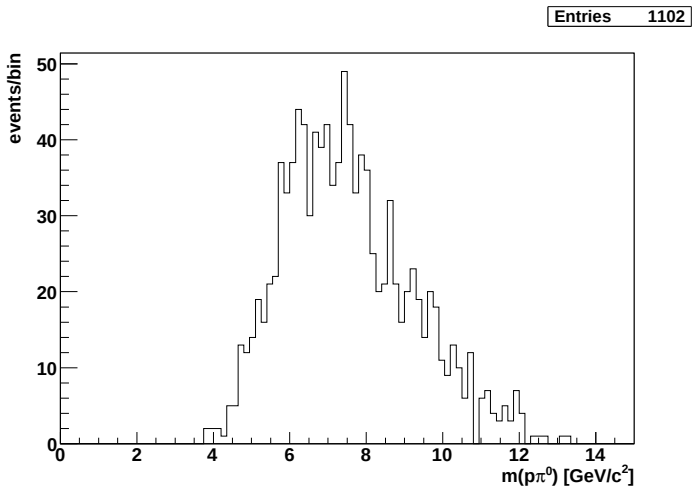

Figure 5.13: *Invariant mass $M_{X\pi^0}$ for the reaction $\mu + N \to \mu' + \omega + (X\pi^0)$ from events in final sample.*

opening angle θ, which, as we have seen, corresponds to an energy threshold for the π^0 at ≈ 11 GeV. If we make the assumption that the π^0 originates from decay $N^* \to N + \pi^0$, and the nucleon N moves, due to its high mass compared to the pion's, with low momentum ($p_N \approx 0$) and low energy ($E_N \sim M_p \approx 1$ GeV), we have roughly for the mass of their bound system:

$$\begin{aligned} M_X &= \sqrt{(E_{\pi^0} + E_N)^2 - (\boldsymbol{p}_{\pi^0} + \boldsymbol{p}_N)^2} \\ &\approx \sqrt{(11+1)^2 - (11)^2} \approx 4.8\,\text{GeV}, \end{aligned} \tag{5.4}$$

which corresponds to the threshold visible in Figure 5.13. In the previous calculation, energy is measured in GeV, and the low momentum of the nucleon and the energy-momentum difference for the π^0 have been neglected (e.g., for low mass nuclear excitations like the N^*'s or $\Delta(1232)$'s, the kinetic energy available to the daughter particles is ≈ 80 MeV, about 10% of the nucleon mass).

Nuclear excitations in the 4-10 GeV/c^2 region, which are potentially present in the data, are excluded by the observed angular distributions: it is found [C$^+$75] that target excitations give a strong asymmetry in the angular $\cos\theta$ distribution, i.e. in the polar orientation of the ω momentum vector relative to the $\omega\pi^0$ in the helicity frame of the latter (see Section 5.4 for a precise definition). It will be shown that this asymmetry is not observed in the data, thus excluding a strong contribution of N^* and confirming the production of a true $\omega\pi^0$ mesonic system.

For low mass N^*, the $\cos\theta$ distribution should strongly peak at $\theta \approx 1$ (cf. [C$^+$75]), i.e. backward π^0 momentum vector in the $\omega\pi^0$ rest frame. This is the region of low π^0 momentum in the laboratory frame, which suffers the

$m(\omega\pi^0)$ [GeV/c^2]	$0.9 < m < 1.1$	$1.1 < m < 1.4$	$1.4 < m < 1.6$
$\lambda \in [0, 1]$	15.7 ± 10.3	19.4 ± 5.2	-2.6 ± 7.7
$\lambda \in [0, 0.95]$	17.5 ± 10.4	16.8 ± 5.3	-1.2 ± 7.9
$\lambda \in [0, 0.9]$	20.1 ± 10.5	15.1 ± 5.4	-0.2 ± 8.0

Table 5.2: *Non ω-related background contribution (in %) for exclusive $(\pi^+\pi^-\pi^0)\pi^0$ sample, in distinct $\omega\pi^0$-mass bins. No p_t^2-cut applied.*

biggest loss due to acceptance: even if production of N^*'s with mass lower than 2-3 GeV/c^2 cannot be excluded, their detection would be extremely hard in the present regime.

5.3 $\omega\pi^0$ mass dependence

The dependence of some background quantities on the reconstructed $\omega\pi^0$-mass has been also examined. The final sample was subdivided into three subsamples defined within the mass windows:

i) $m(\omega\pi^0) < 1.1$ GeV/c^2;

ii) 1.1 GeV/c^2 $< m(\omega\pi^0) < 1.4$ GeV/c^2;

iii) 1.4 GeV/c^2 $< m(\omega\pi^0) < 1.6$ GeV/c^2;

Results for E_{miss} are shown in Figure 5.14.

In addition, the inspection of the λ-distribution was repeated in the three different mass ranges aiming to determine the level of background contribution due to non-ω related events. The background contribution has been calculated from the value of the intercept of the linear fit at $\lambda = 0$.

Table 5.2 lists the results in the various $\omega\pi^0$-mass bins. The data were fitted from $\lambda = 0$ to three different values (corresponding to the three different lines in the same Table) in order to take into account the observed deviation from the expected linearity at $\lambda \approx 1$, possibly due to acceptance, which could cause an overestimation of the background contribution by decreasing the value of the slope of the linear fit and increasing the value of the intercept at $\lambda = 0$ (as indeed observed in the fitted data).

With this in mind, fit values show a decreasing amount of non-ω-related background contamination with increasing 4π mass (the values in last column of Table 5.2 are all compatible with zero, with a possible $\sim 8\%$ background contribution at the 1σ-level not excluded. In the lower $\omega\pi^0$-mass range background contamination levels are correspondingly higher. The relatively big errors are due to the limited statistic.

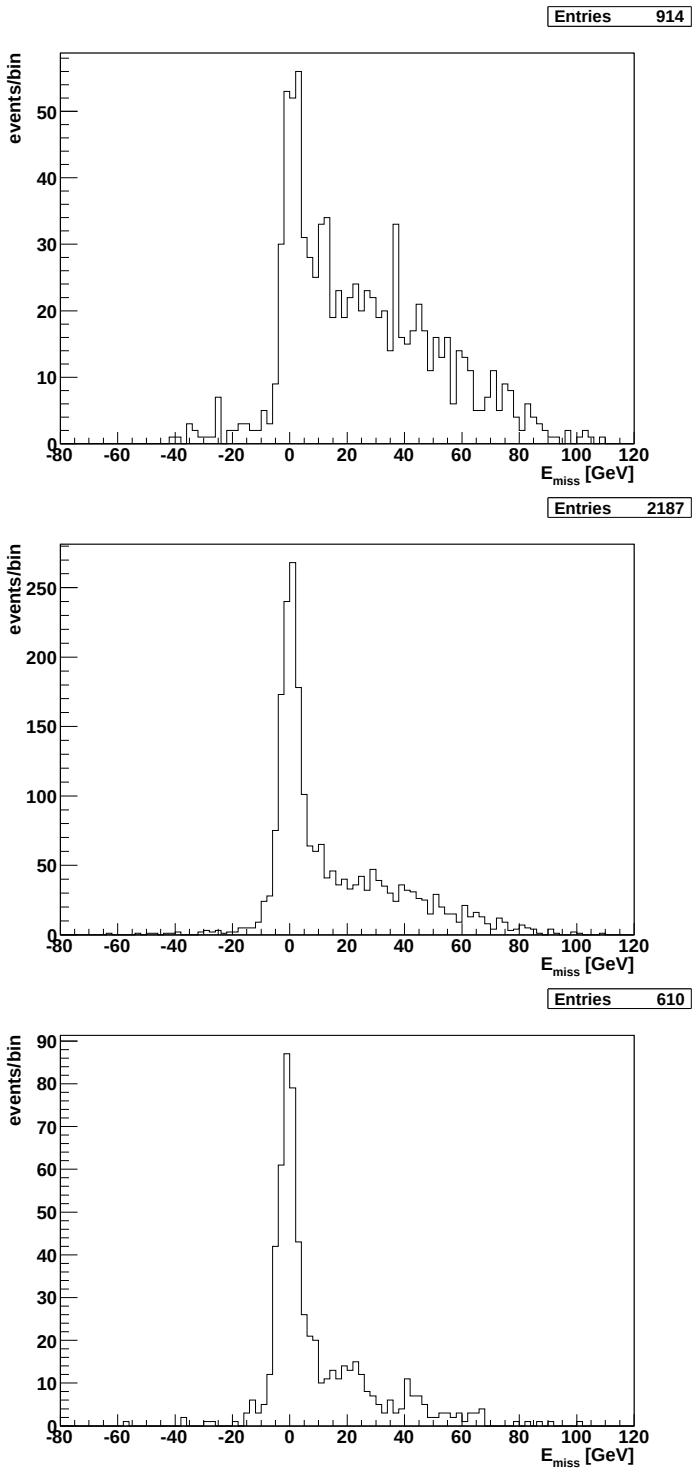

Figure 5.14: *From top to bottom:* E_{miss} *for i)* $m(\omega\pi^0) < 1.1$ *GeV*/c^2*, ii)* 1.1 *GeV*/$c^2 < m(\omega\pi^0) < 1.4$ *GeV*/c^2 *and iii)* 1.4 *GeV*/$c^2 < m(\omega\pi^0) < 1.6$ *GeV*/c^2*. No* p_t^2*-cut was applied here.*

5.4 Angular distributions

We can describe the exclusive $\omega\pi^0$ leptoproduction and subsequent decay chain $\omega\pi^0 \to \omega + \pi^0 \to \pi^+\pi^-\pi^0 + \pi^0$ with the help of four different planes [SW73] (some of the definitions were already introduced in Chapter 1 for clarity):

1. The scattering plane, defined by the trajectories of the incoming (beam) and scattered lepton (muons);

2. The production plane, formed by the virtual photon γ^* and $\omega\pi^0$ trajectories in the γ^*N c.m. frame;

3. The $\omega\pi^0$ decay plane, formed by the direction of flight of the $\omega\pi^0$ in the γ^*N c.m. frame and the direction of flight of one of the two daughter particles in the resonance rest frame (in what follows the direction of the ω will be used);

4. The orientation of the ω decay plane in the ω helicity frame: being a 3-body decay, this is related to the orientation in space of the unit vector
$$\boldsymbol{n} = \frac{\boldsymbol{p}_1 \times \boldsymbol{p}_2}{|\boldsymbol{p}_1 \times \boldsymbol{p}_2|}, \tag{5.5}$$
relative to the ω direction of motion; in the previous formula, $\boldsymbol{p}_1$ and $\boldsymbol{p}_2$ are the momenta of two pions chosen out of the three in the decay $\omega \to \pi^+\pi^-\pi^0$. By definition, $\boldsymbol{n}$ is perpendicular to the decay plane.

Figure 1.2 gives a pictorial illustration of the previous planes and their mutual orientation (except for the ω decay plane, which is not drawn).

We consider the following angles, some of them already briefly introduced in Chapter 1:

- The azimuthal orientation Φ (Figure 1.2) of the scattering plane relative to the production plane, i.e. $\Phi = \angle(\boldsymbol{n}_\mu, \boldsymbol{Y})$, where
$$\boldsymbol{n}_\mu = \frac{\boldsymbol{p}_\mu \times \boldsymbol{p}_{\mu'}}{|\boldsymbol{p}_\mu \times \boldsymbol{p}_{\mu'}|}. \tag{5.6}$$
The incoming and scattered muon momenta $\boldsymbol{p}_\mu$ and $\boldsymbol{p}_{\mu'}$, the momentum of the virtual photon $\boldsymbol{q}$ and the momentum of the produced $\omega\pi^0$ $\boldsymbol{v}$ are all defined in the same reference frame, namely the overall γ^*N center of mass frame. A right handed reference system can be thus defined by $\boldsymbol{X} = \boldsymbol{Y} \times \boldsymbol{Z}$, where
$$\boldsymbol{Y} = \frac{\boldsymbol{q} \times \boldsymbol{v}}{|\boldsymbol{q} \times \boldsymbol{v}|} \tag{5.7}$$

is perpendicular to the production plane, and

$$\boldsymbol{Z} = \frac{\boldsymbol{q}}{|\boldsymbol{q}|} \tag{5.8}$$

is along the direction of the virtual photon. As a result,

$$\cos\Phi = \boldsymbol{n}_\mu \cdot \boldsymbol{Y}, \tag{5.9}$$

$$\sin\Phi = \frac{((\boldsymbol{Y} \times \boldsymbol{n}_\mu) \times \boldsymbol{Y}) \cdot \boldsymbol{n}_\mu}{|(\boldsymbol{Y} \times \boldsymbol{n}_\mu) \times \boldsymbol{Y}|}. \tag{5.10}$$

Note that a boost from the laboratory system to the $\gamma^* N$ c.m. frame along the direction $\boldsymbol{Z}$ does not change the azimuthal orientation of the two planes, the vectors $\boldsymbol{n}_\mu$ and $\boldsymbol{Y}$ being both perpendicular to $\boldsymbol{Z}$.

- The azimuthal orientation ϕ of the $\omega\pi^0$ plane relative to the production plane. Performing a rotation of $\boldsymbol{Z}$ around $\boldsymbol{Y}$ in the direction of motion of $\omega\pi^0$ and subsequently boosting in the $\omega\pi^0$ rest frame, we reach the $\omega\pi^0$ helicity frame, where $\boldsymbol{v}$ is the direction opposite to that of the outgoing nucleon N after interaction. The new axes are thus defined:

$$\boldsymbol{z} = \frac{\boldsymbol{v}}{|\boldsymbol{v}|}, \tag{5.11}$$

$$\boldsymbol{y} = \boldsymbol{Y}, \tag{5.12}$$

$$\boldsymbol{x} = \boldsymbol{y} \times \boldsymbol{z}, \tag{5.13}$$

and the angle ϕ is given by the relations

$$\phi = \angle(\boldsymbol{y}, \boldsymbol{z} \times \boldsymbol{p}_\omega), \tag{5.14}$$

$$\cos\phi = \frac{\boldsymbol{y} \cdot (\boldsymbol{z} \times \boldsymbol{p}_\omega)}{|\boldsymbol{z} \times \boldsymbol{p}_\omega|}, \tag{5.15}$$

$$\sin\phi = -\frac{\boldsymbol{x} \cdot (\boldsymbol{z} \times \boldsymbol{p}_\omega)}{|\boldsymbol{z} \times \boldsymbol{p}_\omega|}, \tag{5.16}$$

where $\boldsymbol{p}_\omega$ is the moment vector of the ω in the $\omega\pi^0$ rest frame As in the previous case, a boost along $\boldsymbol{z}$ from the $\gamma^* N$ in the $\omega\pi^0$ helicity frame leaves the azimuthal orientation ϕ unchanged.

- Also the difference

$$\psi = \phi - \Phi \tag{5.17}$$

has been inspected, this quantity being an important angular variable in the context of SCHC validity in vector meson photo- and electroproduction.

- The polar angle $\theta = \angle(\boldsymbol{p}_\omega, \boldsymbol{z})$ of the momentum of the ω in the $\omega\pi^0$ helicity frame; we have:

$$\cos\theta = \frac{\boldsymbol{p}_\omega}{|\boldsymbol{p}_\omega|} \cdot \boldsymbol{z}. \tag{5.18}$$

- The polar and azimuthal angles $\Omega = (\theta_H, \phi_H)$ of $\boldsymbol{n}$ in the ω helicity frame, where $-\boldsymbol{p}_{\pi^0}$ is the new z-axis $\boldsymbol{z}_H$, oriented opposite to the direction of flight of the π^0 from the $\omega\pi^0$ decay:

$$\theta_H = \angle(\boldsymbol{n}, \boldsymbol{z}_H). \tag{5.19}$$

- In ref. [A$^+$80] the angle θ_A is considered in addition, which define the orientation of $\boldsymbol{n}$ (eq. (5.5)) *respect to* the vector $\boldsymbol{v}$ as defined in the $\gamma^* N$ c.m. This point requires an explanation: the vector $\boldsymbol{n}$ is defined in the ω rest frame, whereas $\boldsymbol{v}$ is defined in the $\omega\pi^0$ rest frame. The definition of θ_A implies, starting from decay plane, a rotation around $\boldsymbol{y}$ of an angle θ to make the direction of $\boldsymbol{v}$ and $\boldsymbol{p}_\omega$ coincide, then a boost in the ω rest frame, then performing a second rotation around $\boldsymbol{y}$ of an angle $-\theta$. The obtained $\boldsymbol{z}'$ axis is thus parallel to $\boldsymbol{v}$, but now defined in the ω rest frame, giving:

$$\cos\theta_A = \boldsymbol{n} \cdot \boldsymbol{z}'. \tag{5.20}$$

- A last angular distribution ψ_V has been inspected for spin-parity analysis. Consider a "spin analyzer" vector $\boldsymbol{V}$ defined in the ω rest frame for different J^P states as [B$^+$74]

  - $J^P = 1^- : \boldsymbol{V} = \boldsymbol{n} \times \boldsymbol{p}_\omega$,
  - $J^P = 1^+ : \boldsymbol{V} = \boldsymbol{n}$;

  the angle ψ_V is the azimuthal orientation of $\boldsymbol{V}$ relative to the muon scattering plane: $\psi_V = \angle(\boldsymbol{V}, \boldsymbol{n}_\mu)$. or

$$\psi_V = \phi_V - \Phi, \tag{5.21}$$

  where ϕ_V is the azimuthal orientation of the vector $\boldsymbol{V}$ with respect to the production plane.

The introduction of the last angular variable ψ_V requires some comments. The choice of the two different forms for the spin analyzer $\boldsymbol{V}$ is in fact a direct consequence of the form of the matrix element for the $1^\pm$ decay modes in $\omega\pi^0$ photoproduction, which we write as given in [B$^+$74]

$$\boldsymbol{\epsilon} \cdot (\boldsymbol{\pi}^+ \times \boldsymbol{\pi}^-)_\omega \times (\boldsymbol{\omega} - \boldsymbol{\pi}^{\mathbf{0}})_{\omega\pi^0}, \tag{5.22}$$

$$(\boldsymbol{\epsilon} \times \boldsymbol{\gamma}) \cdot (\boldsymbol{\pi}^+ \times \boldsymbol{\pi}^-)_\omega, \tag{5.23}$$

for $J^P = 1^-$ and 1^+, respectively; the particle symbols represent the corresponding momenta as measured in the rest frame of the particle (or resonance) given as a subscript (if distinct from the overall γN center-of-mass frame). The matrix elements thus give the azimuthal orientation of the spin analyzer respect to the photon polarization vector.

The choice of ψ_V as defined in eq. (5.21) can be justified also for leptoproduction if we can prove that the polarization vector *is* in the lepton scattering plane. To do so, we examine the form of the photon density matrix as shown by eq. (1.21), pag. 6: there, the matrix was written as valid in the hadron helicity frame; it can be rewritten as [AAB$^+$67]

$$L_{\mu\nu} = \begin{pmatrix} \frac{1}{2}(1+\epsilon) & 0 & -\sqrt{\frac{1}{2}\epsilon(1+\epsilon)} \\ 0 & \frac{1}{2}(1-\epsilon) & 0 \\ -\sqrt{\frac{1}{2}\epsilon(1+\epsilon)} & 0 & \epsilon \end{pmatrix}, \tag{5.24}$$

which corresponds to a photon in an incoherent mixture of two different polarization states described by the two vectors

$$\begin{pmatrix} 0 \\ \sqrt{\frac{1}{2}(1-\epsilon)} \\ 0 \end{pmatrix} \quad \text{and} \quad \begin{pmatrix} \sqrt{\frac{1}{2}(1+\epsilon)} \\ 0 \\ \sqrt{\epsilon} \end{pmatrix} \tag{5.25}$$

(ϵ is defined in eq. (1.22), pag. 7). The first vector has only the y-component[1] different from zero, thus corresponding to a transverse photon polarized perpendicular to the lepton scattering plane, whereas the second vector describes a mixture of transverse (x direction) and longitudinal (z direction) polarization, with the transverse component *in* the scattering plane.

The polarization vector is in this plane for $\epsilon = 1$ (equal contributions from transverse and longitudinal photon polarization to the cross section), whereas the photon is pure transversal for $\epsilon = 0$, with equal contributions in the directions perpendicular and parallel to the scattering plane. In the interval $\epsilon \in [0, 1]$, an ellipsoid characterizes the photon polarization, the axis of the ellipsoid perpendicular to the scattering plane *vanishing for* $\epsilon \to 1$.

As can be seen from Figure 5.6, the present data are characterized by a mean value $\langle\epsilon\rangle \approx 0.65$, with few events at small ϵ: this result shows that the y-component of vectors (5.25) is generally small compared with the x-component. The assumption that in our kinematic range the photon polarization is along the scattering plane is thus a good approximation.

For electroproduction via quasi-real photons, as is the case in the present analysis ($\langle Q^2\rangle \approx 0.1$ (GeV/c^2)^2, see Figure 5.2 top-left), one can thus assume linear polarization of the γ^* in the primary scattering plane and adopt the angular correlation formalism of [SW73], [B$^+$74] and [AAB$^+$67].

Figures 5.15 and 5.16 show for all these angles the observed distributions before acceptance corrections are applied.

The same distributions are shown in Figures 5.17 and 5.18, after introduction of a cut on the $\omega\pi^0$ mass (peak region): 1.1 GeV/$c^2 < m(\omega\pi^0) <$ 1.4 GeV/c^2.

[1] The x, y and z components correspond to the ($\boldsymbol{X}$, $\boldsymbol{Y}$, $\boldsymbol{Z}$) coordinate system as defined in equations (5.7) and (5.8).

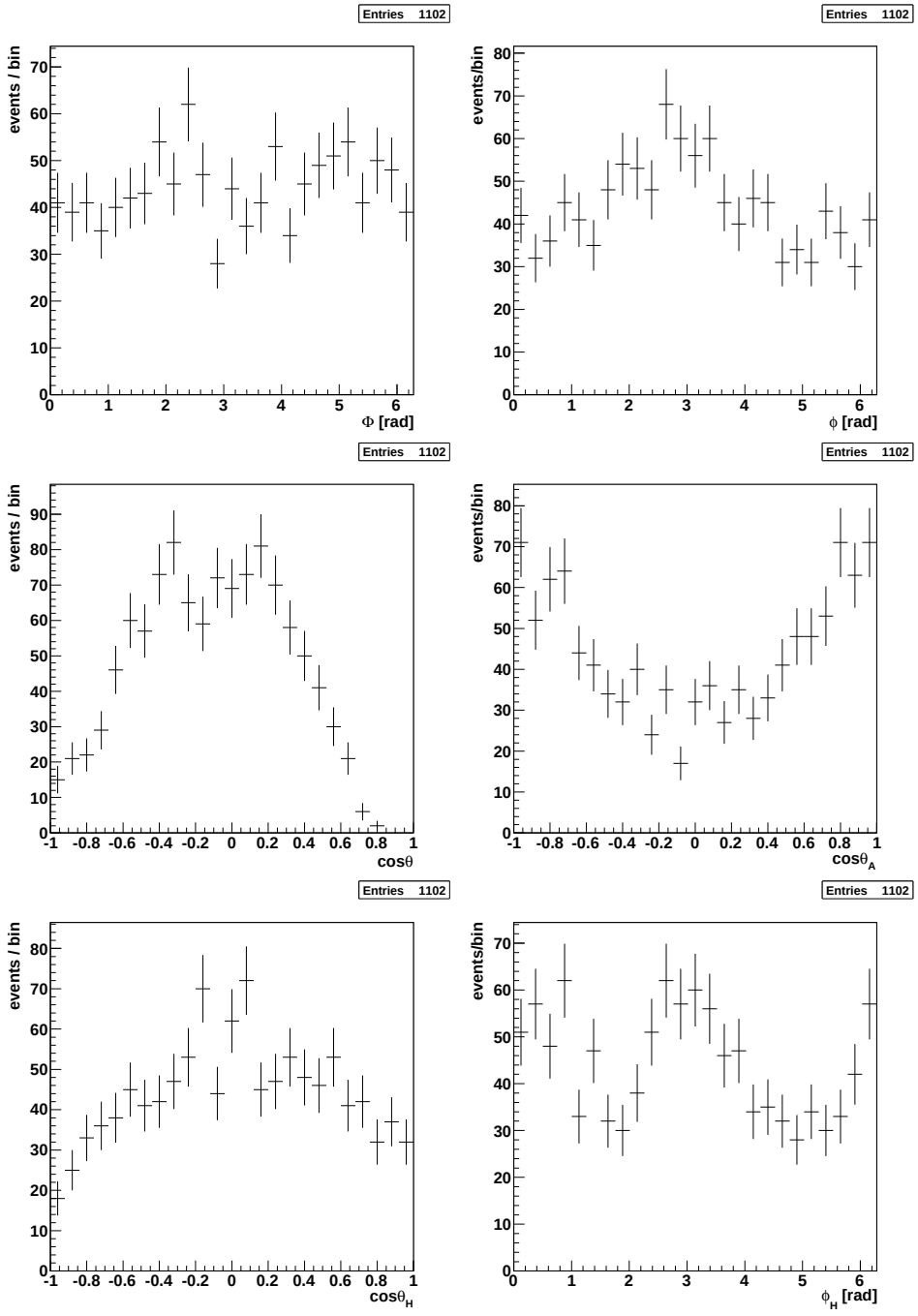

Figure 5.15: *Angular distributions for the final sample, not corrected for acceptance.*

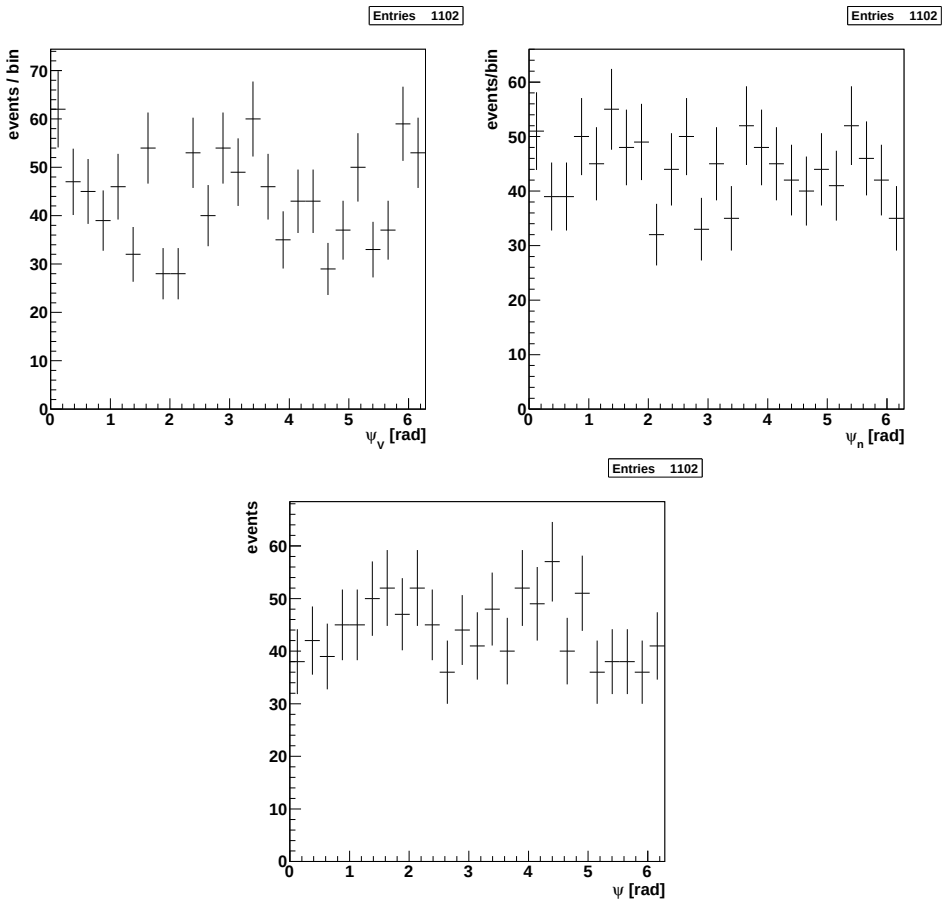

Figure 5.16: *(Continuation) Angular distributions for final sample, not corrected for acceptance.*

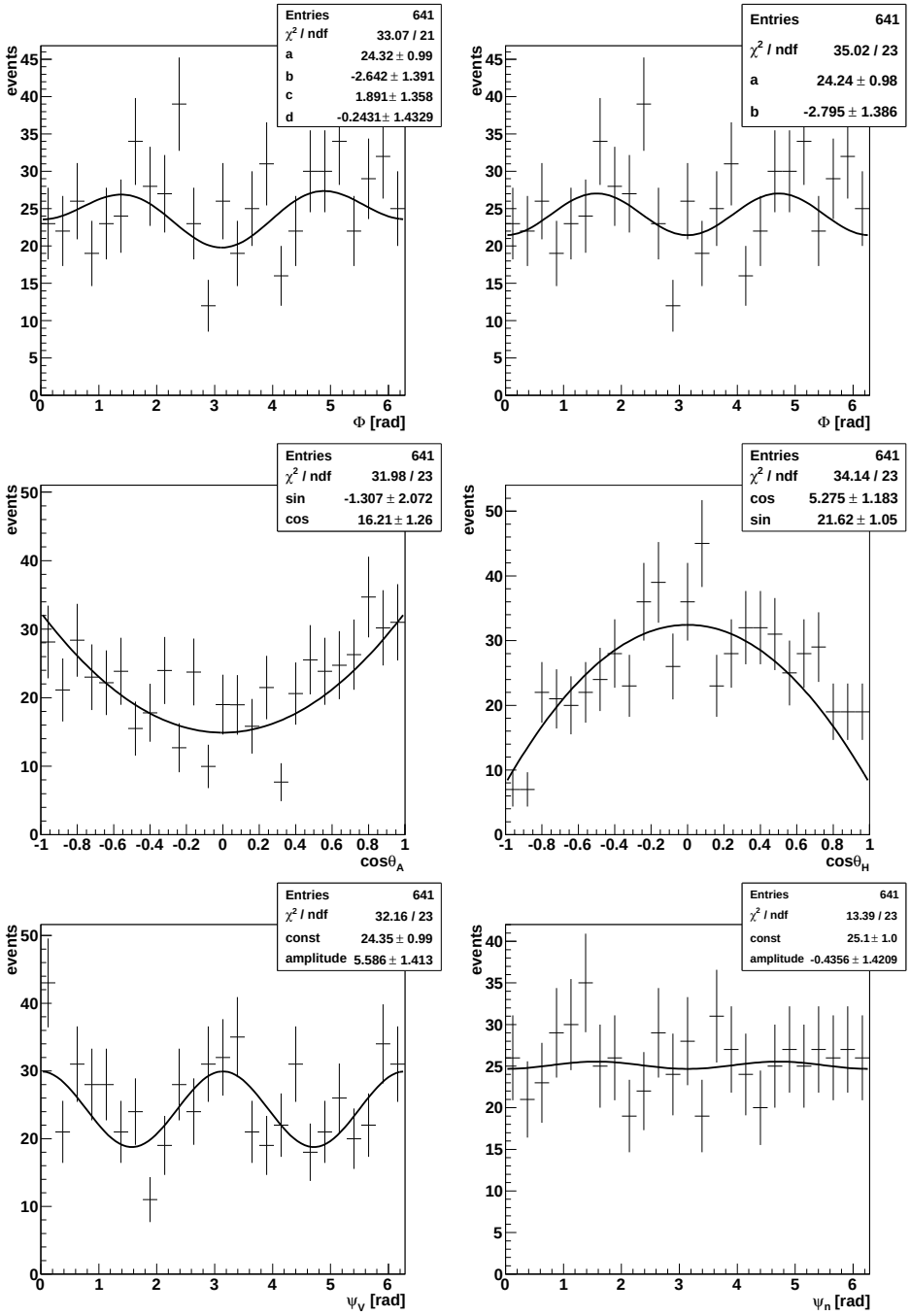

Figure 5.17: *Final sample angular distributions within* 1.1 *GeV*/$c^2 < m(\omega\pi^0) <$ 1.4 *GeV*/c^2.

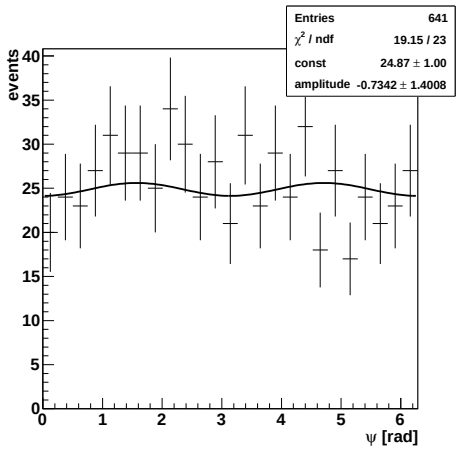

Figure 5.18: *Final sample angular distributions within* 1.1 *GeV*/$c^2 < m(\omega\pi^0) <$ 1.4 *GeV*/c^2.

J^P	$I(\cos\theta)$	$I(\cos\theta_A)$
$1^+(b_1(1235))$	$\sim 1 + x\cos^2\theta$	$\sim \sin^2\theta_A$
$1^-(\rho')$	$\sim 1 + \cos^2\theta$	$\sim 1 + \cos^2\theta_A$

Table 5.3: *SCHC prediction for the decay angular distributions of* $J^P = 1^\pm$ $\omega\pi^0$ *states.*

Assuming SCHC, the two sets of angular distributions in Table 5.3 are predicted [A$^+$80] for the two different spin-parity assignments 1^- and 1^+ to $\omega\pi^0$. The quantity $x \approx 0.07$ is the known D/S-wave amplitude ratio squared of $b_1(1235)$.

The meaning of this quantity can be understood the following way: the ω is a vector meson with quantum number $J^P = 1^-$, whereas the pion is a pseudoscalar $J^P = 0^-$. If we considered the $\omega\pi^0$ meson system as an unstable bound state of the ω and the π^0, we have for its parity

$$P = P_\omega P_{\pi^0}(-1)^L = (-1)^L, \tag{5.26}$$

where L enotes the relative orbital angular momentum of the two particles. It follows that a 1^+ state can assume only *even* values of L, in spectroscopic notation only *s*-, *d*-, ... waves are permitted, whereas a vector meson can assume only *odd* values of L (i.e. *p*-, *f*-, ... waves). This is verified for the case of the $b_1(1235)$, which has a mixture of *s*- and *d*-wave, the latter contributing to the decay amplitude by a factor:

$$\frac{D}{S} = \frac{A(L=2)}{\sqrt{5}A(L=0)} = 0.277 \pm 0.027 \tag{5.27}$$

(cf. [A$^+$08b]) which has been experimentally measured. The factor $\sqrt{5}$ in the previous formula is introduced to take into account the five ($2L + 1 = 5$ for $L = 2$) different possible states.

In appendix, Figures A.10, A.12 and A.13 show the same angular distributions in their dependence on the year of data taking (2004 and 2006).

No fit on the data has been performed at this point, because experimental data must be corrected for acceptance effects, and this information can only be achieved performing a detailed analysis of the spectrometer response by means of a Monte Carlo (MC) simulation. This topic will be the object of the next chapter.

Chapter 6

The Monte Carlo simulation

In this chapter, a detailed overview of the performed Monte Carlo (MC) simulation for the exclusive $\omega\pi^0$ production will be given.

Of particular interest are the acceptance corrections to be applied to the angular distributions examined so far for the determination of the spin-parity (J^P) of the $\omega\pi^0$ system. In fact, the reconstruction of an event is always affected by the geometry acceptance of the apparatus, by the efficiency of particle detection, and also by the efficiency of the reconstruction procedure. Therefore, to gain realistic results from analysis, all these effects must be quantitatively evaluated, and the experimental distributions properly corrected.

The Monte Carlo simulation is the tool to calculate such corrections. It is generally divided in three steps, which form the so called Monte Carlo *chain*:

- The generation of events: this is obtained using a computer program which creates *artificial* events, i.e. a list of particles together with their 4-momenta, randomly generated satisfying some predefined kinematic distribution characteristic of the reaction under investigation.

- The output of the event generator is read by a second program, which simulates the physical processes which take place during the interaction of the generated particles with the material of the detector components. At the end of this process, the position of hits in the tracking detectors, together with time information, showers simulation in the electromagnetic and hadronic calorimeters, radiation in the Cherenkov detectors, the bending of charged particles trajectories in the magnetic fields present, all these processes are simulated and quantitatively determined.

- From the information obtained so far, the same reconstruction program used for real data is used to reconstruct the MC events and

store them in files ready for analysis. At COMPASS, MC data are written in the same format (mDST files) as real data.

At this point, the same routines written by the user to analyze the real data are employed to analyze the reconstructed MC data. A quantitative comparison of the generated and reconstructed MC data puts in evidence the cumulative effect of geometric acceptance, detector and event reconstruction efficiency, which all contribute to the distortions of the various spectra characteristic of real data. After acceptance calculations, real data may be corrected and results of physical interest gained from the analysis.

6.1 The event generator

Due to the vast physics program of COMPASS, many different event generators are used within the Collaboration, each of them tuned to a particular channel under investigation. Unfortunately, for exclusive (vector) meson production by quasi-real photons, the necessity to use external event generators was compelling: for the case of exclusive ρ^0 production with muons, a modified version of DIPSI adapted to the kinematic range of COMPASS was employed by the Collaboration. DIPSI can also simulate the exclusive ϕ and ω electroproduction, but not a $\omega\pi^0$ in the $1^{\pm}$ state. Due to the possible presence of the $b_1(1250)$, also a 1^+ state in the same mass region as of the $\omega\pi^0$ signal and *not* treated by DIPSI, it was decided to write a new simple event generator starting from scratch.

It consists of a ROOT script written in C++, whose task is to write in its output file the particle identity and its 4-momentum for all the particles in an event, this done on an event by event basis. The processes to simulate are:

- the scattering of the incoming beam μ^+ on a nucleon at rest in the laboratory frame;
- the production of the $\omega\pi^0$ system in a given kinematic range, consistent with the muon scattering observed in real data;
- the decay $\omega\pi^0 \to \omega + \pi^0$ in the $\omega\pi^0$ rest frame;
- the $\omega \to \pi^+\pi^-\pi^0$ decay in the ω rest frame;
- the $\pi^0 \to 2\gamma$ decay: this part of the event generator was implemented to gain information about the energy distribution of the resulting four photons in the event; this in the laboratory reference frame and at the generator level. Results are shown in Figure 6.1: at the generator level it is possible to distinguish between the decay photons of the π^0 from $\omega\pi^0$ (the spectator) and those from the pion involved in the ω decay. Due to the different kinematic, the energy spectra of

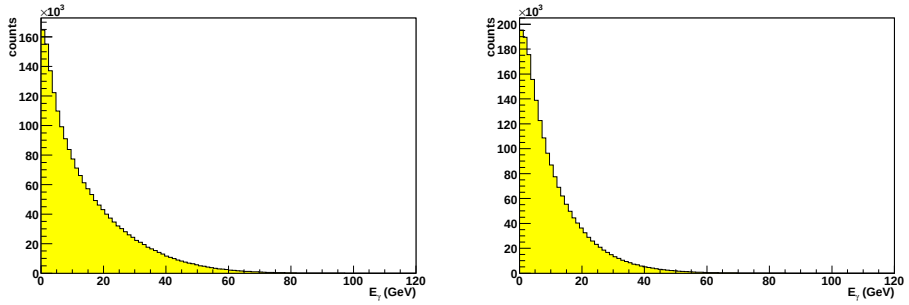

Figure 6.1: *Generated energy spectra (in the laboratory frame) for photons originated by the spectator π^0 decay (left) and from the π^0 coming from the ω decay (right).*

the two photon-pairs are slightly different, as can be seen in Figure 6.1. Photons coming from the decay of the spectator π^0 are slightly more energetic. In addition, knowing the 4-momenta of the photons already at the generator level, makes the detailed determination of the effects of the geometrical acceptance of ECAL2 possible (this topic is discussed in more detail at the end of this chapter). Infact, extrapolating the photon path till the position of ECAL2 ($z \approx 32$ m), it is possible to know if the photon interacts with the active surface of the calorimeter, or it escapes through the hole or over the external border of the detector. As we will see, these features have a major impact on the $\cos\theta$ angular distribution.

Simulation of the decay of a neutral pion may be in addition automatically performed in the second step of the MC chain. This feature was used for the final MC simulation.

Informations about a single event were thus written in the output file describing the reaction in the interaction point as a kind of *star* of outgoing particles and, rather technical aspect, the beam muon was tagged as the only particle from the interaction vertex having a negative momentum p_z, whereas the scattered μ^+, the π^+, π^- and the two π^0's all had $p_z > 0$, the z-axis directed along the beam direction.

Due to the two subsequent decays $\omega\pi^0 \rightarrow \omega + \pi^0 \rightarrow \pi^+\pi^-\pi^0 + \pi^0$, whose decription is best suited in the rest frame of each one of the decaying particles, further complications must be faced. Therefore much attention was paid to the series of rotations and boosts which must be performed going from the rest frames to the laboratory frame, which is the default frame for the further simulation of an event.

All the decay process were simulated to be isotropic, for a precise determination of the acceptance effect on the reconstructed angular distributions.

For the present MC study, a sample of $9 \cdot 10^6$ exclusive $\omega\pi^0$ events were

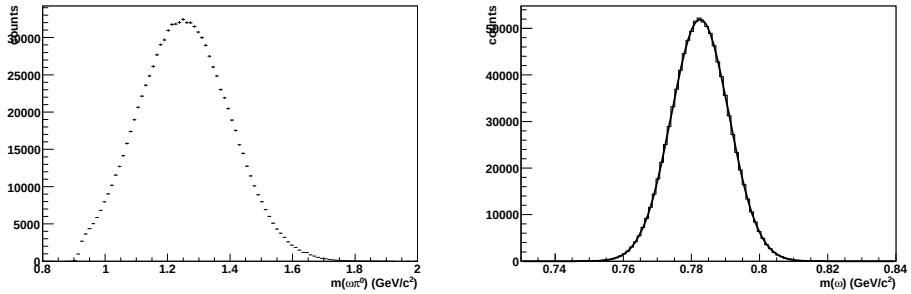

Figure 6.2: *Generated mass-distributions for $\omega\pi^0$ and ω. The near threshold deviation of the first one from a gaussian distribution is due to the constraint $m_{\omega\pi^0} > m_\omega + m_{\pi^0}$ included in the generator itself.*

generated.

6.1.1 The $\omega\pi^0$ decay

As a two-body decay, an isotropic $\omega\pi^0 \to \omega + \pi^0$ decay is very easily simulated. Given a parent particle of mass M decaying to a couple of particle of mass m_1 and m_2, the energy-momentum conservation law dictates

$$p = \frac{\sqrt{(M^2 - (m_1 + m_2)^2)(M^2 - (m_1 - m_2)^2)}}{2M} \tag{6.1}$$

for the absolute value of the momenta of each of the two daughter particles, and energy is calculated from the fundamental relation

$$E_i = \sqrt{p^2 + m_i^2} \qquad i = 1, 2. \tag{6.2}$$

The values for the masses of $\omega\pi^0$ and ω were randomly generated obeying a gaussian distribution with mean value M and width Γ, given by:

$$(M \pm \Gamma)_{\omega\pi^0} = 1250 \pm 150 \text{ MeV}/c^2$$

$$(M \pm \Gamma)_{\omega} = 782 \pm 9 \text{ MeV}/c^2$$

respectively, the last line corresponding to PDG values [A$^+$08b] (Figure 6.2).

The same set of formulae describes the case of π^0 decay into two photons, this time imposing the values $m_1 = m_2 = 0$ which lead to $p = E = M/2$ (in units $c = 1$).

Once the absolute value of the momentum had been calculated, the direction of flight was randomly and uniformly distributed on a sphere centered in the decaying particle, and an isotropic distribution for $\omega\pi^0 \to \omega + \pi^0$ as well as for $\pi^0 \to \gamma\gamma$ thus obtained.

6.1.2 The ω decay

Being a three-body decay, the ω decay is a more complicated process to simulate. The three pions must lie in a plane, due to momentum conservation, but the allowed kinematic configurations are spread into a continuous distribution which may be calculated from the decay matrix element.

It can be shown [SAMacR62] that for vector mesons ($J^P = 1^-$) decaying to three pseudoscalar mesons, the decay amplitude assumes the form:

$$A = |\boldsymbol{p}_0 \times \boldsymbol{p}_1 + \boldsymbol{p}_1 \times \boldsymbol{p}_2 + \boldsymbol{p}_2 \times \boldsymbol{p}_0|^2, \tag{6.3}$$

where $\boldsymbol{p}_i$, $i = 0, 1, 2$, are the momenta of the three pions in the ω rest frame.

A nice method to reproduce the correct probability distribution for the decay kinematic makes use of the Dalitz plot. Already in the original paper [MacARS61], in which the vector nature of the ω meson was proven, information about spin and parity were gained inspecting the intensity point(event)-distribution in a Dalitz plot. A particular decay configuration in a three-body decay can be represented by a point in a plane region. Several versions of a Dalitz plot can be used: we have chosen the so called *symmetric* representation, in which the x and y coordinates in the plane are defined as:

$$x = \frac{T_1 - T_2}{Q\sqrt{3}}, \tag{6.4}$$

$$y = \frac{T_0}{Q} - \frac{1}{3}, \tag{6.5}$$

where T_i, $i = 0, 1, 2$, are the kinetic energies of the three pions in the ω rest frame, calculated from the formula

$$p_i^2 = T_i(2m_i + T_i), \tag{6.6}$$

and the quantity Q, defined as

$$Q = m_\omega - 3m_\pi = T_0 + T_1 + T_2, \tag{6.7}$$

is the Q-value of the decay reaction. In the last equation, as in the following of this section, we have neglected the mass difference between the charged and the neutral pions[1]. The same Dalitz plot and the same quantities x and y can be used to study the kinematic of other three-body decays, like $K \to 3\pi$. For different assignments of J^P quantum numbers, different point distributions in the Dalitz plot are expected (and also observed). This is the feature that makes Dalitz plots so useful for our purpose: if one is able to generate events which reproduce the correct point distribution in the Dalitz plot, this is equivalent to have a set of events with the correct decay distribution.

[1] Without this assumption, the previous formula would read: $Q = m_\omega - 2m_{\pi^\pm} - m_{\pi^0}$.

Phase space alone implies a uniform distribution of points, and it must also be pointed out that not the whole xy-plane represents kinematically allowed configurations: the momentum conservation law must be taken into account. From the relation (6.6) the following equation can be derived (for the pair of pions $(1,2)$; analogous relations are valid for the other two possible pairs):

$$\cos\theta_{12} = \frac{p_0^2 - p_1^2 - p_2^2}{2p_1p_2}. \tag{6.8}$$

Imposing the usual constraint for the existence of the cosinus,

$$-1 \leq \cos\theta \leq 1, \tag{6.9}$$

the kinematically allowed region is delimited by a closed curve, which tends to a circle centered in $x = y = 0$ in the non-relativistic case ($Q \to 0$, i.e. $m_\omega \to 3m_\pi$) and degenerates to an equilateral triangle in the ultra-relativistic case ($Q \to \infty$). Already for ω, with $Q \approx 369$ MeV/c^2, a deviation from the circular shape is easily observed (Figure 6.3).

We need at this point a recipe to reproduce the correct point distribution in the allowed region. It turns out, that for a decay amplitude as in (6.3), the density of points is proportional to the quantity

$$\lambda = \frac{|\boldsymbol{p}_i \times \boldsymbol{p}_j|^2}{|\boldsymbol{p}_i \times \boldsymbol{p}_j|^2_{max}}, \tag{6.10}$$

(compare with equation (5.2)) where the denominator represents the maximum value assumed by the numerator, thus leading to the normalization of λ, now constrained to vary in the interval $[0,1]$. The value 0 is obtained when two pions are collinear or at least one of them at rest, and it corresponds to the border of the Dalitz plot; the maximum value 1 is achieved only in the center of the plot ($x = y = 0$), and corresponds to the unique completely symmetric decay configuration, where the three pions have the same kinetic energy and move away from each other forming three equal angles $\theta_{ij} = \angle(\boldsymbol{p}_i, \boldsymbol{p}_j) = 120°$. Intermediate values of λ correspond to concentric closed curved lines spanning the plot smoothly, with decreasing λ, from the center to the border. The generated event sample can be seen in Figure 6.3. A three dimensional representation in the $xy\lambda$-space is often called *Dalitz-Stevenson* plot (Figure 6.4).

To reproduce the desired linear increase, the value of λ was calculated for every generated point uniformly distributed in the allowed region of the Dalitz plot, and compared with a second quantity λ', randomly chosen from a constant distribution in the interval $[0,1]$. The requirement

$$\lambda' < \lambda \tag{6.11}$$

reproduces the linear increase of λ and the correct point distribution in the Dalitz plot. The reason to adopt (6.11) can be understood this way: if a

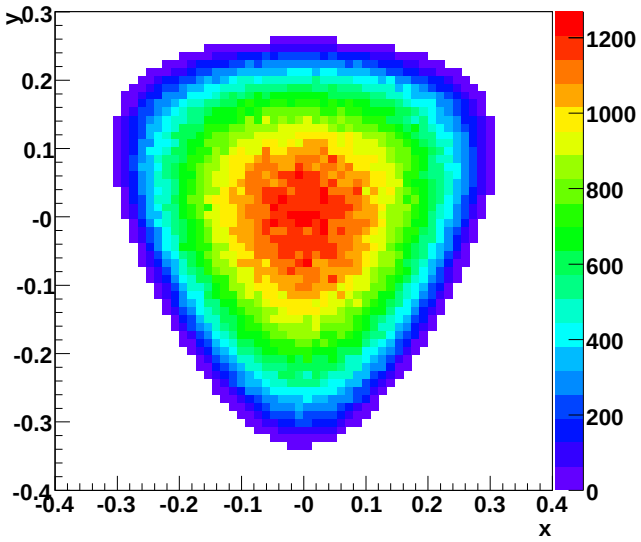

Figure 6.3: *Dalitz plot for the generated* $\omega \to \pi^+\pi^-\pi^0$ *decay. The correct point distribution for a vector meson* ($J^P = 1^-$) *decay in three pseudoscalar is reproduced: the density reaches the maximum in the center of the plot, and goes to zero approaching the border of the kinematically allowed region (in color).*

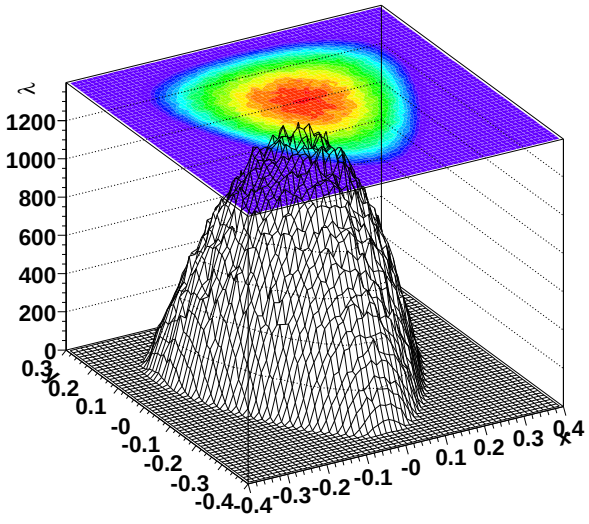

Figure 6.4: *Dalitz-Stevenson plot for the generated* $\omega \to \pi^+\pi^-\pi^0$ *decay (the value* λ *is not normalized).*

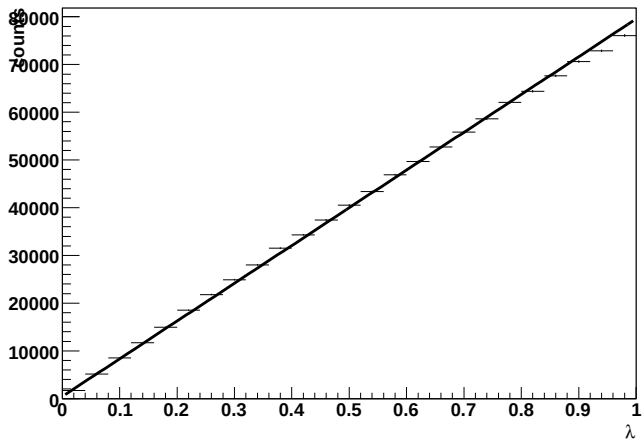

Figure 6.5: *Distribution of λ from equation 6.10, for the generated event sample. A linear fit has been performed to show the correctness of the generating algorithm.*

quantity λ' is uniformly distributed on the interval $[0, 1]$, the probability to obtain, after a random choice, a value lower than a fixed one, say λ_0, is then proportional to λ_0 itself, whereas the probability to have a higher value will be proportional to $1 - \lambda_0$. If we then compare our λ from (6.10) and the chosen λ', we see that high values of λ satisfies (6.11) more often than the case with low values, and this happens following *exactly* a linear behaviour; this is thus obtained for λ in the final sample (Figure 6.5).

Once a particular event has been accepted because satisfying the condition (6.11), the absolute values of the pion momenta can be calculated inverting relations (6.4) and (6.5), and using (6.6) and (6.8) to define the direction of the momenta in the decay plane of the ω. The unit vector

$$\boldsymbol{n} = \frac{\boldsymbol{p}_i \times \boldsymbol{p}_j}{|\boldsymbol{p}_i \times \boldsymbol{p}_j|} \tag{6.12}$$

defines the orientation of the plane in space: a series of arbitrary rotations of $\boldsymbol{n}$ (together with the corresponding momenta $\boldsymbol{p}_i$), performed on an event-by-event basis in such a way, to have the various $\boldsymbol{n}$ uniformly distributed on a unit sphere, leads to the desired isotropic decay distribution for the ω in its rest frame.

The 4-momenta of the three pions can be now calculated as seen by an observer moving with the $\omega\pi^0$ system simply performing a boost $L(-\boldsymbol{\beta}_\omega)$, where the boost vector $\boldsymbol{\beta}_\omega$ corresponds to the velocity of the ω in the $\omega\pi^0$ rest frame, derived from relation (6.1).

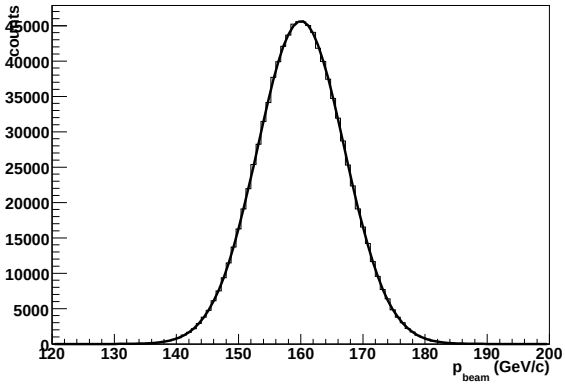

Figure 6.6: *Generated beam momentum* p_{beam} : 160 ± 7 *GeV/c normal distribution.*

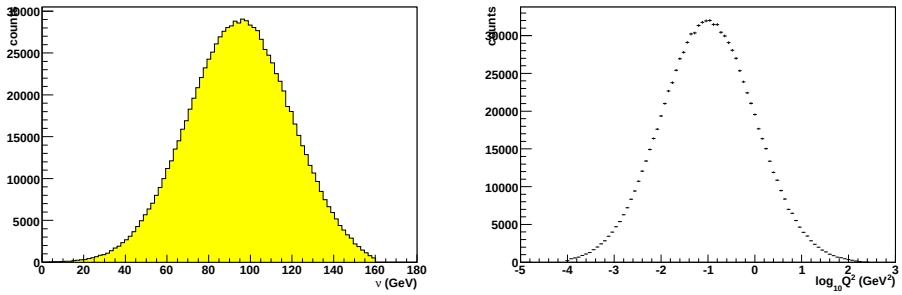

Figure 6.7: *Generated gaussian distributions for the vitual photon energy* $\nu = E - E'$ *(left) and for its squared 4-momentum* Q^2 *(right).*

6.1.3 The beam scattering

As already said, the beam muon was chosen to propagate along the z-axis, with negative momentum p_z, randomly generated from a gaussian distribution centered at the nominal vakue 160 GeV/c and $\sigma = 7$ GeV/c (Figure 6.6), these values chosen to reproduce the measured ones. From the value of the momentum, the beam energy can be easily obtained.

The scattered muon energy ν, was generated obeying a gaussian distribution chosen such as to reproduce the observed behaviour in real data for the $\omega\pi^0$ final sample (Figure 6.7, left). From the formula

$$Q^2 = 4EE' \sin^2 \frac{\theta}{2}, \tag{6.13}$$

the polar distribution θ around the beam axis z can be obtained by inversion, taking into account the relation $E' = E - \nu$; the azimuthal distribution around z was chosen flat in $[0, 2\pi]$. All this leads to the determination of

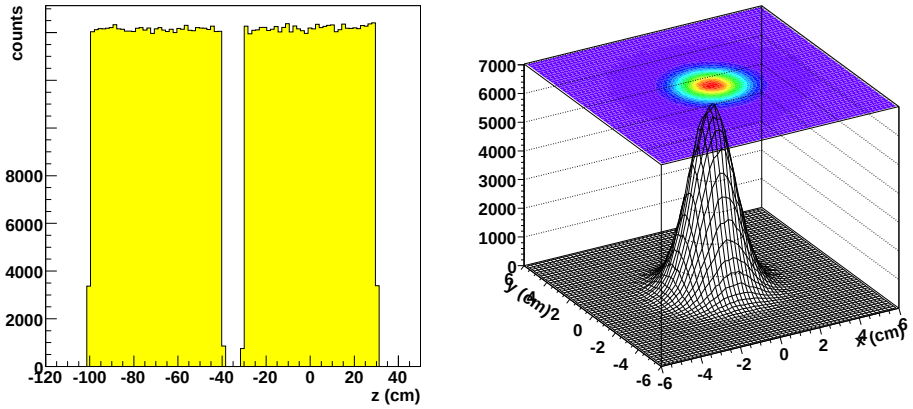

Figure 6.8: *Generated vertex distribution along the beam direction z (left), and in the transversal plane xy (right).*

Q^2, which was simulated obeying a normal distribution adapted to real data results (Figure 6.7, right).

Once the directions of μ and μ' are known, the *scattering* plane orientation can be found by calculating their cross product

$$\boldsymbol{n}_{scatt} = \frac{\boldsymbol{p}_{\mu} \times \boldsymbol{p}_{\mu'}}{|\boldsymbol{p}_{\mu} \times \boldsymbol{p}_{\mu'}|}. \tag{6.14}$$

Note also that the direction of the virtual photon, fixed by $\boldsymbol{q}$, lies in the same plane.

The interaction vertex position, where the scattering takes place, was uniformely distributed in the region corresponding to the target position for year 2004: -100 cm $\leq z_V \leq -40$ cm and -30 cm $\leq z_V \leq 30$ cm. The distribution in the plane perpendicular to z was gaussian, to reproduce the real data (Figure 6.8).

6.1.4 The $\omega\pi^0$ production plane

A boost in the $\boldsymbol{q}$ direction with the correct boost parameter $\boldsymbol{\beta}_q = \boldsymbol{q}/(q_0 + m_N)$ ($q_0 = \nu$ being the time-component of the virtual photon 4-momentum and m_N the nucleon mass), permits to "translate" to the $\gamma^* N$ center of mass frame. The direction of the virtual photon and of the produced $\omega\pi^0$ lie in the same plane, the *production* plane. Their cross product

$$\boldsymbol{n}_{prod} = \frac{\boldsymbol{q} \times \boldsymbol{p}_{\omega\pi^0}}{|\boldsymbol{q} \times \boldsymbol{p}_{\omega\pi^0}|}. \tag{6.15}$$

shows the orientation of the production plane in space. Note that a boost along $\boldsymbol{q}$ doesn't change the azimuthal orientation between the scattering and

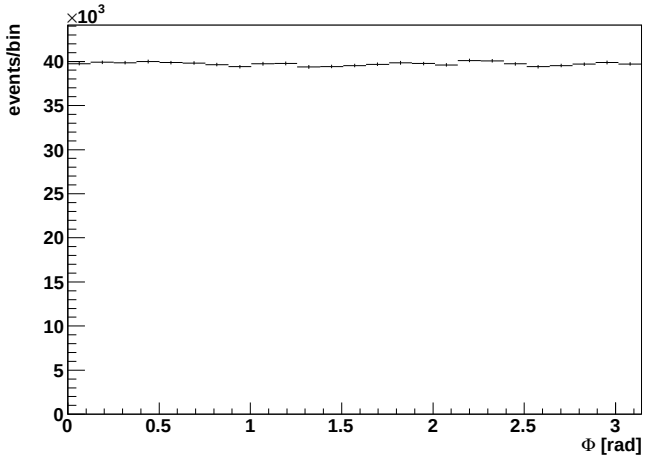

Figure 6.9: *Generated distribution for the orientation (angle Φ) of the production plane relative the scattering plane.*

the production planes, described by the angle Φ. This angle was chosen to obey a constant distribution in $[0, 2\pi]$ (Figure 6.9). This is also the azimuthal orientation of the $\omega\pi^0$ direction relative to the scattering plane. The polar distribution along the direction of the virtual photon was reproduced from the formula

$$\cos\theta_{prod} = 1 + \frac{t}{2|\boldsymbol{q}|^2}, \tag{6.16}$$

where $t = (q - v)^2$ is the squared 4-momentum transfer with the nucleon in reaction $\gamma^* + N \rightarrow \omega\pi^0 + N'$ and was generated following an exponential law $\sim e^{-5t}$ (Figure 6.10) to reproduce the diffractive behaviour observed in the real data. A last boost $L(\boldsymbol{\beta}_{\omega\pi^0})$ in the $\omega\pi^0$ direction leads to the $\omega\pi^0$ *decay*-plane, fixed by the $\omega\pi^0$ and ω momenta. Its orientation is determined by the cross product

$$\boldsymbol{n}_{decay} = \frac{\boldsymbol{p}_{\omega\pi^0} \times \boldsymbol{p}_{\omega}}{|\boldsymbol{p}_{\omega\pi^0} \times \boldsymbol{p}_{\omega}|}. \tag{6.17}$$

The azimuthal orientation relative to the production plane ϕ, and, in addition, the angle $\psi = \phi - \Phi$ are thus easily determined.

A last boost $L(\boldsymbol{\beta}_{\omega})$, where $\boldsymbol{\beta}_{\omega}$ is the ω velocity as seen in the $\omega\pi^0$ rest frame, brings us in the ω rest frame, where the ω decay plane orientation is determined by the vector $\boldsymbol{n}$ in (6.12).

If the chain of boosts and rotations encountered so far is inverted in the appropriate manner, all the interesting 4-momenta derived, for each one of the involved particles, in the different reference frames can be expressed as they would seen by an observer in the laboratory frame. This has been done at the generator level and the values have been stored at the end of the

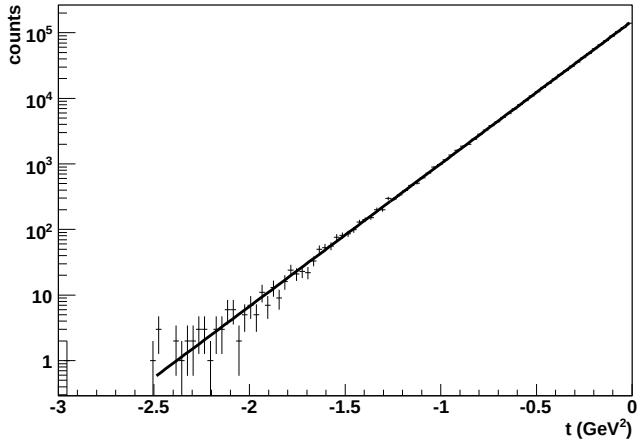

Figure 6.10: *Generated distribution* $\sim e^{-5|t|}$ *for the variable* $t = (q - v)^2$*, where* q *and* v *are the 4-momenta of the virtual photon and produced meson* $\omega\pi^0$*, respectively (logarithmic scale).*

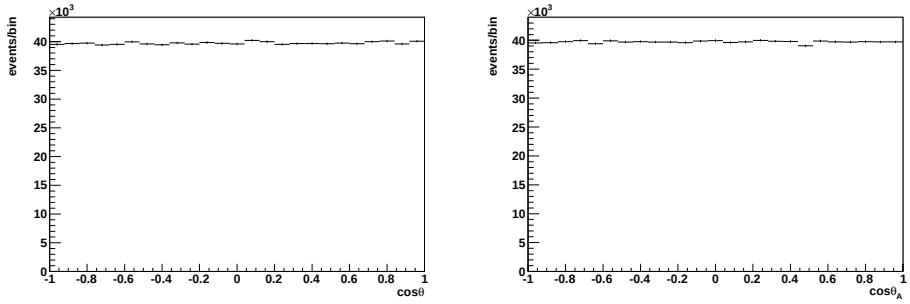

Figure 6.11: *Flat distributions for* $\cos\theta$ *and* $\cos\theta_A$ *at the generator level. The flatness is a consequence of the isotropy imposed to the* $\omega\pi^0$ *and* ω *decays.*

event generation in the output file used in the subsequent step of the MC chain.

6.1.5 Angular distributions

Figure 6.11 shows, for the simulated isotropic $\omega\pi^0$ decay, the $\cos\theta$ and $\cos\theta_H$ distributions[2]: they describe the polar direction of the ω in the $\omega\pi^0$ rest frame, and the orientation of the ω decay plane along z in its own helicity frame, respectively. The resulting flat distributions are a direct consequence of the imposed isotropy of the two subsequent decays $\omega\pi^0 \to \omega + \pi^0 \to \pi^+\pi^-\pi^0 + \pi^0$.

[2]for a definition of these angles, see the previous chapter.

6.2 Detector response and MC event reconstruction

To reproduce the interaction of particles in a generated event with the detector, the COMGEANT[3] program is used by the COMPASS Collaboration.

It is derived from a "frozen" version of the GEANT3[4] simulation tool, developed during the last decades at CERN.

The binary file from the event generator containing the event description on an event-by-event basis constitutes the input for COMGEANT. Specifying in an *option file* the various configuration parameters, like the detector geometry and setup, which depends on the year of data taking and/or physics program conducted, the number of events to simulate, the list of physical process that a charged or neutral particle undergoes travelling through the spectrometer, depending on the particle nature (hadron, lepton or photon) and energy, all these informations result in a so called ZEBRA file, which contains the *raw data*, like position of the hits in tracking detectors, time characteristic of the signals, energy deposit of the hadronic and electromagnetic shower in the calorimeters, Cherenkov radiation in the RICH, and so on.

These raw data are subsequently elaborated by the event reconstruction program CORAL, and the reconstructed events are finally stored in mDST files, in analogy to real data.

A graphical representation of simulated particle interactions in a $\omega\pi^0$ produced event and subsequent decays as seen by COMGEANT can be viewed in Figure 6.12, where a section of the detector layout and the tracks and calorimeter showers are shown (the various colors correspond to different particle types).

Version 7.02 of COMGEANT was used in this analysis, linked to a CORAL version released at the end of March 2007.

To use CORAL, one needs to specify in an *option file* what kind of detector configuration has been used by COMGEANT.

To speed up the simulation, a second possibility forseen by the programs was employed: simulated detector information was not written in the ZEBRA files, instead a so called *pipe*, based on a FIFO[5] mechanism, sent the COMGEANT output for the *single* event directly to CORAL for reconstruction. This method had the advantage of saving time and space on computer storage system without loss of precision in the MC simulation.

The resulting mDSTs with the reconstructed events at the end of the MC chain, were ready for use in the analysis of the MC data, performed with the same routines already written for real data analysis.

[3] http://valexakh.web.cern.ch/valexakh/wwwcomg/index.html
[4] http://wwwasd.web.cern.ch/wwwasd/geant/index.html
[5] First-In, First-Out

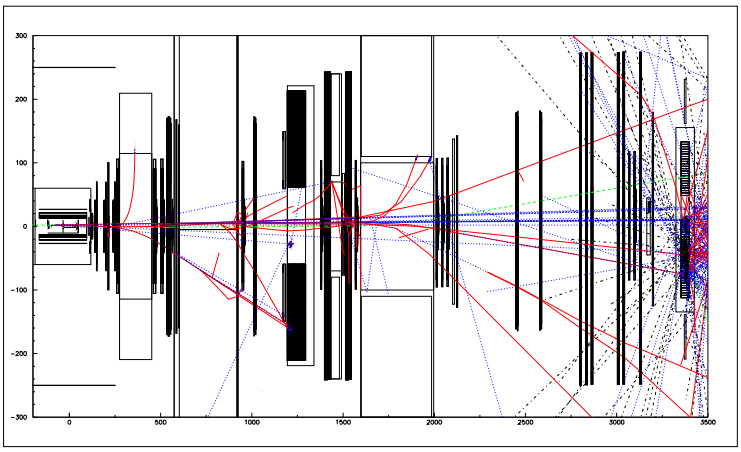

Figure 6.12: *A partial view (from above) of the detector layout (from two-cell target to ECAL2 region) for year 2004, as seen by COMGEANT, together with the simulated charged and neutral tracks and produced showers in the calorimetry, for a single generated $\omega\pi^0$-event. Different colors and line types correspond to different particle types (*e.g.*, solid-red: electrons and hadrons; dashed-green: muons; dotted-blue: photons). The bending of the scattered μ^+ in the field of the second magnet SM2, positioned at $z \approx 1750$ cm from target ($z \approx 0$) can be seen.*

6.3 MC and real data comparison and acceptance corrections

We are now able to compare reconstructed MC data with the generated ones. From the $9 \cdot 10^6$ generated events, only 30541 exclusive $\omega\pi^0$ events could be fully reconstructed, corresponding to about 0.3% of the originally generated sample.

We consider the two following aspects of the reaction:

1. kinematic of the reaction;
2. angular distributions.

6.3.1 The kinematic of reaction

The first important question concerns the exclusivity of the reaction: Figure 6.13 (left) shows the reconstructed missing energy, as defined in equation (4.6): the peak, centered at 1.21 GeV is slightly shifted toward positive values from the nominal value at 0, and the width (from a gaussian fit) is about 1.7 GeV. This is in agreement with the experimentally observed peak in real data, and coherent with the cut -4 GeV $< E_{miss} <$ 6 GeV adopted for the exclusive sample in 2004 data. The same figure (right) shows the

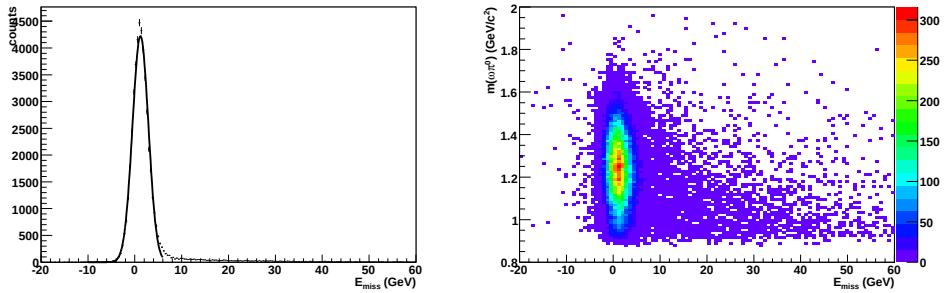

Figure 6.13: *Reconstructed missing energy for generated exclusive $\omega\pi^0$ production (left) and $\omega(\pi^+\pi^-\pi^0)\pi^0$ invariant mass vs. E_{miss} (right).*

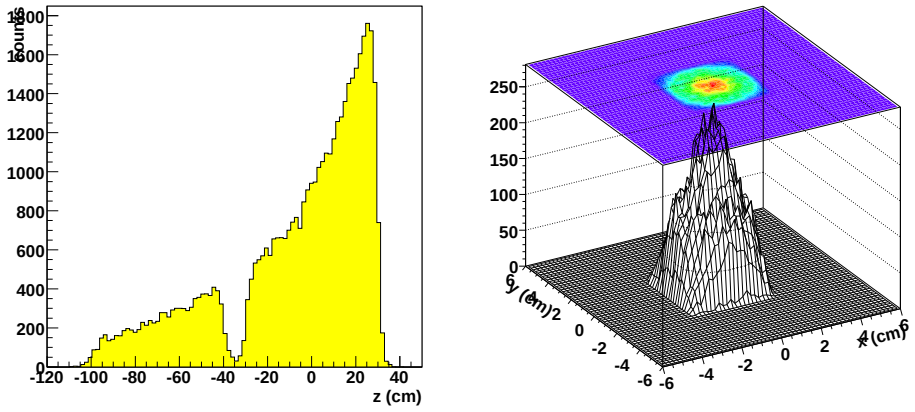

Figure 6.14: *Reconstructed z-coordinate of the best primary vertex (left), and corresponding transversal distribution in the xy plane (right), MC data.*

$\omega(\pi^+\pi^-\pi^0)\pi^0$ mass dependence on the missing energy. As for the case of real data, even if not so dominant, the low $\omega\pi^0$-mass region shows a more intense contribution of inexclusive events.

Figure 6.14 shows the reconstructed position of the vertex interaction, identified from analysis routine as the best primary vertex. The strong acceptance effects observed reproduce well the vertex distribution of real data: only about 19% of the reconstructed vertices lie in the upstrem cell, whereas 78% in the downstream. The remaining fraction of $\sim 3\%$ are vertices erroneously reconstructed outside the geometrical range along z of the target, due to the finite position resolution originating in the reconstruction process. The xy coordinates are reproduced quite correctly, even if a deviation from the generated 2-dimensional normal distribution cannot be denied. In fact, if we compare the result of a gaussian fit for real data (RD) and MC,

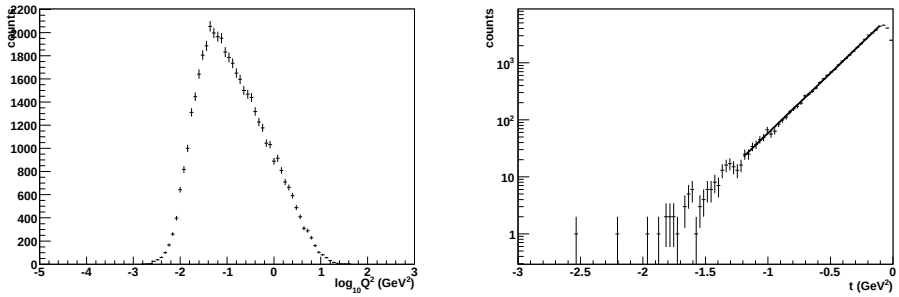

Figure 6.15: *Reconstructed Q^2 of the virtual photon (left), and t-distribution, logarithmic scale. The diffractive exponential fall for high values of t is not particularly affected by acceptance (MC data).*

we obtain the values

$$\sigma_{RD} = 0.79 \pm 0.02\,\text{cm} \tag{6.18}$$

$$\sigma_{MC} = 1.26 \pm 0.01\,\text{cm} \tag{6.19}$$

It also seems, that in the MC chain, an artificial reconstruction domain $[-2,2] \times [-2,2]$ cm^2 is included by default (see the square basis in Figure 6.14, right).

Figure 6.15 shows the resulting Q^2 distribution. A clear acceptance distorsion in the spectrum can be observed: in particular, events with $Q^2 > 0.1$ GeV^2 suffer a heavier loss.

Concerning the t-distribution, the result of reconstruction is shown in the same figure (on the right): the exponential behaviour, typical of diffractive production, is not strongly affected by acceptance, even if the region in which an exponential fit is unambiguous is somewhat narrower; in addition, the value of the slope is correctly reproduced.

Of particular interest is the reconstruction of the quantity λ. Figure 6.16 shows this distribution, with a linear fit superimposed. This is a particularly important result: no significant distorsion is observed as due to the reconstruction procedure, apart from a small shift of the intersection point of the fit line with the y axis, which could introduce a "fake" background of the order of $\sim 5\%$. This results favours the correctness of the interpretation as *true* ω signal in real data and of the background estimation procedure without the need of acceptance correction.

The $\omega\pi^0$ and ω masses are shown in Figure 6.17. The most important feature in the $\omega\pi^0$ spectrum is the clear deviation from a gaussian in the low-mass region of the spectrum. The cut in the ω mass spectrum is an artefact of the imposed cut 750 MeV/$c^2 < m(\pi^+\pi^-\pi^0) <$ 815 MeV/c^2 during data selection. It is found that the MC ω peak, characterized by

$$(M_\omega \pm \Gamma_\omega)_{recon} = 773 \pm\ 13 \quad \text{MeV}/c^2$$

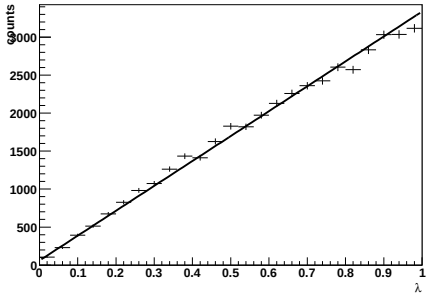

Figure 6.16: *Reconstructed λ distribution (equation (6.10)), MC data. No significative acceptance effects are observed.*

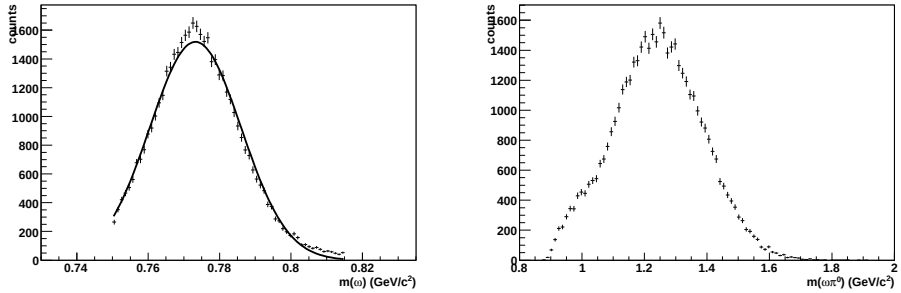

Figure 6.17: *Reconstructed $\omega(\pi^+\pi^-\pi^0)$ (left) and $\omega(\pi^+\pi^-\pi^0)\pi^0$ (right) invariant mass, MC data.*

is shifted toward lower mass relative to real data by an amount of ~ 9 MeV/c^2. Also the width increases by ~ 4 MeV/c^2.

To gain a better understanding of the acceptance bias on the $\omega\pi^0$ mass, a second MC was performed, with a slightly modified event generation routine for exclusive events: the $\omega\pi^0$ mass distribution was chosen to be flat (Figure 6.18, top-left) from threshold (0.95 GeV/c^2) up to 3.9 GeV/c^2, leaving all other features unchanged. After the full event reconstruction chain, the distorsion of the $\omega\pi^0$ mass spectrum due to acceptance results in the same Figure (top-right). Data points have been fitted using a sixth-degree polynomial, the acceptance correction factors calculated on a bin-by-bin basis as the ratio of the value of the fit function in the bin center over the maximum value assumed by the fit function in the range 1 GeV/c^2 $< m(\omega\pi^0) <$ 2.8 GeV/c^2.

The general behaviour is a constant decrease in acceptance with increasing $\omega\pi^0$-mass, which reaches $\approx$54% at 2 GeV/c^2; a very quick decrease near threshold is expected: this behaviour could explain what observed in the same mass region in the real data. A comparison of $\omega\pi^0$ mass spectra and mass dependent acceptance can be seen in Figure 4.9, Chapter 4 (cf. [BD08])

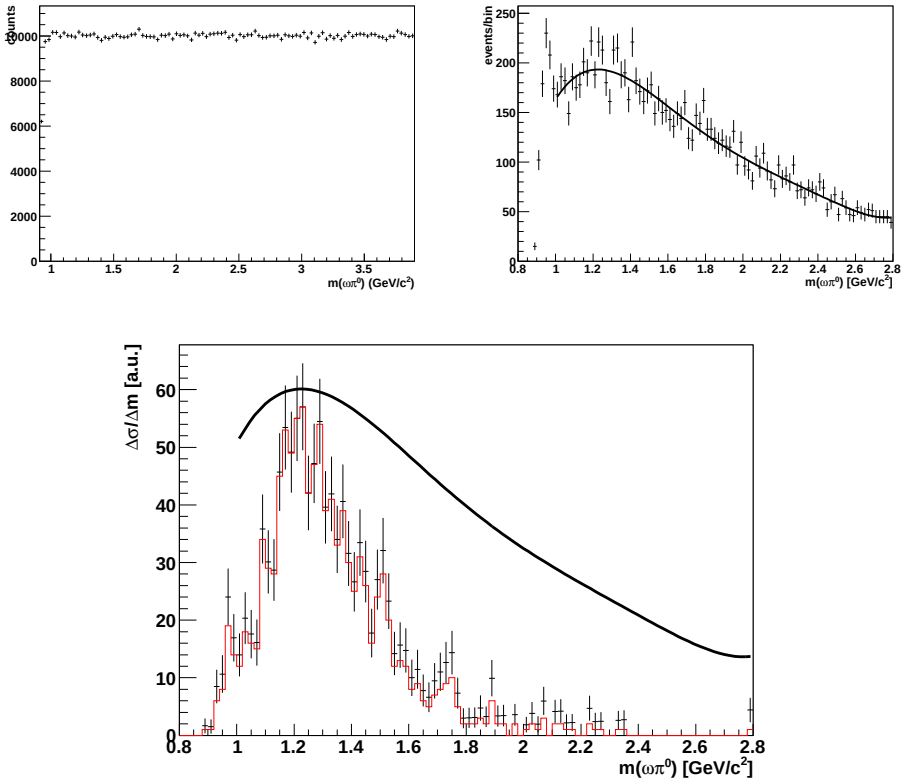

Figure 6.18: *Generated flat distribution for exclusive $\omega\pi^0$ invariant mass spectrum (top-left): the effect of detector geometry, detection and recontruction efficiencies contribution to the $\omega\pi^0$ mass dependent overall acceptance is shown in the same mass range (top-right).Bottom: the $\omega\pi^0$ mass spectrum before (in red) and after acceptance correction (in black); the acceptance dependence on the mass is also shown (continuous line).*

for already published preliminary results concerning 2004 data only, and in the histogram in Figure 6.18, where the $\omega\pi^0$ mass spectrum after acceptance correction (in black) is shown superimposed to the uncorrected spectrum (in red): very small deviation are seen, the larger correction corresponding to mass values well above the interesting region for ρ and b_1 production.

In addition, if we compare the recontructed $\omega\pi^0$ mass for the generated gaussian and flat distribution, we see that in the first case the region covered by reconstructed MC data reaches only values around 1.6 GeV/c^2; in the same interval, the acceptance variation evinced from the MC simulation for a flat mass distribution is of the order of $\approx 20\%$.

These results show that the structure seen in real data at $\sim$1.25 GeV/c^2 is not an artefact due to acceptance, but a real signal.

6.4 Angular distributions: MC results

The peformed MC study enables the determination of the bias introduced by the spectrometer acceptance on the various angular distributions considered so far; this is a most important aspect in view of a J^P determination of the $\omega\pi^0$ system.

Figures 6.19 and 6.20 show the MC reconstructed angular distributions,as defined in the previous Chapter.

The distributions relative to $\cos\theta$ and $\cos\theta_H$ must be compared with the corresponding ones in Figure 6.11. The angle θ shows a strong deviation from the isotropic behaviour due to acceptance.

For the angle θ_A the effect is not so pronounced: the acceptance decreases by 10% from $\theta = 0°(180°)$ to $\theta = 90°$.

For the scattering and production plane azimuthal orientation Φ, isotropy is maintained by the reconstruction, as can be see by comparison with Figure 6.9.

This happens to be the case also for the angle ψ_V, whose distribution after reconstruction is shown in Figure 6.20. This fact assures that the sinusoidal modulation observed in real data is not an artefact due to acceptance, but a characteristic of the observed $\omega\pi^0$ signal. As explained in the previous chapter, the $\omega\pi^0$ production and subsequent decay chain were generated isotropic.

The Φ distribution has been fitted using the function [B$^+$88]

$$I(\Phi) = a + b\cos 2\Phi + c\sin 2\Phi, \tag{6.20}$$

which is the expected distribution in case of photoproduction. Parity conservation implies $c = 0$, whereas SCHC leads to $b = 0$; if both conditions are valid, a constant distribution results. Fitting the MC distribution, we obtain for the fit parameters the values

$$\begin{aligned} a =& 1220 \pm 7, \\ b =& -2.88 \pm 9.86, \\ c =& 7.046 \pm 9.902. \end{aligned} \tag{6.21}$$

The last two are consistent with zero. We can thus assume that for Φ, isotropy is maintained and no acceptance corrections are needed.

On the contrary, the polar angle θ shows a strong influence of acceptance. The events with $\cos\theta \approx 1$ are not efficiently reconstructed or even completely lost; these events corresponds to decays with the ω emitted in the forward direction, i.e. almost parallel to $\omega\pi^0$ momentum; this implies that the π^0 moves along the backward direction. Taking into account the effect of the boost to laboratory system, this gives in general low energy pions, for which the opening angle between the two decay photons is larger than for high energetic π^0's; the probability that at least one of them escape

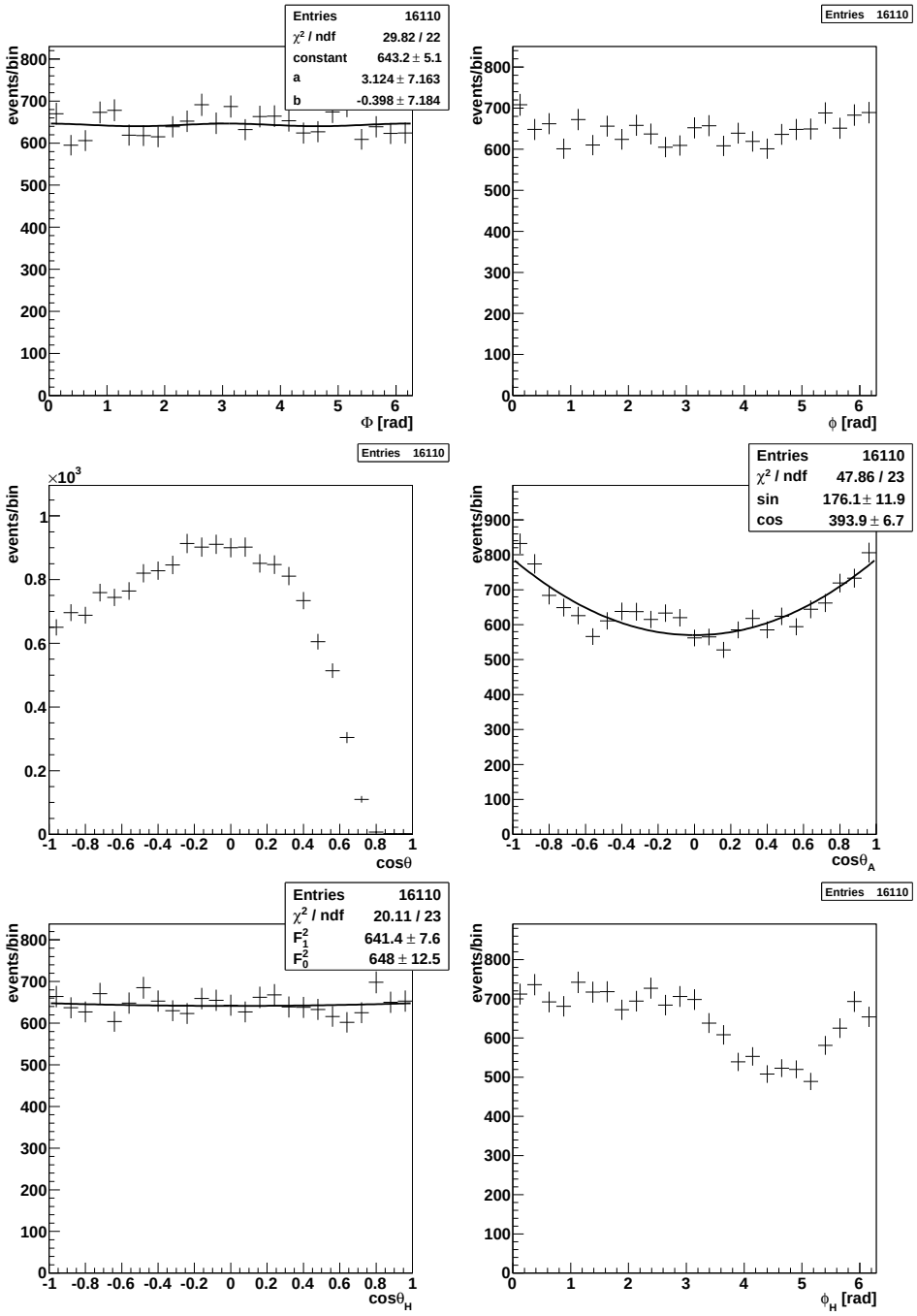

Figure 6.19: *Final sample angular distributions, MC data. For fits, see text.*

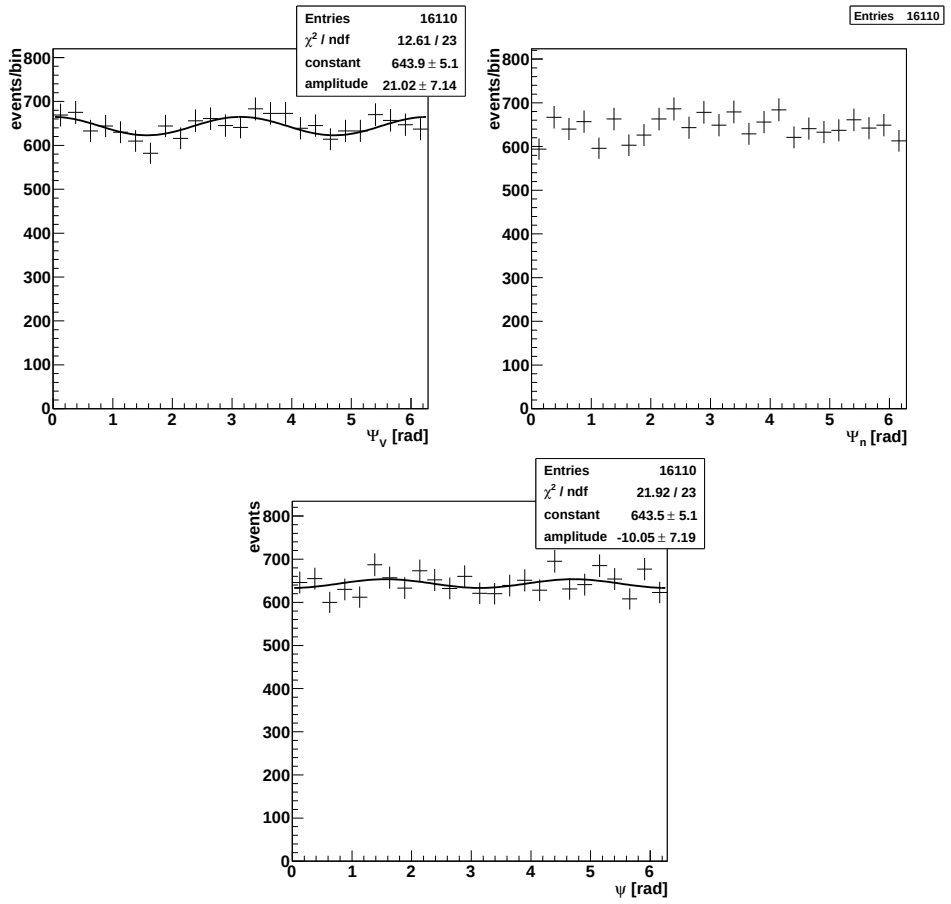

Figure 6.20: *(Continuation) Final sample angular distributions, MC data. For fits, see text.*

detection in the active area of ECAL2 is thus high, and the corresponding event sample reduced. On the other side, $\cos\theta \approx -1$ corresponds to pions which move in the forward direction with respect to the $\omega\pi^0$ direction, which implies high energies once the boost to laboratory frame has been performed. This enhances the probability that *at least one* of the four decay photons escapes detection propagating through the ECAL2 hole near the center. This effect has been studied already at event generator level by extrapolating photon tracks to the nominal z position along the beam axis of the active ECAL2 surface (Figure 6.21). The deviation from the generated isotropic θ distribution is caused by the two effects.

Also the angle θ_A used in ref. [A$^+$80] shows a deviation from isotropy corresponding to a minimum in the region $\cos\theta_A \sim 0$. This is also observed in the real data, which makes correcting for acceptance in this case unavoidable.

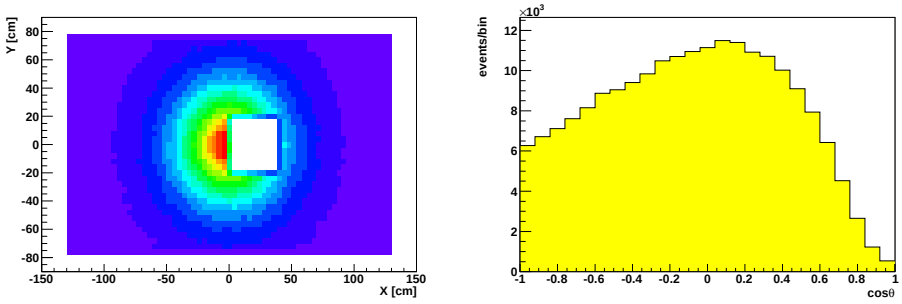

Figure 6.21: *Photon position (left; 4 entries per generated event) and geometrical acceptance for* $\cos\theta$ *(right) at the MC generator level. Deviations from isotropy are caused by the loss of* at least *one photon outside the outer boarder of the calorimeter (*$\cos\theta \sim 1$*) or in the central hole* $(\cos\theta \sim -1)$.

Last but not least, the $\cos\theta_H$ distribution has been fitted using the function

$$f(x) = a(1-x^2) + bx^2 \qquad (x = \cos\theta_H), \tag{6.22}$$

to reproduce the expected distribution (see ref. [B$^+$88])

$$\frac{dN}{d\cos\theta_H} = \frac{3N}{2}[|F_1|^2 \sin^2\theta_H + |F_0|^2 \cos^2\theta_H] \tag{6.23}$$

where F_λ is the decay amplitude of an ω of helicity $\lambda = 0, \pm 1$ and N the number of reconstructed events. The meaning of these equations will be discussed in the next Chapter.

Isotropy corresponds to $|F_0|^2 = |F_1|^2$; this is equivalent to $a = b$.

The determined fit parameters

$$\begin{aligned} a =& 1225 \pm 10.5, \\ b =& 1212 \pm 17.2, \end{aligned} \tag{6.24}$$

show that also in the case of θ_H, isotropy is maintained, and acceptance corrections are not needed.

For the angle ψ_V a fit with the function

$$f(\psi_V) = a + b\cos 2\psi_V \tag{6.25}$$

gives:

$$a = 1221 \pm 7.0, \tag{6.26}$$

$$b = 30.28 \pm 9.87. \tag{6.27}$$

These values correspond to a deviation from isotropy at about the 2.5% level. Again, we may avoid to introduce acceptance corrections, at least as a first good approximation, eventually correcting *a posteriori* the numerical values obtained for this angular distribution.

6.5 Acceptance corrected data

Figure 6.22 shows the considered angular distributions after acceptance corrections, if needed. For θ_A the correction was obtained by fitting the MC data with the function

$$f(x) = a(1-x) + b(1+x), \qquad (x = \cos\theta_A), \tag{6.28}$$

and correcting real data bin-by-bin by a factor $f_i = f(0)/f(x_i)$, where x_i is the center of the i-th bin. The fitting function was chosen this way, to take into account the possible sinus and cosinus contributions to the signal.

The fit parameters a and b, which take into account the contribution from a sinus and cosinus dependence typical of a 1^+ and 1^- signal respectively (Table 5.3), have the values:

$$\begin{aligned} a &= 4.60 \pm 3.55 \\ b &= 41.33 \pm 2.08 \end{aligned} \tag{6.29}$$

This points to a small contribution of 1^+ relative to 1^- (the ratio is 0.111 ± 0.091) if SCHC holds, consistent with the results of ref. [A$^+$80].

In Figure 6.22 the $\cos\theta_H$ distribution is also shown. This angle is particularly interesting, because the corresponding distribution depends [B$^+$88] *only* on the decay of the $\omega\pi^0$ and *not* on the production mechanism, thus being sensitive to J^P of the decaying system in a model independent way.

Concerning the angle θ, a particular treatment is required, and the discussion is postponed until the next Chapter (subsection 7.4.3).

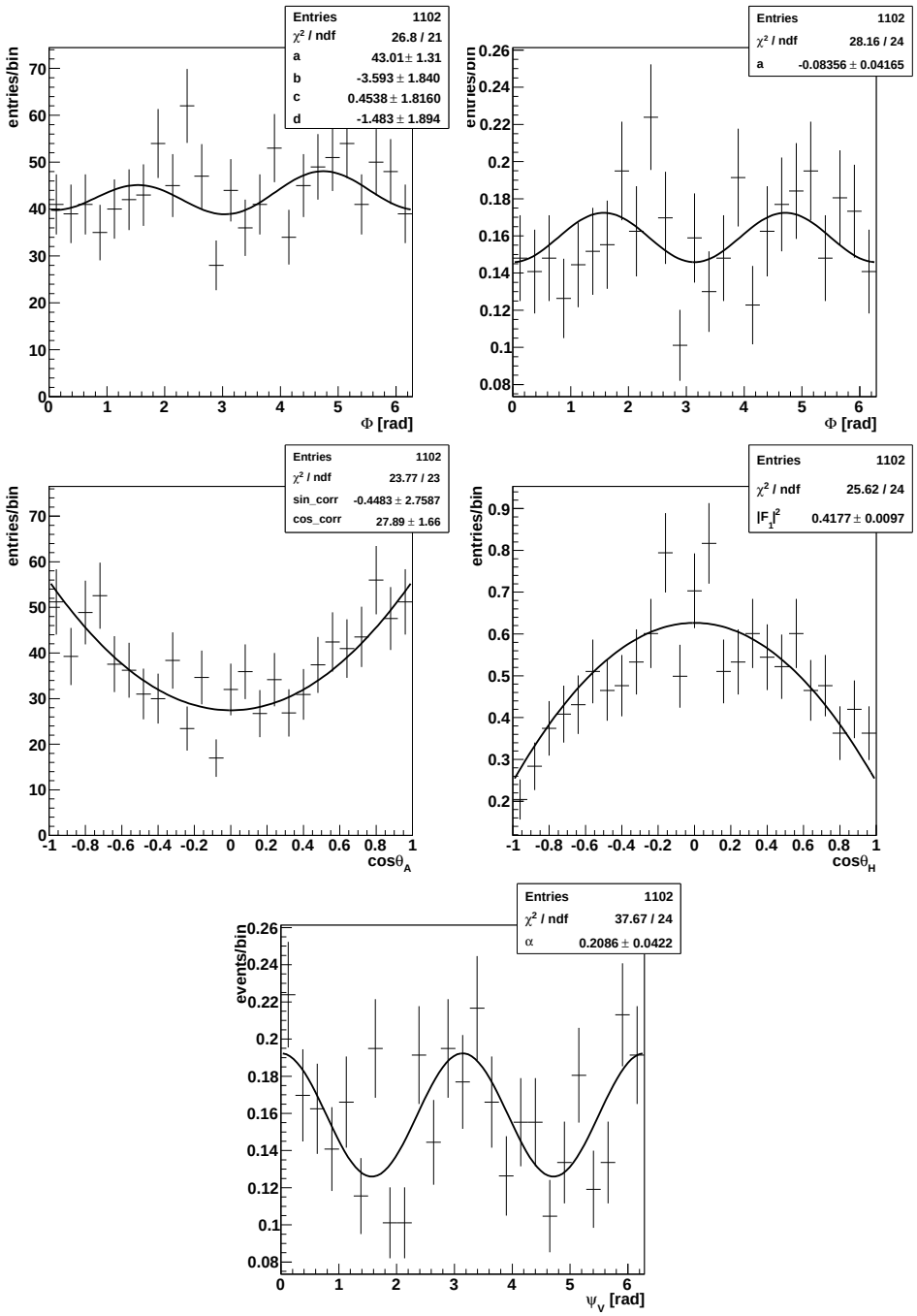

Figure 6.22: *Angular distributions (acceptance corrected in case of θ_A) and fits (see text). For angle θ, see subsection 7.4.3.*

Chapter 7

Angular correlations and the spin-parity of the $\omega\pi^0$

In the present chapter we concentrate on the study of various angular distributions in the exclusive leptoproduction of $\omega\pi^0$ and subsequent decays. The purpose is a quantitative determination of the different possible spin-parity contributions J^P for the observed structure.

Following various suggestions from different authors, we inspect these angular distributions after acceptance corrections obtained from the MC results shown in the previous chapter.

In this chapter we proceed along two ways: we first examine a particular set of *moments* and some related expressions which are strictly dependent on the spin-parity of the $\omega\pi^0$ system; secondly, an appropriate fit for the extraction of the ω decay amplitude squared $|F_1|^2$ is performed, which in turn allows the determination of the 1^- spin-parity contribution to the $\omega\pi^0$ final sample.

The two methods serve the same purpose, and should furnish compatible results.

7.1 (Partial) Partial Wave Analysis (PWA): the $H(lmLM)$ moments

As done in [C$^+$75], we describe the subsequent decays $\omega\pi^0 \to \omega + \pi^0 \to (\pi^+\pi^-\pi^0) + \pi^0$ by the joint angular distribution $I(\Omega, \Omega_H)$, with $\Omega = (\theta, \phi)$ and $\Omega_H = (\theta_H, \phi_H)$ (for a definition of these angles, see Section 5.4, pag. 65). The first pair of angles gives the decay angular distribution of the $\omega\pi^0$ in its helicity frame, the latter does the same but for the orientation in space of the ω decay plane in the ω helicity frame by means of the vector $\boldsymbol{n}$ perpendicular to the plane (see definition by eq. (5.5), pag. 65).

For a quantitative study of the J^P contributions to the $\omega\pi^0$ final sample, we can expand the joint angular distribution $I(\Omega, \Omega_H)$ in a series of Wigner

D-function[1] products:

$$I(\Omega,\Omega_H)=\sum_{lmLM}\left(\frac{2l+1}{4\pi}\right)\left(\frac{2L+1}{4\pi}\right)H(lmLM)D^{L*}_{Mm}(\phi,\theta)D^{l*}_{m0}(\phi_H,\theta_H), \tag{7.1}$$

where the sum extends over all the possible combinations of the integers $lmLM$ and the coefficients (the moments) $H(lmLM)$ in the series are in general complex numbers[2]. These moments are thus the mean values

$$H(lmLM)=\langle D^{L}_{Mm}(\phi,\theta)D^{l}_{m0}(\phi_H,\theta_H)\rangle. \tag{7.2}$$

relative to the distribution $I(\Omega,\Omega_H)$. Each moment can be written as a product of three terms,

$$H(lmLM)=t^*_{LM}f_{Llm}\langle 10l0|10\rangle, \tag{7.3}$$

where the first factor, the *generalized multipole parameter*, depends *only* on the production of the $\omega\pi^0$ system, the second term describes the decay $\omega\pi^0\to\omega+\pi^0$, and the third factor is a Clebsh-Gordan coefficient related to the decay of the ω (spin $J=1$). More precisely we can write:

$$t^*_{LM}=\left(\frac{2J'+1}{2J+1}\right)^{1/2}\sum_{\Lambda\Lambda'}\rho_{\Lambda\Lambda'}\langle J'\Lambda' LM|J\Lambda\rangle, \tag{7.4}$$

$$f_{Llm}=\sum_{\lambda\lambda'}F_\lambda F^*_{\lambda'}\langle J'\lambda' LM|J\lambda\rangle\langle 1\lambda' lm|1\lambda\rangle. \tag{7.5}$$

For details on the formalism, see [C$^+$75] and [Chu]. In all the previous formulae, the parameter $lmLM$ are related to the spin or orbital angular momentum state and corresponding projection along the chosen quantization axis for the production (L and M) of the $\omega\pi^0$ system with possible interference between spin states J and J', and subsequent $\omega\pi^0\to\omega+\pi^0$ decay (l and m), respectively.[3]

Already the first investigations of $\omega\pi^0$ production by means of polarized and unpolarized photon or hadron beams, clearly showed that spin contributions $0^-, 1^+$ and 1^- were sufficient to explain the data, and no higher spin contribution was needed. In addition, a 0^- contribution to the signal (which would correspond to a non-$q\bar{q}$ state, since C-parity is also negative) was found to be small, expecially in the peak region, and always compatible with zero. Following these lines, we thus assume the $\omega\pi^0$ signal to be

[1] for a definition, see Appendix B.

[2] because the D's in general are complex.

[3] Rigorously, one has to take into account also the contribute of the parity $P(P')$ associated to the spin state $J(J')$, thus having, for interference terms, the spin density matrices $\rho^{J^P J'^{P'}}_{\Lambda\Lambda'}$ and the two helicity amplitudes $F^{J^P}_{\lambda}$ and $F^{J'^{P'}}_{\lambda'}$, generalizing those of eqs. (7.4) and (7.5).

compatible with the presence of only two components 1^+ and 1^-. It can be thus shown [A$^+$84] that a set of 25 different moments is needed and is sufficient to describe the data, and one can limit the partial wave analysis fit to values $(lmLM) \leq 2$.

The physical content is extracted from the data if the so called *symmetrized* moments are considered, as defined in [A$^+$84]:

$$H^{\pm}(\alpha) = \frac{1}{2}\Re\mathrm{e}\langle D^L_{Mm}(\phi,\theta)D^l_{m0}(\phi_H,\theta_H) \pm (-1)^{L-M} D^L_{M-m}(\phi,\theta)D^l_{m0}(\phi_H,\theta_H)\rangle \tag{7.6}$$

with $\alpha = \{lmLM\}$. These moments can be normalized to have $H(0000) = 1$, in order to have

$$\int I(\Omega,\Omega_H)d\Omega d\Omega_H = 1. \tag{7.7}$$

for the joint angular distribution. The reason to consider symmetrized moments comes from the need to avoid the complications that arise from the presence of interferences between different spin-parity states in the production of the $\omega\pi^0$ system.

In practice, to disentangle the possible different spin-parity contributions, one has to consider the sums (the moments)

$$H_s(lmLM) = \sum_i^N D^L_{Mm}(\phi_i,\theta_i)D^l_{m0}(\phi_{Hi},\theta_{Hi}) \tag{7.8}$$

over the N reconstructed $\omega\pi^0$ events in the final sample (or in a given $\omega\pi^0$ mass bin subsample); for the i-th event, the measured decay angles (ϕ_i,θ_i) and (ϕ_{Hi},θ_{Hi}) are used. The corresponding symmetrized sums (moments) are thus:

$$H^{\pm}_s(\alpha) = \frac{1}{2}\Re\mathrm{e}\sum_i^N \Big(D^L_{Mm}(\Omega_i)D^l_{m0}(\Omega_{Hi}) \pm (-1)^{L-M} D^L_{M-m}(\Omega_i)D^l_{m0}(\Omega_{Hi}) \Big). \tag{7.9}$$

The considered moments are thus once again proportional to the mean value of the product of the two D-functions (analogous of eq. (7.2))

$$H_s(lmLM) = N\langle D^L_{Mm}(\Omega)D^l_{m0}(\Omega_H)\rangle, \tag{7.10}$$

or, for the symmetrized case,

$$H^{\pm}_s(lmLM) = N\frac{1}{2}\Re\mathrm{e}\langle D^L_{Mm}(\Omega)D^l_{m0}(\Omega_H) \pm (-1)^{L-M} D^L_{M-m}(\Omega)D^l_{m0}(\Omega_H)\rangle \tag{7.11}$$

the constant of proportionality being the number of events N.

From eq. (7.8), it follows:

$$H_s(0000) = H^+_s(0000) = N. \tag{7.12}$$

In view of a J^P determination, it is particularly useful to consider the following linear combinations of moments [C$^+$75]:

$$H_s(0000) + 5H_s(2000) = N\langle 3/2(5\cos^2\theta_H - 1)\rangle = 3N|F_0|^2 \tag{7.13}$$

$$H_s(0000) - 5/2H_s(2000) = N\langle 3/4(3 - 5\cos^2\theta_H)\rangle = 3N|F_1|^2 \tag{7.14}$$

$$\begin{aligned}\Delta_{J^P}(LM) = &\left[\frac{2L(L+1)}{3(L-1)(L+2)}\right]^{1/2}\cdot \\ &\cdot [H_s(00LM) - 5/2H_s(20LM)] + \\ &- P(-1)^{J-1}\left[1 - \frac{L(L+1)}{2J(J+1)}\right]5H_s(22LM).\end{aligned} \tag{7.15}$$

Again, N is the number of $\omega\pi^0$ events in a given mass bin, where the previous moments are calculated; J and P are the total spin and parity of the resonance.

The first two linear combinations are directly related to the ω decay amplitude F_λ in the helicity state $\lambda = 0, \pm 1$, respectively.

The linear combination of eq. (7.15) will be considered for the two cases[4] (corresponding to $L = 2$, $M = 0$) $\Delta_{1^+}(20)$ and $\Delta_{1^-}(20)$ only[5].

The explicit expressions for the two Δ's are:

$$\Delta_{1^+}(20) = H_s(0020) - \frac{5}{2}H_s(2020) + \frac{5}{2}H_s(2220), \tag{7.16}$$

$$\Delta_{1^-}(20) = H_s(0020) - \frac{5}{2}H_s(2020) - \frac{5}{2}H_s(2220), \tag{7.17}$$

the only difference being in the sign of the last term. The explicit form of the D-functions products for the moments $H_s(0020)$, $H_s(2020)$ and $H_s(2220)$ is shown in Table 7.1.

In addition, simple calculations [C$^+$75] from eq. (7.15) show that the following equalities hold:

$$\begin{aligned}\Delta_{1^+}(20) &= \Delta_{2^+}(20), \\ \Delta_{1^-}(20) &= \Delta_{2^-}(20).\end{aligned} \tag{7.18}$$

We are therefore not able to distinguish between the cases 1^+ and 2^+ or between 1^- and 2^- (this is in general true also for the corresponding Δ's with $M \neq 0$. Cf. [C$^+$75]); nevertheless, neglecting spin values higher than 1 as possible contributions to the $\omega\pi^0$ production and decay, an assumption in

[4]For a pure spin J resonance, L may run from 0 to $2J$ only, as can be evinced from the Clebsh-Gordan coefficient in eq. (7.4): infact the helicity $\Lambda(\Lambda')$ can vary between $-J$ and J, assuming $2J + 1$ possible value; for the extreme case $\Lambda = J$ and $\Lambda' = -J$ (or vice versa) from the Clebsh-Gordan constraint $\Lambda' + M = \Lambda$ follows that M can assume values between 0 and $2J$, the same thus also valid for L. In addition, parity conservation during *decay* allows *even* L values only. Thus $L = 0, 2$ for $J = 1$ (cf. [C$^+$75]).

[5]The formula (7.15) has no meaning for $J = 0$.

Moment	$D^L_{Mm}(\Omega)D^l_{m0}(\Omega_H)$
$H_s(0000)$	1
$H_s(0020)$	$\frac{1}{2}(3\cos^2\theta - 1)$
$H_s(2020)$	$\frac{1}{4}(3\cos^2\theta - 1)(3\cos^2\theta_H - 1)$
$H_s(2220)$	$\frac{3}{8}\sin^2\theta\sin^2\theta_H\cos 2\phi_H$
$H_s(2000)$	$\frac{1}{2}(3\cos^2\theta_H - 1)$

Table 7.1: *D-function products for some moments $H_s(lmLM)$ used in the analysis.*

line with results of past experiments, we are still in the position to distinguish between states of opposite parity 1^+ and 1^-.

The interest in the two quantities $\Delta_{1^+}(20)$ and $\Delta_{1^-}(20)$, and, more generally, in each $\Delta_{J^P}(LM)$, is due to the fact that, if the resonance is in a pure state J^P, then $\Delta_{J^P}(LM)$ *is identically zero* [C$^+$75]. The absence of a 1^- contribution should reveal itself through experimental results compatible with $\Delta_{1^+}(20) = 0$.

Figure 7.1 shows the results concerning the moments encountered so far for final sample events in the mass window 0.9 GeV/c^2 $< m(\omega\pi^0) <$ 1.8 GeV/c^2, subdivided in nine equally broad mass bins, each 100 MeV/c^2 wide. Errors have been calculated using the formula [C$^+$75]:

$$\delta H_s(lmLM)^2 = \sum_i \left(D^L_{Mm}(\phi_i, \theta_i) D^l_{m0}(\phi_{Hi}, \theta_{Hi}) \right)^2, \tag{7.19}$$

which is a particular case of the more general formula for moment correlations

$$\delta H_s(lmLM)\delta H_s(l'm'L'M') = \sum_i D^L_{Mm}(\Omega_i) D^l_{m0}(\Omega_{Hi}) D^{L'}_{M'm'}(\Omega_i) D^{l'}_{m'0}(\Omega_{Hi}), \tag{7.20}$$

once we put $\{lmLM\} = \{l'm'L'M'\}$.

Acceptance corrections have also been applied. Infact, from definition in eq. (7.8), the moments shown are calculated as a sum of different terms, each dependent from the single $\omega\pi^0$ event and characterized by a set of four different values of the angular distribution $\cos\theta$, ϕ, $\cos\theta_H$ and ϕ_H; these distributions are of course affected by acceptance (see Figure 6.19, pag. 94).

The event-dependent corrections have been introduced this way: for each event, the corresponding contribution to the moment has been calculated and weighted in the sum (7.8) by a factor

$$\alpha_i = \frac{1}{A_i(\cos\theta_i, \phi_{Hi})}, \tag{7.21}$$

where A_i is the acceptance associated to the i-th event and obtained from the generated and recontructed MC event distributions in the 2-dimensional

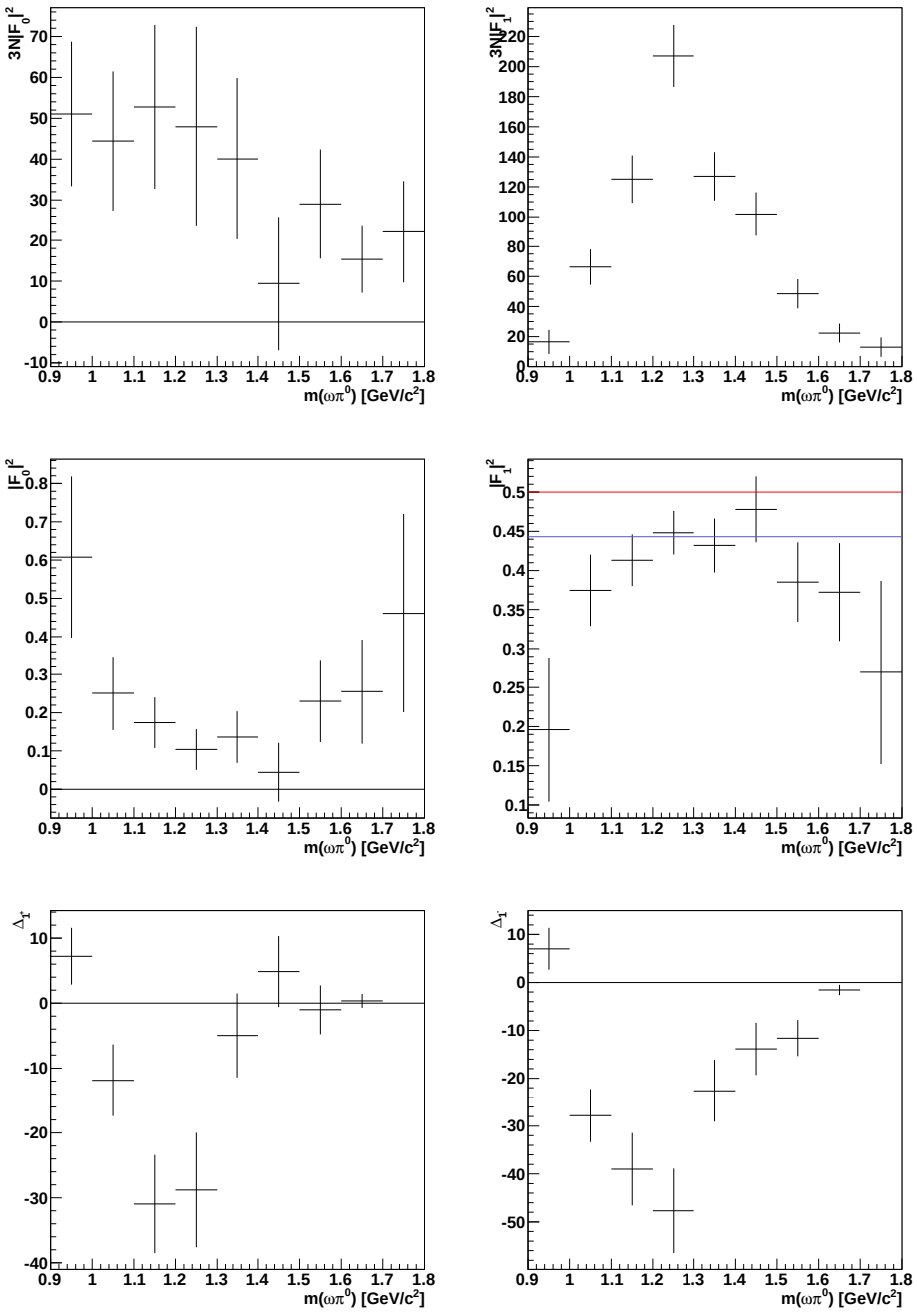

Figure 7.1: $3N|F_0|^2$, $3N|F_1|^2$, $|F_0|^2$, $|F_1|^2$, $\Delta_{1^+}(20)$ *and* $\Delta_{1^-}(20)$ *for events in the final sample with* $\cos\theta < 0$. *Corrected for acceptance. Red line: pure* 1^- *signal. Blue line: pure* $b_1(1235)$.

$(\cos\theta, \phi_H)$ space, subdivided in 24 × 24 bins:

$$A_i = \frac{N^i_{MC}}{N^i_{gen}}. \tag{7.22}$$

Here N^i_{MC} is the number of reconstructed MC data in the $(\cos\theta, \phi_H)$ bin corresponding to the i-th event, whereas N^i_{gen} is the same quantity at the generator level. The other two angular coordinates ϕ and $\cos\theta_H$, which also enter in the description of the $\omega\pi^0$ decay, have not been used for the correction, being themselves not affected by distorsion due to acceptance, as can also be seen in Figure 6.19. After the introduction of the coefficients α_i, the resulting sum was normalized respect to the mean value of the inverses of the acceptances A_i, to give the final acceptance corrected moment:

$$H^{corr}_s(lmLM) = \frac{\sum_i^N \alpha_i H^i_s(\Omega_i, \Omega_{Hi})}{\sum_i^N \alpha_i}. \tag{7.23}$$

Due to the strong distorsions observed in the $\cos\theta$ distribution, expecially in the region $\cos\theta \sim 1$, and the resulting big uncertainties thus implicit in the acceptance correction procedure, we have taken advantage of the symmetry $\theta \to -\theta$ in this angular distribution, which in turn follows from the presence of *only even* powers of $\cos\theta$ in the D-function products for the moments used (see Table 7.1), and limited ourselves only to the event sample corresponding to the range $\cos\theta < 0$, less suffering from acceptance induced distorsions. The results shown in Figures 7.1 to 7.4 (they refer to different p_t^2 ranges) are all related to this subsample. The p_t^2-ranges were defined as:

- $p_t^2 < 0.15$ (GeV/c)^2 (coherent scattering);
- 0.15 (GeV/c)^2 $< p_t^2 <$ 0.5 (GeV/c)^2 (incoherent scattering);
- 0.15 (GeV/c)^2 $< p_t^2 <$ 1 (GeV/c)^2 ("*extended*" incoherent scattering).

The values assumed by the linear combination of moments eq. (7.14), which is proportional to $|F_1|^2$, confirm the absence of a dominant 0^- contribution to the data, because this would imply $|F_1|^2 = 0$ (see ref. [C$^+$75]). This feature is also present in every p_t^2-subrange examined.

In addition, for the case of $|F_1|^2$ only, the effect of background due to non-ω-related events intruding the exclusive sample was taken into account and the appropriate correction performed. For the different p_t^2-windows, results are shown in Figure 7.5. The entity of background was determined inspecting the λ distribution corresponding to each one of the mass bins, and assuming for the background an isotropic distribution implying $|F_1|^2_{bkg} = 0.333$. When data in a bin are missing, it means that the correction procedure has given values lying outside the plotted range, thus lacking of significance.

Turning our attention to Δ_{1^+} and Δ_{1^-}, we can see in Figure 7.1 that the observed values deviate significantly from zero in the region $m(\omega\pi^0) \approx 1250$

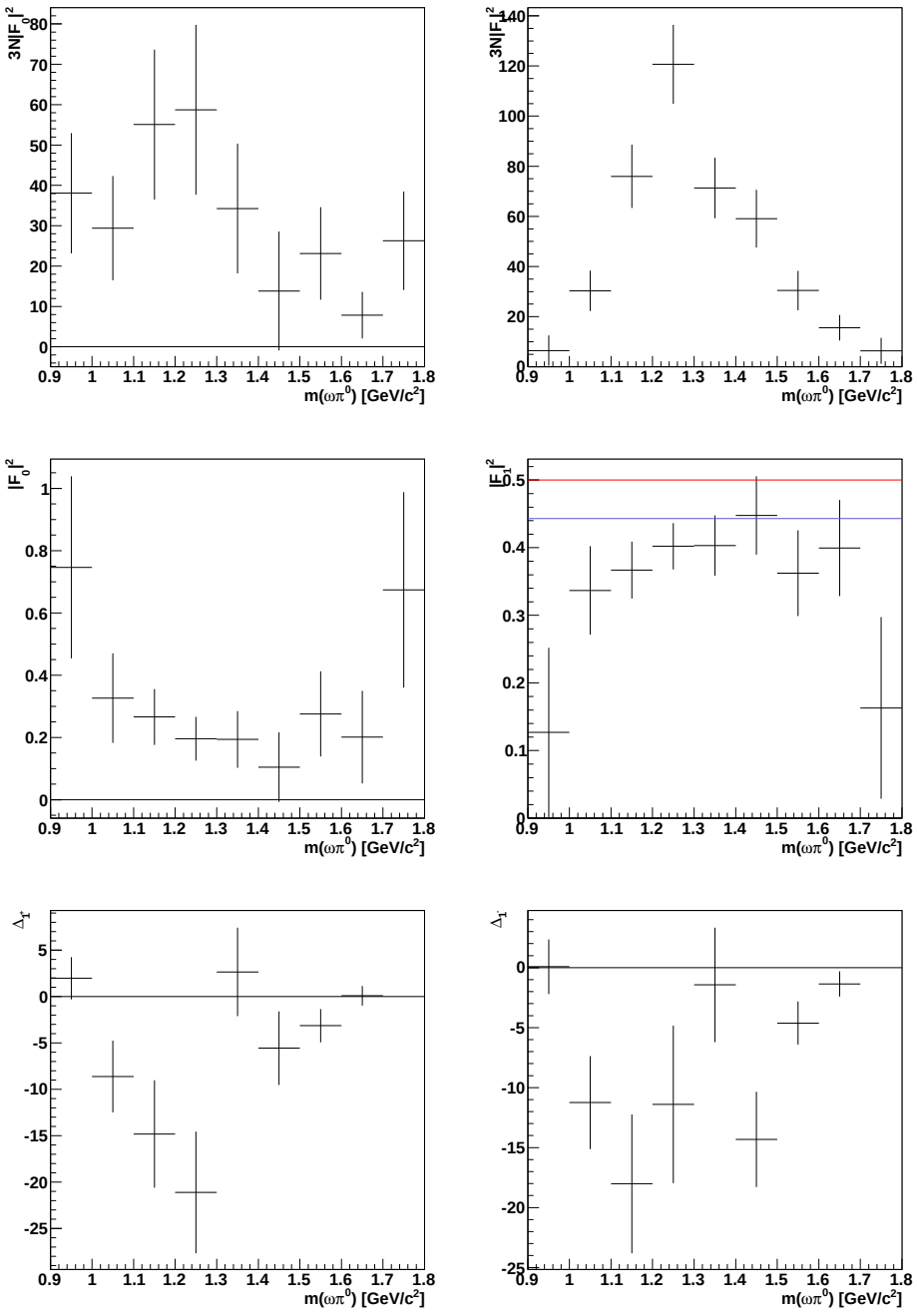

Figure 7.2: $3N|F_0|^2$, $3N|F_1|^2$, $|F_0|^2$, $|F_1|^2$, $\Delta_{1^+}(20)$ *and* $\Delta_{1^-}(20)$ *for final sample with* $p_t^2 < 0.15$ *(GeV/c)*^{2} *and* $\cos\theta < 0$. *Corrected for acceptance. Red line: pure* 1^- *signal. Blue line: pure* $b_1(1235)$.

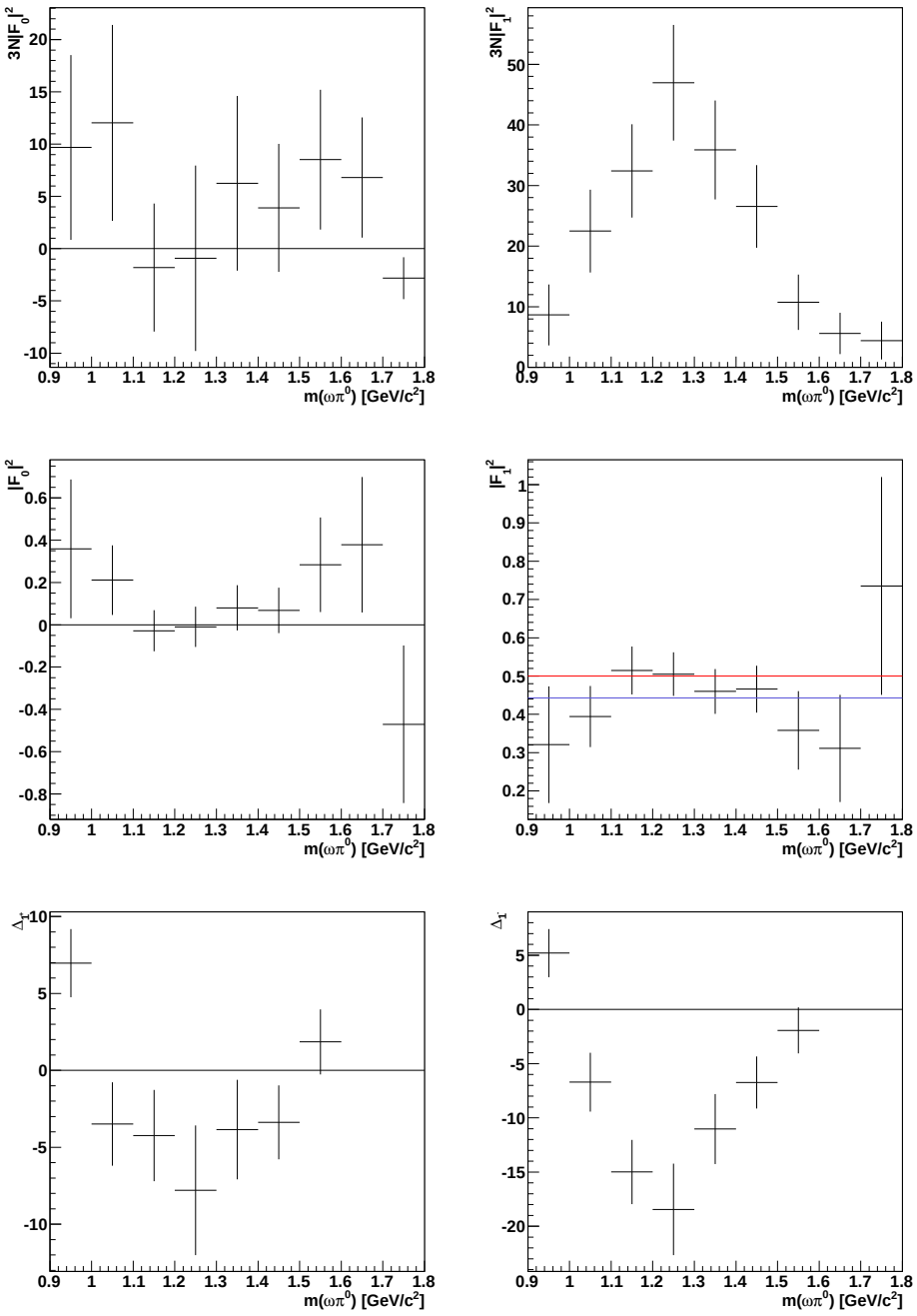

Figure 7.3: $3N|F_0|^2$, $3N|F_1|^2$, $|F_0|^2$, $|F_1|^2$, $\Delta_{1^+}(20)$ *and* $\Delta_{1^-}(20)$ *for final sample with* 0.15 *(GeV/c)*$^2 < p_t^2 < 0.5$ *(GeV/c)*^{2} *and* $\cos\theta < 0$. *Corrected for acceptance. Red line: pure* 1^- *signal. Blue line: pure* $b_1(1235)$.

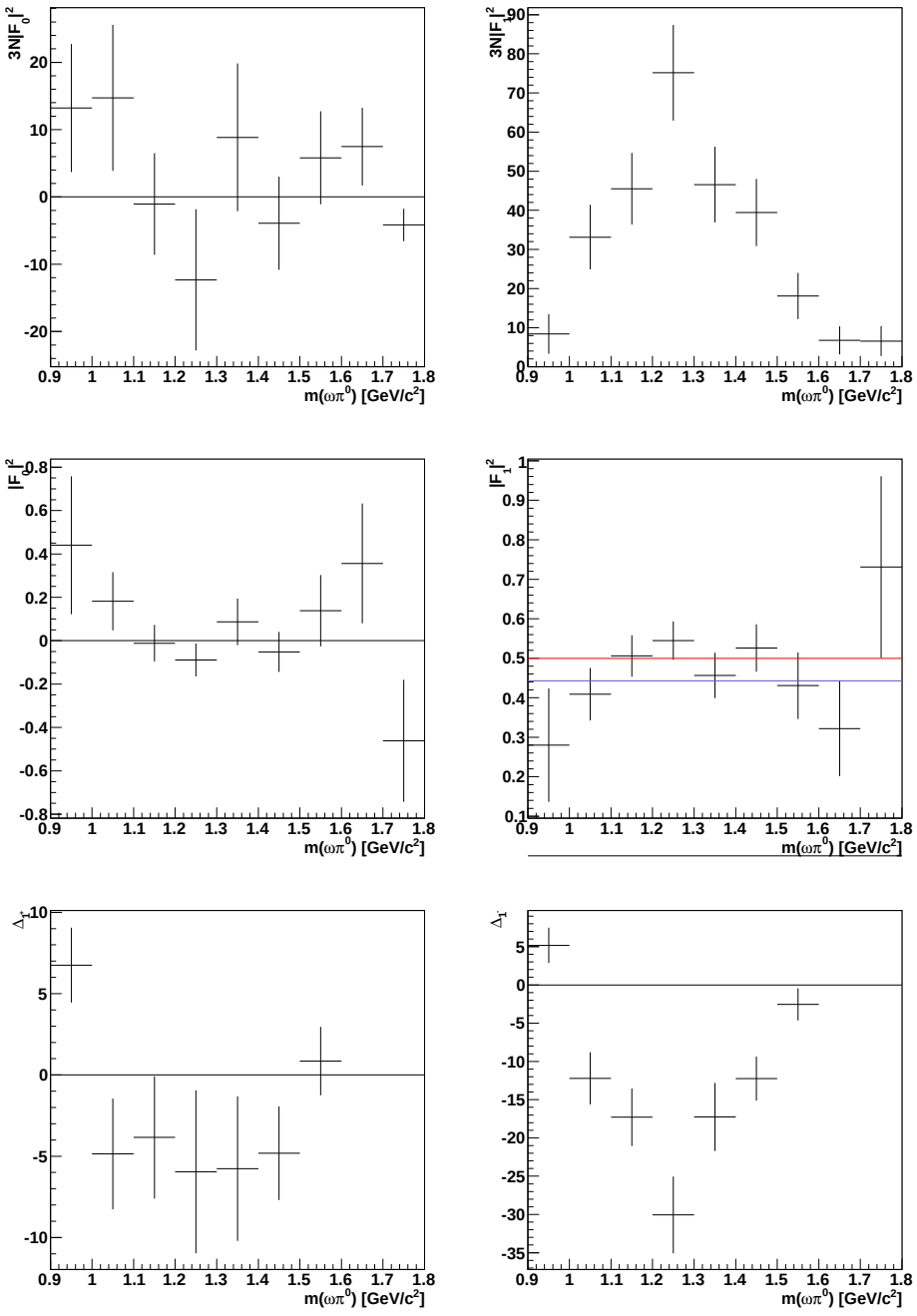

Figure 7.4: $3N|F_0|^2$, $3N|F_1|^2$, $|F_0|^2$, $|F_1|^2$, $\Delta_{1^+}(20)$ *and* $\Delta_{1^-}(20)$ *for final sample with* 0.15 *(GeV/c)*$^2 < p_t^2 < 1$ *(GeV/c)*^{2} *and* $\cos\theta < 0$. *Corrected for acceptance. Red line: pure* 1^- *signal. Blue line: pure* $b_1(1235)$.

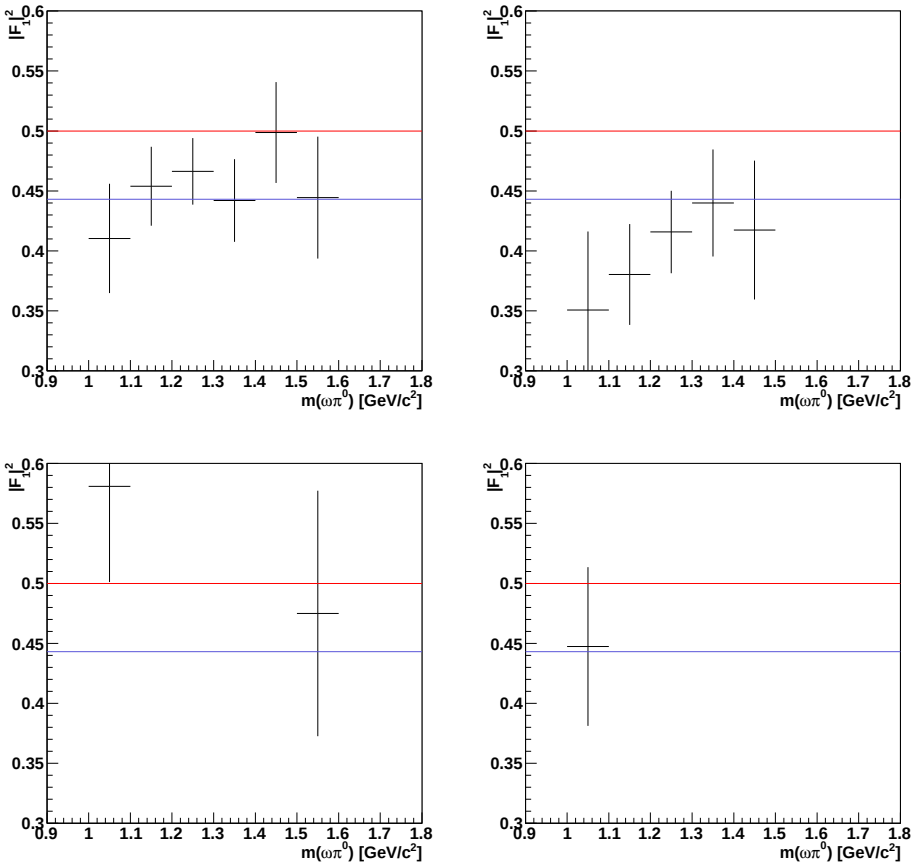

Figure 7.5: $|F_1|^2$ *for events in the final sample with* $\cos\theta < 0$. *Corrected for acceptance and background. From left to right, top to bottom: i) no* p_t^2 *cut, ii) coherent, iii) incoherent and iv) extended incoherent scattering.*

MeV/c^2. This is strongly in favour of the presence in our sample of *both* the 1^+ and 1^- states. This property is maintained in each one of the p_t^2 ranges considered so far to characterize the event samples corresponding to coherent scattering on nuclei or incoherent scattering off quasi-free nucleons (Figures 7.2 to 7.4).

The properties of the various linear combinations of moments are rather independent on the values of p_t^2, with a single exception for $|F_0|^2$. As can be seen in Figures 7.2, 7.3 and 7.4, $|F_0|^2$ assumes small values around zero in the peak region for incoherent scattering, i.e. high values of p_t^2; $|F_0|^2 = 0$ implies for J^P to belong to the so called *natural* spin-parity series $1^-, 2^+, 3^-, \ldots$, i.e.

$$P = (-1)^J \tag{7.24}$$

as a general rule. This characteristic is compatible with a possible growing contribution of the 1^--state for incoherent production off quasi-free nucleons (high p_t^2) as compared to the coherent production off nuclei (low p_t^2).

For comparison, Figure 7.6 shows the same set of moments as seen in the reaction $\pi^+ p \to \omega\pi^+ p$ (from ref. [C$^+$75]) at a center-of-mass mean energy $\langle W \rangle \approx 7.1$ GeV and $t < 1$ (GeV/c)^2. The most notable difference is in the behaviour of $\Delta_{1^+}(20)$ in their data, which is compatible with zero at least up to a mass $m(\omega) \approx 1.4$ GeV/c^2. This is in contrast with our data and strongly supported the 1^+ assignment to the $b_1(1235)$ in that case.

A possible explanation of the different results may be invoked, considering the different production mechanisms: at COMPASS, leptoproduction takes place via quasi-real photon exchange, and the (virtual) photon has the same $J^{PC} = 1^{--}$ quantum numbers of a vector meson: this may explain a possible enhancement of 1^- state with respect to hadron induced diffractive processes like in πp scattering, where the J^{PC} quantum numbers of the exchanged particle and the exchanged relative orbital angular momentum play a major role.

7.2 The spin matrix elements $\rho_{00}^{\pm}$

The two spin density matrix elements ρ_{00}^+ and ρ_{00}^-, which appear in the generalized multipole parameters t_{LM} and describe the production of an $\omega\pi^0$ system of parity $P = \pm 1$ in helicity state 0, respectively, have been also investigated. This is made possible by taking into account the relations between the moments listed in Table 7.2 and the other quantities that appear there (see ref. [A$^+$84]). The listed moments are function of the number of $\omega\pi^0$ events N^+ and N^- with parity $+1$ and -1, respectively, and the decay amplitude squared $|F_1|^2$ for an ω in the helicity state $\lambda = \pm 1$. Substituting these relations into equations (7.16) and (7.17), one obtains the two

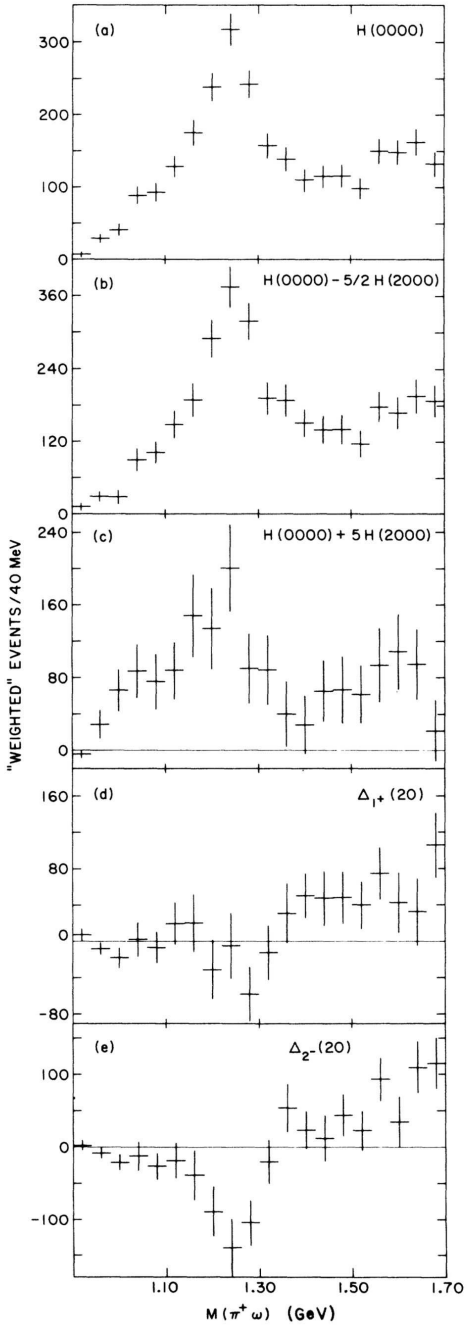

FIG. 5. Moments as functions of $M(\pi^+\omega)$ for $t'<1.0$ $(\mathrm{GeV}/c)^2$ with non-ω background subtraction and after compensating for Δ^{++} cut: (a) $H(0000)=M(\pi^+\omega)$ spectrum; (b) $H(0000)+5H(2000)=N\langle\frac{25}{3}(5\cos^2\beta-1)\rangle$; (c) $H(0000)-\frac{5}{2}H(2000)=N\langle\frac{3}{4}(3-5\cos^2\beta)\rangle$; (d) Δ_1+(20), Δ_2-(20).

Figure 7.6: *Moments for $\pi^+p\to\omega\pi^+p$ at $\langle W\rangle\approx 7.1$ GeV. From ref. [C+75].*

$NH_s^+(0020)$	$\frac{1}{5}N^+(3\rho_{00}^+ - 1)(1 - 3\|F_1\|^2) - \frac{1}{10}N^-(3\rho_{00}^- - 1)$
$NH_s^+(2020)$	$\frac{1}{25}N^+(3\rho_{00}^+ - 1)(2 - 3\|F_1\|^2) - \frac{1}{50}N^-(3\rho_{00}^- - 1)$
$NH_s^+(2220)$	$\frac{3}{25}N^+(3\rho_{00}^+ - 1)\|F_1\|^2 - \frac{3}{50}N^-(3\rho_{00}^- - 1)$

Table 7.2: *Dependence of some moments on the spin matrix elements $\rho_{00}^{\pm}$, the ω decay amplitude squared $|F_1|^2$ and the number of events $N^{\pm}$ in a state $J^{\pm}$, respectively.*

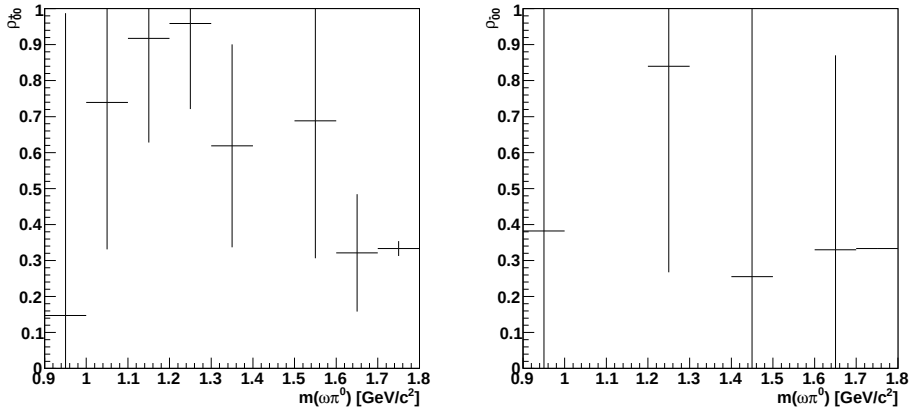

Figure 7.7: ρ_{00}^+ *(left) and* ρ_{00}^- *(right) for events in the final sample with* $\cos\theta < 0$. *Corrected for acceptance.*

important results[6]:

$$\Delta_{1^+}(20) = -\frac{3}{10}N^-(3\rho_{00}^- - 1), \tag{7.25}$$

$$\Delta_{1^-}(20) = -\frac{3}{5}N^+(3\rho_{00}^+ - 1)|F_1|^2, \tag{7.26}$$

which inverted respect to the ρ's give:

$$\rho_{00}^- = \frac{1}{3}\left(-\frac{10}{3}\cdot\frac{\Delta_{1^+}}{N^-} + 1\right), \tag{7.27}$$

$$\rho_{00}^+ = \frac{1}{3}\left(-\frac{5}{3}\cdot\frac{\Delta_{1^-}}{N^+|F_1|^2} + 1\right). \tag{7.28}$$

Moreover, the quantities $|F_1|^2$ and N^- are related[7]: to a pure 1^- sample ($N^- = N$ and $N^+ = 0$) corresponds a value $|F_1|^2 = 1/2$, whereas for pure b_1 ($N^+ = N$ and $N^- = 0$) we have $|F_1|^2 = 0.443 \pm 0.008$, as a consequence of the presence of the s- and d-waves components (see Table 7.3). For arbitrary

[6]Here we only sketch the line of reasoning, the detailed calculations are shown in Appendix C.

[7]And N^+, of course, as a consequence of the trivial assumption $N^+ + N^- = N$.

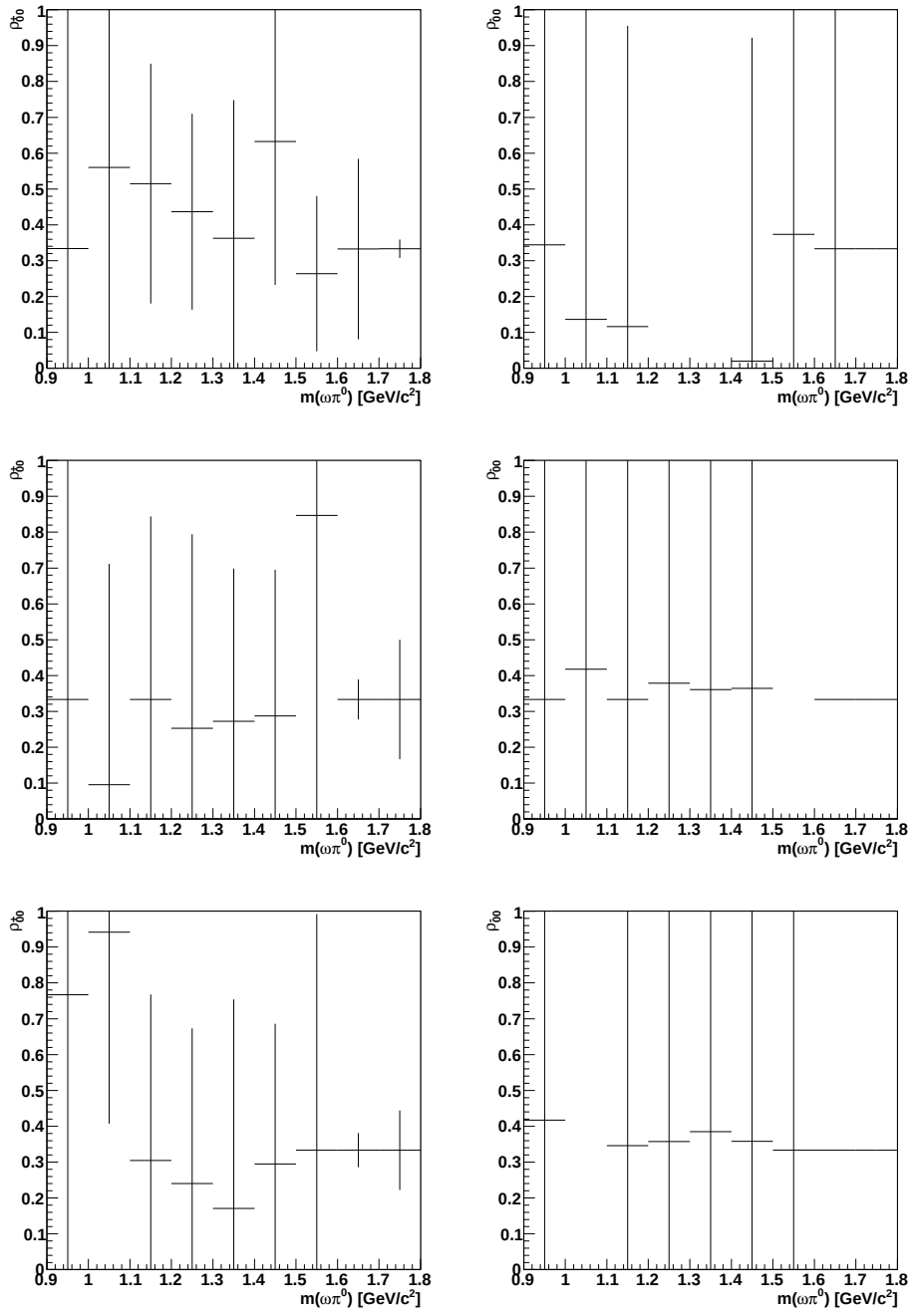

Figure 7.8: ρ_{00}^{+} *(left) and* ρ_{00}^{-} *(right) for events in the final sample with* $\cos\theta < 0$. *Corrected for acceptance. Top to bottom: i) coherent scattering, ii) incoherent scattering, iii) incoherent scattering with* $p_t^2 < 1$ *(GeV/*c*)*^{2}.

values of N^- (and N^+) between the two extremes 0 and N, we have the corresponding value between 0.5 and 0.443. If we assume that the measured value $|F_1|^2$ results from a contribution of both the 1^+ and 1^- states, we can thus write the desired relation:

$$|F_1|^2 = \frac{1}{2}x + (1-x)(0.443 \pm 0.008), \tag{7.29}$$

with $x = N^-/N$. With $B = 0.443 \pm 0.008$, and solving for x leads to:

$$x = \frac{|F_1|^2 - B}{1/2 - B}, \tag{7.30}$$

which, written in the previous equations for the ρ's, gives:

$$|F_1|^2 = B - \frac{10}{3} \cdot \frac{\Delta_{1^+}}{N} \cdot \frac{1/2 - B}{3\rho_{00}^- - 1}, \tag{7.31}$$

$$|F_1|^2 = \frac{1}{4}\left(1 \pm \sqrt{1 + 16 \cdot \frac{5\Delta_{1^-}(1/2 - B)}{3N(3\rho_{00}^+ - 1)}}\right). \tag{7.32}$$

The last two formulae show the explicit dependence of $|F_1|^2$ on the considered spin matrix elements. The errors for $|F_1|^2$, once we neglect the small contribution due to B, are due only to the corresponding errors for Δ_{1^+} and Δ_{1^-}. A detailed derivation can be found in Appendix C. Note that from the same formulae we obtain i) for pure 1^+ (i.e. $\Delta_{1^+} = 0$) again $|F_1|^2 = B = 0.443 \pm 0.008$ and ii) for pure 1^- (i.e. $\Delta_{1^-} = 0$) the expected value $|F_1|^2 = 1/2$. The obtained dependence of $|F_1|^2$ on $\rho_{00}^{\pm}$ is shown in the Figures 7.9 to 7.11, together with the dependence for the error (green line and band).

With the aim of a check for consistency, the dependence illustrated was compared with the $|F_1|^2$ value obtained from a direct calculation of the moments; a pictorial view of the results is shown in Figures 7.9 to 7.11 for a subsample corresponding to the mass window $1.1 < m(\omega\pi^0) < 1.4$ GeV/c^2 ($\omega\pi^0$-peak). The different Figures concern different cuts on the variable p_t^2: no cut at all (Figure 7.9), $0.15 < p_t^2 < 0.5$ (GeV/c)^2 (Figure 7.10) and $0.15 < p_t^2 < 1$ (GeV/c)^2 (Figure 7.11), respectively. The evaluated $|F_1|^2$ and relative error are represented by the black line and band. In the same plots, the red line indicates the $|F_1|^2$ value for a pure 1^- state, the blue line corresponds to pure $b_1(1235)$, the black line with error band is the measured value obtained from eq. (7.14), i.e. directly from momentum sum over events. Results points to a small value for ρ_{00}^- compatible with 0, and ρ_{00}^+ in the region around 0.6. These results are in accord with those of ref. [A$^+$84], where a dominant b_1 contribution was found. On the contrary, if one examines the incoherent (or "extended" incoherent, i.e. up to 1 (GeV/c)^2) sample only, the extracted value for ρ^- dramatically changes, assesting to ~ 0.5.

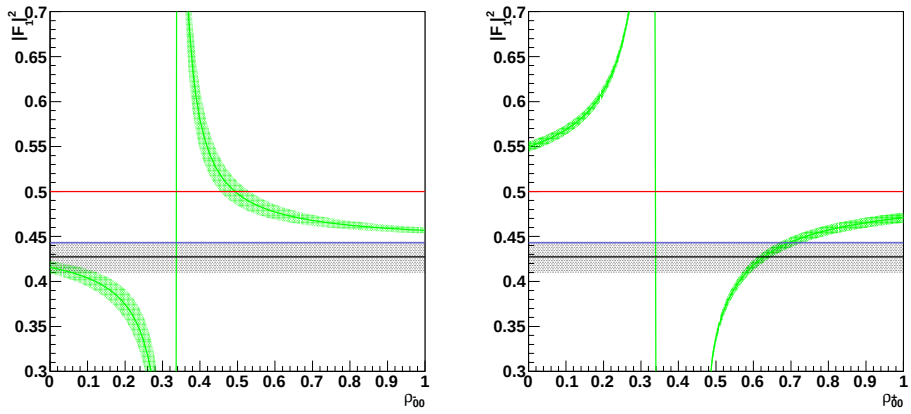

Figure 7.9: $|F_1|^2$ *dependence on* ρ_{00}^- *(left) and* ρ_{00}^+ *(right), for events within the* $\omega\pi^0$*-peak region* $1.1 < m(\omega\pi^0) < 1.4$ *GeV*/c^2.

Results concerning ρ_{00}^+ are of problematic interpretation, the branches of the theoretical curves not intersecting the band corresponding to the $|F_1|^2$ in the physical region $0 < \rho_{00}^{\pm} < 1$. One must also consider the effect of the limited statistic on the final values of the various moments $H_s(lmLM)$ and the corresponding big errors which enter in the evaluation of the theoretical curves by the corresponding errors from the two Δ's.

It must be also well kept in mind that the value $|F_1|^2$ in the previous plots is already corrected for background contribution due to the non-ω associated events which intrude the exclusive $\omega\pi^0$ final sample. Such estimation proceeds via the λ-distribution. Again, the resulting fits for λ suffer due to the low statistic in our samples.

7.3 Extraction of the 1^- contribution: the $\cos\theta_H$-fit method

A useful property of $H_s(0000)$ and $H_s(2000)$ *only*, is their independence on the production mechanism and/or interference effects between different spin-parity states [B$^+$88].

In particular we concentrate our attention on the moment $H_s^+(2000)$, which enters in the formula for the θ_H angular distribution, namely

$$\frac{dN}{d\cos\theta_H} = \frac{N}{2}\left[1 + \frac{5}{2}H_s^+(2000)(3\cos^2\theta_H - 1)\right], \tag{7.33}$$

which depends *only* on the spin-parity of the resonance (cf. [B$^+$88]).

The previous equation can be rewritten in terms of the helicity decay

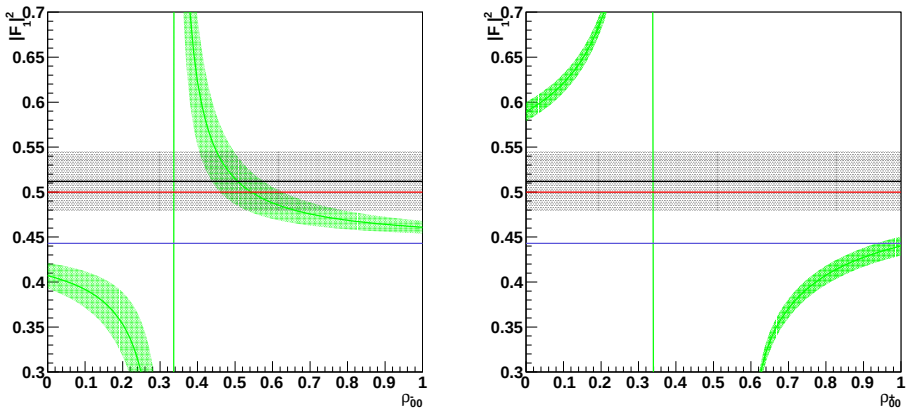

Figure 7.10: $|F_1|^2$ *dependence on* ρ^-_{00} *(left) and* ρ^+_{00} *(right), for events within* $1.1 < m(\omega\pi^0) < 1.4$ *GeV/*c^2 *and* $0.15 < p_t^2 < 0.5$ *(GeV/*c*)*^{2}.

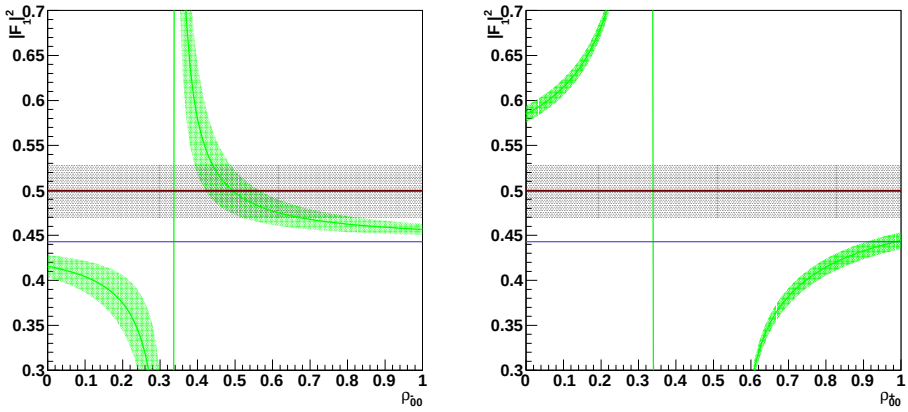

Figure 7.11: $|F_1|^2$ *dependence on* ρ^-_{00} *(left) and* ρ^+_{00} *(right), for events within* $1.1 < m(\omega\pi^0) < 1.4$ *GeV/*c^2 *and* $0.15 < p_t^2 < 1$ *(GeV/*c*)*^{2}.

J^P	$\lvert F_1\rvert^2$
0^-	0
1^-	0.5
1^+ (s-wave)	0.333
$b_1(1235)$	0.443 ± 0.008

Table 7.3: $|F_1|^2$ *for different spin-parity pure states.*

amplitude F_λ for an ω with helicity $\lambda = 0, \pm 1$, as already anticipated:

$$\frac{dN}{d\cos\theta_H} = \frac{3}{2}N(|F_1|^2 \sin^2\theta_H + |F_0|^2 \cos^2\theta_H), \tag{7.34}$$

which is equivalent to the probability distribution

$$W(\cos\theta_H) = \frac{1}{N}\cdot\frac{dN}{d\cos\theta_H} = \frac{3}{2}(|F_1|^2 \sin^2\theta_H + |F_0|^2 \cos^2\theta_H). \tag{7.35}$$

Let us recall the relation

$$2|F_1|^2 + |F_0|^2 = 1, \tag{7.36}$$

which is obtained integrating eq. (7.35) over the integration variable $\cos\theta_H$. The factor 2 has its origin in the weight of the helicity states $\lambda = \pm 1$ relative to the state with $\lambda = 0$, due to the equality $|F_1|^2 = |F_{-1}|^2$, a consequence of parity conservation in the decay of $\omega\pi^0$.

Table 7.3 lists the expected values for the case of pure 0^-, 1^-, 1^+ in s-wave and $b_1(1235)$, whose decay has s- and d-wave contributions, with the relative intensity given by the ratio[8]

$$\frac{d}{s} = 0.277 \pm 0.027, \tag{7.37}$$

which is an experimentally determined parameter (cf. relation (5.27), pag. 72).

The $\cos\theta_H$ distribution has already been shown in Figure 6.22. Our purpose is to obtain the value of $|F_1|^2$ from the observed data. One could try a fit using the function

$$a(1-x^2) + bx^2 \qquad (x = \cos\theta_H), \tag{7.38}$$

but equation (7.36) tells us that the parameters a and b are correlated: $2a + b = 1$. We must thus proceed in another way, to take this correlation into account.

Attention has been paid in order to avoid two possible sources of error:

[8] from PDG [A$^+$08b].

1. as a first step, the single bin content has been rescaled by a constant factor, in order to preserve the normalization condition (eq. (7.36)) of the fitting function in the domain $[-1, 1]$ of $\cos\theta_H$;

2. the width of the error bars (the errors shown in the following plots are statistical) has been also rescaled to preserve the values of the relative errors in each bin[9].

From equation (7.36), we can write equation (7.35) as a function of $\cos\theta_H$ only:

$$W(\cos\theta_H) = \frac{3}{2}[|F_1|^2 + (1 - 3|F_1|^2)\cos^2\theta_H]; \tag{7.39}$$

data point may be thus fitted using the function

$$f(x) = \frac{3}{2}[a + (1 - 3a)x^2] \qquad (x = \cos\theta_H), \tag{7.40}$$

the resulting parameter a from fit being the desired value $|F_1|^2$. From the data we obtain:

$$|F_1|^2 = 0.418 \pm 0.010, \tag{7.41}$$

which is outside the limits 0.5 (for pure 1^-) and 0.443 ± 0.008 (for pure b_1), see Table 7.3.

Also the dependence of $|F_1|^2$ on the $\omega\pi^0$-mass and/or p_t^2 has been examined. The $\omega\pi^0$ mass spectrum was subdivided in three regions correponding to

- $0.9\ \text{GeV}/c^2 < m(\omega\pi^0) < 1.1\ \text{GeV}/c^2$;
- $1.1\ \text{GeV}/c^2 < m(\omega\pi^0) < 1.4\ \text{GeV}/c^2$ ($\omega\pi^0$ peak region);
- $1.4\ \text{GeV}/c^2 < m(\omega\pi^0) < 1.6\ \text{GeV}/c^2$.

The p_t^2-ranges were chosen as in the previous sections.

Tables 7.4 and 7.5 list the $|F_1|^2$ values obtained from fitting the $\cos\theta_H$ experimental distributions corresponding to these different $m(\omega\pi^0)$- and p_t^2-windows. The original plots with the fit curves are shown in Appendix D.

We see that $|F_1|^2$ often lies outside the limits fixed by the pure J^P states 1^- and b_1: only in the peak region and for incoherent scattering $|F_1|^2$ assumes values within these limits, in that case unequivocally pointing toward a presence of the 1^-contribution. For this particular subsample, the distribution fit result is shown in Figure 7.12.

Nevertheless, to reach at this point any conclusion is clearly too premature: the important aspect which was not considered here is the background contribution to the $\cos\theta_H$ distribution.

[9]A function for this purpose is already implemented in ROOT and has been widely used in this analysis.

Selection	$\lvert F_1\rvert^2$
-	0.418 ± 0.010
$p_t^2 < 0.15$	0.401 ± 0.012
$0.15 < p_t^2 < 0.5$	0.437 ± 0.019
$0.15 < p_t^2 < 1$	0.452 ± 0.016

Table 7.4: $|F_1|^2$*: p_t^2-dependence.*

Selection	$0.9 < m < 1.1$	$1.1 < m < 1.4$	$1.4 < m < 1.6$
-	0.407 ± 0.029	0.446 ± 0.011	0.458 ± 0.020
$p_t^2 < 0.15$	0.402 ± 0.040	0.427 ± 0.014	0.445 ± 0.027
$0.15 < p_t^2 < 0.5$	0.368 ± 0.067	0.486 ± 0.020	0.374 ± 0.062
$0.15 < p_t^2 < 1$	0.422 ± 0.050	0.474 ± 0.019	0.398 ± 0.048

Table 7.5: $|F_1|^2$*: $\omega\pi^0$-mass and p_t^2-dependence.*

7.3.1 Background contribution to $|F_1|^2$

As already explained, from the study of the λ-distribution it has been possible to determine the contribution to our final sample due to the non-ω-related $\pi^+\pi^-\pi^0\pi^0$ events which intrude the exclusive events.

In Table 7.6 the p_t^2-dependence of this non-ω-related events contribution is shown, the listed values obtained from the intercept at $\lambda = 0$ from a linear fit of the corresponding data. This has been done for the fit interval $\lambda \in [0, 0.9]$ to avoid possible falsifications due to acceptance-related deviations from linearity sometimes observed at $\lambda \approx 1$.

Table 7.7 shows in addition the $m(\omega\pi^0)$-dependence using the same fit procedure. To determine the value of $|F_1|^2$ corresponding to background, which we denote hereafter with $|F_1|^2_{bkg}$, we have examined, for exclusive events, the correponding $\cos\theta_H$ distribution in the two side bands left and right to the ω-peak, and defined by:

- 650 MeV/c^2 $< m(\pi^+\pi^-\pi^0) <$ 725 MeV/c^2;
- 835 MeV/c^2 $< m(\pi^+\pi^-\pi^0) <$ 910 MeV/c^2;

Selection	%
-	19.1 ± 4.4
$p_t^2 < 0.15$	21.0 ± 5.7
$0.15 < p_t^2 < 0.5$	15.5 ± 9.0
$0.15 < p_t^2 < 1$	10.2 ± 6.9

Table 7.6: *Non ω-related percentage contribution to the exclusive $\omega\pi^0$ final sample: p_t^2-dependence.*

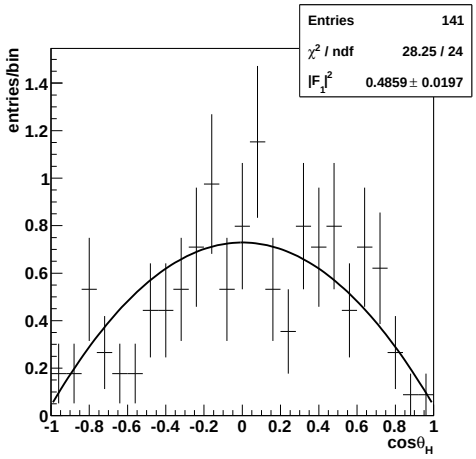

Figure 7.12: $\cos\theta_H$ *distribution and* $|F_1|^2$ *from fit for events in the* $\omega\pi^0$*-peak region from incoherent scattering off quasi-free nucleons.*

Selection	$0.9 < m < 1.1$	$1.1 < m < 1.4$	$1.4 < m < 1.6$
-	25.0 ± 13.7	15.7 ± 5.6	$0.0^{+10.8}_{-0.0}$
$p_t^2 < 0.15$	31.6 ± 21.4	18.0 ± 7.5	$9.1^{+15.8}_{-9.1}$
$0.15 < p_t^2 < 0.5$	$72.3^{+27.7}_{-42.1}$	$0.8^{+11.3}_{-0.8}$	55.9 ± 30.2
$0.15 < p_t^2 < 1$	48.3 ± 35.6	$0.0^{+5.2}_{-0.0}$	25.7 ± 23.6

Table 7.7: *Non* ω*-related percentage contribution to the exclusive* $\omega\pi^0$ *sample.* p_t^2*- and* $\omega\pi^0$*-mass-dependence.*

the aim was to gain information about $|F_1|^2_{bkg}$ from a fit of this data sample. Figure 7.13 shows the results (year 2004 data only). The selected sample corresponds to exclusive $\pi^+\pi^-\pi^0\pi^0$ events with one and only one identified $\omega\pi^0$, taking this time a broader window for the ω selection: 650 MeV/c^2 $< m(\pi^+\pi^-\pi^0) <$ 950 MeV/c^2 (top-left in the Figure: 3π invariant mass). Choosing such a broad mass window for the ω has the drawback to shrink the final statistics in the sample, as compared with our main selection: in fact, broadening the $(\pi^+\pi^-\pi^0)$-mass window to select "good" ω's, enhances the relative weight of events with two (or more) ω-candidates, which must be discarded, *even if* one of these candidates *is* indeed a true ω and the second a fake. This results in the observed loss in statistic and lower signal-to-background ratio. On the other hand, a broad mass window makes the study of the $\cos\theta_H$ distribution in the two side-bands possible. These correspond to non-ω related exclusive events, and give information about the background contribution to $|F_1|^2$. That the side-bands sample is ω-free can be seen from the corresponding λ-distribution, which is flat (Figure 7.13, top-right). The third histogram in the same Figure shows the

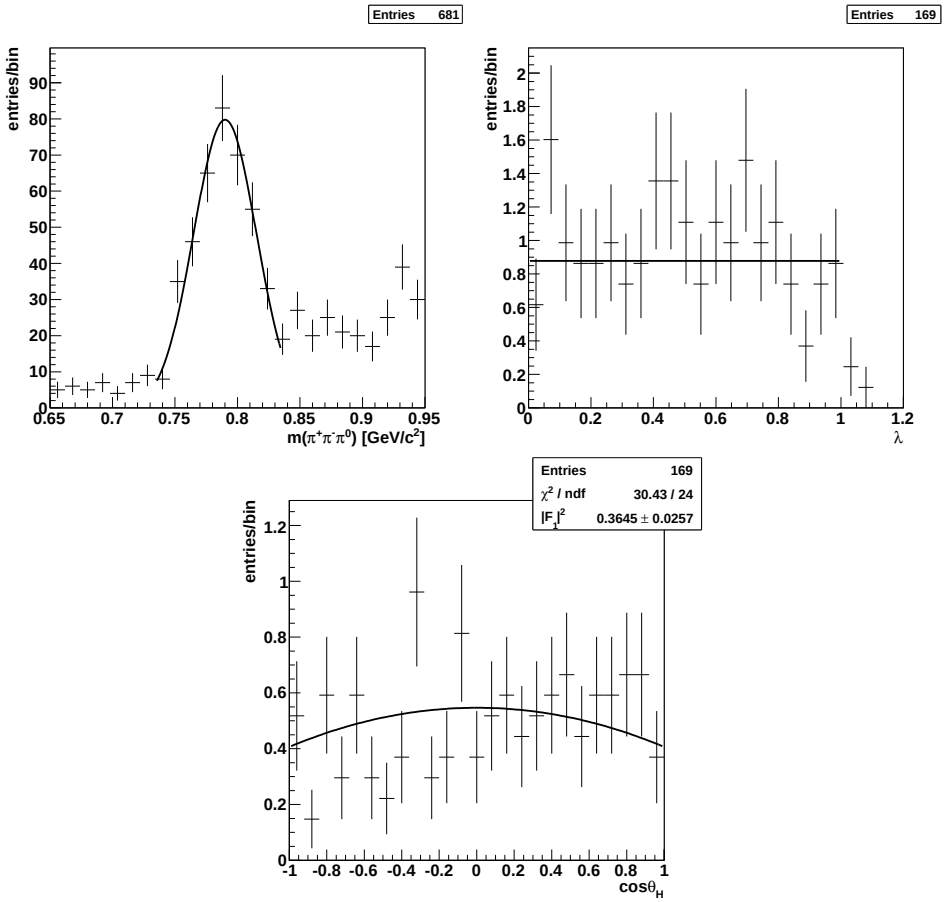

Figure 7.13: $\pi^+\pi^-\pi^0$ *invariant mass,* λ*-distribution for the side-bands region (non-*ω *sample, see text) and corresponding* $\cos\theta_H$ *distribution with fitted* $|F_1|^2$ *value. No* p_t^2*-cut.*

$\cos\theta_H$ distribution, with the value obtained from fit:

$$|F_1|^2 = 0.365 \pm 0.026. \tag{7.42}$$

This points toward a light anisotropy[10], though being constrained in the interval $[0.339, 0.391]$ at the 1σ-level.

Also a possible contribution of ρ mesons in the exclusive 4π-sample has been considered: in Figure 7.14 the $\pi^\pm\pi^0$ invariant mass spectra corresponding to different $m(\pi^+\pi^-\pi^0)$-windows are shown: the resulting spectra prove the presence of $\rho^\pm$ mesons which may come from a $\rho^+\rho^-$ background contribution to the signal. In the same Figure, the $\cos\theta_H$ distribution corresponding to events within the ω-peak is plotted after the removal of events corresponding to the mass range

$$600\,\mathrm{MeV}/c^2 < m(\pi^\pm\pi^0) < 900\,\mathrm{MeV}/c^2 \tag{7.43}$$

(*anti-ρ* cut). The introduction of this cut results in the value $|F_1|^2 = 0.382 \pm 0.075$, which is compatible with that in equation (7.42). At the 1σ-level: $|F_1|^2 \in [0.307, 0.458]$. Note also the very low statistic which characterizes this sample.

For completeness, we have examined the non exclusive region in the side band 10 GeV $< E_{miss} <$ 20 GeV with the purpose to determine the value of $|F_1|^2$ characteristic of the non-exclusive 4π-events which may intrude the exclusive peak: the $|F_1|^2$ values obtained from fit are lower than for the exclusive sample, as seen in Tables 7.8 and 7.9. A good approximation

Selection	$\lvert F_1\rvert^2$
-	0.376 ± 0.019
$p_t^2 < 0.15$	0.346 ± 0.027
$0.15 < p_t^2 < 0.5$	0.362 ± 0.030
$0.15 < p_t^2 < 1$	0.375 ± 0.027

Table 7.8: *p_t^2-dependence of $|F_1|^2$ for events in 10 GeV $< E_{miss} <$ 20 GeV.*

consists in taking $|F_1|^2_{bkg} = 0.333$, independent of any cut on the $\omega\pi^0$ mass and/or p_t^2. In addition, the corresponding λ-distribution for these non-exclusive events is shown in Figure 7.15; the usual linear fit gives, for the non-ω contribution to the sample, the value $100^{+0}_{-6}\%$, and $100^{+0}_{-8}\%$ for the $\omega\pi^0$-peak region only. This shows that the non-exclusive events, visible on the right side of the exclusivity spectrum (Figure 4.6, pag. 43), are completely non-ω-related.

It is then natural to assume the non-ω contribution to the exclusive peak to be isotropically distributed with a corresponding $|F_1|^2_{bkg} = 0.333$, which can be taken as a correction factor for the data shown in Tables 7.4 and 7.5.

[10]Remember: $|F_1|^2 = |F_{-1}|^2$ from parity conservation in $\omega\pi^0$ decay, and $|F_{-1}|^2 = |F_0|^2 = |F_1|^2$ for isotropy, thus giving $|F_{-1}|^2 = |F_0|^2 = |F_1|^2 = 1/3$ in that case.

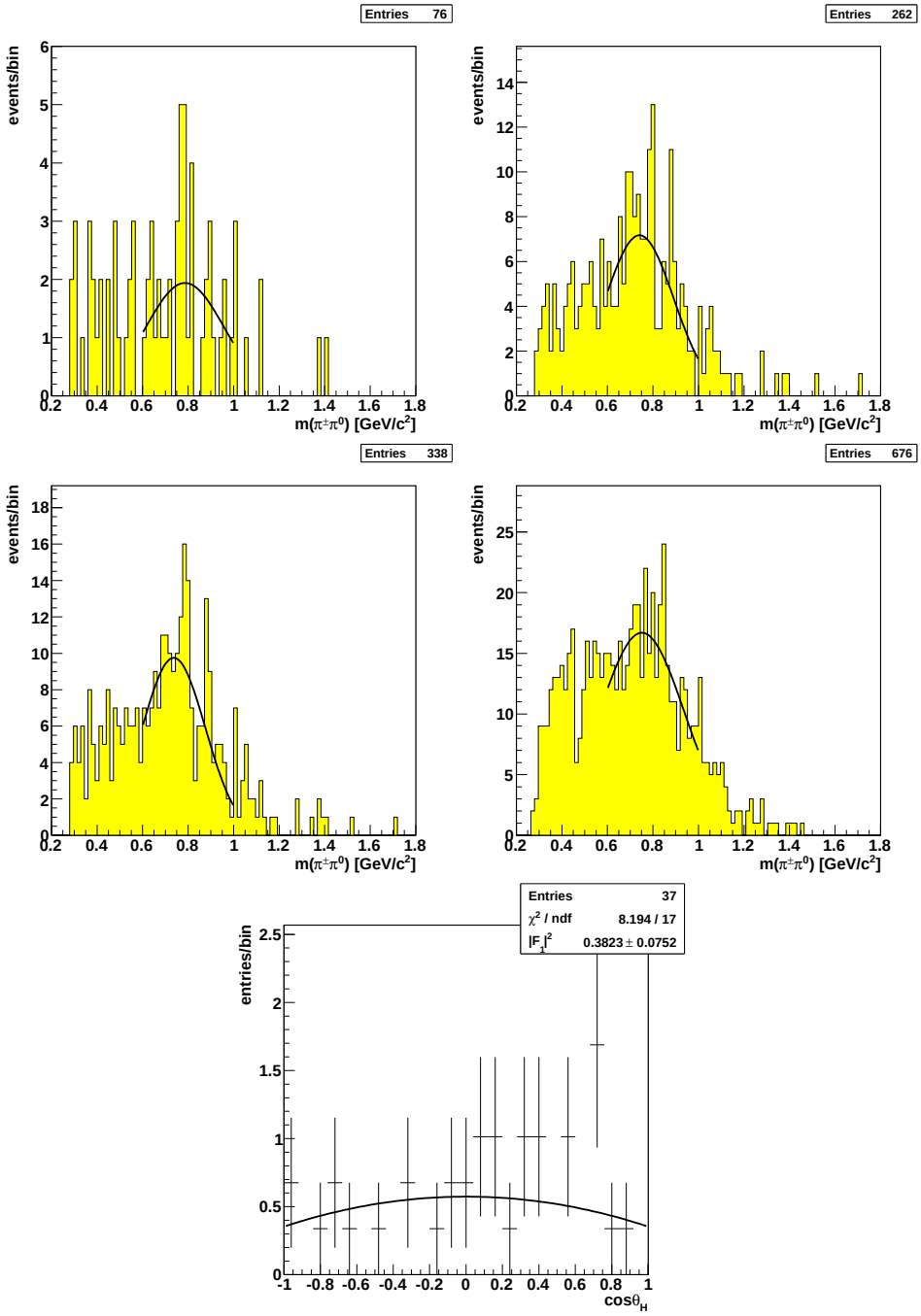

Figure 7.14: $\pi^{\pm}\pi^0$ *mass spectrum for low-mass (top-left), high-mass (top-right)* ω*-side-bands, the sum of the two (middle-left) and* ω*-peak region (middle-right). Bottom: fitted* $\cos\theta_H$ *distribution in* ω*-peak with anti-*ρ *cut (see text).*

Selection	$0.9 < m < 1.1$	$1.1 < m < 1.4$	$1.4 < m < 1.6$
-	0.418 ± 0.034	0.369 ± 0.027	0.387 ± 0.049
$p_t^2 < 0.15$	0.395 ± 0.060	0.355 ± 0.036	0.326 ± 0.118
$0.15 < p_t^2 < 0.5$	0.418 ± 0.117	0.307 ± 0.051	0.695 ± 0.419
$0.15 < p_t^2 < 1$	0.399 ± 0.076	0.357 ± 0.044	0.406 ± 0.189

Table 7.9: $m(\omega\pi^0)$- *and* p_t^2*-dependence of* $|F_1|^2$ *for events in* 10 *GeV* $< E_{miss} <$ 20 *GeV.*

The results obtained so far thus suggest to consider two different scenarios for the background contribution:

i) $|F_1|^2_{bkg} = 0.333$ (isotropy);

ii) $|F_1|^2_{bkg} = 0.4$;

the last value chosen for an estimation of the effects due to systematics.

7.3.2 Correction to $|F_1|^2$

The value of $|F_1|^2$ after correction (i.e., the "true" value), from now on written $|F_1|^2_{corr}$, was calculated using the equation

$$(1 - B)|F_1|^2_{corr} + B|F_1|^2_{bkg} = |F_1|^2, \tag{7.44}$$

which gives:

$$|F_1|^2_{corr} = \frac{|F_1|^2 - B|F_1|^2_{bkg}}{1 - B}. \tag{7.45}$$

The meaning of each quantity is self-explaining: B is the contribution of background in the final sample, as listed for the various p_t^2 and/or $m(\omega\pi^0)$ cuts in Tables 7.6 and 7.7; $|F_1|^2_{bkg}$ will take the two values 0.333 and 0.4, as discussed in the previous section. The observed value $|F_1|^2$ is thus interpreted as the weighted mean of the background contribution $|F_1|^2_{bkg}$ and the "true" value $|F_1|^2_{corr}$ which can be now calculated. Errors for $|F_1|^2_{corr}$ are determined by means of the error propagation law applied to eq. (7.45):

$$\Delta|F_1|^2_{corr} = \sqrt{\left(\frac{\partial|F_1|^2_{corr}}{\partial|F_1|^2}\right)^2(\Delta|F_1|^2)^2 + \left(\frac{\partial|F_1|^2_{corr}}{\partial B}\right)^2(\Delta B)^2}, \tag{7.46}$$

where the partial derivatives are

$$\frac{\partial|F_1|^2_{corr}}{\partial|F_1|^2} = \frac{1}{1 - B}, \tag{7.47}$$

$$\frac{\partial|F_1|^2_{corr}}{\partial B} = \frac{|F_1|^2 - |F_1|^2_{bkg}}{(1 - B)^2}. \tag{7.48}$$

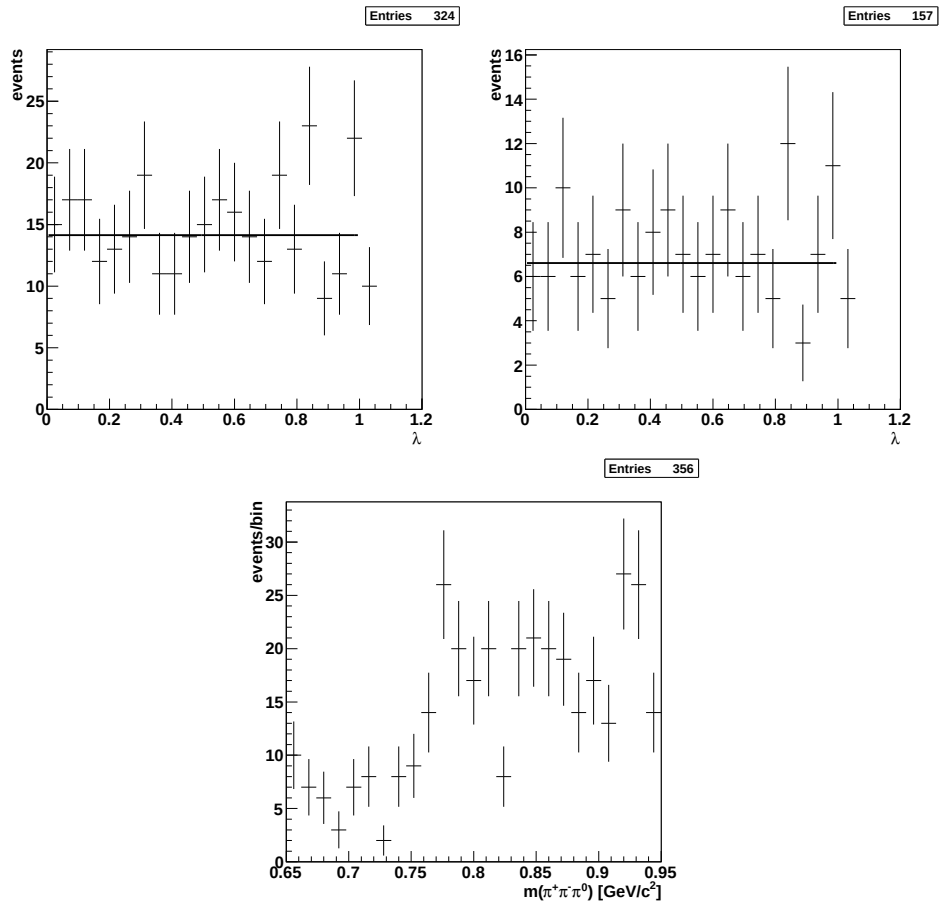

Figure 7.15: *λ-distribution for the non-exclusive $\omega\pi^0$ sample in* 10 *GeV* $< E_{miss} <$ 20 *GeV (top-left), within the $\omega\pi^0$-peak region (top-right), and corresponding $m(\pi^+\pi^-\pi^0)$ spectrum (bottom).*

In this formula, the only quantities assumed with errors are $|F_1|^2$ and B.

Tables 7.10 and 7.11 show the calculated values $|F_1|^2_{corr}$, with $|F_1|^2_{bkg} = 0.333$. In Figure 7.16 the numerical values listed in those Tables are graphically represented, compared with those for *pure* 1^- (red line) and *pure* b_1 (the blue band resulting from the error on D/S ratio).

It is interesting to observe that for the case of incoherent production off quasi-free nucleons, and in general for the $\omega\pi^0$-peak region, the measured value $|F_1|^2_{corr} = 0.487 \pm 0.026$ lies between the two values for pure 1^- and b_1 production, pointing towards an *approximately equal contribution* in our final sample of both 1^+ and 1^- states.

Figure 7.17 shows the same set of values about $|F_1|^2_{corr}$, this time obtained from the direct evaluation of the moments in eq. (7.14). As for the values from fit, a background contribution $|F_1|^2_{bkg} = 0.333$ was assumed to

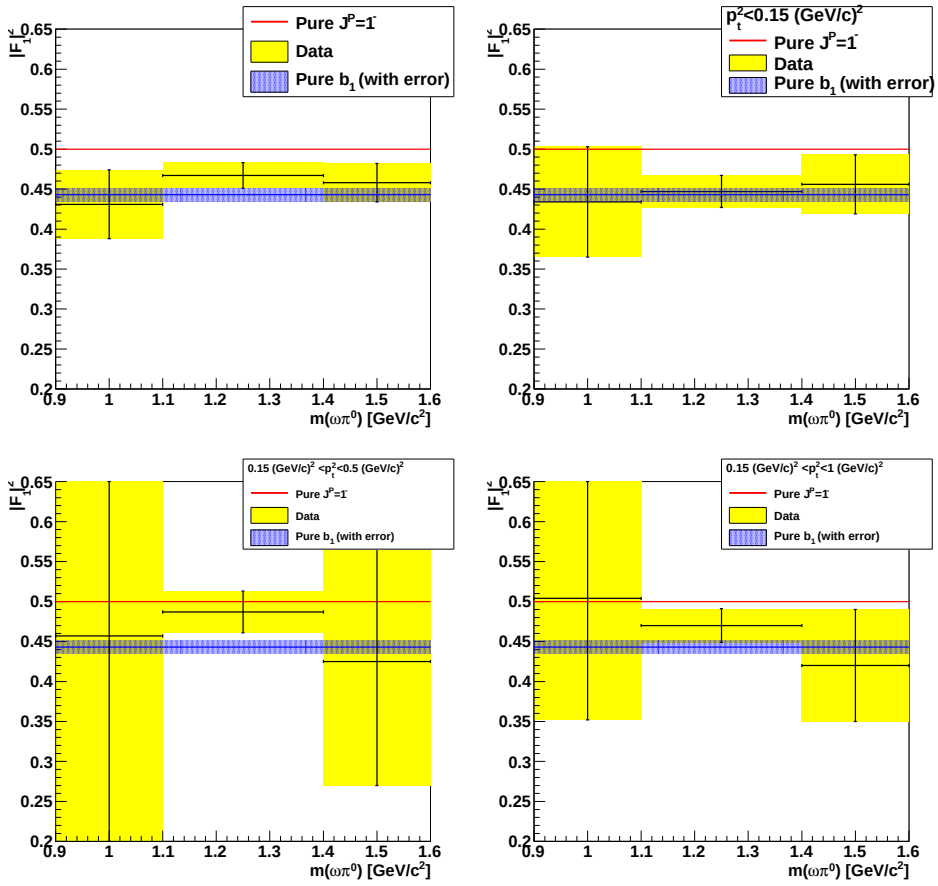

Figure 7.16: *Fits results for the ω decay amplitude $|F_1|^2$ with and without cuts on p_t^2, compared with pure 1^- (red line) and pure $b_1(1235)$ (blue band for D/S error). $|F_1|^2_{bkg} = 0.333$.*

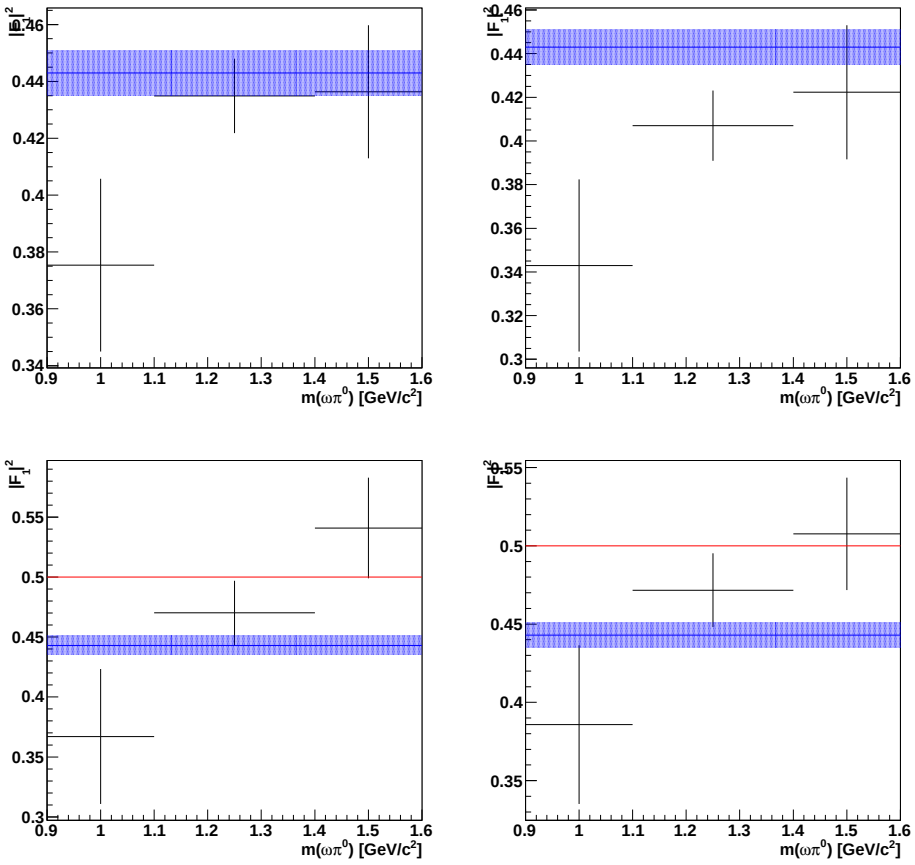

Figure 7.17: $|F_1|^2_{corr}$ *calculated using eq.* (7.14). *From left to right, top to bottom: i) no* p_t^2*-cut; ii)* $p_t^2 < 0.15$ *GeV*^{2}*; iii)* $0.15 < p_t^2 < 0.5$ *GeV*^{2}*; iv)* $0.15 < p_t^2 < 1$ *GeV*^{2}*. Red line: pure* 1^- *signal; blue band: pure* $b_1(1235)$*, with error from* D/S *ratio. Background contribution:* $|F_1|^2_{bkg} = 0.333$.

Selection	$\lvert F_1\rvert^2_{corr}$
-	0.438 ± 0.013
$p_t^2 < 0.15$	0.419 ± 0.017
$0.15 < p_t^2 < 0.5$	0.456 ± 0.026
$0.15 < p_t^2 < 1$	0.465 ± 0.021

Table 7.10: $|F_1|^2_{corr}$*: p_t^2-dependence.* $|F_1|^2_{bkg} = 0.333$.

Selection	$0.9 < m < 1.1$	$1.1 < m < 1.4$	$1.4 < m < 1.6$
-	0.431 ± 0.043	0.467 ± 0.016	$0.458^{+0.024}_{-0.020}$
$p_t^2 < 0.15$	0.434 ± 0.067	0.447 ± 0.020	$0.456^{+0.037}_{-0.032}$
$0.15 < p_t^2 < 0.5$	$0.457^{+0.271}_{-0.306}$	$0.487^{+0.026}_{-0.020}$	0.425 ± 0.155
$0.15 < p_t^2 < 1$	0.504 ± 0.152	$0.474^{+0.020}_{-0.019}$	0.420 ± 0.070

Table 7.11: $|F_1|^2_{corr}$*: p_t^2- and $m(\omega\pi^0)$-dependence.* $|F_1|^2_{bkg} = 0.333$.

correct the data. The entity of background was taken equal to the one used in the fit method (Tables 7.6 and 7.7). The numerical values for $|F_1|^2_{corr}$ are now listed in Table 7.12.

In Figure 7.18 the same procedure used for Figure 7.16 has been applied, this time fixing the correction for background $|F_1|^2_{bkg} = 0.4$. Tables 7.13 and 7.14 correspond to Tables 7.10 and 7.11. The differences between the two sets of values may be taken as an estimation of the size of the systematic error contribution from background.

A preliminary conclusion: data from coherent scattering show a major contribution from the 1^+ state, pointing to an enhanced production of $b_1(1235)$ in this range, whereas the 1^- contribution is evident in the incoherent scattering regime. The lower and higher $\omega\pi^0$-mass regions suffer from the poor statistics, resulting in broad error bars, even if a dominance of the 1^+ state seems to characterize the data.

Selection	$0.9 < m < 1.1$	$1.1 < m < 1.4$	$1.4 < m < 1.6$
-	0.375 ± 0.041	0.435 ± 0.017	$0.436^{+0.026}_{-0.023}$
$p_t^2 < 0.15$	0.343 ± 0.058	0.407 ± 0.021	$0.422^{+0.037}_{-0.035}$
$0.15 < p_t^2 < 0.5$	$0.366^{+0.206}_{-0.209}$	$0.470^{+0.031}_{-0.027}$	0.540 ± 0.171
$0.15 < p_t^2 < 1$	0.385 ± 0.104	$0.475^{+0.025}_{-0.024}$	0.508 ± 0.073

Table 7.12: $|F_1|^2_{corr}$*: p_t^2- and $m(\omega\pi^0)$-dependence.* $|F_1|^2_{bkg} = 0.333$. *From moments.*

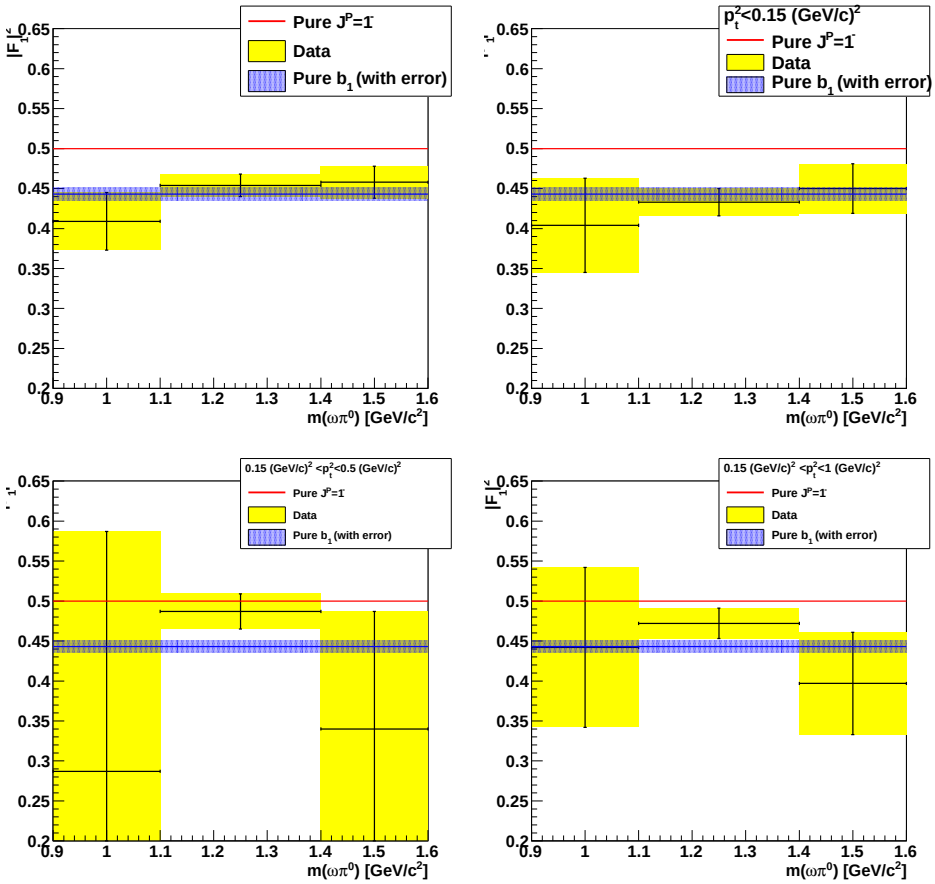

Figure 7.18: *Fits results for the ω decay amplitude $|F_1|^2$ with and without cuts on p_t^2, compared with pure 1^- (red line) and pure $b_1(1235)$ (blue band for D/S-error).* $|F_1|^2_{bkg} = 0.4$.

Selection	$\lvert F_1\rvert^2_{corr}$
-	0.422 ± 0.012
$p_t^2 < 0.15$	0.401 ± 0.016
$0.15 < p_t^2 < 0.5$	0.443 ± 0.023
$0.15 < p_t^2 < 1$	0.458 ± 0.018

Table 7.13: $|F_1|^2_{corr}$*: p_t^2-dependence.* $|F_1|^2_{bkg} = 0.4$.

Selection	$0.9 < m < 1.1$	$1.1 < m < 1.4$	$1.4 < m < 1.6$
-	0.409 ± 0.039	0.454 ± 0.014	$0.458^{+0.021}_{-0.020}$
$p_t^2 < 0.15$	0.404 ± 0.059	0.433 ± 0.017	$0.450^{+0.031}_{-0.030}$
$0.15 < p_t^2 < 0.5$	$0.283^{+0.269}_{-0.300}$	$0.487^{+0.022}_{-0.020}$	0.340 ± 0.147
$0.15 < p_t^2 < 1$	0.442 ± 0.100	0.474 ± 0.019	0.397 ± 0.064

Table 7.14: $|F_1|^2_{corr}$*: p_t^2- and $m(\omega\pi^0)$-dependence.* $|F_1|^2_{bkg} = 0.4$.

7.3.3 $J^P = 1^-$ fraction in the $\omega\pi^0$ final sample

Tables 7.15 and 7.16 show the extracted $J^P = 1^-$ percentage contribution to the signal under the assumption that no 0^- contribution is present.

Selection	1^- (%)
-	$0.0^{+18.6}_{-0.0}$
$p_t^2 < 0.15$	-
$0.15 < p_t^2 < 0.5$	$22.8^{+46.9}_{-22.8}$
$0.15 < p_t^2 < 1$	38.6 ± 37.8

Table 7.15: $J^P = 1^-$ *percentage contribution to the* $\omega\pi^0$ *final sample.* p_t^2*-dependence.* $|F_1|^2_{bkg} = 0.333$

For $|F_1|^2$ directly calculated from moment $H_s^+(2000)$, results are shown in Tables 7.17 and 7.18. In both cases, one can see that sometimes there is no entry (indicated with a "-"): this means that the result of the calculation lies outside the natural interval 0-100% more than at the 1σ-level and must be discarded. The asymmetric notation for errors is used, due to the entity of the errors themselves. If the calculated value for the 1^- percentage lies below(above) 0%(100%) we have rounded the results to 0%(100%) *if and only if* the error bars overlap the significative range 0-100%: e.g., a result from calculation as -8.8 ± 27.4 has been written as $0.0^{+18.6}_{-0.0}$, whereas a result like 165 ± 142 is written as 100^{+0}_{-77}. In some p_t^2- or $\omega\pi^0$-mass subranges measurements are so imprecise that no better expression than 100^{+0}_{-100} or 0^{+100}_{-0} can be found, not particularly significative: the cause of this lies

Selection	$0.9 < m < 1.1$	$1.1 < m < 1.4$	$1.4 < m < 1.6$
-	$0.0^{+56.2}_{-0.0}$	42.1 ± 29.2	$26.3^{+43.4}_{-26.3}$
$p_t^2 < 0.15$	0^{+100}_{-0}	$7.0^{+37.4}_{-7.0}$	$22.8^{+65.8}_{-22.8}$
$0.15 < p_t^2 < 0.5$	25^{+75}_{-25}	$77.2^{+22.8}_{-35.2}$	0^{+100}_{-0}
$0.15 < p_t^2 < 1$	100^{+0}_{-100}	$54.4^{+35.7}_{-33.9}$	0^{+84}_{-0}

Table 7.16: $J^P = 1^-$ *percentage contribution to the* $\omega\pi^0$ *final sample.* p_t^2*- and* $m(\omega\pi^0)$*-dependence.* $|F_1|^2_{bkg} = 0.333$.

Selection	1^- (%)
-	$0.0^{+20.0}_{-0.0}$
$p_t^2 < 0.15$	-
$0.15 < p_t^2 < 0.5$	$26.3^{+50.2}_{-26.3}$
$0.15 < p_t^2 < 1$	43.9 ± 41.1

Table 7.17: $J^P = 1^-$ *percentage contribution to the* $\omega\pi^0$ *final sample.* p_t^2*-dependence (from* $H_s^+(2000)$*).* $|F_1|^2_{bkg} = 0.333$

Selection	$0.9 < m < 1.1$	$1.1 < m < 1.4$	$1.4 < m < 1.6$
-	$0.0^{+27.5}_{-0.0}$	$8.8^{+34.1}_{-8.8}$	$21.1^{+48.6}_{-21.1}$
$p_t^2 < 0.15$	0^{+72}_{-0}	-	$15.8^{+71.2}_{-15.8}$
$0.15 < p_t^2 < 0.5$	72^{+28}_{-72}	$70.2^{+29.8}_{-58.0}$	100^{+0}_{-100}
$0.15 < p_t^2 < 1$	0^{+100}_{-0}	$66.7^{+33.3}_{-45.9}$	100^{+0}_{-77}

Table 7.18: $J^P = 1^-$ *percentage contribution to the* $\omega\pi^0$ *final sample.* p_t^2*- and* $m(\omega\pi^0)$*-dependence (from* $H_s^+(2000)$*).* $|F_1|^2_{bkg} = 0.333$.

mainly in the poor statistic that characterizes such samples. This cannot be avoided and results cannot be improved.

The method for the calculation is simple: let x be the intensity of the 1^- signal in the final sample, $|F_1|^2_{corr}$ the value after the correction applied for the presence of background, assumed to be isotropic in the angle θ_H ($|F_1|^2_{bkg} = 0.333$), and $B = 0.443 \pm 0.008$ the value of $|F_1|^2$ for a pure $b_1(1235)$. We may write:

$$0.5 \cdot x + B \cdot (1 - x) = |F_1|^2_{corr}, \tag{7.49}$$

which gives

$$x = \frac{|F_1|^2_{corr} - B}{0.5 - B}. \tag{7.50}$$

The error Δx is determined from the error propagation law, which gives:

$$\Delta x = \sqrt{\left(\frac{\partial x}{\partial |F_1|^2_{corr}}\right)^2 (\Delta |F_1|^2_{corr})^2 + \left(\frac{\partial x}{\partial B}\right)^2 \Delta B^2}; \tag{7.51}$$

the partial derivatives are:

$$\frac{\partial x}{\partial |F_1|^2_{corr}} = \frac{1}{1/2 - B}, \tag{7.52}$$

$$\frac{\partial x}{\partial B} = \frac{|F_1|^2_{corr} - 1/2}{(1/2 - B)^2}. \tag{7.53}$$

The errors $\Delta|F_1|^2_{corr}$ are taken from Tables 7.10 to 7.14, whereas the error for pure b_1 from Table 7.3. As explained, the $|F_1|^2 = 1/2$ value for pure 1^-

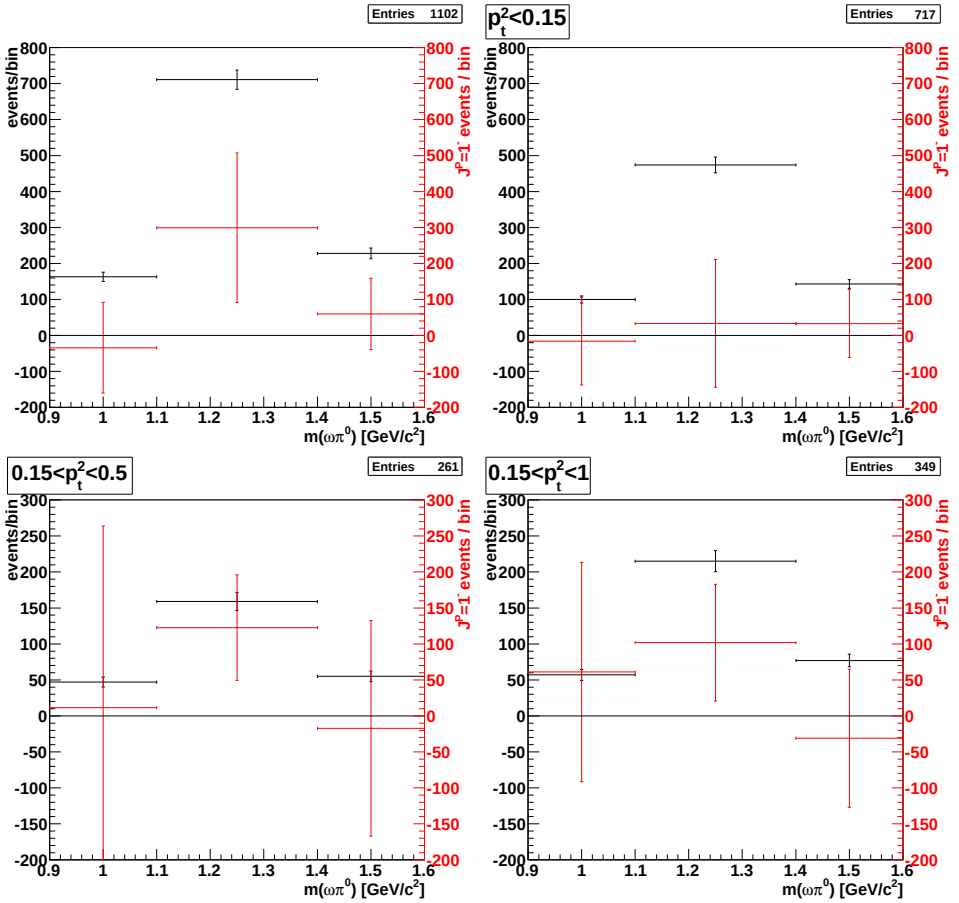

Figure 7.19: $J^P = 1^-$ *intensity (red) in the* $\omega\pi^0$ *final sample (black) with and without* p_t^2*-cuts. The errors for the* 1^- *contribution are calculated using eqs.* (7.51) *and* (7.54). $|F_1|^2_{bkg} = 0.333$.

has no error, the error for b_1 resulting from the precision with which the D/S-ratio is known from experiment.

If now N and N^- are the numbers of events in a given mass bin and of the corresponding 1^- contribution, respectively, then $N^- = xN$ and the error for N^- is easily calculated:

$$\Delta N^- = \sqrt{x^2 \Delta N^2 + N^2 \Delta x^2}. \tag{7.54}$$

Figures 7.19 shows the results for the contribution of the 1^- state (in red) to the final sample (in black), with and without the different p_t^2-cuts applied so far. For the same set of data, but $|F_1|^2_{corr}$ derived from direct calculation of the moment $H_s^+(2000)$, we obtain the results shown in Figure 7.20.

For the case $|F_1|^2_{bkg} = 0.4$, the corresponding results can be seen in

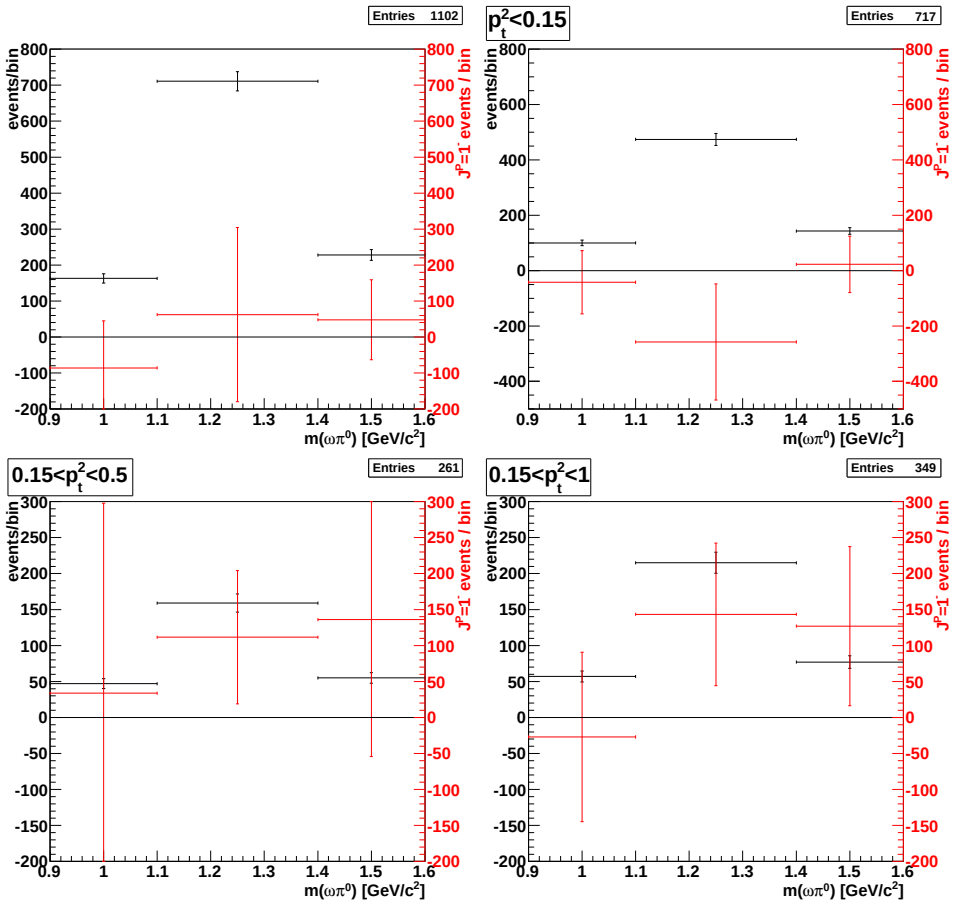

Figure 7.20: $J^P = 1^-$ *intensity (red) in the* $\omega\pi^0$ *final sample (black) with and without* p_t^2*-cuts. The errors for the* 1^- *contribution are calculated using eqs.* (7.51), (7.54) *and* (7.33). $|F_1|^2_{bkg} = 0.333$. *From moment* $H_s^+(2000)$.

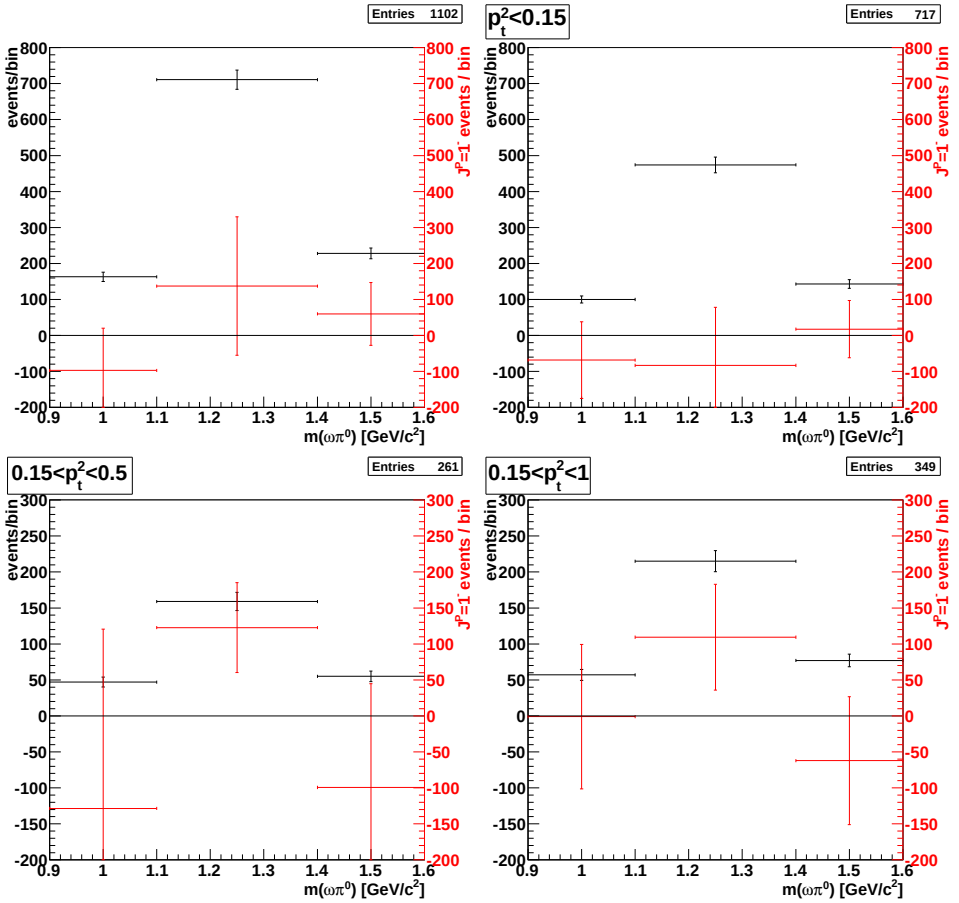

Figure 7.21: $J^P = 1^-$ *intensity (red) in the* $\omega\pi^0$ *final sample (black) with and without* p_t^2*-cuts. The errors for the* 1^- *contribution are calculated from eqs.* (7.51) *and* (7.54). $|F_1|^2_{bkg} = 0.4$

Figures 7.21 (from fit) and 7.22 (from the moment $H_s^+(2000)$). The corresponding numerical percentage values are listed in Tables 7.19 and 7.20 (for the fit method), and Tables 7.21 and 7.22 (from moment $H_s^+(2000)$).

A general conclusion: even if the values $|F_1|^2_{corr}$ and the corresponding calculated 1^- contributions vary in each $\omega\pi^0$-mass and p_t^2 window, the data, expecially in the $\omega\pi^0$-peak region and for incoherent scattering, point towards a 1^- and 1^+ contribution of *similar size*.

Table 7.23 shows, for the measured 1^- contribution, a comparison of results of previous experiments at different center-of-mass energy $\langle W \rangle$, together with the corresponding value obtained in our analysis.

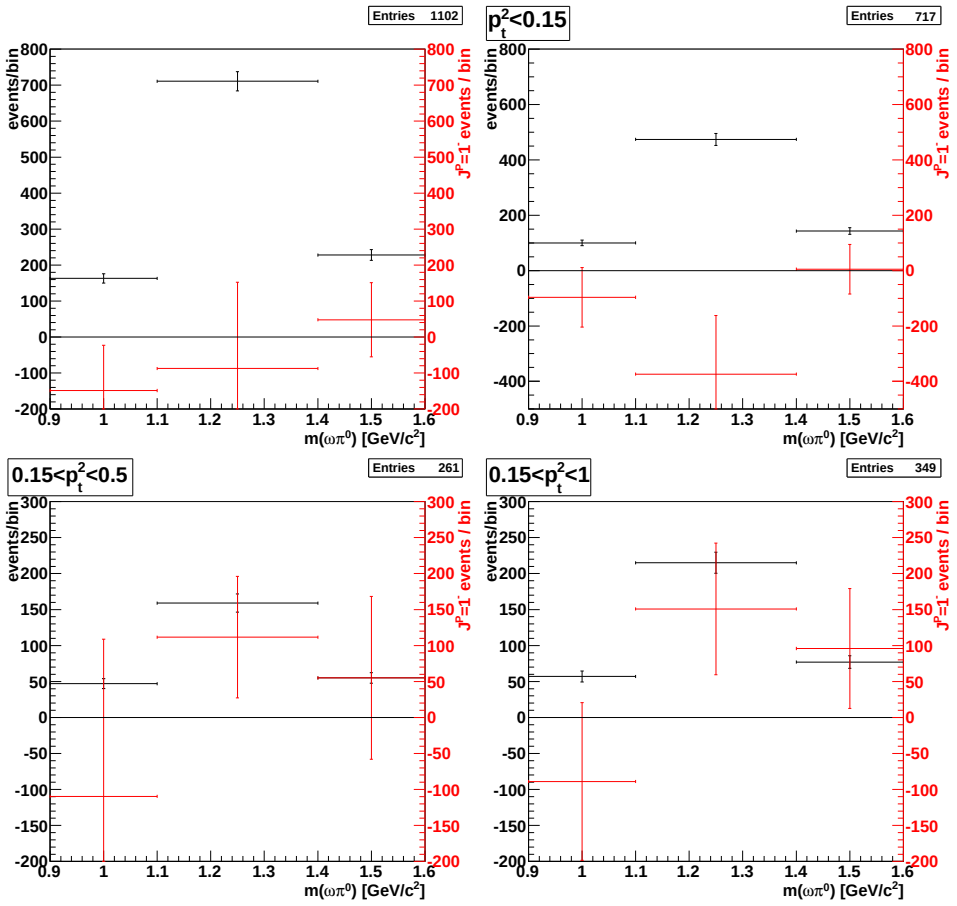

Figure 7.22: $J^P = 1^-$ *intensity (red) in the* $\omega\pi^0$ *final sample (black) with and without* p_t^2*-cuts. The errors for the* 1^- *contribution are calculated from eqs.* (7.51) *and* (7.54). $|F_1|^2_{bkg} = 0.4$. *From moment* $H_s^+(2000)$.

Selection	1^- (%)
-	-
$p_t^2 < 0.15$	-
$0.15 < p_t^2 < 0.5$	$0.0^{+42.7}_{-0.0}$
$0.15 < p_t^2 < 1$	$26.3^{+33.2}_{-26.3}$

Table 7.19: 1^- *contribution in the* $\omega\pi^0$ *final sample.* $|F_1|^2_{bkg} = 0.4$.

Selection	$0.9 < m < 1.1$	$1.1 < m < 1.4$	$1.4 < m < 1.6$
-	$0.0^{+12.4}_{-0.0}$	$19.3^{+27.0}_{-19.3}$	$26.3^{+38.3}_{-26.3}$
$p_t^2 < 0.15$	0^{+38}_{-0}	$0.0^{+16.6}_{-0.0}$	$12.3^{+55.8}_{-12.3}$
$0.15 < p_t^2 < 0.5$	0^{+100}_{-0}	$77.2^{+22.8}_{-38.7}$	0^{+80}_{-0}
$0.15 < p_t^2 < 1$	0^{+100}_{-0}	54.4 ± 33.9	0^{+34}_{-0}

Table 7.20: 1^- *contribution in the* $\omega\pi^0$ *final sample.* $|F_1|^2_{bkg} = 0.4$.

7.3.4 The λ-cut

The analysis conducted so far has been repeated for the event subsample in the interval $\lambda \in [0.2, 1]$. The corresponding results are shortly discussed in Appendix F.

The purpose of these second analysis was the gain of a purer, more background-free $\omega\pi^0$-sample, resulting in a better determination of the 1^- contribution. This is understandable, if we consider that for small values of λ, the relative contribution of background, which is constant in the interval $[0, 1]$, is higher if compared to the sample corresponding to higher values of λ.

Some conclusion on the effect of the λ-cut: even if the values of background with the cut applied are correspondigly lower than in the case without the cut, no particular improvement seems to be gained for the corrected values $|F_1|^2_{corr}$; this can be explained by the reduced statistic due to the cut, which affects already the *uncorrected* values $|F_1|^2$: these are infact systematically lower than the corresponding without the λ-cut. The effect of lower background seems thus to be compensated by the reduced values for each $|F_1|^2$.

In the following, we will neglect the cut on λ.

7.4 SCHC versus non-SCHC interpretation

A cross section measurement for the exclusive $\omega\pi^0$ photoproduction gave a dependence on the photon energy E_γ (in GeV) of the form [A$^+$84]

$$\sigma(E_\gamma) = \sigma(39)\left(\frac{39}{E_\gamma}\right)^\alpha, \tag{7.55}$$

Selection	1^- (%)
-	-
$p_t^2 < 0.15$	-
$0.15 < p_t^2 < 0.5$	$5.3^{+45.8}_{-5.3}$
$0.15 < p_t^2 < 1$	$29.8^{+38.1}_{-29.8}$

Table 7.21: 1^- *contribution in the* $\omega\pi^0$ *final sample.* $|F_1|^2_{bkg} = 0.4$. *From* $H_s^+(2000)$.

Selection	$0.9 < m < 1.1$	$1.1 < m < 1.4$	$1.4 < m < 1.6$
-	-	$0.0^{+21.4}_{-0.0}$	$21.1^{+45.2}_{-21.1}$
$p_t^2 < 0.15$	0^{+11}_{-0}	-	$3.5^{+62.9}_{-3.5}$
$0.15 < p_t^2 < 0.5$	0^{+100}_{-0}	$70.2^{+29.8}_{-52.8}$	100^{+0}_{-100}
$0.15 < p_t^2 < 1$	0^{+35}_{-0}	$70.2^{+29.8}_{-42.3}$	100^{+0}_{-82}

Table 7.22: 1^- *percentage contribution in the* $\omega\pi^0$ *final sample.* $|F_1|^2_{bkg} = 0.4$. *From* $H_s^+(2000)$.

in the energy range $20 \leq E_\gamma \leq 70$ GeV. In the previous empirical formula the measured parameters are

$$\sigma(39) = 0.86 \pm 0.27\,\mu\text{b}, \tag{7.56}$$

$$\alpha = 0.6 \pm 0.2. \tag{7.57}$$

This behaviour is in contrast with two expectations for reaction mechanism involving either pure pomeron exchange, which should result in an increase of σ with energy, or pure reggeon exchange, which would require a faster decrease towards higher energies than the one observed.

Donnachie [Don05] has proposed an interpretation which involves both reggeon and pomeron exchange, not interfering with each other. In this context, the reggeon exchange mechanism is mainly associated with the production of the b_1, whereas the pomeron is completely associated to the production of a 1^- state.

Equation (7.55) can be rewritten [Don05] in term of W as

$$\sigma(W^2) = A(W^2)^{2\epsilon} + \frac{B}{(W^2)^{2\eta}}, \tag{7.58}$$

with the coefficients

$$\begin{aligned} A &= 0.107\,\mu\text{b}, \\ B &= 29.15\,\mu\text{b}, \end{aligned} \tag{7.59}$$

obtained from a fit of the available experimental data; the exponents are

Reaction	$\langle W \rangle$ [GeV]	1^- (%) [Ref.]
πp	7.1	≤ 10 [C$^+$75]
γp	6.2	≤ 10 [A$^+$84]
γp	8.6	≈ 20 [B$^+$88]
μp	13.5	42.1 ± 29.2 [this work]
		$77.2^{+22.8}_{-45.7}$ [this work]

Table 7.23: *Reaction type, mean energy range and 1^--contribution from past experiments and COMPASS data (the last entry refers to incoherent scattering only).*

[DK02]:

$$\epsilon = 0.08$$
$$\eta = 0.4525. \tag{7.60}$$

The first term on the right side in eq. (7.58) is the pomeron contribution which implies SCHC, as experimentally well known, whereas the second term, mainly associated to b_1 production, gives the reggeon contribution.

The transition $\gamma^* \rightarrow b_1$ violates the Gribov-Morrison rule, which requires that the change of spin ΔJ and the change in parity to be related as

$$P_{out} = P_{in}(-1)^{\Delta J}; \tag{7.61}$$

because of the opposite parities of the γ^* and b_1, ΔJ must be odd for photoproduction of the latter, and the process would also imply a spin flip at quark level. The (virtual) photon can be infact considered, as assumed in the Vector Meson Dominance (VMD) model, to consist of a $q\bar{q}$ pair in a triplet state, where the b_1 meson is a $q\bar{q}$ in a singlet state. Pomeron exchange is on the other side experimentally observed to conserve helicity at high degree and thus this would imply that the diffractive production of b_1 would go through spin-flip pomeron (thus non-SCHC) and/or reggeon exchange, and we may thus write for the cross section:

$$\sigma(\gamma^* p) \approx \sigma_{SCHC}(\rho') + \sigma_{spin-flip}(b_1) \tag{7.62}$$

The first term gives the cross section for 1^- production from SCHC pomeron exchange. Equation (7.58) has been verified up to HERA energies of $\langle W \rangle \approx 200$ GeV. If we apply it to the mean value $\langle W \rangle \approx 13.5$ GeV characteristic of COMPASS, we can foresee an almost equal contribution $\sigma(\rho') \approx \sigma(b_1)$ to the data. Data shown in the previous sections support such a scenario.

We can check the validity of these ideas in three different ways:

- inspection of the angle Φ-distribution: non-SCHC spin-flip contribution should cause anisotropy [GKS02];

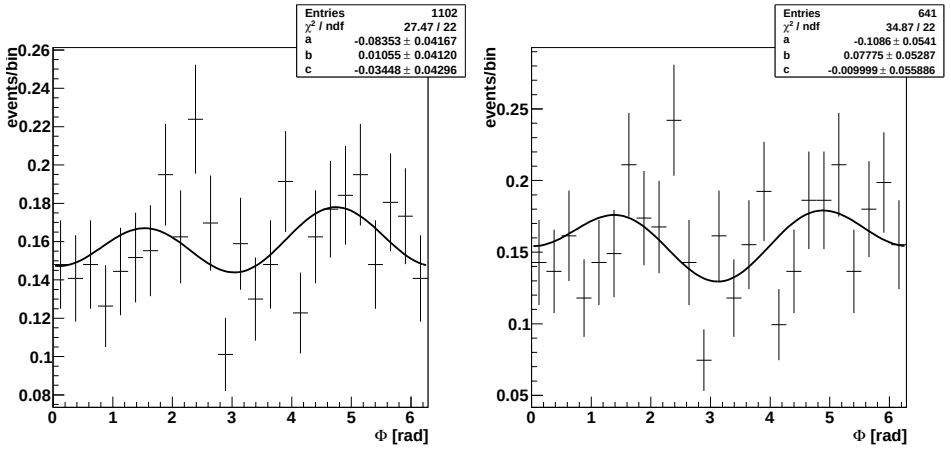

Figure 7.23: Φ-*distribution for final sample (left) and for events in the* $\omega\pi^0$*-peak region (right). Fit function as in eq.* (7.63).

- the SCHC contribution results in a modulation $\sim \cos 2\psi_V$ in the angular distribution ψ_V [B$^+$74];
- the $\cos\theta$ distribution must be forward-backward symmetric, since spin-flip and non-spin-flip contributions are incoherent, i.e. the $l = 1$ decay for 1^- state and the $l = 0, 2$ decay of b_1 do not interfere.

It is the purpose of the next sections to discuss these aspects.

7.4.1 Φ angular distribution

Figure 7.23 (left) reproduces the distribution for the angle Φ for the final sample. The data points have been fitted using the formula (1.35), pag. 9, which gives the expected distribution for vector meson leptoproduction, and which we rewrite in the simplified form:

$$I(\Phi) = \frac{1}{2\pi}(1 + a\cos 2\Phi + b\cos\Phi + c\sin\Phi). \tag{7.63}$$

In the same Figure (right) the contribution of the events in the final sample corresponding to the $\omega\pi^0$-peak region is shown together with the fit result from the same fit function. The dependence of the Φ-distribution on the standard p_t^2 and/or $m(\omega\pi^0)$ cuts have also been examined, and the values of the fitted parameters determined. In the majority of cases the contributions of $\cos\Phi$ and $\sin\Phi$ are not statistically significant, but in the central $m(\omega\pi^0)$ region a contribution is found at the 2σ-level.

This behaviour suggests to perform a second fit to the data, using the simplified formula derived from eq. (7.63) taking $b = c = 0$. The formula

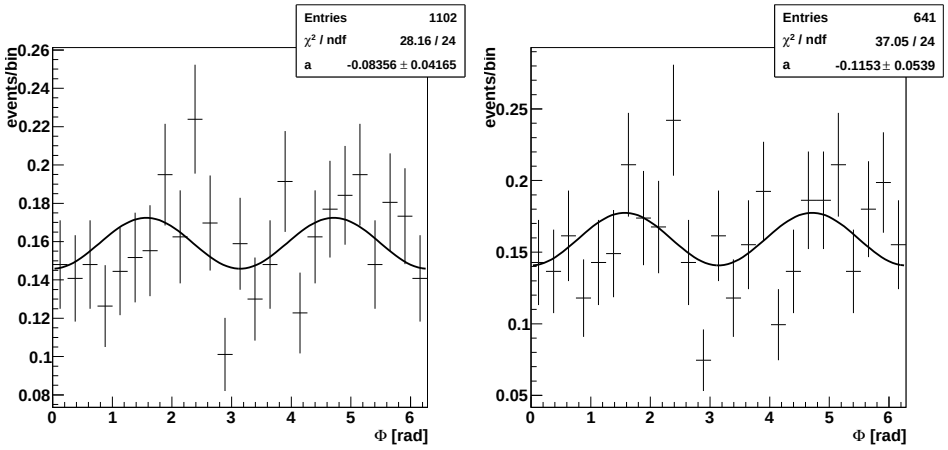

Figure 7.24: *Final sample angular distribution Φ (left), and for events in the $\omega\pi^0$-peak region (right). Fit function as in eq.* (7.64) *with $b = 0$ (parity conservation).*

Selection	a
-	-0.084 ± 0.043
$p_t^2 < 0.15$	-0.031 ± 0.053
$0.15 < p_t^2 < 0.5$	-0.180 ± 0.088
$0.15 < p_t^2 < 1$	-0.215 ± 0.077

Table 7.24: *Amplitude a (eq.* (7.64)*) of the* $\cos 2\Phi$ *modulation, p_t^2-dependence.*

thus obtained coincides with the general distribution in photoproduction [B$^+$88]:

$$I(\Phi) = \frac{1}{2\pi}(1 + a\cos 2\Phi + b\sin 2\Phi); \tag{7.64}$$

once the assumption of parity conservation, which implies $b = 0$, is taken into account, resulting in a single $\cos 2\Phi$ modulation. We obtain from our data the value

$$a = -0.084 \pm 0.042, \tag{7.65}$$

as can be seen in Figure 7.24. The minus sign is a consequence of the convexity/concavity of the fit curve, which best adapt to the experimental points. In the same Figure (right) the result $a = -0.115 \pm 0.054$ for the $\omega\pi^0$-peak region is shown.

As already done for the angle θ_H, the dependence on the $\omega\pi^0$-mass and p_t^2 was also examined, and numerical results for a are listed in Tables 7.24 and 7.25. These values show that, without applying the cut on the $\omega\pi^0$-mass, the amplitude a, i.e. the percentage violation of SCHC, grows with p_t^2: for coherent scattering the value is compatible with zero, which is indication

Selection	$0.9 < m < 1.1$	$1.1 < m < 1.4$	$1.4 < m < 1.6$
-	-0.003 ± 0.126	-0.115 ± 0.057	0.032 ± 0.100
$p_t^2 < 0.15$	0.346 ± 0.160	-0.086 ± 0.070	-0.144 ± 0.131
$0.15 < p_t^2 < 0.5$	-0.149 ± 0.278	-0.153 ± 0.126	-0.056 ± 0.217
$0.15 < p_t^2 < 1$	-0.355 ± 0.236	-0.241 ± 0.112	0.059 ± 0.178

Table 7.25: *Amplitude a of the $\cos 2\Phi$ modulation, $m(\omega\pi^0$-mass- and p_t^2-dependence.*

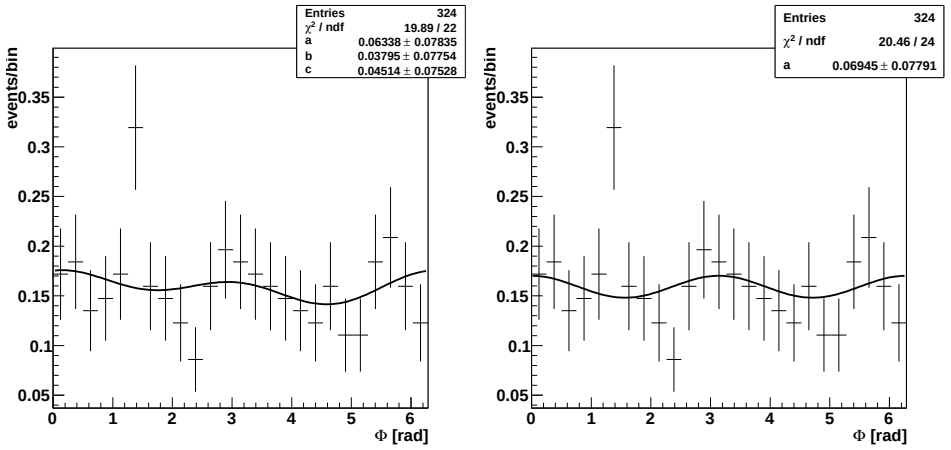

Figure 7.25: *Φ-distribution for non-exclusive events within 10 GeV $< E_{miss} <$ 20 GeV. Fit as for electro- (left) and photoproducton (right), with conservation of parity assumed.*

of an s-channel helicity conserving production mechanism, whereas for incoherent scattering off quasi-free nucleons, the SCHC-violating contribution is in the range 10-20 % at the 1σ-level.

If, on the other hand, we consider the $\omega\pi^0$-mass dependence only, we see that near threshold and for the mass window right to the peak region, a is again compatible with zero, whereas in the peak region itself a value of the order 6-16 % (1σ-level) is observed.

The presence of background has not been discussed so far. If we make the assumption that the Φ-distribution corresponding to non-ω-related events is flat (the same distribution for non-exclusive $\omega\pi^0$ events in the range 10 GeV $< E_{miss} <$ 20 GeV which, as previously seen, is characterized by a flat λ-distribution, is indeed flat also for Φ, as seen in Figure 7.25, right, giving a fit value $a = 0.069 \pm 0.078$, compatible with zero), then we can estimate the corrected value a_{corr} from the already measured percentage contribution of non-ω related events in the exclusive sample (for these values, see Tables 7.6 and 7.7). In addiction, the Φ-distribution for exclusive $(\pi^+\pi^-\pi^0)\pi^0$ events in the side bands to the ω-peak, is shown in Figure 7.26. A deviation from

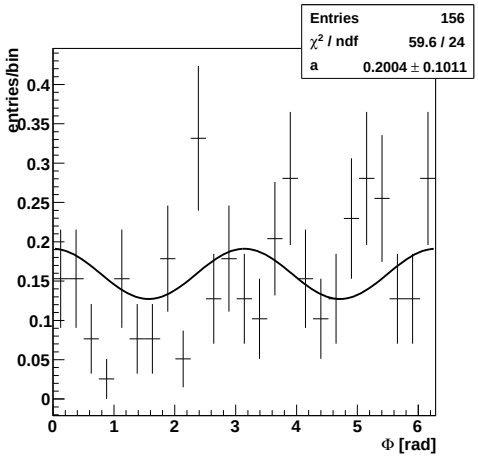

Figure 7.26: Φ-*distribution for events in the* ω*-peak side bands.*

flatness of the order of 20.0 ± 10.1 % is present at the 1σ-level.

We may thus write:

$$(1-b)\cdot a_{corr} + b \cdot a_{bkg} = a, \tag{7.66}$$

where a_{bkg} is the value ascribed to the background component, and b its relative contribution. This leads to the result

$$a_{corr} = \frac{a - b \cdot a_{bkg}}{1-b}, \tag{7.67}$$

and, taking $a_{bkg} = 0$:

$$a_{corr} = a \cdot \frac{1}{1-b}. \tag{7.68}$$

The corresponding new error Δa_{corr} can be calculated from the error propagation law

$$\Delta a_{corr} = \sqrt{\left(\frac{\partial a_{corr}}{\partial a}\right)^2 (\Delta a)^2 + \left(\frac{\partial a_{corr}}{\partial b}\right)^2 (\Delta b)^2} \tag{7.69}$$

with partial derivatives

$$\frac{\partial a_{corr}}{\partial a} = \frac{1}{1-b}, \tag{7.70}$$

$$\frac{\partial a_{corr}}{\partial b} = \frac{a - a_{bkg}}{(1-b)^2}. \tag{7.71}$$

The last derivative reduces to

$$\frac{\partial a_{corr}}{\partial b} = \frac{a}{(1-b)^2} \tag{7.72}$$

Selection	a_{corr}
-	-0.102 ± 0.051
$p_t^2 < 0.15$	-0.039 ± 0.064
$0.15 < p_t^2 < 0.5$	-0.209 ± 0.095
$0.15 < p_t^2 < 1$	-0.238 ± 0.079

Table 7.26: *Amplitude of the* $\cos 2\Phi$ *modulation, corrected for background;* p_t^2*-dependence.*

Selection	$0.9 < m < 1.1$	$1.1 < m < 1.4$	$1.4 < m < 1.6$
-	-0.003 ± 0.127	-0.136 ± 0.064	0.032 ± 0.092
$p_t^2 < 0.15$	0.455 ± 0.189	-0.102 ± 0.079	-0.154 ± 0.120
$0.15 < p_t^2 < 0.5$	-0.257 ± 0.626	-0.154 ± 0.108	-0.129 ± 0.430
$0.15 < p_t^2 < 1$	-0.480 ± 0.323	-0.235 ± 0.090	0.062 ± 0.205

Table 7.27: *Amplitude of the* $\cos 2\Phi$ *modulation, corrected for background;* $\omega\pi^0$*-mass- and* p_t^2*-dependence.*

for $a_{bkg} = 0$. We have not studied the dependence of the a_{bkg} on the p_t^2 and $\omega\pi^0$-mass, so we will take the constant value $a_{bkg} = 0.200 \pm 0.101$.

The values a_{corr} with their dependence on p_t^2 and/or $m(\omega\pi^0)$ are listed in Tables 7.26 and 7.27. Subtracting a constant contribution to the data, obviously increases the value of a_{corr} with respect to the corresponding a, as observed in the Tables.

The conclusion from the angle Φ distribution: the data reveal the presence of a non-SCHC contribution, which seems to be characteristic of the incoherent scattering off quasi free nucleons rather than the coherent scattering off the nucleus, whose corresponding values are small and/or consistent with zero. The non-s-channel-helicity conserving production characterizes also the $\omega\pi^0$-peak region, growing in intensity together with p_t^2. In the peak region and for incoherent scattering we observe a violation of the order $15.4 \pm 10.8\%$, compatible with the presence of a SCHC violating production of b_1. The contribution for SCHC from b_1 is negligible, as can be seen by inspection of the $\cos\theta_A$ distribution (see section 7.4.4, pag. 148).

7.4.2 ψ_V angular distribution

In this section we show the results obtained for the azimuthal orientation ψ_V of the spin analyzer $\boldsymbol{V}$ defined in Section 5.4, pag. 65, for the case of a $J^P = 1^-$ assignment to the $\omega\pi^0$ system.

Tables 7.28 and 7.29 resume the results of the various fit to the experimental data (shown in Appendix G) from the expected fit function

$$I(\psi_V) = \frac{1}{N} \cdot \frac{dN}{d\psi_V} = \frac{1}{2\pi}(1 + \alpha \cos 2\psi_V). \tag{7.73}$$

Selection	α (%)
-	20.9 ± 4.4
$p_t^2 < 0.15$	24.2 ± 5.4
$0.15 < p_t^2 < 0.5$	7.7 ± 9.5
$0.15 < p_t^2 < 1$	16 ± 8

Table 7.28: *Fit results for α from ψ_V angular distribution.*

Selection	$0.9 < m < 1.1$	$1.1 < m < 1.4$	$1.4 < m < 1.6$
-	0.8 ± 14.1	22.9 ± 5.7	40.4 ± 10.1
$p_t^2 < 0.15$	-11.0 ± 16.2	27.6 ± 7.0	51.5 ± 13.2
$0.15 < p_t^2 < 0.5$	-10.5 ± 26.3	9.2 ± 15.4	12.3 ± 22.0
$0.15 < p_t^2 < 1$	5.0 ± 23.8	16.5 ± 12.2	35.9 ± 18.5

Table 7.29: *Fit results for α from ψ_V angular distribution: p_t^2- and $\omega\pi^0$-mass-dependence.*

Data points for ψ_V were at first rescaled, in order to have a normalized integral of the fit function. Error bars in each bin have been also rescaled, to preserve the relative errors in each bin. As an example, Figure 7.27 shows the final sample ψ_V distribution (left) together with the corresponding distribution relative to the $\omega\pi^0$-peak subsample (right).

If we interprete the parameter α as a indicator of the amount of SCHC-contribution in the data, we obtain a value compatible with ∼20%. A more detailed study of the dependence on the $\omega\pi^0$-mass shows that near threshold α is compatible with 0, and this behaviour independent of p_t^2; in addition, SCHC production mechanisms becomes more important with increasing $\omega\pi^0$-mass. In the peak region this contribution reaches ∼23 % mean value.

The dependence on p_t^2 does not change the conclusion in the low mass range. A possible distinction seems to appear for the two cases of coherent and incoherent scattering: in the first case ($p_t^2 < 0.15$ (GeV/c)^2), data clearly show an s-channel helicity conserving production mechanism, which for the high $\omega\pi^0$-mass window can be as high as ∼40-60 %, whereas for incoherent production on the quasi-free nucleons (0.15 (GeV/c)$^2 < p_t^2 < 0.5$ (GeV/c)^2) this behaviour is absent in the peak region, and is compatible with at most a few percent contribution in the higher mass range. This conclusion is somewhat relaxed if one allows a higher upper limit $p_t^2 < 1$ (GeV/c)^2. One must always keep in mind the effect of the limited statistic in the first case, and the possible contribution of non exclusive events in the latter.

As done for the angle Φ, also the possible contribution from non-ω background in the exclusivity peak region has been inspected, assuming its behaviour similar as in the non exclusive side band between 10 and 20 GeV.

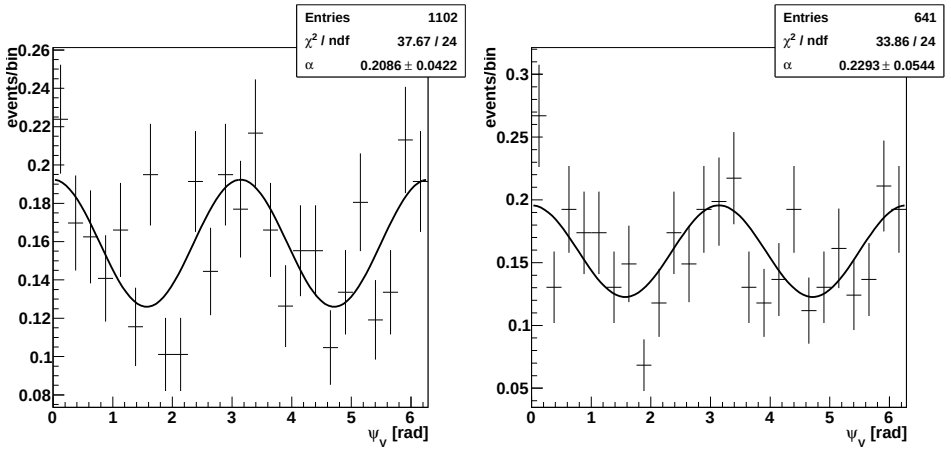

Figure 7.27: *Final sample ψ_V-distribution (left) and within the $\omega\pi^0$-peak window (right). No p_t^2-cut applied.*

Selection	α (%)
-	27.9 ± 5.8
$p_t^2 < 0.15$	33.0 ± 7.5
$0.15 < p_t^2 < 0.5$	10.7 ± 11.4
$0.15 < p_t^2 < 1$	18.8 ± 9.2

Table 7.30: *Fit results for α from ψ_V angular distribution. Corrected for background.*

The result of the fit are shown in Figure 7.28 (left), and for the subsample in the $\omega\pi^0$-peak window (right). As can be seen, the data are in both cases consistent with a uniform distribution.

The same distribution but for the exclusive events in the previously defined side bands to the ω-peak is shown in Figure 7.29. The anisotropy is of the order of 9 ± 10 %, thus showing no significant deviation from flatness.

If we proceed as in the previous section, taking for background a value $\alpha = -0.08867 \pm 0.10155$ as obtained from the data in Figure 7.29 and for the amount of background the values evinced from the λ distribution, we obtain the background corrected values for ψ_V now listed in Tables 7.30 and 7.31.

Generally, the values after correction are bigger than before, the difference being neglectable in the interesting p_t^2- and $m(\omega\pi^0)$-windows, which, as we saw, are characterized by a lower contamination from background and higher statistic.

We conclude that the already calculated values for α give an already realistic estimate of the SCHC contribution to the $\omega\pi^0$ signal in the regions of interest. Better precision is of course reached by using the correct(ed)

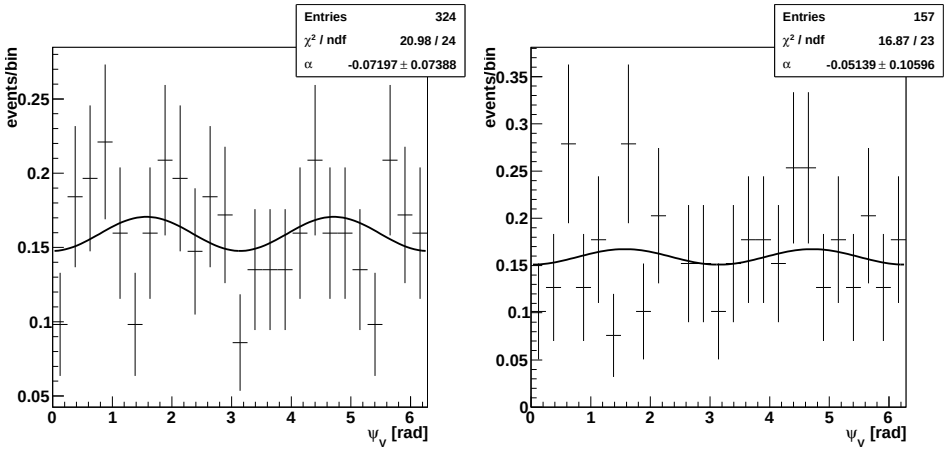

Figure 7.28: ψ_V-*distribution for non exclusive events within* 10 *GeV* $< E_{miss} <$ 20 *GeV (left) and* $\omega\pi^0$*-peak window (right).*

Selection	$0.9 < m < 1.1$	$1.1 < m < 1.4$	$1.4 < m < 1.6$
-	4.0 ± 18.9	28.8 ± 7.2	$40.4^{+11.4}_{-10.1}$
$p_t^2 < 0.15$	-12.0 ± 23.7	35.6 ± 9.5	$57.5^{+18.6}_{-16.0}$
$0.15 < p_t^2 < 0.5$	$-14.8^{+95.1}_{-95.4}$	$9.3^{+15.7}_{-15.5}$	39.1 ± 59.7
$0.15 < p_t^2 < 1$	18.0 ± 49.6	$16.5^{+12.3}_{-12.2}$	51.4 ± 31.4

Table 7.31: *Fit results for* α *from* ψ_V *angular distribution:* p_t^2*- and* $\omega\pi^0$*-mass-dependence. Corrected for background.*

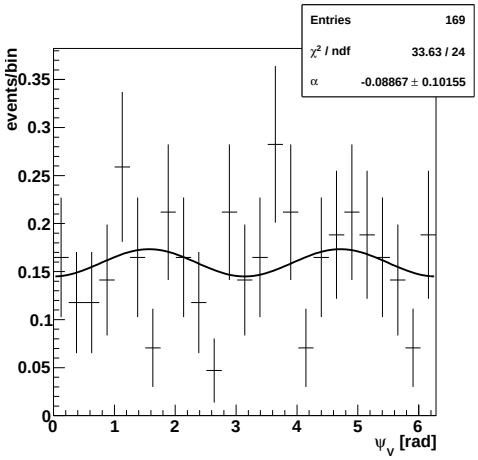

Figure 7.29: *ψ_V-distribution for exclusive events in the side bands to the ω-peak.*

values.

We can thus estimate the SCHC at the level of 22-33% for the whole final sample, and 22-35% in the $\omega\pi^0$-peak region (at the 1σ-level).

7.4.3 The angle θ

Particular attention was paid to the acceptance correction for the angle θ. Figure 7.30 shows the reconstructed distribution for the final sample (top-left), the reconstructed $\omega\pi^0$ events from MC data corresponding to two isotropically generated subsequent decays $\omega\pi^0 \to \omega + \pi^0 \to (\pi^+\pi^-\pi^0) + \pi^0$ (top-right), and the real data after acceptance correction, performed on a bin-by-bin basis (bottom-left). For the i-th bin, the acceptance

$$A_i = \frac{N_i^{reco}}{N_i^{gen}} \tag{7.74}$$

has been calculated from reconstructed and generated MC data, and the final distribution after correction was determined from the formula

$$N_i^{corr} = \frac{N_i}{A_i} = \frac{N_i N_i^{gen}}{N_i^{reco}}. \tag{7.75}$$

In the previous formulae, N_i^{reco} is the i-th bin content for reconstructed MC data, N_i^{gen} the corresponding quantity but for MC generated data, N_i the corresponding bin content for real data, and N_i^{corr} the acceptance corrected value. The errors in the acceptance corrected distribution have been calculated using the error propagation law, which for formula (7.75)

reads[11]

$$\frac{\Delta N_i^{corr}}{N_i^{corr}} = \sqrt{\left(\frac{\Delta N_i}{N_i}\right)^2 + \left(\frac{\Delta N_i^{reco}}{N_i^{reco}}\right)^2}. \tag{7.76}$$

In addition, Figure 7.30 shows the forward-backward asymmetry for the $\cos\theta$ distribution. Defining F_i and B_i as the bin contents in i-th forward and backward bin, symmetrical to the central value $\cos\theta = 0$, respectively ($i = 1, 2, \ldots, 13$; the $\cos\theta$ plots were subdivided into 26 bins), the following quantity has been calculated:

$$A_{FB}^i = \frac{F_i - B_i}{F_i + B_i}. \tag{7.77}$$

Once more, the corresponding errors δA_{FB}^i are obtained applying the error propagation law, with the resulting expressions for partial derivatives:

$$\frac{\partial A_{FB}^i}{\partial F_i} = \frac{2B_i}{(F_i + B_i)^2}, \tag{7.78}$$

$$\frac{\partial A_{FB}^i}{\partial B_i} = -\frac{2F_i}{(F_i + B_i)^2}. \tag{7.79}$$

A graphical representation of the results is shown in Figure 7.30 (bottom-right); Figure 7.31 shows the same plots for events within the $\omega\pi^0$-peak region.

7.4.4 The angle θ_A

Finally, the $\cos\theta_A$ distribution for the final sample can be seen in Figure 7.32. It has been fitted using the formula

$$\begin{aligned} I(\cos\theta_A) &= I^+(\cos\theta_A) + I^-(\cos\theta_A) = \\ &= \alpha(1 - \cos^2\theta_A) + \beta(1 + \cos^2\theta_A), \end{aligned} \tag{7.80}$$

where the first term refers to the distribution expected for a pure 1^+ state, whereas the second term is the contribution of the pure 1^- state in case of SCHC. The fit results after normalization:

$$\begin{aligned} \alpha &= 0.000^{+0.031}_{-0.000}, \\ \beta &= 0.378 \pm 0.022, \end{aligned}$$

The normalization condition for eq. (7.80) gives:

$$\frac{4}{3}\alpha + \frac{8}{3}\beta = 1. \tag{7.81}$$

[11] The formula is correct if and only if $N_i^{reco} \ll N_i^{gen}$, as is the case in the present work, the ratio reco/gen being lower than 1%.

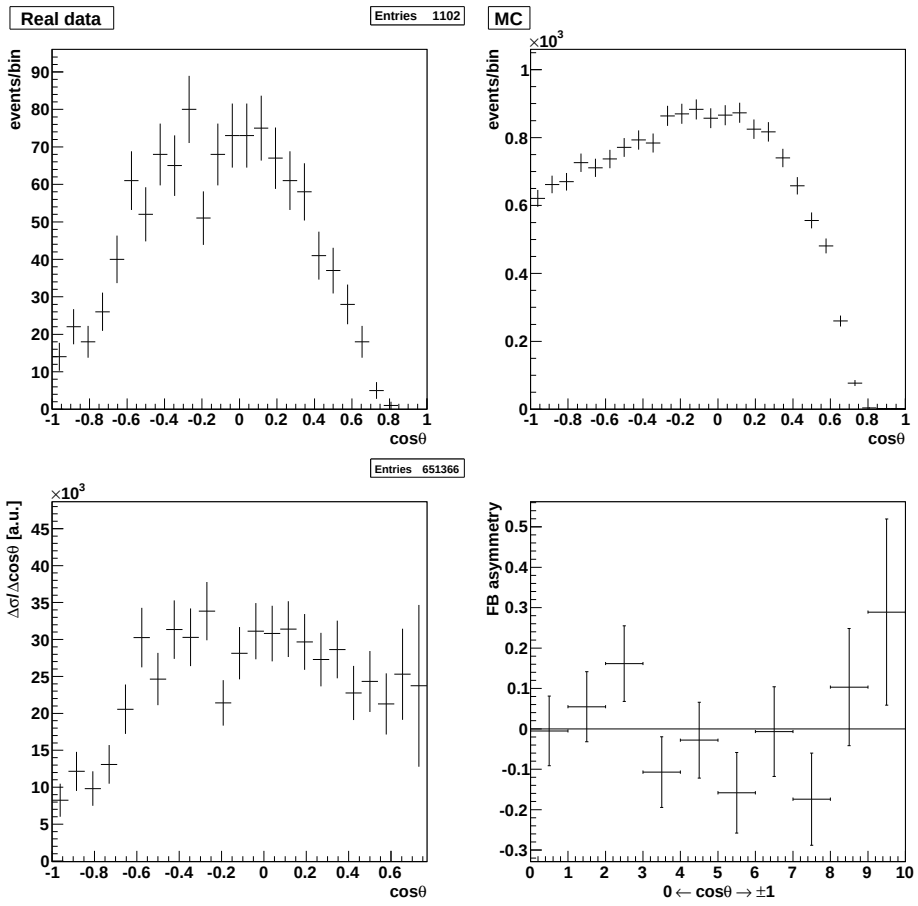

Figure 7.30: *Real data, MC reconstructed events, acceptance corrected final sample and* A^i_{FB}.

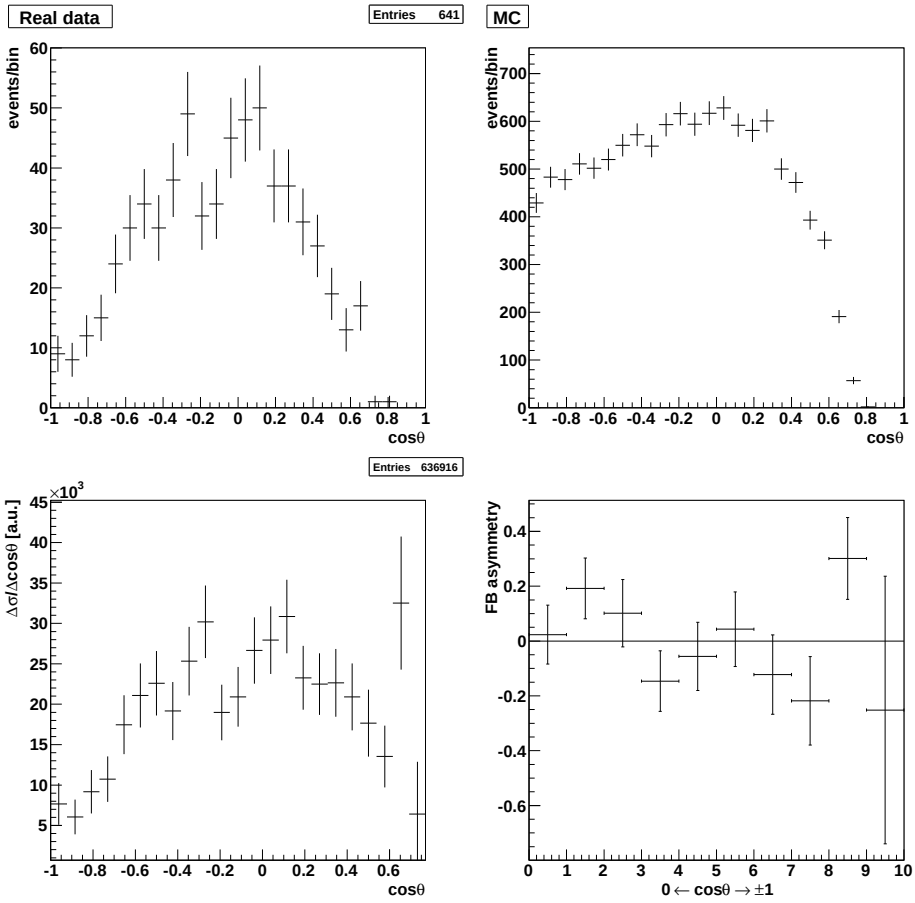

Figure 7.31: *As in Figure 7.30, but for events within the $\omega\pi^0$-peak region.*

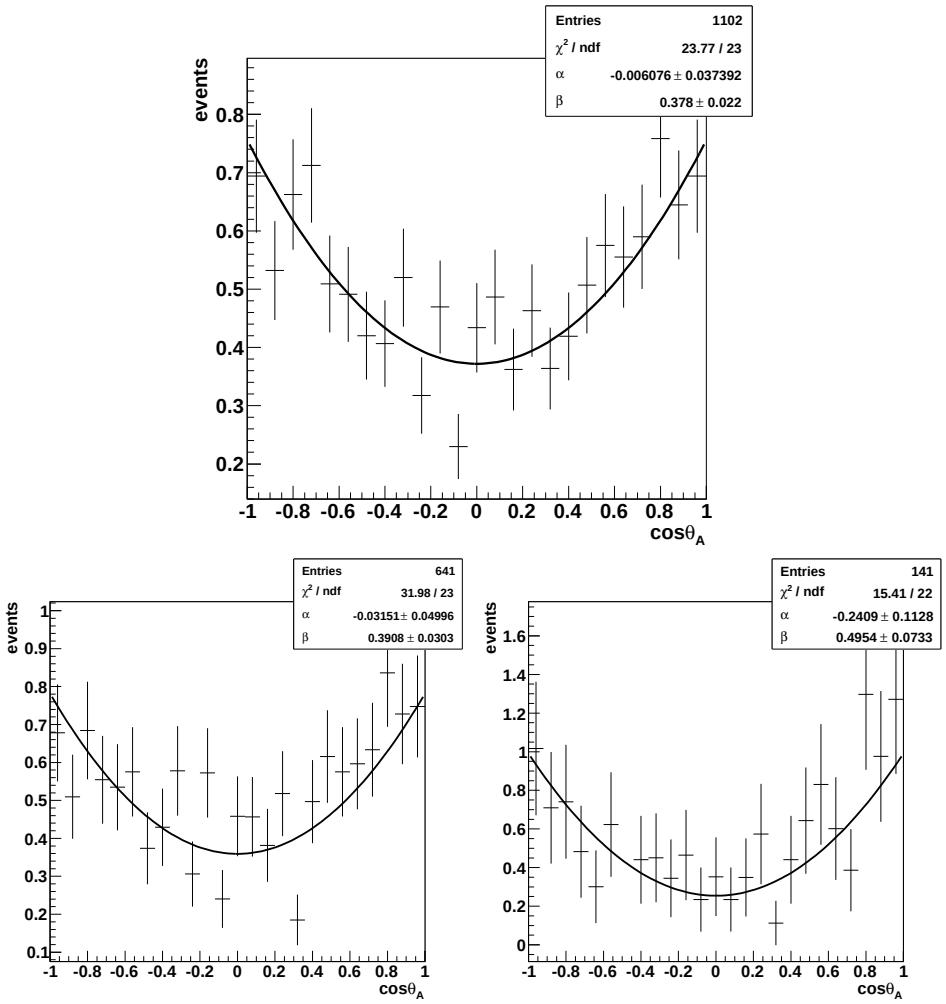

Figure 7.32: *Acceptance corrected* $\cos\theta_A$ *distribution (normalized) for the final sample (top) and in the* $\omega\pi^0$*-peak region with (right) and without the incoherent scattering selection cut on* p_t^2*. Assuming the validity of SCHC, data are compatible with a dominance of the* 1^- *contribution (*1^+ *upper limit:* 4.2% *(*2.5% *in the peak,* 0.0% *for incoherent scattering)).*

Taking this into account, we see that the data clearly show a dominance of the cosinus (second term in eq. (7.80)) over the sinus component. Assuming SCHC, this implies a dominant 1^- contribution, in accord to earlier results of ref. [A$^+$80]. We are thus lead to the conclusion that no $b_1(1235)$ is produced conserving helicity (from the fit values and eq. (7.81), we estimate a 4.2% upper limit for a 1^+ state, which reduces to 2.5% in the $\omega\pi^0$-peak region), thus proving the s-channel helicity conserving yield mainly due to an $\omega\pi^0$ system in the 1^- state.

Chapter 8

Conclusion

Unfortunately the decay $B^0 \to \omega\pi^0$
is extremely difficult to observe,
as therefore also is the helicity of the B.
F. J. Gilman *et al.*, 1970[1]

In the previous chapters we have discussed the analysis made on COMPASS data taken during the year 2004 and 2006 campaigns of the scattering of a polarized muon beam of 160 GeV/c momentum impinging against a polarized ^{6}LiD target and subsequent production of an $\omega\pi^0$ system, decaying via the chain $\omega\pi^0 \to \omega + \pi^0 \to (\pi^+\pi^-\pi^0) + \pi^0$. The exclusive sample has been clearly seen in the $\pi^+\pi^-\pi^0\pi^0$ invariant mass spectrum once the cut corresponding to the ω mass is applied to the $\pi^+\pi^-\pi^0$ subsystem. This sample is affected by a non-ω related background contamination, which shows also traces of a competing exclusive $\rho^+\rho^-$ production. The background amounts to 19$\pm$4% of the whole final sample statistics, 16$\pm$6% in the $\omega\pi^0$-peak region ($1.1 < m(\omega\pi^0) < 1.4$ GeV/c^2), decreasing to a value $< 11\%$ for incoherent scattering (in peak).

The dynamic of the reaction is characterized by low $\langle x_B \rangle$ and $\langle Q^2 \rangle$ (quasi real photoproduction); the numerical values, together with those for the center-of-mass energy in the $\gamma^* N$ rest frame $\langle W \rangle$ and the exchanged momentum squared t (which follows an exponential decay with slope b, consistent with a diffractive production mechanism) are resumed in Table 8.1. The value for the b is in accord with those found in the literature for photoproduction (see, e.g., ref. [A$^+$84]).

The final sample statistics is highly reduced mainly because of the geometrical and overall acceptance of the calorimetry (we limit for 2006 data to ECAL2 only, in order to ease the comparison with the 2004 data): a

[1] From [GPSS70]. B^0 is, in the old notation, the neutral component of the isospin triplet ($I = 1$) of the $J^P = 1^+$ state, i.e. the $b_1(1235)$.

$\langle x_B \rangle$	10^{-3}
$\langle Q^2 \rangle$	10^{-1} (GeV/c^2)^2
$\langle W \rangle$	13.5 GeV
b	5.27 ± 0.29 GeV^{-2}

Table 8.1: *Kinematics of the polarized leptoproduction reaction* $\mu + N \rightarrow \mu' + \omega\pi^0 + N$ *at COMPASS.*

Monte Carlo simulation shows an overall factor $\sim 0.5\%$ for the ratio of reconstructed over generated events.

A performance study for ECAL2 has been made, considering exclusive ω production for simplification. The time (period) dependence study was also performed. The major source of background under the π^0-peak in the $\gamma\gamma$ invariant mass spectrum is due to *few bad performing crystals*, which fire up to 10^2-10^3 more often than neighbouring ones; most of them are *associated to low-energy clusters and/or to clusters reconstructed with a low number of crystals*. In addition, examining the crystal dependence and contribution to the $\gamma\gamma$ spectrum, it has been possible to demonstrate that *the inaccuracies of the energy calibration relative to the single crystal are not the main source of the experimental* π^0 *width*.

The main goal of the thesis has been the quantitative determination of the possible presence of a $J^P = 1^-$ contribution in the $\omega\pi^0$ signal. This has been performed inspecting the various angular distributions which characterize the decay of an $\omega\pi^0$ system in the various helicity frames in the decay chain. The issue of s-channel-helicity conservation (SCHC) has been also analyzed.

Angular distributions are very sensitive to acceptance effects, thus requiring a precise determination of the resulting distortions. A stand-alone Monte Carlo generator for isotropically produced and decaying $\omega\pi^0$ system has been written from scratch. In addition, the dependence of the acceptance on the $\omega\pi^0$ mass and λ distribution has been studied, *confirming the interpretation of the enhancement seen (the* b_1 *region) as a true phenomenon and not an artifact due to acceptance.*

The spin-parity study has followed two different paths:

i) the method of the moments $H(lmLM)$ (and some of their linear combinations);

ii) the fit method, involving the angular distribution $\cos\theta_H$.

In both cases, the $\omega\pi^0$-mass- and p_t^2-dependence has been also examined. Particular attention has been paid to results in the $\omega\pi^0$-peak region, where the statistics is high enough to increase the precision of the results at a significative level. Corrections due to acceptance and for the background contamination in the final sample have been also applied.

Selection	$\|F_1\|^2_{corr}$	$J^P = 1^-$ (%)
$\omega\pi^0$ final sample	0.438 ± 0.013	< 20
$\omega\pi^0$ peak region	0.467 ± 0.016	42 ± 29
$\omega\pi^0$ peak region & incoherent scattering	$0.487^{+0.026}_{-0.020}$	$77.2^{+22.8}_{-35.2}$

Table 8.2: $|F_1|^2_{corr}$ *and* 1^- *percentage contribution for the* $\omega\pi^0$ *final sample and subsamples of major interest.*

The two moments $\Delta_{1^+}(20)$ and $\Delta_{1^-}(20)$ show *the incompatibility with the hypothesis of the presence of* only *one spin-parity assignment to the resonance observed*: infact, both Δ's differ from zero in the peak region. In particular, for incoherent scattering, the $|F_0|^2$ values near zero strongly point towards the presence of a natural spin-parity $J^P = 1^-$ contribution, which seems to be suppressed in the coherent scattering region, where a dominance of 1^+ (from b_1) may explain the data.

Concerning production, the two spin matrix elements ρ^+_{00} and ρ^-_{00} for a $\omega\pi^0$ system produced in an helicity state 0 and parity $+1$ or -1, respectively, give results resembling those of ref. [A$^+$84], with low values for ρ^-_{00}, *compatible with a preferred production in helicity states* ± 1 *for the* 1^- *state.*

Turning to the fit of the $\cos\theta_H$ distribution, the values $|F_1|^2$ (corrected for background) have been determined and used to calculate the 1^- contribution to the signal. The results are listed in Table 8.2. Numerical values obtained from the moments $H(lmLM)$ are compatible with the listed ones within uncertainties. The values obtained for the peak region (with and without the selection of events produced by incoherent scattering) *give evidence for a* 1^- *contribution*, even if the relative errors are admittedly high. The relative 1^- contribution is *in accord with expectations of an approximately equal contribution for* 1^+ *and* 1^- from a model [Don05] for production involving non-interfering pomeron and reggeon exchange at the energies available at COMPASS ($\langle W \rangle \sim 13.5$ GeV). Within this scenario, the pomeron is associated to 1^- production via SCHC, whereas the reggeon exchange is mostly involved in 1^+ production of b_1. That the two *are not interfering* is shown by the forward-backward asymmetry in the $\cos\theta$ distribution: *the measured value is consistent with 0.*

Turning to the SCHC issue, the analysis of the Φ angular distribution shows a modulation of the order of $10 \pm 5\%$ in the final sample, and $15 \pm 11\%$ in the peak region for incoherent scattering. *These are deviations from the flatness expected for an SCHC-mechanism*; nevertheless, in the incoherent scattering regime, where the contribution of the 1^--state is higher, the flatness condition is fulfilled within the 2σ-level.

That the 1^+*-state* (b_1) *contribution is* not *produced conserving helicity* is demonstrated by the $\cos\theta_A$ distribution: *with the assumption of SCHC, data require a dominant* 1^- *contribution.* A 4.2% upper limit (2.5% in the

peak region) for the 1^+-state SCHC contribution can be extracted.

In addition, the orientation of the spin analyzer associated to $J^P = 1^-$ relative to the muon scattering plane and described by the angle ψ_V, shows a $\cos 2\psi_V$ modulation of the order of $30 \pm 7\%$ in the peak region, though decreasing to $9^{+16}_{-9}\%$ for incoherent scattering. The presence of this modulation proves the *existence of a SCHC mechanism for* $J^P = 1^-$, $\omega\pi^0$-*production* in the data.

At the end of this work, we can make some suggestions for a further improvement in the analysis of the $\omega\pi^0$ channel in leptoproduction at COMPASS, dictated from the experience gained. In particular, we consider the following points important:

i) improvement of the neutral cluster selection procedure, to avoid large combinatorial background, thus gaining higher purity for the final sample;

ii) improvement in statistics of the $\omega\pi^0$ final sample performing the analysis also of the newly produced 2007 data;

iii) data analysis with the information from ECAL1, even if it is now well known that this calorimeter's performance was not optimal in year 2006. Situation has improved during 2007.

In addition, the study of the recent hadron data, taken during year 2008 with a charged pion beam impinging against a liquid hydrogen target, may show elements of interest: the "historical" channel $\pi^\pm + p \to \omega\pi^\pm + p$ may lead, due to COMPASS' high statistics capabilities, to improvement in the precision of the already available data.

But for the author of this thesis it is time to stop here.

Appendix A

Year 2004 and 2006 results

In this appendix, some of the results shown in the main part of this thesis and concerning the whole final sample are illustrated in their dependence on the year of data taking (2004 and 2006). No quantitative consideration are put forth. For a definition of the represented quantities, see the main text part of the present work.

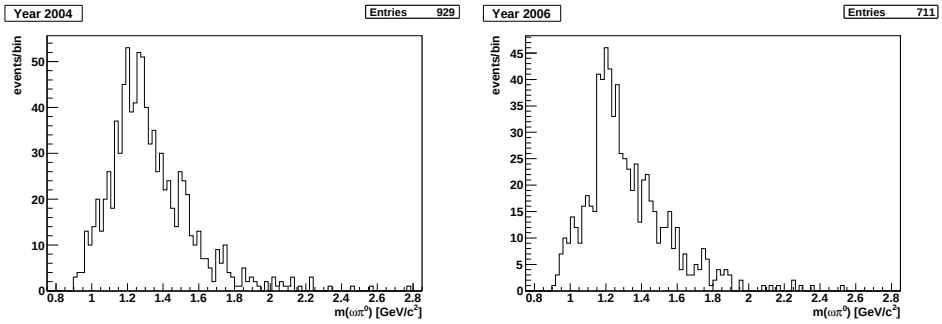

Figure A.1: $\omega\pi^0$-*mass (not acceptance corrected).*

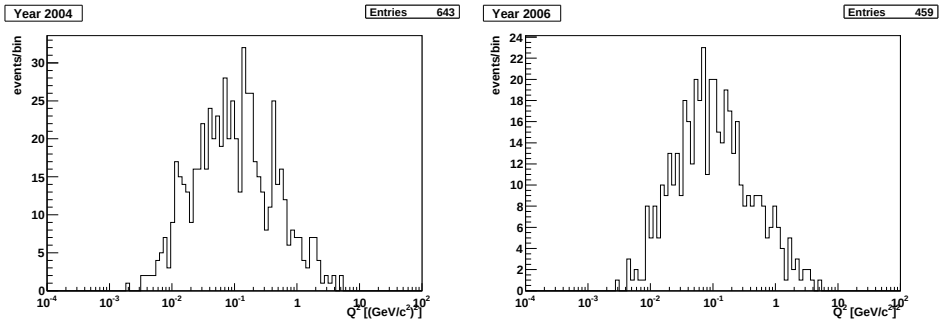

Figure A.2: Q^2-*distribution.*

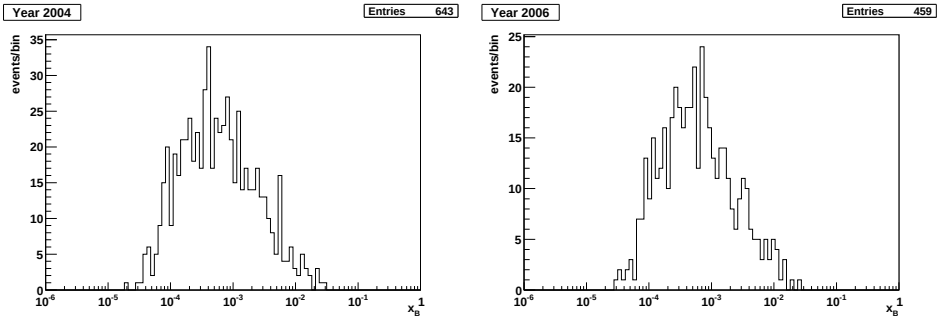

Figure A.3: x_B-*distribution.*

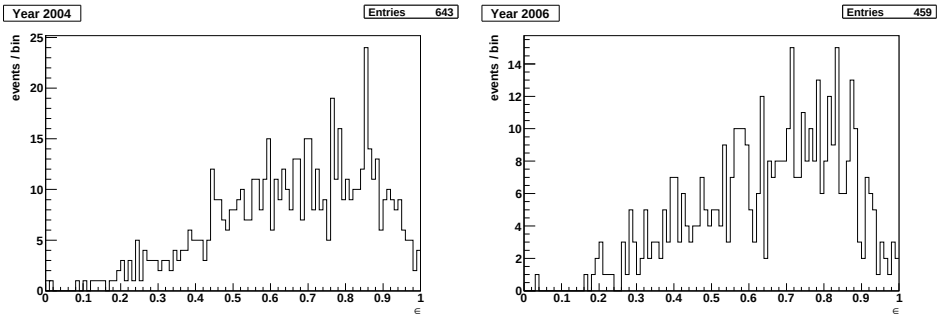

Figure A.4: ϵ-*distribution.*

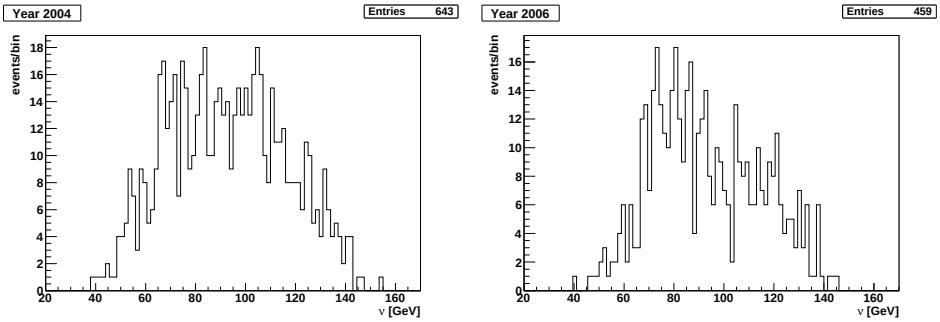

Figure A.5: ν-*distribution.*

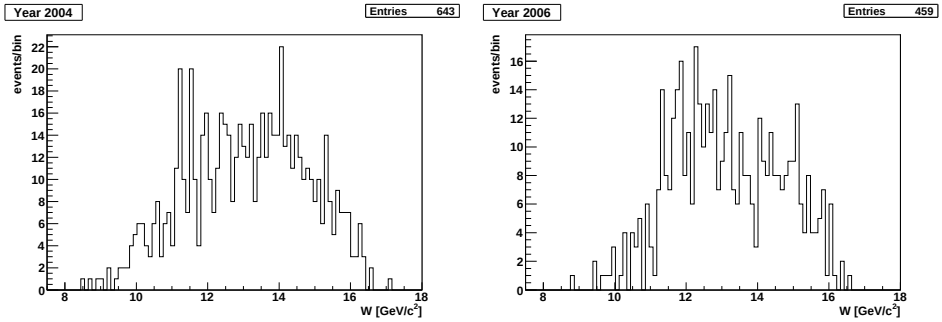

Figure A.6: $\gamma^* p$ *center-of-mass energy* W.

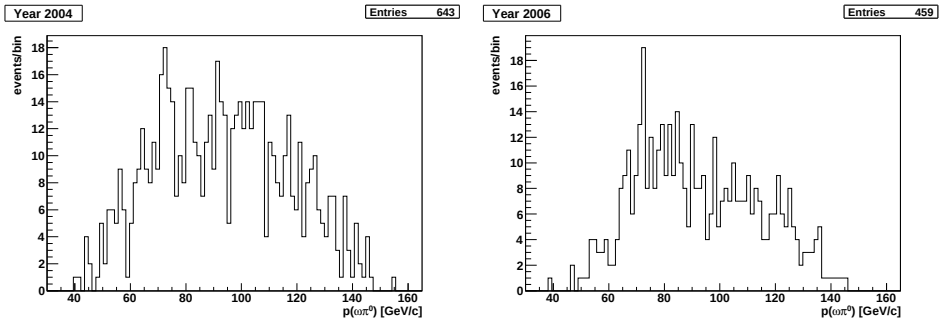

Figure A.7: $\omega\pi^0$*-momentum distribution in the laboratory system.*

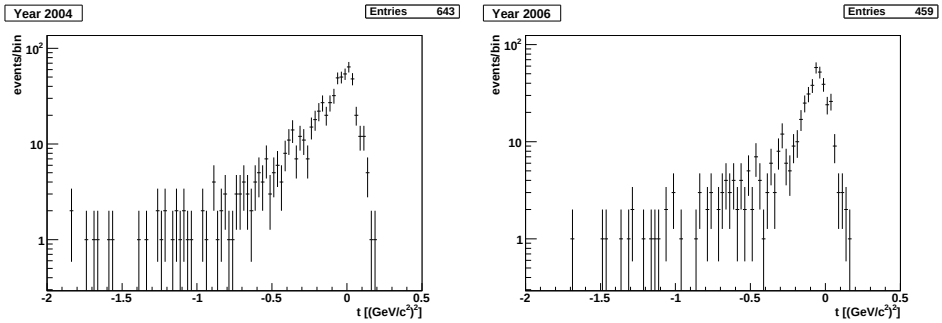

Figure A.8: *t-distribution.*

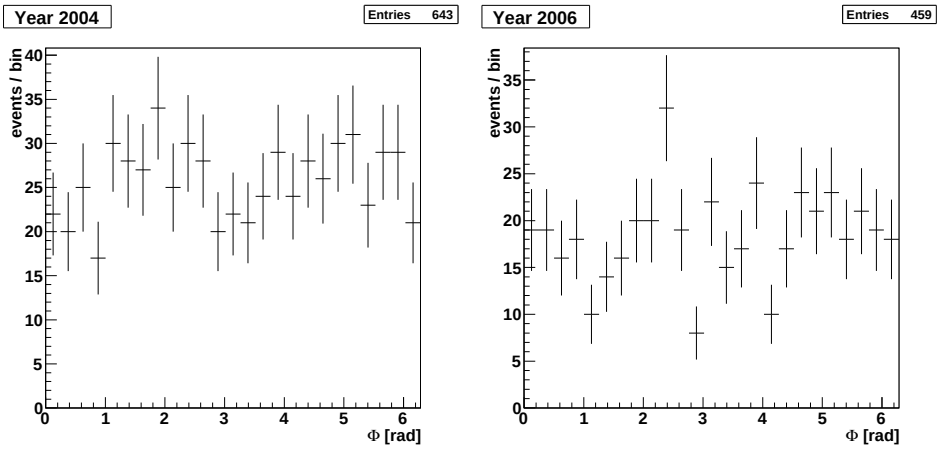

Figure A.9: *Azimuthal orientation Φ between scattering and production plane for $\omega\pi^0$ final sample; year 2004 (left) and 2006 (right).*

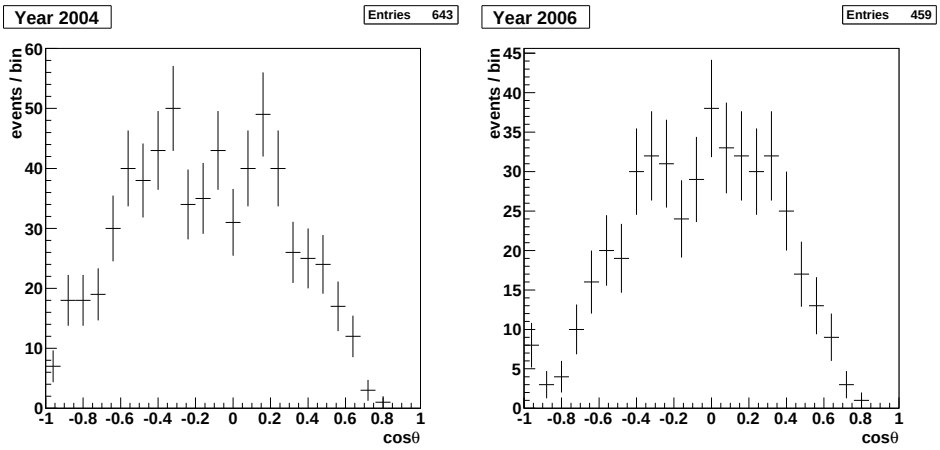

Figure A.10: $\cos\theta$ *distribution for $\omega\pi^0$ final sample for year 2004 (left) and 2006 (right).*

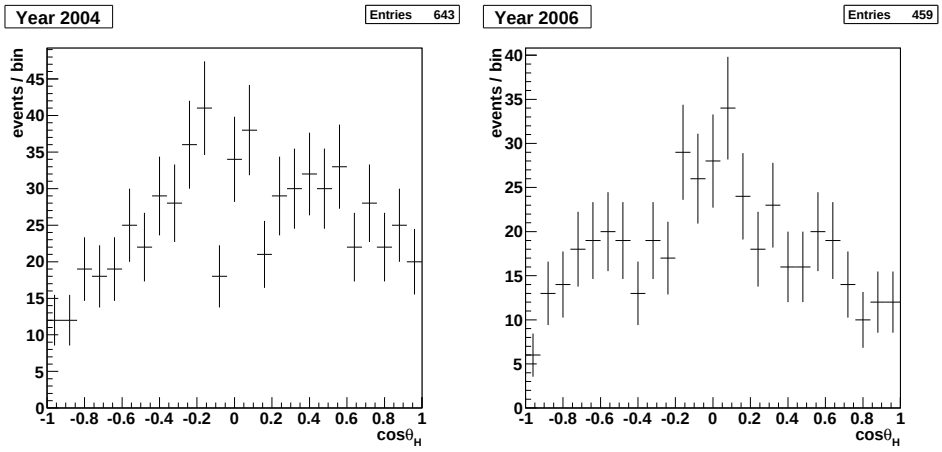

Figure A.11: *Polar orientation* $\cos\theta_H$ *of the* ω *decay plane in the helicity frame for final sample; year 2004 (left) and 2006 (right).*

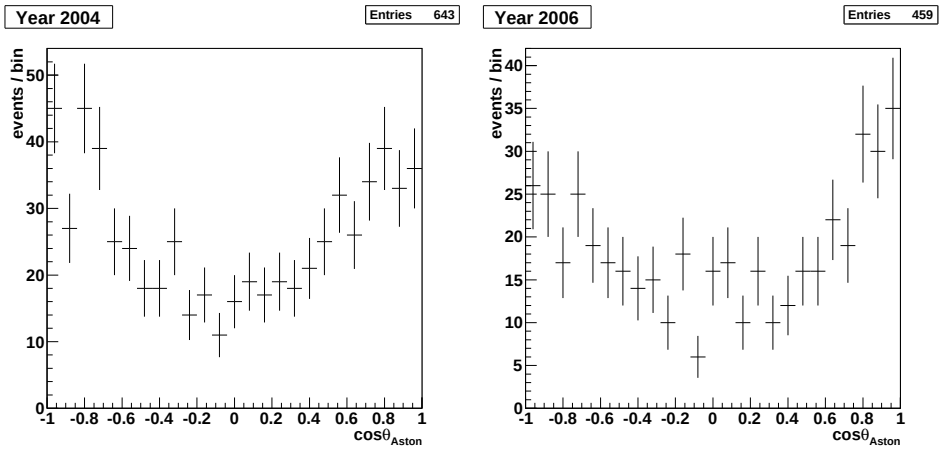

Figure A.12: $\cos\theta_A$ *distribution for* $\omega\pi^0$ *final sample for year 2004 (left) and 2006 (right).*

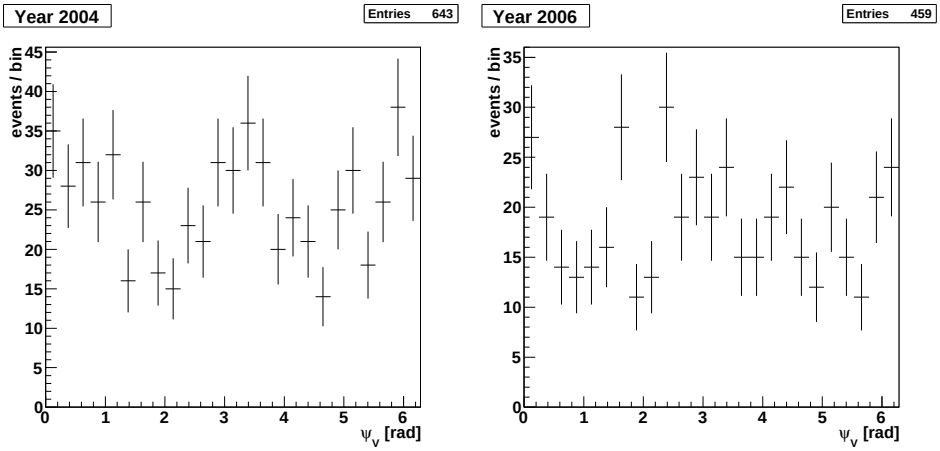

Figure A.13: *Azimuthal distribution ψ_V for a $J^P = 1^-$ spin analyzer; $\omega\pi^0$ final sample for year 2004 (left) and 2006 (right).*

Appendix B

Wigner D-functions

Wigner D-functions appear naturally in the evaluation of the amplitudes

$$\langle J, M'|R(\alpha,\beta,\gamma)|J, M\rangle = D^J_{M'M}(\alpha,\beta,\gamma) \tag{B.1}$$

between angular momentum states of a particle or system of particles with total angular momentum J and projections on an arbitrary but fixed quantization axis characterized by the quantum numbers M and M', respectively. $R(\alpha,\beta,\gamma)$ is an operator associated to a rotation in space described by the Euler angles α, β and γ.

In particular:

$$\langle J, M'|R(\phi,\theta,0)|J, M\rangle = e^{-iM'\phi} d^J_{M'M}(\theta), \tag{B.2}$$

the $d^J_{M'M}(\theta)$ being one of the so called *small* Wigner d-matrix, whose entries are products of trigonometric functions in the variable θ.

The $D^J_{M'M}$ and $d^J_{M'M}$ have thus dimension $2J+1$, and the explicit form for the latter, for integer values of J up to $J=2$ (the only ones used in the present work), are listed below.

$J = 0$:

$$1 \tag{B.3}$$

$J = 1$:

$$\begin{pmatrix} \frac{1+\cos\theta}{2} & \frac{\sin\theta}{\sqrt{2}} & \frac{1-\cos\theta}{2} \\ -\frac{\sin\theta}{\sqrt{2}} & \cos\theta & \frac{\sin\theta}{\sqrt{2}} \\ \frac{1-\cos\theta}{2} & -\frac{\sin\theta}{\sqrt{2}} & \frac{1+\cos\theta}{2} \end{pmatrix} \tag{B.4}$$

$J = 2$:

$$
\begin{pmatrix}
(\frac{1+\cos\theta}{2})^2 & \frac{1+\cos\theta}{2}\sin\theta & \frac{\sqrt{6}}{4}\sin^2\theta & \frac{1-\cos\theta}{2}\sin\theta & (\frac{1-\cos\theta}{2})^2 \\
-\frac{1+\cos\theta}{2}\sin\theta & \frac{1+\cos\theta}{2}(2\cos\theta-1) & -\sqrt{\frac{3}{2}}\sin\theta\cos\theta & \frac{1-\cos\theta}{2}(2\cos\theta+1) & \frac{1-\cos\theta}{2}\sin\theta \\
\frac{\sqrt{6}}{4}\sin^2\theta & -\sqrt{\frac{3}{2}}\sin\theta\cos\theta & \frac{3}{2}\cos^2\theta-\frac{1}{2} & \sqrt{\frac{3}{2}}\sin\theta\cos\theta & \frac{\sqrt{6}}{4}\sin^2\theta \\
-\frac{1-\cos\theta}{2}\sin\theta & \frac{1-\cos\theta}{2}(2\cos\theta+1) & -\sqrt{\frac{3}{2}}\sin\theta\cos\theta & \frac{1+\cos\theta}{2}(2\cos\theta-1) & -\frac{1+\cos\theta}{2}\sin\theta \\
(\frac{1-\cos\theta}{2})^2 & -\frac{1-\cos\theta}{2}\sin\theta & \frac{\sqrt{6}}{4}\sin^2\theta & -\frac{1+\cos\theta}{2}\sin\theta & (\frac{1+\cos\theta}{2})^2
\end{pmatrix}
\tag{B.5}
$$

Appendix C

$|F_1|^2$ dependence on $\rho_{00}^{\pm}$

In this appendix we want to examine in full detail the relation between the ω decay amplitude squared $|F_1|^2$ and the two spin density matrix elements $\rho_{00}^{\pm}$, which characterize the production of the $\omega\pi^0$ system of spin-parity $1^{\pm}$ in an helicity state 0 (or, better, using Dirac ket notation, in a state corresponding to the projector $|\lambda\rangle\langle\lambda'| = |0\rangle\langle 0|$).

From the expression of the moments listed in Table 7.2, pag. 112 (see ref. [A$^+$84]), which we rewrite for ease here:

$$NH_s^+(0020) = \frac{1}{5}N^+(3\rho_{00}^+ - 1)(1 - 3|F_1|^2) - \frac{1}{10}N^-(3\rho_{00}^- - 1), \tag{C.1}$$

$$NH_s^+(2020) = \frac{1}{25}N^+(3\rho_{00}^+ - 1)(2 - 3|F_1|^2) - \frac{1}{50}N^-(3\rho_{00}^- - 1), \tag{C.2}$$

$$NH_s^+(2220) = \frac{3}{25}N^+(3\rho_{00}^+ - 1)|F_1|^2 - \frac{3}{50}N^-(3\rho_{00}^- - 1), \tag{C.3}$$

inserting into the equations (7.16) and (7.17), pag. 102,

$$\Delta_{1^+}(20) = H_s(0020) - \frac{5}{2}H_s(2020) + \frac{5}{2}H_s(2220), \tag{C.4}$$

$$\Delta_{1^-}(20) = H_s(0020) - \frac{5}{2}H_s(2020) - \frac{5}{2}H_s(2220), \tag{C.5}$$

leads, for their common part, to:

$$\begin{aligned} H(0020) - \frac{5}{2}H(2020) &= \frac{1}{5}N^+(3\rho_{00}^+ - 1)(1 - 3|F_1|^2) - \frac{1}{10}N^-(3\rho_{00}^- - 1) + \\ &- \frac{1}{10}N^+(3\rho_{00}^+ - 1)(2 - 3|F_1|^2) - \frac{1}{20}N^-(3\rho_{00}^- - 1) = \\ &= N^+(3\rho_{00}^+ - 1)\left(\frac{1}{5} - \frac{3}{5}|F_1|^2 - \frac{1}{5} + \frac{3}{10}|F_1|^2\right) + \\ &- N^-(3\rho_{00}^- - 1)\left(\frac{1}{10} + \frac{1}{20}\right) = \\ &= -\frac{3}{10}N^+(3\rho_{00}^+ - 1)|F_1|^2 - \frac{3}{20}N^-(3\rho_{00}^- - 1). \end{aligned} \tag{C.6}$$

The third moment in the additions $H(2220)$ gives for Δ_{1^+} and Δ_{1^-} opposite contributions, resulting in

$$\begin{aligned}\Delta_{1^+} &= -\frac{3}{10}N^+(3\rho_{00}^+ - 1)|F_1|^2 - \frac{3}{20}N^-(3\rho_{00}^- - 1) + \\ &+ \frac{3}{10}N^+(3\rho_{00}^+ - 1)|F_1|^2 - \frac{3}{20}N^-(3\rho_{00}^- - 1) = \\ &= -\frac{3}{10}N^-(3\rho_{00}^- - 1), \end{aligned} \tag{C.7}$$

and

$$\begin{aligned}\Delta_{1^-} &= -\frac{3}{10}N^+(3\rho_{00}^+ - 1)|F_1|^2 - \frac{3}{20}N^-(3\rho_{00}^- - 1) + \\ &- \frac{3}{10}N^+(3\rho_{00}^+ - 1)|F_1|^2 + \frac{3}{20}N^-(3\rho_{00}^- - 1) = \\ &= -\frac{3}{5}N^+(3\rho_{00}^+ - 1)|F_1|^2. \end{aligned} \tag{C.8}$$

Inverting (C.7) and C.8 we obtain:

$$3\rho_{00}^- - 1 = -\frac{10}{3}\cdot\frac{\Delta_{1^+}}{N^-}, \tag{C.9}$$

$$3\rho_{00}^+ - 1 = -\frac{5}{3}\cdot\frac{\Delta_{1^-}}{N^+|F_1|^2}. \tag{C.10}$$

We note now that N^- (and also $N^+ = N - N^-$) can be restated as a function of $|F_1|^2$, the last two equations thus giving the searched relation between $|F_1|^2$ and $\rho_{00}^{\pm}$. Infact, defining $x = N^-/N$, we can write

$$\begin{aligned}|F_1|^2 &= F_- x + B(1-x) \\ &= \frac{1}{2}x + (0.443 \pm 0.008)(1-x) \end{aligned} \tag{C.11}$$

with $F_- = 1/2$ the value of $|F_1|^2$ for a pure 1^- spin-parity state (ρ meson) and $B = 0.443 \pm 0.008$ the corresponding value for a pure $b_1(1235)$ contribution to the $\omega\pi^0$ signal. Solving for x, we can write

$$x = \frac{N^-}{N} = \frac{|F_1|^2 - B}{1/2 - B} \tag{C.12}$$

which can be now written into eq. (C.9) and (C.10). Let us consider the two cases separately.

C.1 $|F_1|^2$ dependence on ρ_{00}^-

Taking equation (C.9), we can write

$$\begin{aligned}3\rho_{00}^- - 1 &= -\frac{10}{3}\cdot\frac{\Delta_{1^+}}{N^-} = -\frac{10}{3}\cdot\frac{\Delta_{1^+}}{N}\cdot\frac{N}{N^-} \\ &= -\frac{10}{3}\cdot\frac{\Delta_{1^+}}{N}\cdot\frac{1/2 - B}{|F_1|^2 - B} \end{aligned} \tag{C.13}$$

which leads finally to

$$|F_1|^2 = B - \frac{10}{3} \cdot \frac{\Delta_{1^+}}{N} \cdot \frac{1/2 - B}{3\rho_{00}^- - 1} \tag{C.14}$$

This is precisely the formula used to produce the plots in Chapter 7. Note that the formula has no meaning for $\rho_{00}^- = 1/3$. From last equation, an estimation of the corresponding error can be easily derived: neclecting the small contribution of B, we see that the only contribution comes from Δ_{1^+}, for a fixed value of ρ_{00}^-, leading to

$$\delta|F_1|^2 = \frac{10}{3} \cdot \frac{1/2 - B}{N(3\rho_{00}^- - 1)} \delta\Delta_{1^+}. \tag{C.15}$$

We also see that the error for $|F_1|^2$ depends also on ρ_{00}^-.

C.2 $|F_1|^2$ dependence on ρ_{00}^+

For the case of ρ_{00}^+ calculation are more cumbersome, but proceed on the same line as done in the previous section. The analogous of equation (C.13) is now[1]:

$$\begin{aligned} 3\rho_{00}^+ - 1 &= -\frac{5}{3} \cdot \frac{\Delta_{1^-}}{N^+|F_1|^2} = -\frac{5}{3} \cdot \frac{\Delta_{1^-}}{N|F_1|^2} \cdot \frac{N}{N^+} \\ &= -\frac{5}{3} \cdot \frac{\Delta_{1^-}}{N|F_1|^2} \cdot \frac{1/2 - B}{1/2 - |F_1|^2}, \end{aligned} \tag{C.16}$$

i.e. a quadratic dependence

$$(1/2 - |F_1|^2)|F_1|^2 = -\frac{5}{3} \cdot \frac{\Delta_{1^-}}{N} \frac{1/2 - B}{3\rho_{00}^+ - 1}. \tag{C.17}$$

Solving for $|F_1|^2$ we obtain

$$4|F_1|^2 = 1 \pm \sqrt{1 - \frac{16\alpha}{3\rho_{00}^+ - 1}}, \tag{C.18}$$

with

$$\alpha = -\frac{5}{3} \frac{\Delta_{1^-}}{N} (1/2 - B). \tag{C.19}$$

The corresponding errors are

$$\delta|F_1|^2 = \left(1 - \frac{16\alpha}{3\rho_{00}^+ - 1}\right)^{-1/2} \left(-\frac{2}{3\rho_{00}^+ - 1}\right) \delta\alpha, \tag{C.20}$$

with

$$\delta\alpha = -\frac{5}{3} \cdot \frac{1/2 - B}{N} \delta\Delta_{1^-}. \tag{C.21}$$

The last two equation together give the desired numerical value for $\delta|F_1|^2$ in dependence on ρ_{00}^+ and Δ_{1^-}.

[1] we recall that $N^+/N = (N - N^-)/N = 1 - N^-/N$.

Appendix D

$|F_1|^2$ values from $\cos\theta_H$-distribution fit

In this Appendix, titles of histograms refer to the corresponding $\omega\pi^0$-mass range, the meaning being the following:

- Low mass: $0.9 < m(\omega\pi^0) < 1.1$ GeV/c^2;
- Middle mass: $1.1 < m(\omega\pi^0) < 1.4$ GeV/c^2;
- High mass: $1.4 < m(\omega\pi^0) < 1.6$ GeV/c^2;

No title indicates the lack of a cut on the mass (i.e. the whole statistic).

This conventions are those adopted in the main part of this work and extend also to the various histograms shown in other Appendices.

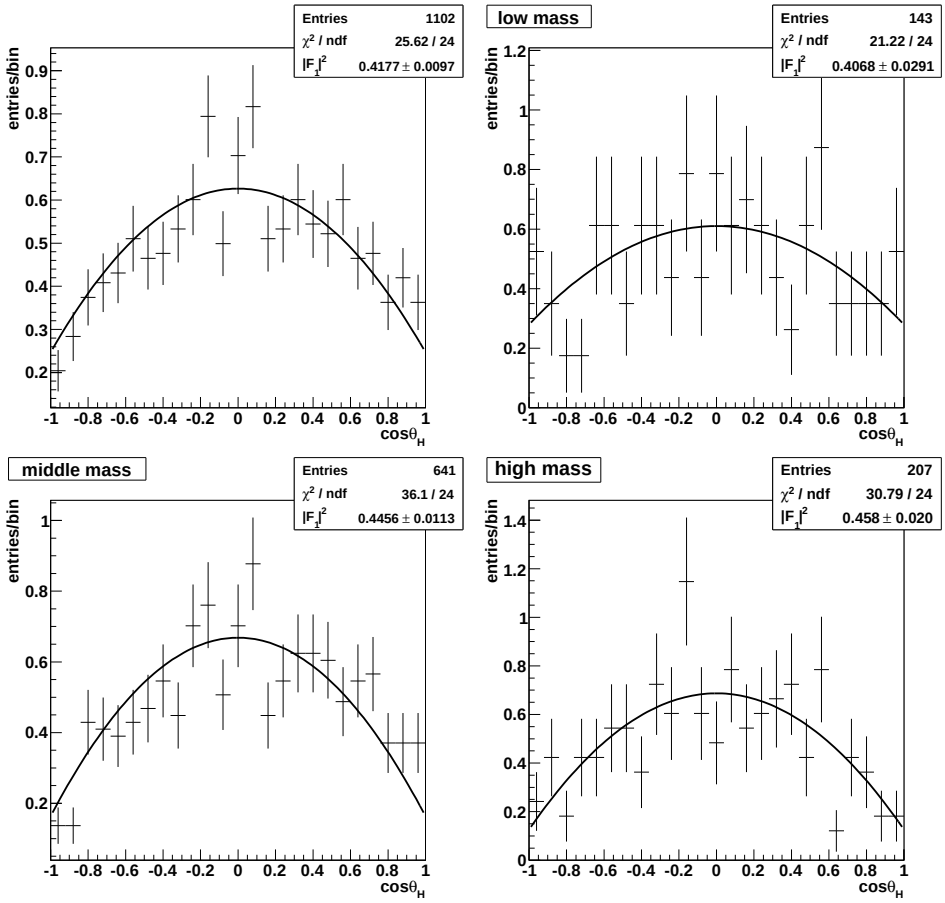

Figure D.1: $\omega\pi^0$-*mass dependence.*

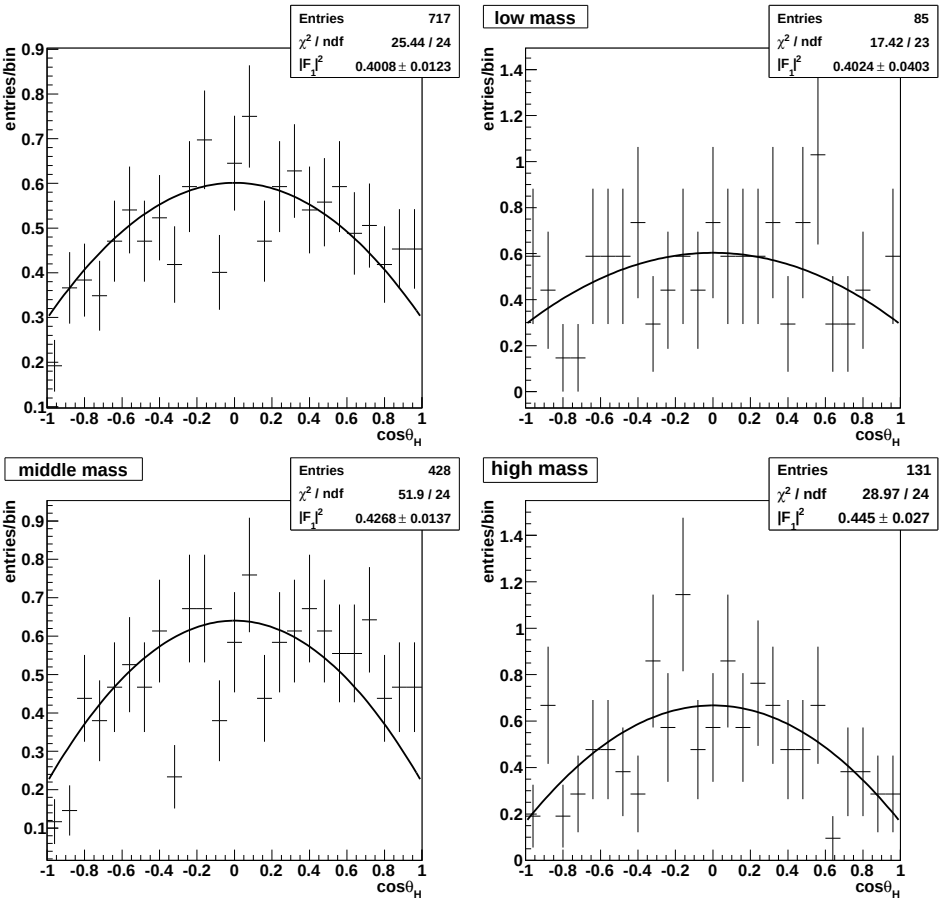

Figure D.2: $\omega\pi^0$-*mass dependence and* $p_t^2 < 0.15$ *(GeV/*c*)*^{2}.

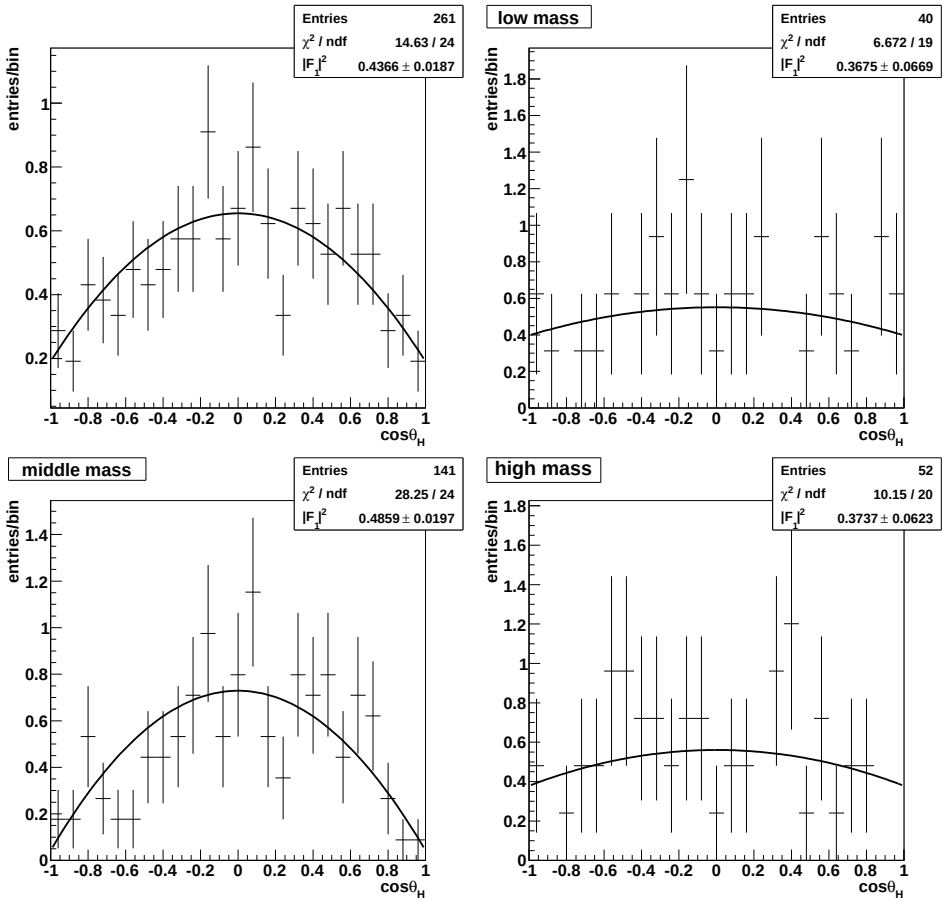

Figure D.3: $\omega\pi^0$-*mass dependence and* 0.15 *(GeV/c)*$^2 < p_t^2 < 0.5$ *(GeV/c)*^{2}.

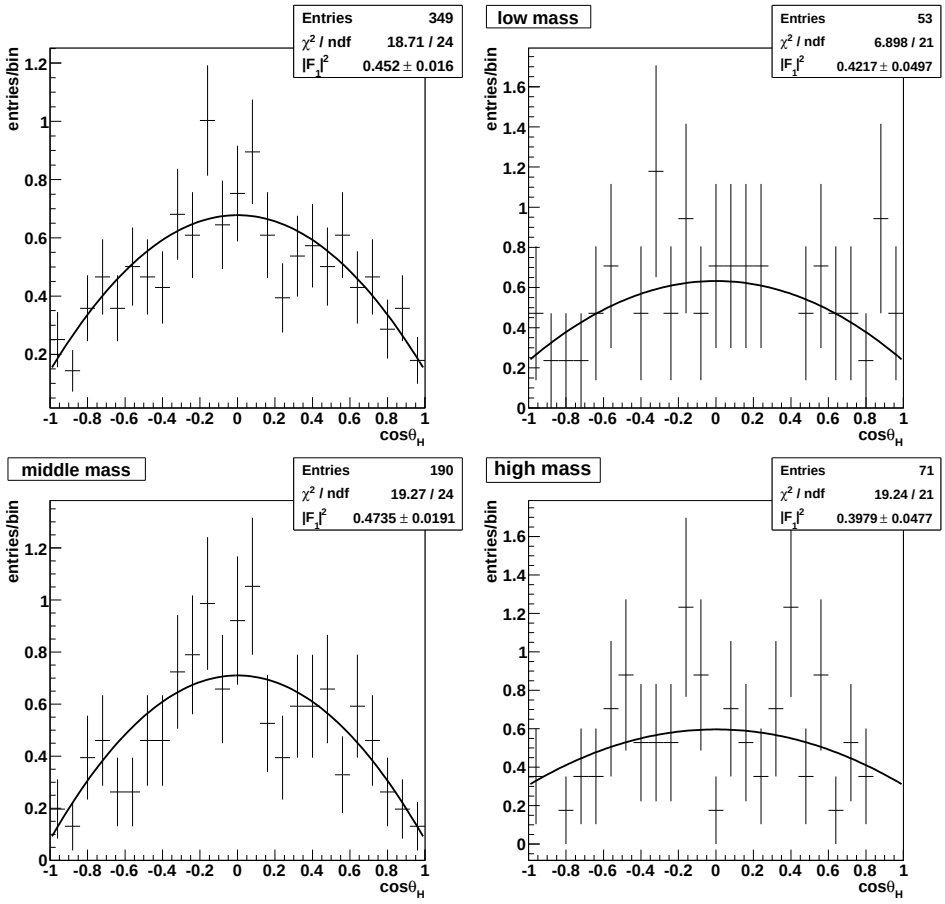

Figure D.4: $\omega\pi^0$-*mass dependence and* 0.15 *(GeV/c)*$^2 < p_t^2 < 1$ *(GeV/c)*^{2}.

Appendix E

Non-ω background from λ-distribution fit

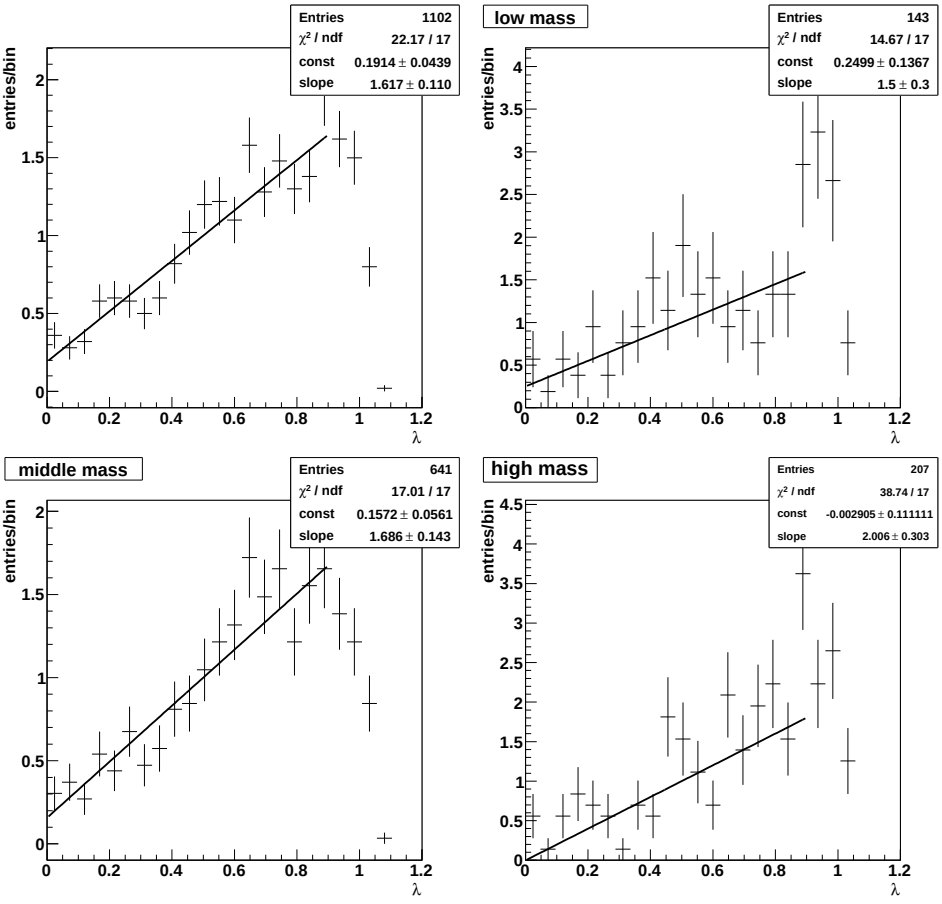

Figure E.1: $\omega\pi^0$-*mass dependence.*

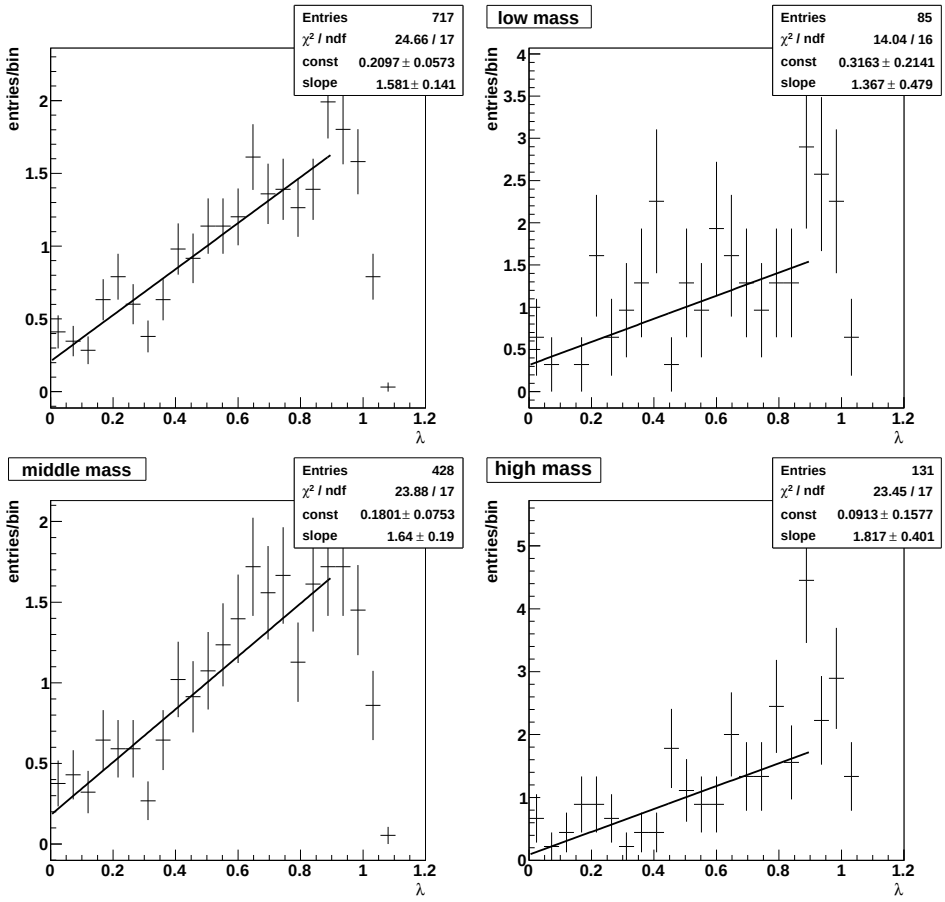

Figure E.2: $\omega\pi^0$-*mass dependence and* $p_t^2 < 0.15$ *(GeV/c)*^{2}.

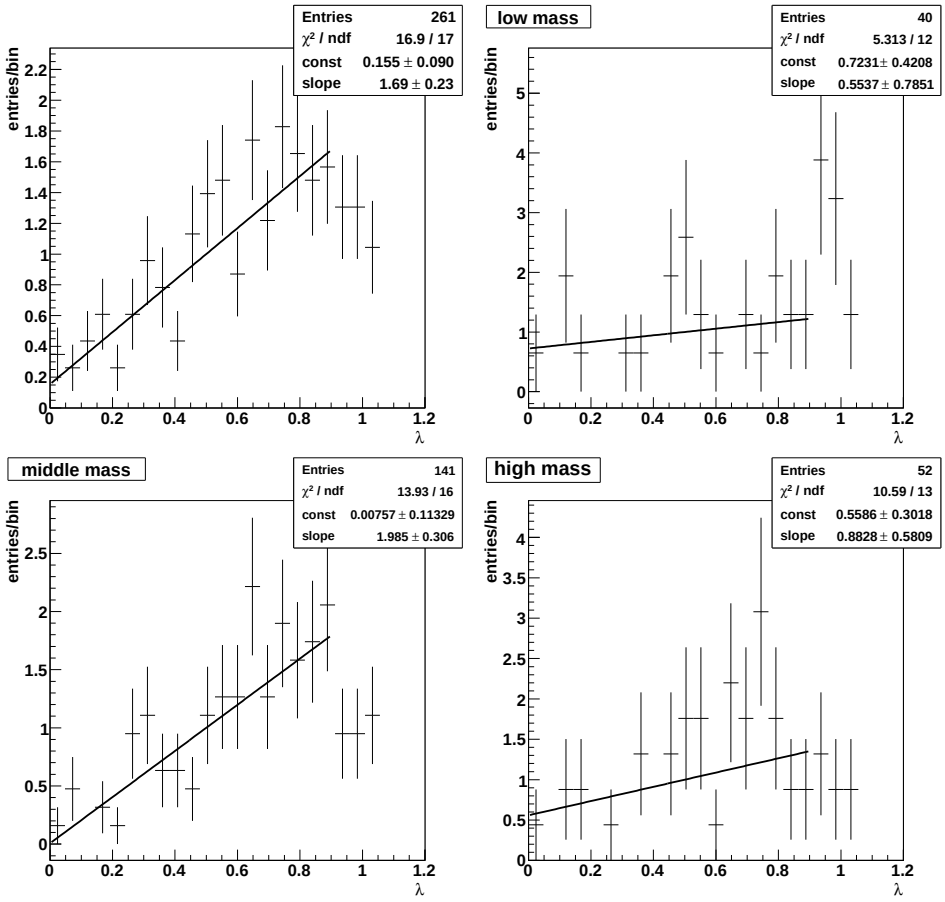

Figure E.3: $\omega\pi^0$-*mass dependence and* 0.15 *(GeV/c)*$^2 < p_t^2 < 0.5$ *(GeV/c)*^{2}.

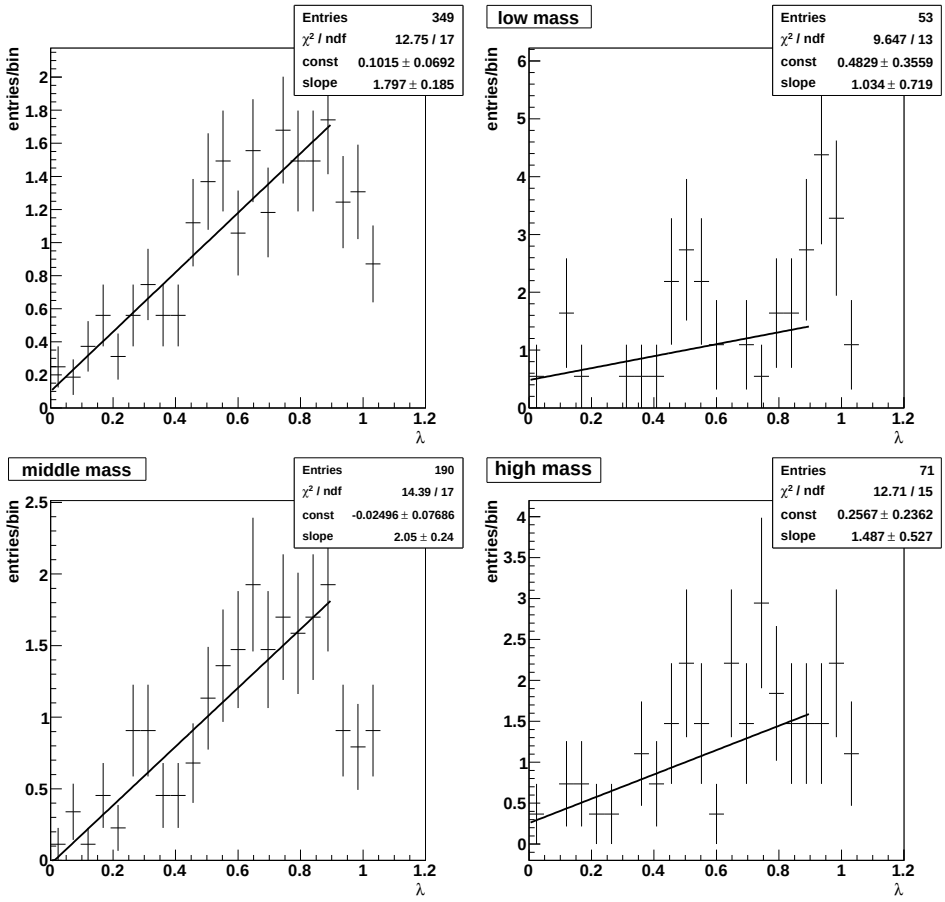

Figure E.4: $\omega\pi^0$-*mass dependence and* 0.15 *(GeV/c)*$^2 < p_t^2 < 1$ *(GeV/c)*^{2}.

Appendix F

$\cos\theta_H$ distribution fit for $\lambda > 0.2$

In this Appendix, results obtained performing a data analysis along the same lines as in the main part of the present work, are shown, but limited to the data sample corresponding to $\lambda \in [0.2, 1]$.

F.1 $|F_1|^2$ values from fit

Considering only the data sample corresponding to the interval $\lambda \in [0.2, 1]$, we have a set of values for $|F_1|^2$ from fit as shown in Tables F.1 and F.2.

Selection	$\lvert F_1\rvert^2$
-	0.418 ± 0.010
$p_t^2 < 0.15$	0.400 ± 0.013
$0.15 < p_t^2 < 0.5$	0.436 ± 0.019
$0.15 < p_t^2 < 1$	0.451 ± 0.016

Table F.1: $|F_1|^2$ *with* $\lambda \in [0.2, 1]$*:* p_t^2*-dependence.*

Selection	$0.9 < m < 1.1$	$1.1 < m < 1.4$	$1.4 < m < 1.6$
-	0.406 ± 0.030	0.445 ± 0.012	0.453 ± 0.021
$p_t^2 < 0.15$	0.406 ± 0.042	0.425 ± 0.015	0.426 ± 0.028
$0.15 < p_t^2 < 0.5$	0.374 ± 0.064	0.485 ± 0.021	0.357 ± 0.067
$0.15 < p_t^2 < 1$	0.419 ± 0.047	0.478 ± 0.019	0.368 ± 0.050

Table F.2: $|F_1|^2$ *with* $\lambda \in [0.2, 1]$*:* $\omega\pi^0$*-mass and* p_t^2*-dependence.*

The corresponding histograms can be seen in Figures F.1 to F.4.

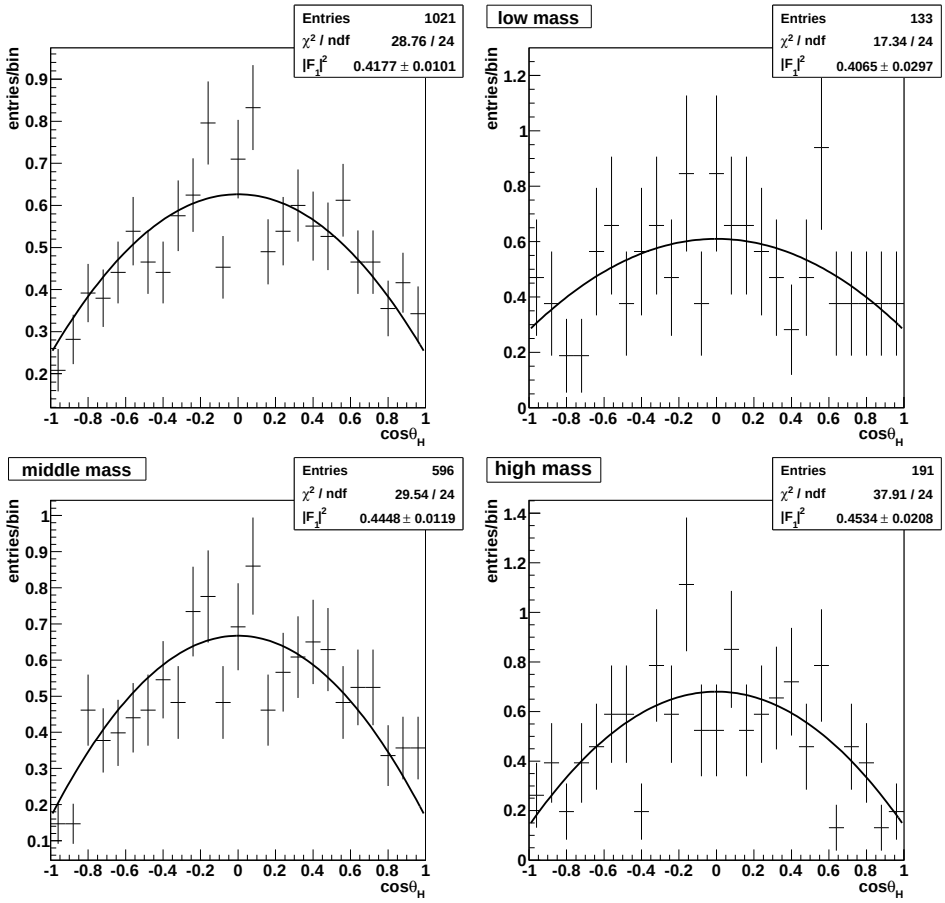

Figure F.1: $\omega\pi^0$-*mass dependence.* λ-*cut.*

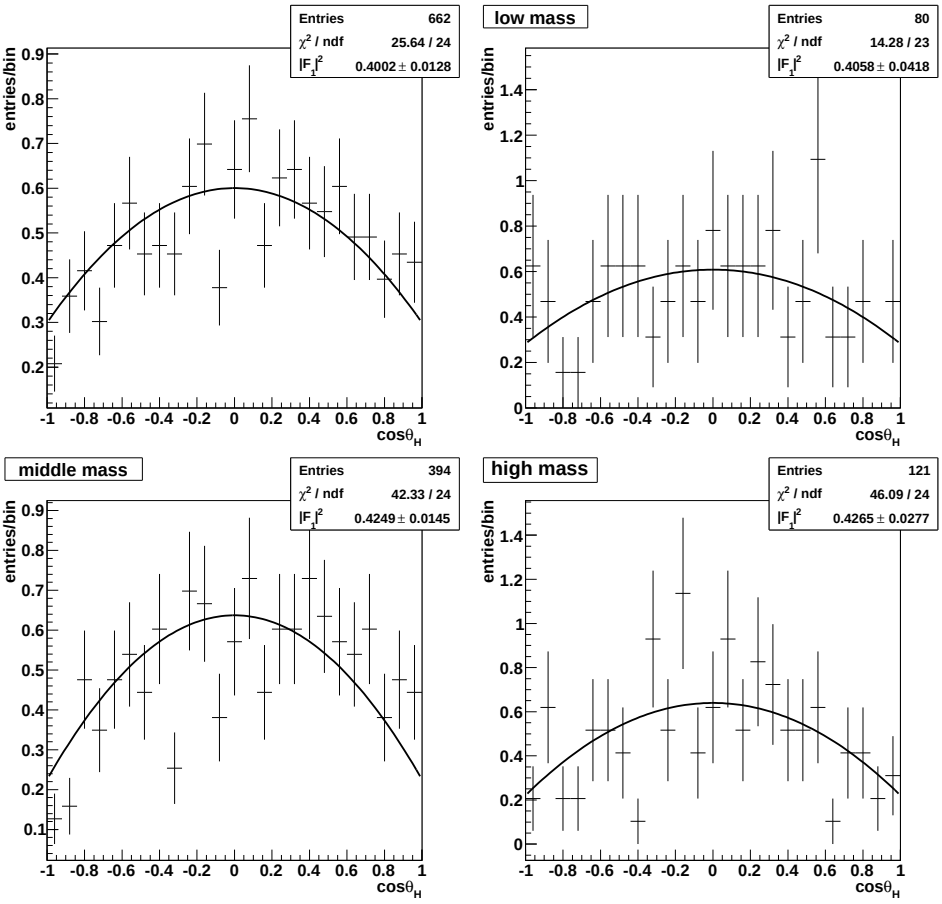

Figure F.2: $\omega\pi^0$-*mass dependence and* $p_t^2 < 0.15$ *(GeV/c)*^{2}*.* λ*-cut.*

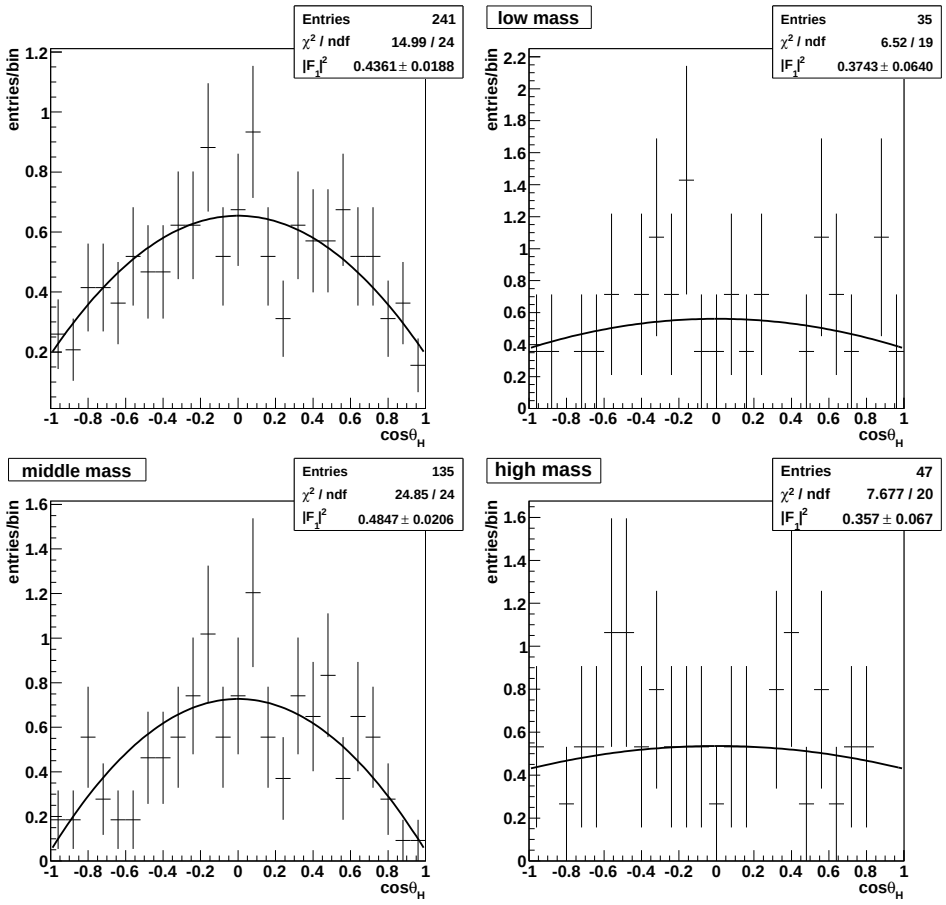

Figure F.3: $\omega\pi^0$-*mass dependence and* 0.15 *(GeV/c)*$^2 < p_t^2 < 0.5$ *(GeV/c)*^{2}. λ-*cut.*

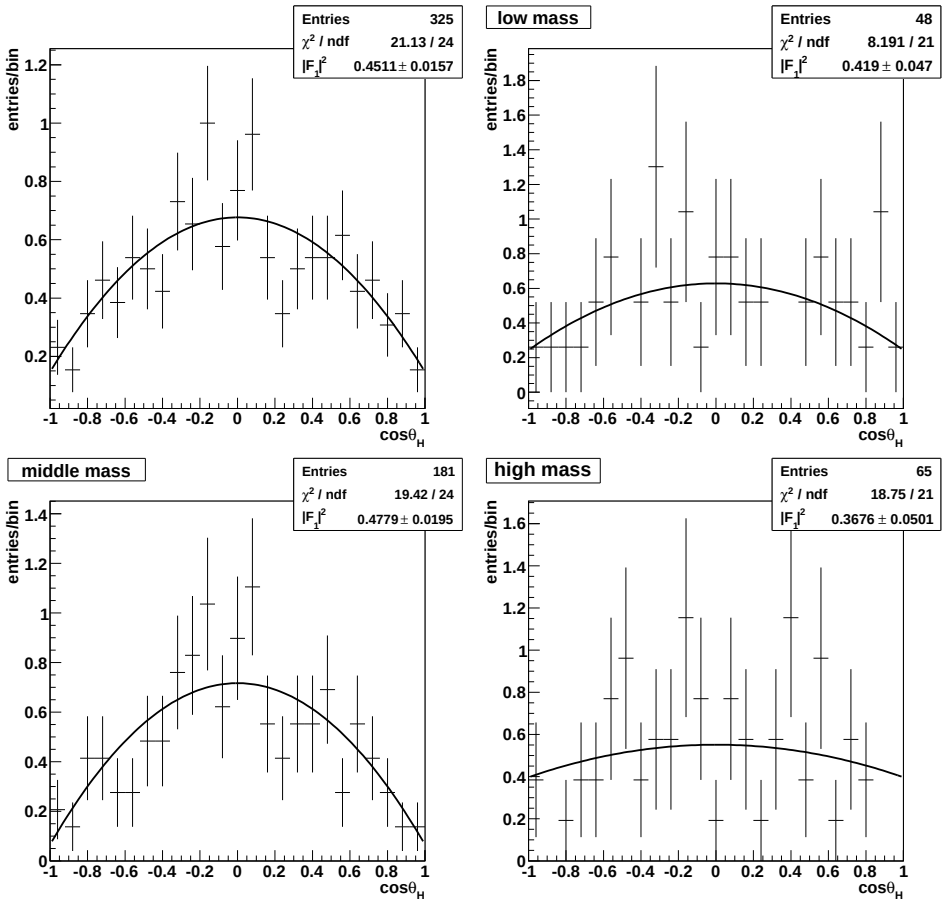

Figure F.4: *$\omega\pi^0$-mass dependence and* 0.15 *(GeV/c)^2* $< p_t^2 <$ 1 *(GeV/c)^2. λ-cut.*

Selection	(%)
-	16.5 ± 3.8
$p_t^2 < 0.15$	18.1 ± 4.9
$0.15 < p_t^2 < 0.5$	13.3 ± 7.7
$0.15 < p_t^2 < 1$	8.6 ± 5.9

Table F.3: *Non-ω background contribution to the final sample with λ-cut. p_t^2-dependence.*

Selection	$0.9 < m < 1.1$	$1.1 < m < 1.4$	$1.4 < m < 1.6$
-	21.7 ± 11.9	13.5 ± 4.8	-0.2 ± 9.3
$p_t^2 < 0.15$	27.8 ± 18.8	15.5 ± 6.5	7.7 ± 13.3
$0.15 < p_t^2 < 0.5$	68.5 ± 39.9	0.6 ± 9.6	51.3 ± 27.7
$0.15 < p_t^2 < 1$	43.8 ± 32.3	-2.1 ± 6.4	22.3 ± 20.6

Table F.4: *Non-ω background contribution to the final sample with λ-cut. p_t^2- and $m(\omega\pi^0)$-dependence.*

F.2 Non-ω background contribution and $|F_1|^2_{corr}$

Tables F.3 and F.4 list the non-ω percentage contribution (in %) to the final sample with $\lambda \in [0.2, 1]$ (in the following, the λ-*cut*).

Tables F.5 and F.6 shows the corresponding $|F_1|^2_{corr}$ after correction for background with $|F_1|^2_{bkg} = 0.333$.

Tables F.7 and F.8 shows the results corresponding to $|F_1|^2_{bkg} = 0.4$.

F.3 1^- contribution

For $|F_1|^2_{bkg} = 0.333$, results are listed in Tables F.9 and F.10. A graphical representation can be seen in Figure F.5.

For the case $|F_1|^2_{bkg} = 0.4$ see Tables F.11 and F.12. The corresponding plots are in Figure F.6.

Selection	$\lvert F_1\rvert^2_{corr}$
-	0.434 ± 0.013
$p_t^2 < 0.15$	0.415 ± 0.016
$0.15 < p_t^2 < 0.5$	0.452 ± 0.024
$0.15 < p_t^2 < 1$	0.462 ± 0.019

Table F.5: $|F_1|^2_{corr}$ *for final sample with λ-cut.* $|F_1|^2_{bkg} = 0.333$.

Selection	$0.9 < m < 1.1$	$1.1 < m < 1.4$	$1.4 < m < 1.6$
-	0.427 ± 0.041	0.462 ± 0.016	0.453 ± 0.024
$p_t^2 < 0.15$	0.434 ± 0.064	0.442 ± 0.019	0.434 ± 0.033
$0.15 < p_t^2 < 0.5$	0.463 ± 0.262	0.486 ± 0.025	0.382 ± 0.140
$0.15 < p_t^2 < 1$	0.486 ± 0.121	0.475 ± 0.021	0.377 ± 0.066

Table F.6: $|F_1|^2_{corr}$ *for final sample with* λ*-cut.* p_t^2*- and* $m(\omega\pi^0)$*-dependence.* $|F_1|^2_{bkg} = 0.333$.

Selection	$\lvert F_1\rvert^2_{corr}$
-	0.421 ± 0.012
$p_t^2 < 0.15$	0.400 ± 0.016
$0.15 < p_t^2 < 0.5$	0.442 ± 0.022
$0.15 < p_t^2 < 1$	0.456 ± 0.018

Table F.7: $|F_1|^2_{corr}$ *for final sample with* λ*-cut.* $|F_1|^2_{bkg} = 0.4$.

Selection	$0.9 < m < 1.1$	$1.1 < m < 1.4$	$1.4 < m < 1.6$
-	0.408 ± 0.038	0.452 ± 0.014	0.453 ± 0.021
$p_t^2 < 0.15$	0.408 ± 0.058	0.429 ± 0.017	0.429 ± 0.030
$0.15 < p_t^2 < 0.5$	0.318 ± 0.228	0.485 ± 0.022	0.312 ± 0.146
$0.15 < p_t^2 < 1$	0.434 ± 0.086	0.476 ± 0.020	0.358 ± 0.065

Table F.8: $|F_1|^2_{corr}$ *for final sample with* λ*-cut.* p_t^2*- and* $m(\omega\pi^0)$*-dependence.* $|F_1|^2_{bkg} = 0.4$.

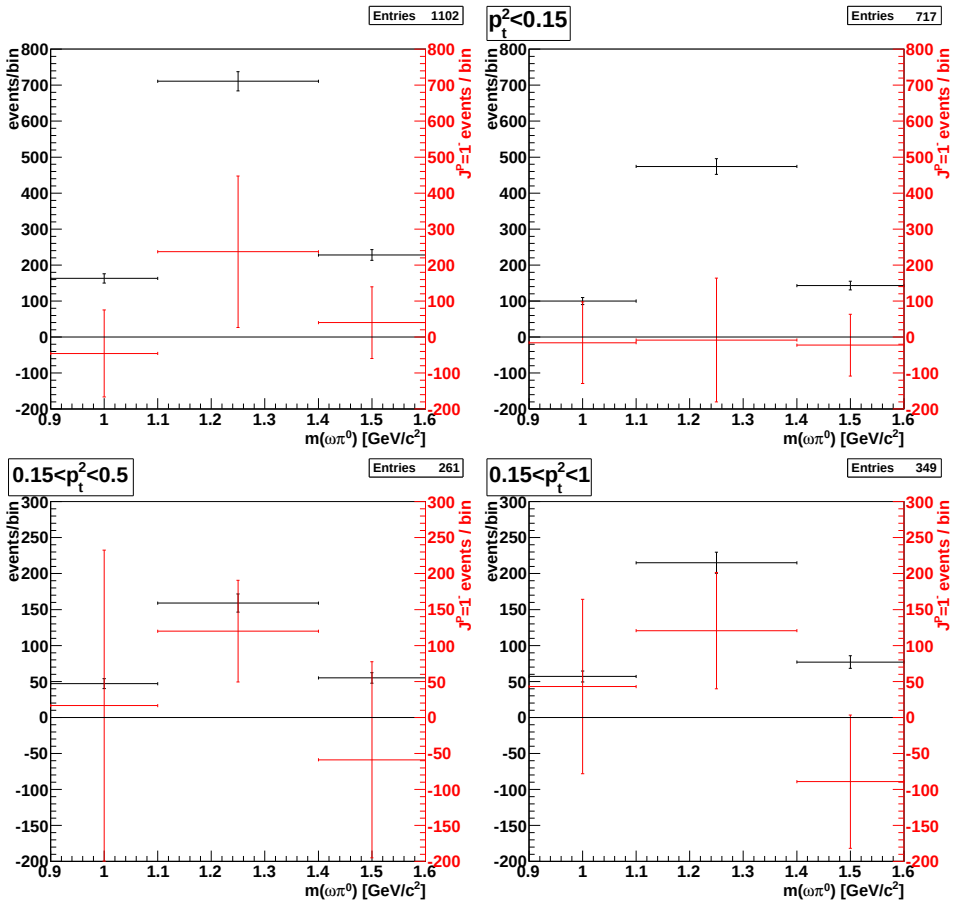

Figure F.5: $J^P = 1^-$ *intensity (red) in the* $\omega\pi^0$ *final sample (black) with and without* p_t^2*-cuts. The error for the* 1^- *contribution is calculated from eqs.* (7.51) *and* (7.54). $|F_1|^2_{bkg} = 0.333$, λ*-cut.*

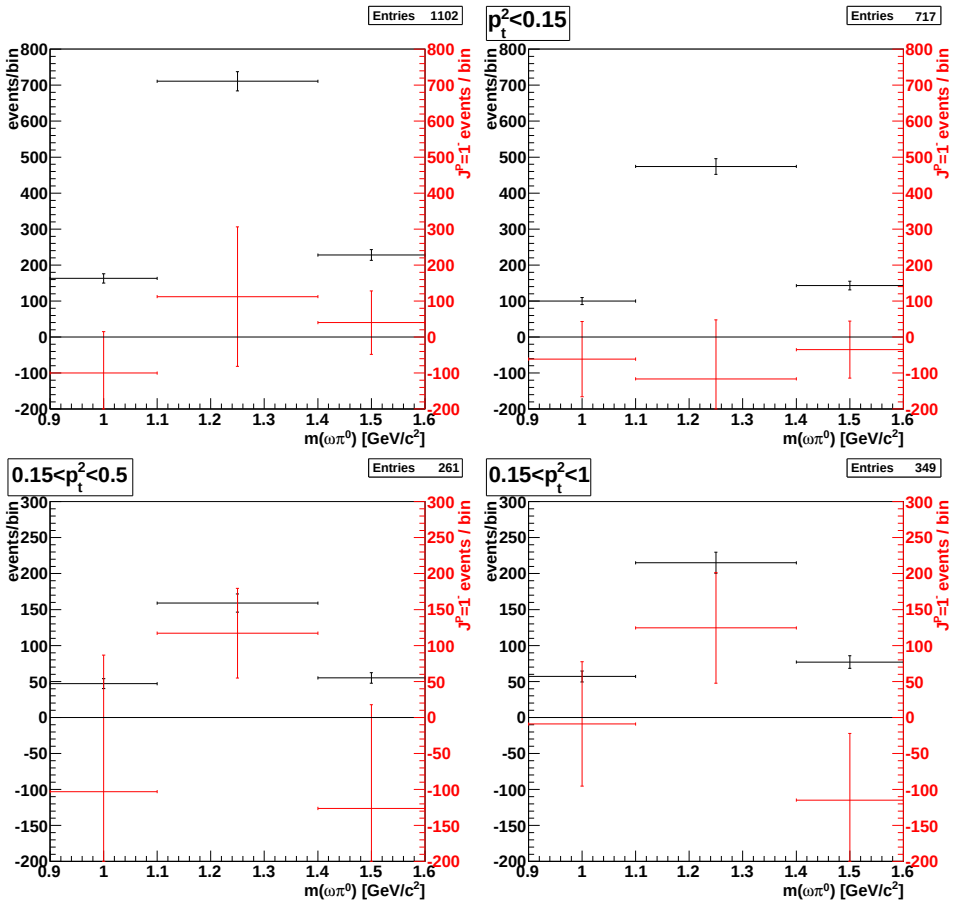

Figure F.6: $J^P = 1^-$ *intensity (red) in the* $\omega\pi^0$ *final sample (black) with and without* p_t^2*-cuts. The error for the* 1^- *contribution is calculated from eqs.* (7.51) *and* (7.54). $|F_1|^2_{bkg} = 0.4$, λ*-cut.*

Selection	1^- (%)
-	-15.8 ± 28.0
$p_t^2 < 0.15$	-49.1 ± 35.0
$0.15 < p_t^2 < 0.5$	15.8 ± 43.7
$0.15 < p_t^2 < 1$	33.3 ± 34.6

Table F.9: 1^- *contribution in the* $\omega\pi^0$ *final sample.* $|F_1|^2_{bkg} = 0.333$, λ*-cut.*

Selection	$0.9 < m < 1.1$	$1.1 < m < 1.4$	$1.4 < m < 1.6$
-	-28.1 ± 74.1	33.3 ± 29.6	17.5 ± 43.7
$p_t^2 < 0.15$	-16 ± 113	-1.8 ± 36.3	-15.8 ± 60.1
$0.15 < p_t^2 < 0.5$	35 ± 460	75.4 ± 44.0	-107 ± 247
$0.15 < p_t^2 < 1$	75 ± 212	56.1 ± 37.4	-116 ± 120

Table F.10: 1^- *contribution in the* $\omega\pi^0$ *final sample.* $|F_1|^2_{bkg} = 0.333$, λ*-cut.*

Selection	1^- (%)
-	-38.6 ± 28.7
$p_t^2 < 0.15$	-75.4 ± 37.3
$0.15 < p_t^2 < 0.5$	-1.8 ± 41.2
$0.15 < p_t^2 < 1$	22.8 ± 33.4

Table F.11: 1^- *contribution in the* $\omega\pi^0$ *final sample.* $|F_1|^2_{bkg} = 0.4$, λ*-cut.*

Selection	$0.9 < m < 1.1$	$1.1 < m < 1.4$	$1.4 < m < 1.6$
-	-61.4 ± 70.4	15.8 ± 27.3	17.5 ± 38.6
$p_t^2 < 0.15$	-61 ± 104	-24.6 ± 34.6	-24.6 ± 55.5
$0.15 < p_t^2 < 0.5$	-219 ± 403	73.7 ± 38.8	-230 ± 260
$0.15 < p_t^2 < 1$	-16 ± 152	57.9 ± 35.6	-149 ± 119

Table F.12: 1^- *contribution in the* $\omega\pi^0$ *final sample.* $|F_1|^2_{bkg} = 0.4$, λ*-cut.*

Appendix G

Angular distributions dependence on p_t^2 and/or $m(\omega\pi^0)$

In this appendix, the various histograms corresponding to the angular distributions examined in the present work are shown with the proper fits superimposed; these are the source of the numerical values listed in the various Tables of Chapter 7.

The dependence of the experimental results on p_t^2- and/or $\omega\pi^0$-mass is illustrated.

For better understanding of histogram titles:

- Low mass: $0.9 < m(\omega\pi^0) < 1.1$ GeV/c^2;
- Middle mass: $1.1 < m(\omega\pi^0) < 1.4$ GeV/c^2;
- High mass: $1.4 < m(\omega\pi^0) < 1.6$ GeV/c^2;

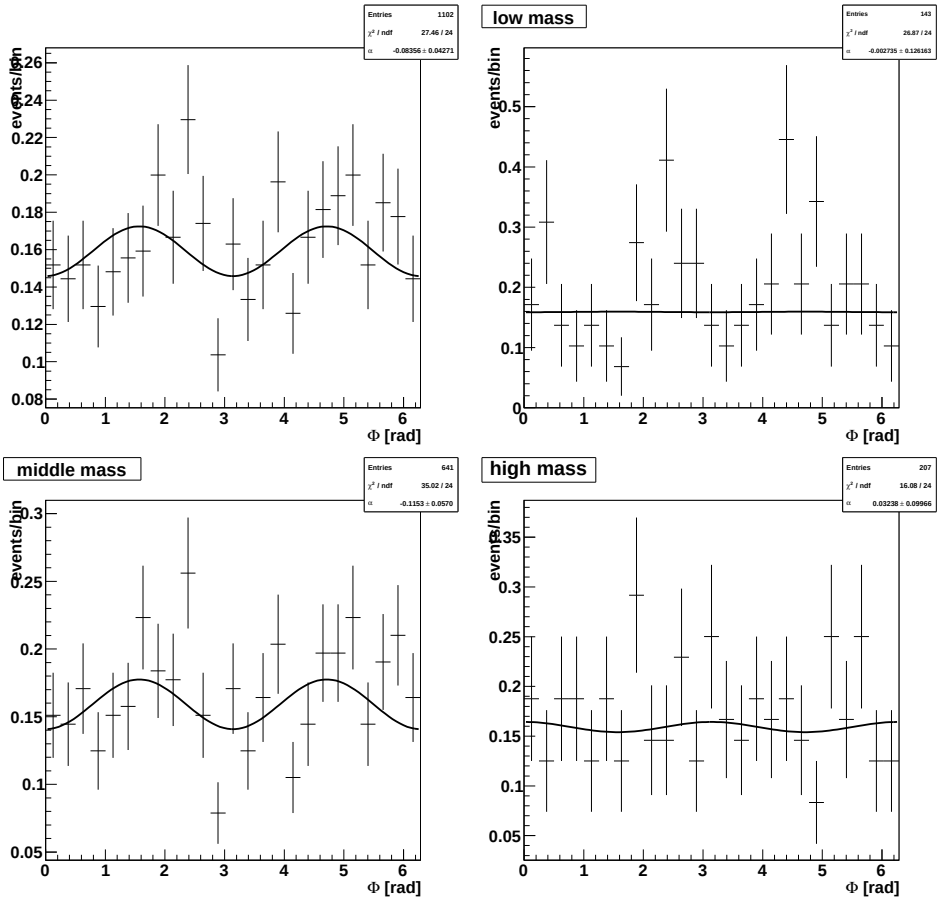

Figure G.1: *Angle Φ: $\omega\pi^0$-mass dependence.*

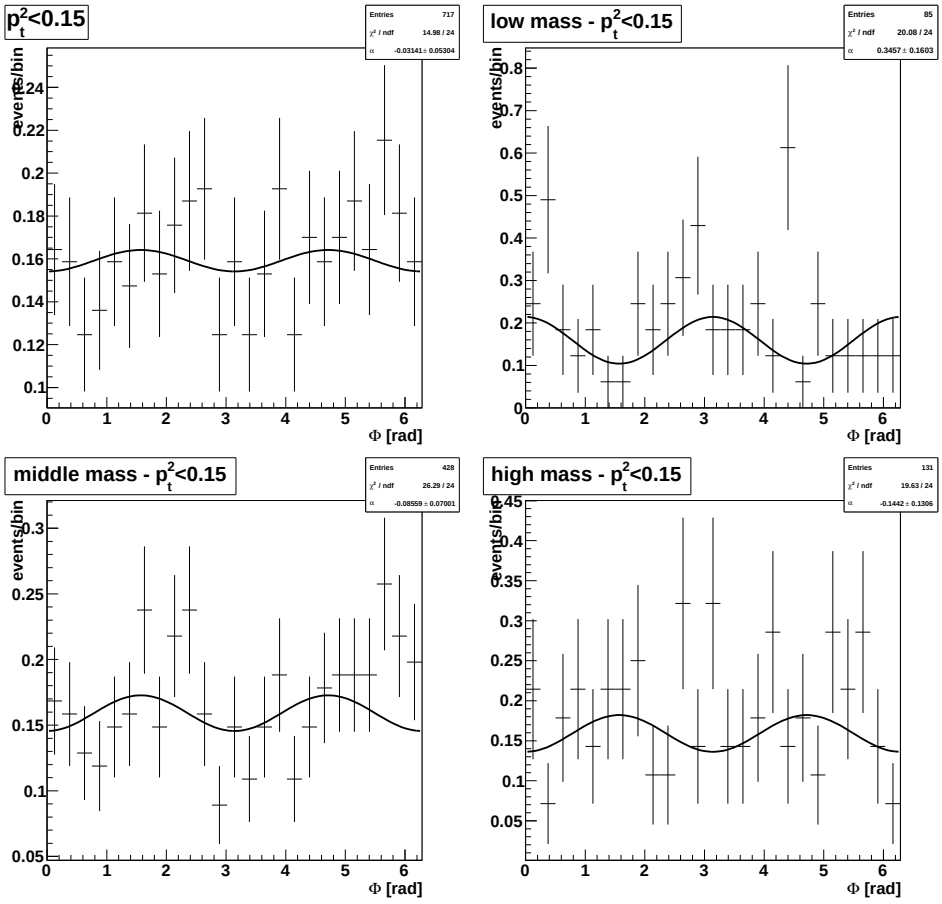

Figure G.2: *Angle Φ: $\omega\pi^0$-mass dependence. Coherent scattering $p_t^2 < 0.15$ (GeV/c)^2.*

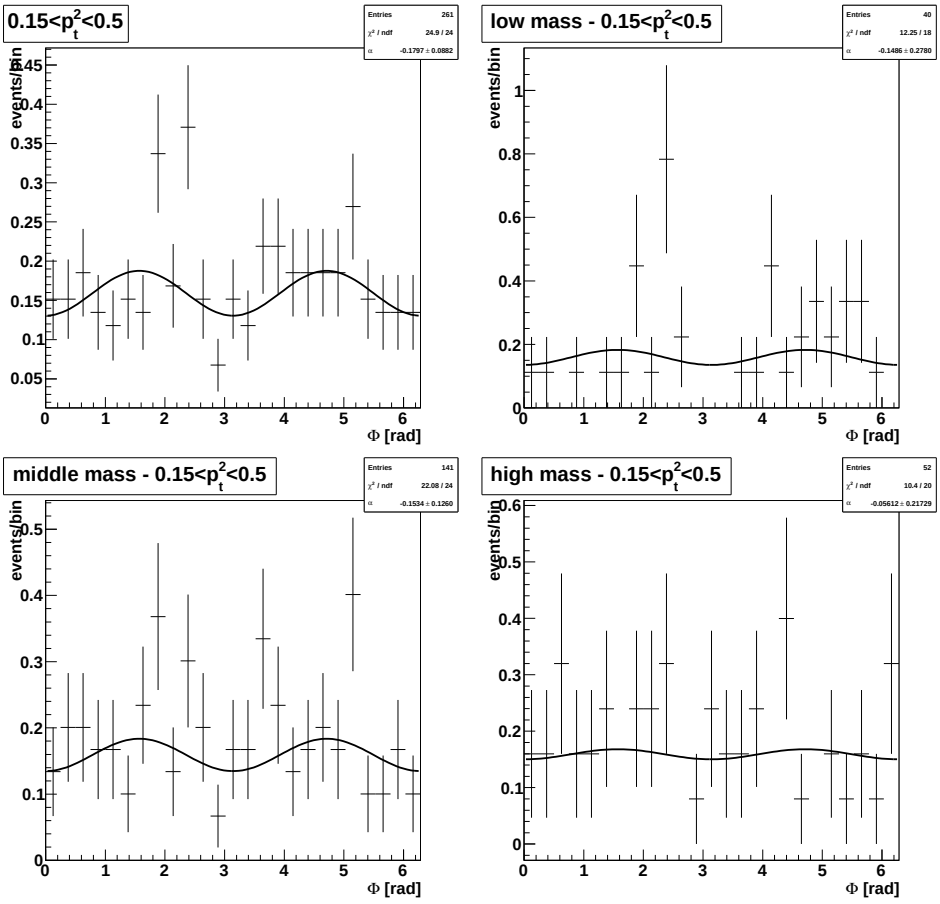

Figure G.3: *Angle* Φ*:* $\omega\pi^0$*-mass dependence. Incoherent scattering* $0.15 < p_t^2 < 0.5$ *(GeV/c)*^{2}.

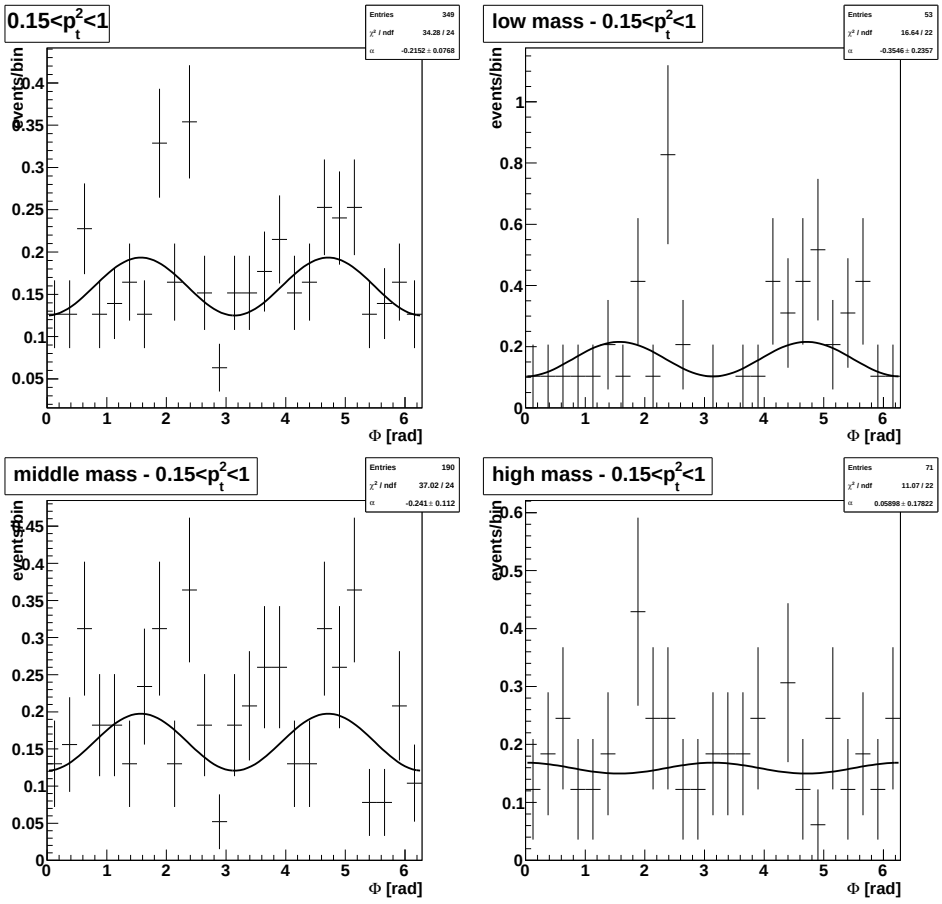

Figure G.4: *Angle* Φ*:* $\omega\pi^0$*-mass dependence. Inoherent scattering* $0.15 < p_t^2 < 1$ *(GeV/c)*^{2}*.*

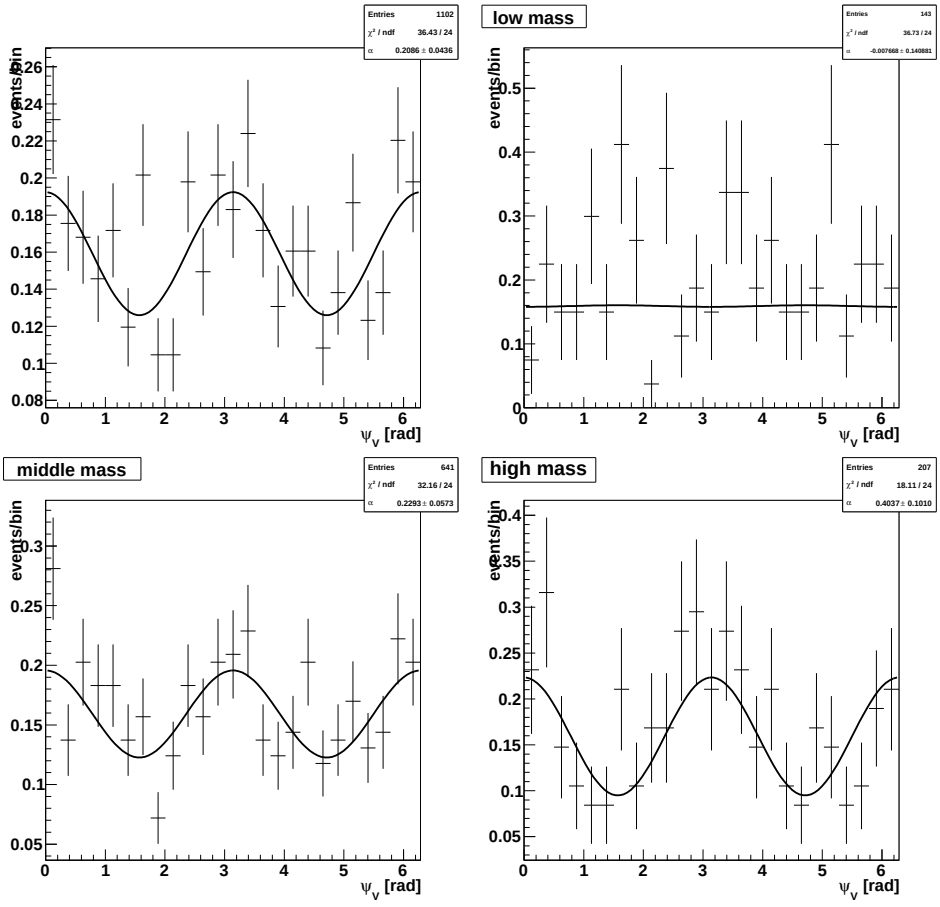

Figure G.5: *Angle ψ_V: $\omega\pi^0$-mass dependence.*

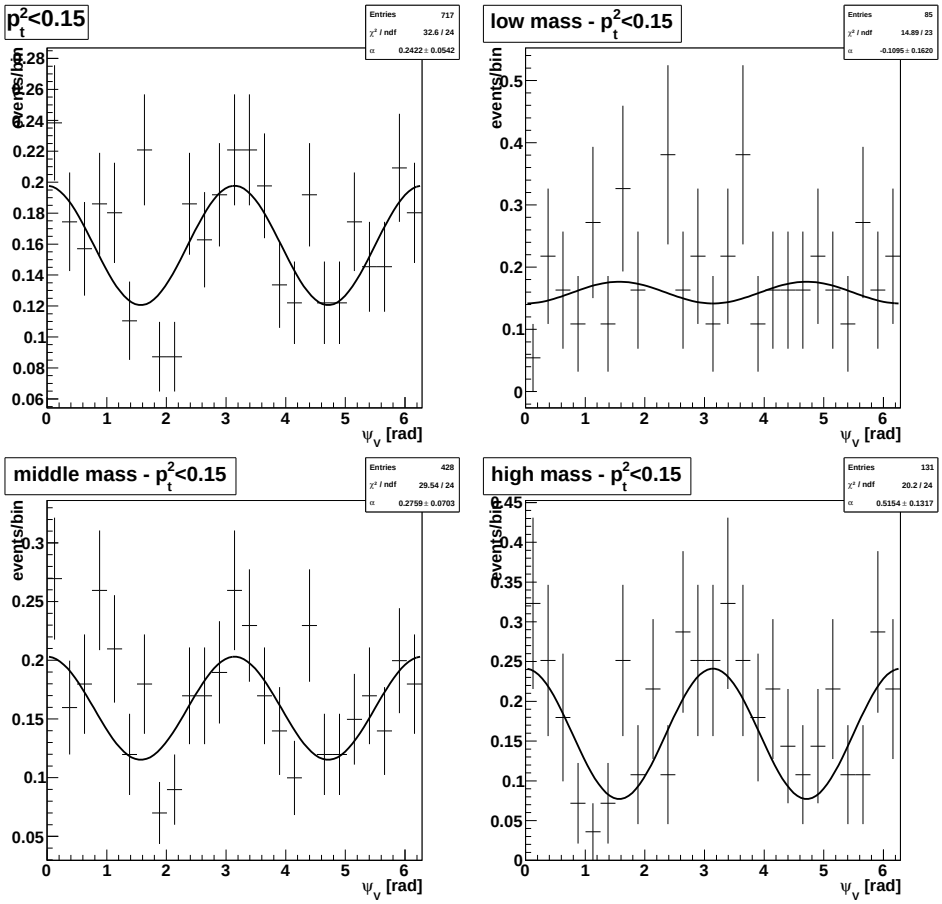

Figure G.6: *Angle ψ_V: $\omega\pi^0$-mass dependence. Coherent scattering $p_t^2 < 0.15$ (GeV/c)^2.*

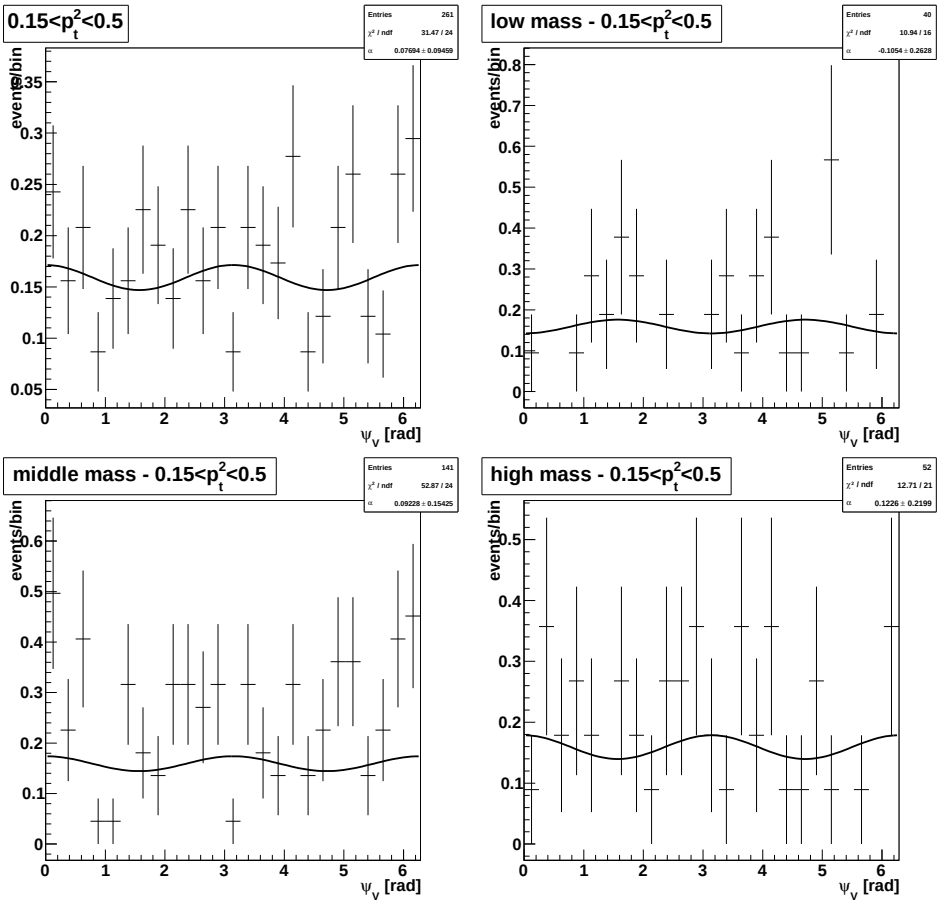

Figure G.7: *Angle ψ_V: $\omega\pi^0$-mass dependence. Incoherent scattering* $0.15 < p_t^2 < 0.5$ *(GeV/c)*^{2}.

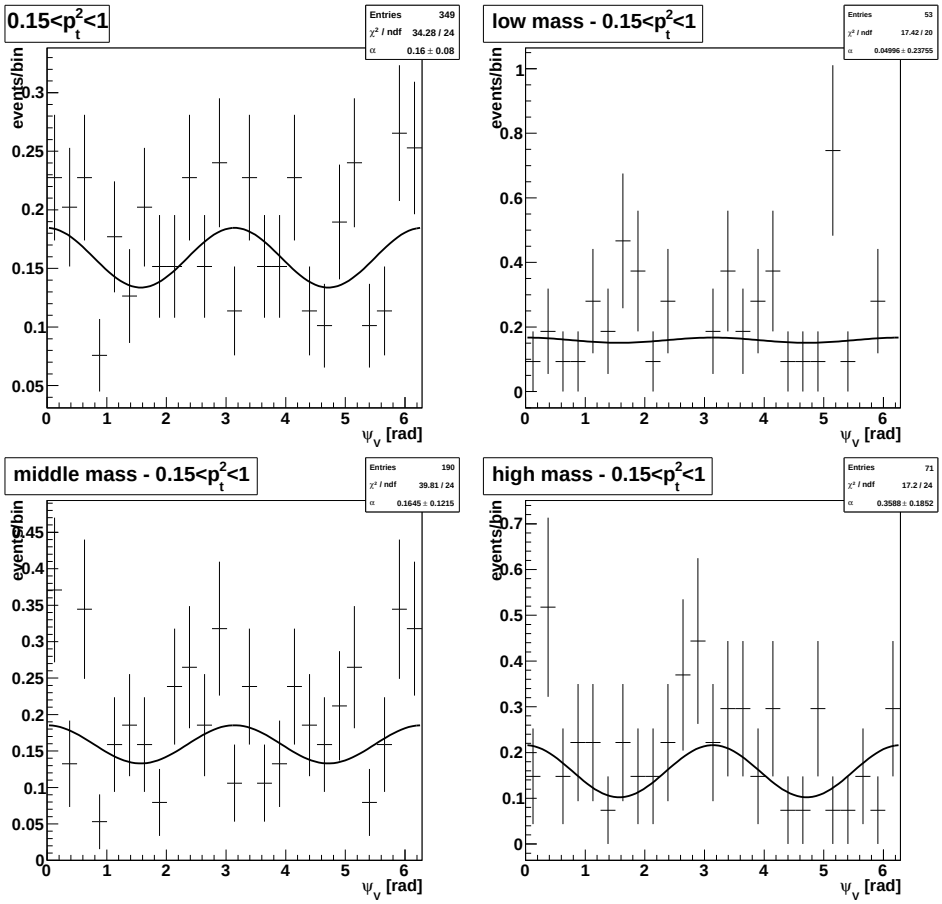

Figure G.8: *Angle ψ_V: $\omega\pi^0$-mass dependence. Inoherent scattering* $0.15 < p_t^2 < 1$ *(GeV/c)*^{2}.

Appendix H

Dependence on Q^2

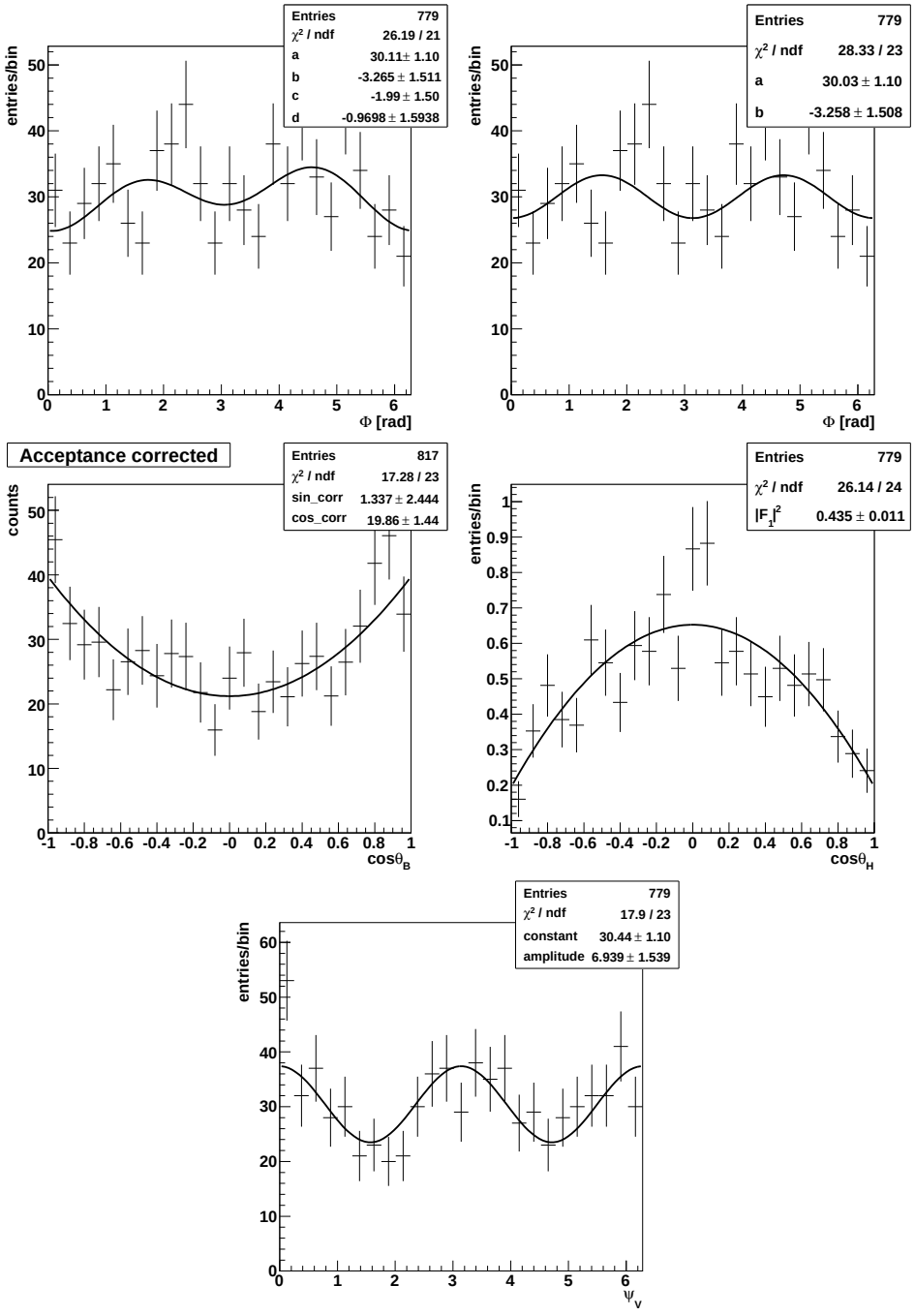

Figure H.1: *Acceptance corrected angular distributions with* $Q^2 > 0.1$ *(GeV/*c^2*)*^{2}.

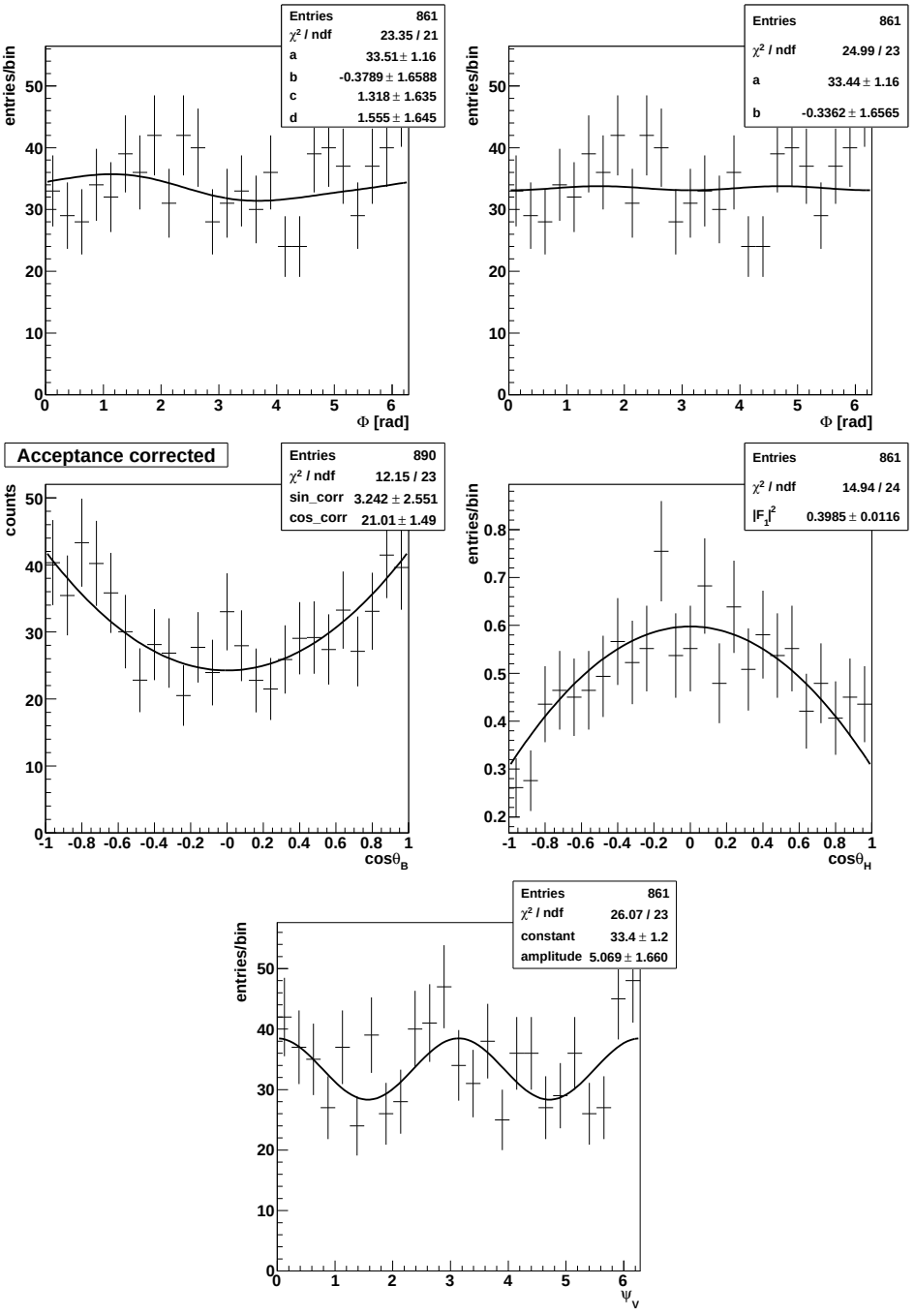

Figure H.2: *Acceptance corrected angular distributions with* $Q^2 < 0.1$ *(GeV/*c^2*)*^{2}.

Appendix I

Forward-backward asymmetry A_{FB}

The following four sets of histograms show the $\cos\theta$ distribution for real data (top-left), MC simulation (top-right), acceptance corrected data (bottom-left) and extracted forward-backward asymmtery A^i_{FB}, in dependence of the i-th bin symmetrical to the central value at $\cos\theta = 0$, and on the year of data taking (2004 and 2006).

The last two Figures correspond to the first two, with the additional cut $1.1 < m(\omega\pi^0) < 1.4$ GeV/c^2 imposed.

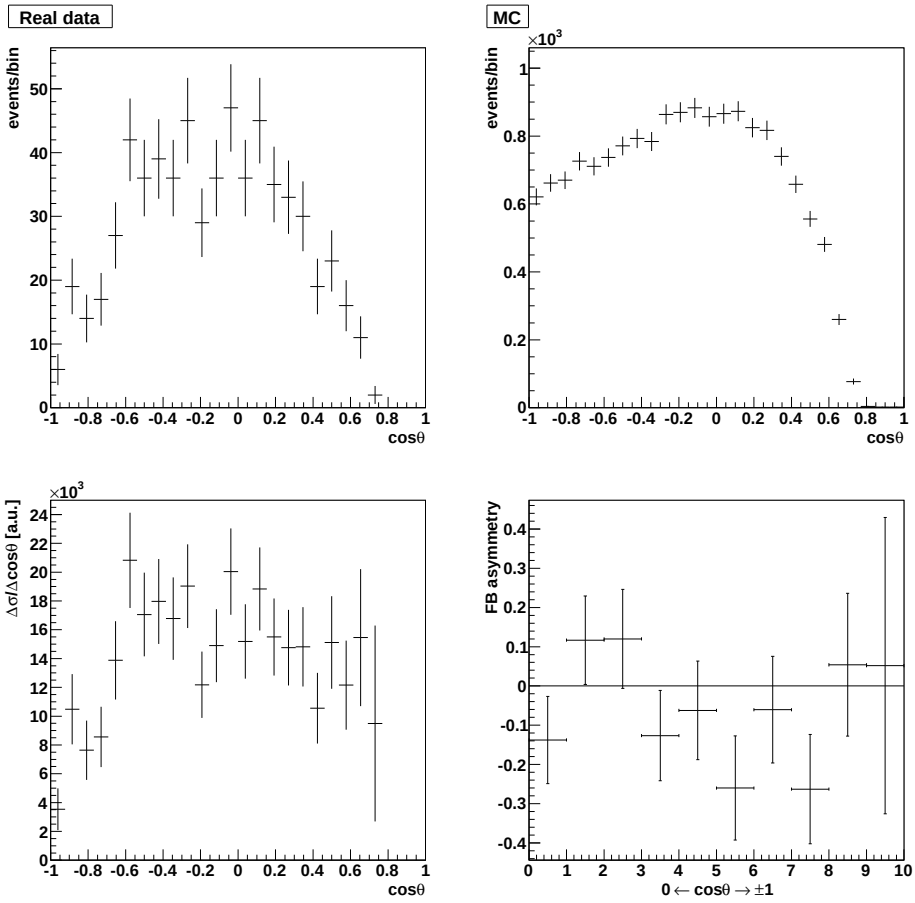

Figure I.1: *Real data, Monte Carlo data, acceptance corrected data and A_{FB} asymmetry - year 2004.*

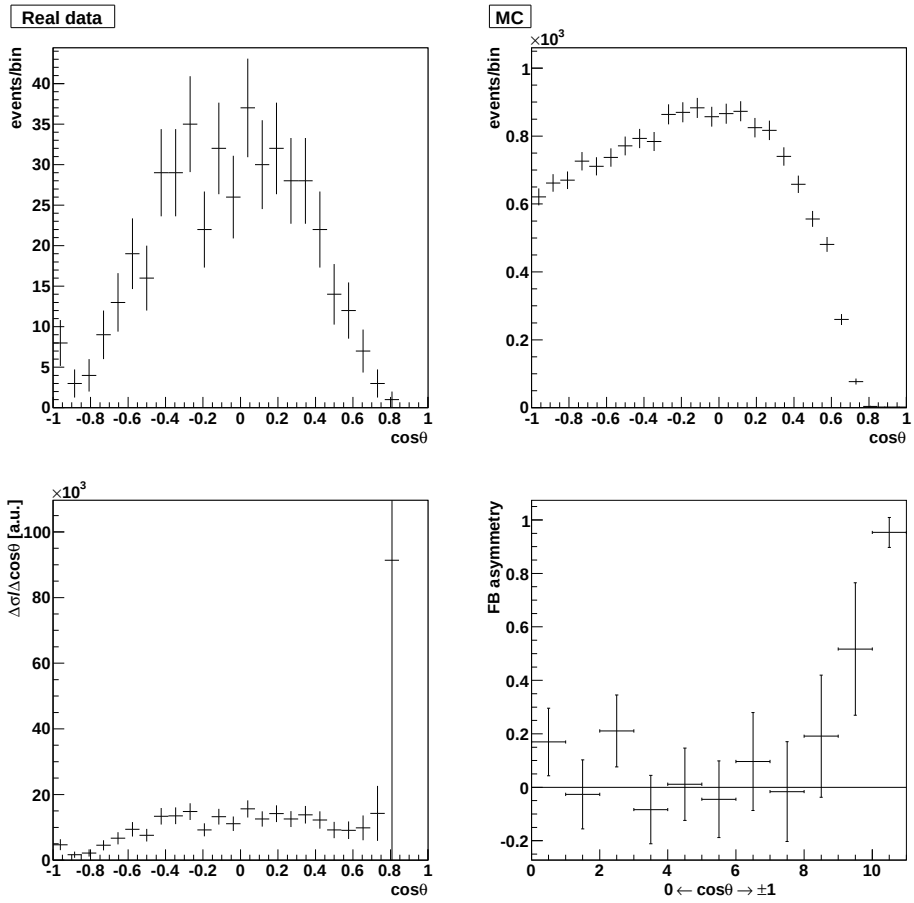

Figure I.2: *Real data, Monte Carlo data, acceptance corrected data and A_{FB} asymmetry - year 2006.*

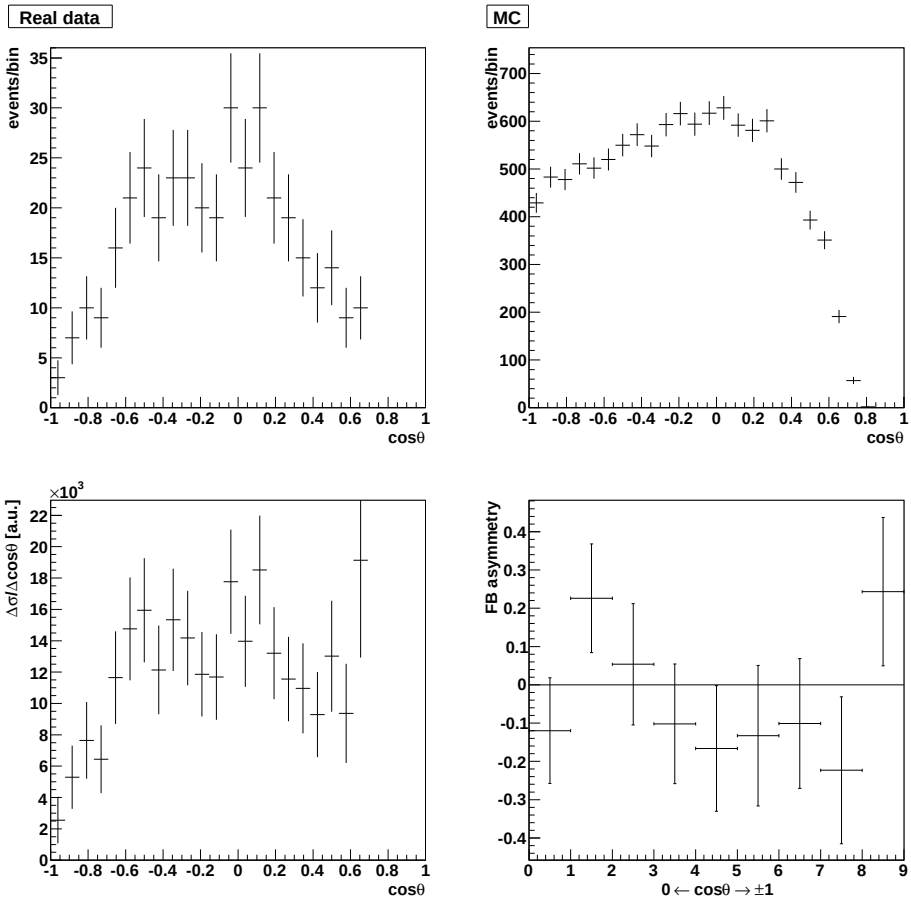

Figure I.3: *Real data, Monte Carlo data, acceptance corrected data and A_{FB} asymmetry - year 2004, $\omega\pi^0$-peak region.*

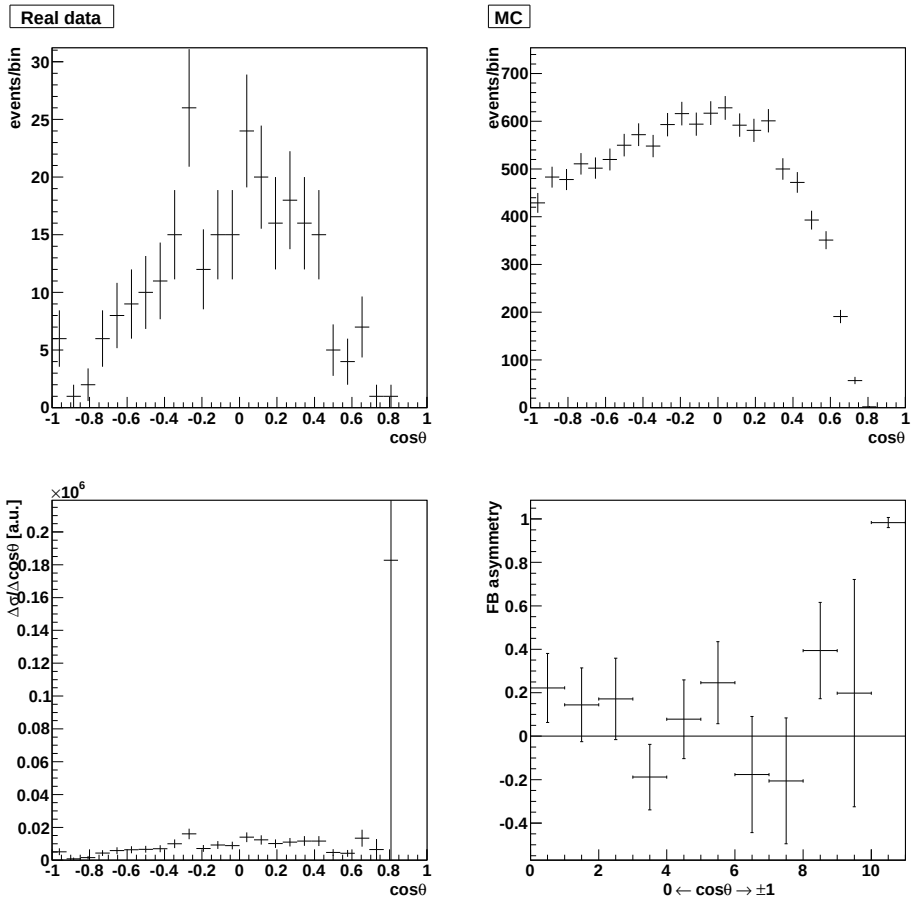

Figure I.4: *Real data, Monte Carlo data, acceptance corrected data and* A_{FB} *asymmetry - year 2006,* $\omega\pi^0$*-peak region.*

Acknowledgments

At the end of this "adventure", I am happy to feel myself obliged to thank the many people who helped me during these past years.

Prof. Martin Faessler, which gave me the opportunity to start the work within his group, and always showed me with kindness his interest for the work done. I could thus rejoin the elementary particle physics community after an *intermezzo* in the physics of low temperatures...

Prof. Wolfgang Dünnweber, without whose help very few of the lines in the previous pages could have been written. His vast experience and keen insight in every physical problem encountered along the way was always determinant for the successful completion of the present work.

Mrs Meike Dlaboha, which has honoured me with her friendship, for exquisitely chatting with me during the "hard times", and for the countless occasions in which she helped me fighting burocracy.

Dr. Dimitri Ryabchikov, for the nice discussions about the definition and role of spin analyzers.

Prof. Črtomir Zupančič, for the help about photon polarization topics in leptoproduction.

Dr. Jürgen Neumayr, for the pleasant daily conversations about the "this and that" during our traditional coffee times, unfortunately too soon interrupted by his leap into the "world of patents".

My colleagues and friends in Garching, past and present, which enriched my days with their company, their nice discussions and professional interaction with me: Jean-Francois, Tobias, Sabine, Zoha. It was a great pleasure to be a part of such an "international cluster"!

All the people in the COMPASS Collaboration, whose work made my work possible.

And, finally, a special thought für meine schöne Sibylle, for making my days beautiful even when it pours and all seems grey.

Thank you, Sib,
once more and as long time ago,
für deine Liebe und Geduld.

Bibliography

[A+80] D. Aston et al. Observation of an $\omega\pi^0$ state of mass 1.25 GeV produced by photons of energy 20-70 GeV. *Physics Letters B*, 92(1-2):211 – 214, 1980.

[A+84] M. Atkinson et al. A spin-parity analysis of the $\omega\pi^0$ enhancement photoproduced in the energy range 20 to 70 GeV. *Nuclear Physics B*, 243(1):1 – 28, 1984.

[A+92] E. Aker et al. The Crystal Barrel spectrometer at LEAR. *Nuclear Instruments and Methods in Physics Research Section A: Accelerators, Spectrometers, Detectors and Associated Equipment*, 321(1-2):69 – 108, 1992.

[A+04] C. Amsler et al. Study of antiproton annihilation on neutrons into $\omega\pi^-\pi^0$. *Nuclear Physics A*, 740(1-2):130 – 146, 2004.

[A+05a] E.S. Ageev et al. Measurement of the spin structure of the deuteron in the DIS region. *Physics Letters B*, 612(3-4):154 – 164, 2005.

[A+05b] E.S. Ageev et al. Search for the Pentaquark at COMPASS. *The European Physical Journal C - Particles and Fields*, 41(4):469 – 474, 2005.

[A+05c] V. Yu. Alexakhin et al. First Measurement of the Transverse Spin Asymmetries of the Deuteron in Semi-inclusive Deep Inelastic Scattering. *Phys. Rev. Lett.*, 94(20):202002, May 2005.

[A+06] E.S. Ageev et al. Gluon polarization in the nucleon from quasi-real photoproduction of high-pT hadron pairs. *Physics Letters B*, 633(1):25 – 32, 2006.

[A+07a] P. Abbon et al. The COMPASS experiment at CERN. *Nuclear Instruments and Methods in Physics Research Section A: Accelerators, Spectrometers, Detectors and Associated Equipment*, 577(3):455 – 518, 2007.

[A+07b] E.S. Ageev et al. A new measurement of the Collins and Sivers asymmetries on a transversely polarised deuteron target. *Nuclear Physics B*, 765(1-2):31 – 70, 2007.

[A+07c] V.Yu. Alexakhin et al. The deuteron spin-dependent structure function and its first moment. *Physics Letters B*, 647(1):8 – 17, 2007.

[A+07d] V.Yu. Alexakhin et al. Spin asymmetry and the spin-dependent structure function of the deuteron at low values of x and q^2. *Physics Letters B*, 647(5-6):330 – 340, 2007.

[A+08a] M. Alekseev et al. The polarised valence quark distribution from semi-inclusive DIS. *Physics Letters B*, 660(5):458 – 465, 2008.

[A+08b] C. Amsler et al. Review of Particle Physics. *Physics Letters B*, 667(1-5):1 – 6, 2008. Review of Particle Physics.

[A+09a] M. Alekseev et al. Collins and Sivers asymmetries for pions and kaons in muon-deuteron DIS. *Physics Letters B*, 673(2):127 – 135, 2009.

[A+09b] M. Alekseev et al. Gluon polarisation in the nucleon and longitudinal double spin asymmetries from open charm muoproduction. *Physics Letters B*, 676(1-3):31 – 38, 2009.

[AAB+67] C. W. Akerlof, W. W. Ash, K. Berkelman, C. A. Lichtenstein, A. Ramanauskas, and R. H. Siemann. Measurement of the pion form factor. *Phys. Rev.*, 163(5):1482–1497, Nov 1967.

[B+74] J. Ballam et al. A search for b and ϱ'(1250) production in the reaction $\gamma p \to p\pi^+\pi^-+$ neutrals at 2.8, 4.7 and 9.3 GeV. *Nuclear Physics B*, 76(3):375 – 399, 1974.

[B+88] J. E. Brau et al. Production and decay properties of the $\omega\pi^0$ state at 1250 MeV/c^2 produced by 20-GeV polarized photons on hydrogen. *Physical Review D*, 37(9), 1988.

[BD08] M. Bettinelli and W. Duennweber. Exclusive $\omega\pi^0$ production with muons. *The European Physical Journal A - Hadrons and Nuclei*, 38(2):155 – 158, 2008.

[BdGS04] E. Burtin, N. d'Hose, O.A. Grajek, and A. Sandacz. Angular distributions and $R = \sigma_L/\sigma_T$ for exclusive ρ^0 production. COMPASS Note 12, 2004.

[BKT96] G Baum, J Kyynrinen, and A Tripet. Compass: a proposal for a common muon and proton apparatus for structure and spectroscopy. Technical Report CERN-SPSLC-96-14. SPSLC-P-297, CERN, Geneva, 1996.

[C+75] S. U. Chung et al. Spin-parity analysis of the B meson. *Physical Review D*, 11(9):2426 – 2440, 1975.

[CA+] The COMPASS Collaboration, M. Alekseev, et al. Double spin asymmetry in exclusive ρ^0 muoproduction at COMPASS. *The European Physical Journal C - Particles and Fields*, 52(2):255 – 265.

[Chu] Suh Urk Chung. Spin formalisms. CERN, Geneva, 1969 - 1970.

[DK02] A. Donnachie and Yu S. Kalashnikova. Light-Quark Vector-Meson Spectroscopy. *AIP Conference Proceedings*, 619(1):5 –, 2002.

[Don05] A. Donnachie. Evidence for quark spin-flip in pomeron exchange. *Physics Letters B*, 611(3-4):255 – 259, 2005.

[GKS02] O. A. Grajek, A. Korzenev, and A. Sandacz. Exclusive ρ^0 and ϕ production from COMPASS 2002 data. COMPASS Note 15, 2002.

[GPSS70] F. J. Gilman, J. Pumplin, A. Schwimmer, and L. Stodolsky. Helicity conservation in diffraction scattering. *Physics Letters B*, 31(6):387 – 390, 1970.

[JW59] M. Jacob and G. C. Wick. On the general theory of collisions for particles with spin. *Annals of Physics*, 7(4):404 – 428, 1959.

[KKMN08] Vladimir Kolosov, Oleg Kouznetsov, Alain Magnon, and Frank Nerling. Present performances of COMPASS electromagnetic calorimetry from data analysis. COMPASS Note 5, 2008.

[Led95] A. A. Lednev. Electron shower transverse profile measurement. *Nuclear Instruments and Methods in Physics Research Section A: Accelerators, Spectrometers, Detectors and Associated Equipment*, 366(2-3):292 – 297, 1995.

[MacARS61] B. C. Maglić, L. W. Alvarez, A. H. Rosenfeld, and M. L. Stevenson. Evidence for a $T = 0$ Three-Pion Resonance. *Phys. Rev. Lett.*, 7(5):178–182, Sep 1961.

[Moi03] M. A. Moinester. Hybrid Meson Production via Pion Scattering from Nuclear Coulomb Field. Hybrid Meson Production via Ultra-Peripheral Pion Scattering from a Virtual Photon Target. (hep-ex/0301023):10 p, Jan 2003.

[SAMacR62] M. L. Stevenson, L. W. Alvarez, B. C. Maglić, and A. H. Rosenfeld. Spin and Parity of the ω Meson. *Phys. Rev.*, 125(2):687–690, Jan 1962.

[SW73] K. Schilling and G. Wolf. How to analyse vector-meson production in inelastic lepton scattering. *Nuclear Physics B*, 61:381 – 413, 1973.